Derivation and analysis of hydrological parameters from ground-based GNSS stations

vorgelegt von
Tzvetan Simeonov Simeonov
ORCID: 0000-0001-9007-7084

von der Fakultät VI Planen Bauen Umwelt
der Technischen Universität Berlin
zur Erlangung des akademischen Grades

Doktor der Naturwissenschaften
Dr. rer. nat.

Promotionsausschuss:
Vorsitzender: Prof. Frank Flechtner
Gutachter: Prof. Jens Wickert
Gutachter: Doz. Guergana Guerova
Gutachter: Prof. Felix Norman Teferle

Tag der wissenschaftlichen Aussprache: 3. Dezember 2020

Berlin 2021

It takes two parents to raise a child.
In real life I only had one.
It takes one supervisor to create a scientist.
In my academic life I had two.

Dedicated to my mother
and to my PhD mother and father Guergana Guerova and Jens Wickert.

Abstract

The ability to measure multiple environmental parameters, such as atmospheric water vapour, soil moisture and snow height with the same hardware is the main advantage of Global Navigation Satellite System (GNSS) environmental measurements over other observation techniques. In this thesis state-of-art ground-based GNSS methods for environmental monitoring are used to derive atmospheric water vapour and soil moisture, to observe their dynamics on local, regional and global scales and to analyse both short-term case studies and long-term climatological monitoring.

The GNSS Meteorology method of observing the atmospheric water vapour through the GNSS signal delay in the atmosphere is applied to several stations in Bulgaria and compared to simulations with the Weather Research and Forecast (WRF) model, as well as to radiosonde measurements. All the data from these experiments is stored in the Sofia University Atmospheric Data Archive (SUADA), specifically developed as a foundation for the atmospheric studies in this work. A study of the 2007 heatwave for station Sofia shows 6% lower Integrated Water Vapour (IWV), compared to the 2001-2010 mean. A trend analysis of all available GNSS and radiosonde time series for station Sofia for the time period between 2000-2019 shows an increase in the IWV of $0.8\frac{kg}{m^2}/decade$ on average from reprocessed GNSS datasets and an increase of $0.6\frac{kg}{m^2}/decade$ from the radiosonde measurements. A dedicated GNSS processing campaign using the NAPEOS software and employing a Precise Point Positioning (PPP) strategy is undertaken for measurements of IWV over a network of Bulgarian stations for one year. The GNSS derived IWV is used to evaluate the seasonal and diurnal variations of the WRF model and to analyse severe weather events.

The single antenna ground-based GNSS Reflectometry (GNSS-R) method is used to estimate the soil moisture Volumetric Water Content (VWC) and snow height in GNSS stations in Germany and on a global scale. A dedicated software package for processing signal strength observations from GNSS ground stations is further developed to estimate soil moisture and snow height using the GNSS-R method. The software is validated, showing 0.98 correlation with data from an independent processing center. The GFZ Reflectometry and Atmospheric Database (GRAD) is designed to archive soil moisture observations from GNSS-R and Time Domain Reflectometry (TDR), as well as atmospheric parameters and model data.

In two experimental stations (Marquardt and Fürstensee) in Germany, VWC is monitored between 2014-2019 with specially installed high-end and low-cost GNSS antennae and receivers. The GNSS-R VWC retrievals are compared to collocated TDR and gravimetric measurements. The results show that the soil moisture retrievals, obtained from the low-cost receivers, show lower correlation (0.67), than the high-end receivers (0.75) when compared to TDR. Gravimetric measurements are used to calibrate the residual VWC from GNSS-R. An analysis of the error budget of the GNSS-R observations of soil moisture is done, based on the high-end receiver results.

All stations in the International GNSS Service (IGS) global network are individually tested for soil moisture observation capabilities. Out of 506 stations in this global network only 30 stations (6%) are found to satisfy the requirements for GNSS-R observations, namely: reflections coming from flat grasslands. The Volumetric Water Content (VWC) observations are compared with results from the ECMWF Reanalysis model's 5^{th} implementation - ERA5. The comparisons show fair correlation between the two datasets with ERA5 overestimating the residual VWC in most sites. Each station is discussed separately with an emphasis on station surroundings and climate conditions.

A new 1-dimensional empirical soil moisture model is developed to quantify the relation between VWC in the soil and atmospheric water vapour. Several different implementations of the model, based on temperature, water vapour and precipitation are discussed and compared to GNSS-R and TDR soil moisture observations in experimental station Marquardt. The resulting model is applied to GNSS stations from the IGS network for further assessment. The comparisons with GNSS-R derived soil moisture show higher correlation, than the soil moisture, derived in the ERA5 and are higher than 0.6. Contrary to the ERA5, the model does not overestimate the residual soil moisture in the stations.

A new technique for snow height measurement is validated in a GNSS-R setup in Antarctic station Neumayer III. This new technique shows improved characteristics to the classical single antenna ground-based GNSS-R snow height determination method. The validation is done in an environment of constant snow accumulation. The results from the different techniques show very similar results with correlation between the de-trended GNSS-R and snow buoy measurements of above 0.85. Snow height is also determined in the 7 IGS stations within the continental climate zones. The results are compared with the ERA5, local snow height measurements and climate normals.

Zusammenfassung

Das Erfassen von Umweltdaten mit dem Globale Navigationssatellitensystem (GNSS) hat gegenüber anderen Beobachtungstechniken einen entscheidenden Vorteil: es können mehrere Parameter wie zum Beispiel der atmosphärischer Wasserdampf, Bodenfeuchtigkeit und Schneehöhen mit einem einzigen Hardwaresystem erfasst werden. In dieser Arbeit wird aufgezeigt wie modernste bodengestützte GNSS-Methoden zur Umweltüberwachung eingesetzt werden können um atmosphärischen Wasserdampf und Bodenfeuchte abzuleiten und deren Variabilität auf lokaler, regionaler und globaler Ebene zu analysieren und sie sowohl in kurzfristige Fallstudien als auch in langfristige klimatologische Beobachtungen zu implementieren.

Die GNSS-Meteorologie-Technologie nutzt Verzögerungen in den GNSS Signalen zur Beobachtung des atmosphärischen Wasserdampfs in der Atmosphäre. Diese Methode wird auf mehrere Stationen in Bulgarien angewandt und mit Simulationen mit dem Modell für Wetterforschung und -vorhersage (WRF) sowie mit Radiosondenmessungen verglichen. Alle Daten aus diesen Experimenten werden im Atmosphärendatenarchiv der Universität Sofia (SUADA) gespeichert, welches speziell für die atmosphärischen Studien in dieser Arbeit angelegt wurde.

Eine Untersuchung der Hitzewelle im Sommer 2007 für die Station Sofia zeigt eine um 6% niedrigere integrierte Wasserdampfmenge (IWV) im Vergleich zum Mittelwert von 2001-2010. Eine Trendanalyse aller verfügbaren GNSS- und Radiosonden-Zeitreihen für die Station Sofia im Zeitraum zwischen 2000-2019 zeigt einen Anstieg des IWV von durchschnittlich 0,8$\frac{kg}{m^2}/Dekade$ aus den wiederaufbereiteten GNSS-Datensätzen und einen Anstieg von 0,6$\frac{kg}{m^2}/Dekade$ aus den Radiosonden-Messungen. Eine Kampagne zur Messungen des IWV wird über die Dauer von einem Jahr über ein Netzwerk bulgarischer Stationen durchgeführt. Das Ziel ist es die Verarbeitung der GNSS-Signale mit der NAPEOS-Software unter Anwendung der präzisen Punktpositionierung (PPP) zu testen. Der abgeleitete IWV wird zur Validierung der jahreszeitlichen und tageszeitlichen Schwankungen des WRF-Modells und zur Analyse von Unwetterereignissen verwendet.

Die bodengebundene GNSS Reflektometrie (GNSS-R) Methode wird zur Abschätzung des volumetrischen Wassergehalts (VWC) und der Schneehöhe an GNSS-Stationen in Deutschland und auf globaler Ebene verwendet. Ein spezielles Software-Paket zur Verarbeitung von Signalstärke-Beobachtungen von GNSS-Bodenstationen wird weiterent-

wickelt, um Bodenfeuchte und Schneehöhe mit Hilfe der GNSS-R-Methode abzuschätzen. Die Software ist validiert und zeigt eine Korrelation von 0,98 mit Daten eines unabhängigen Verarbeitungszentrums. Die GFZ-Reflektometrie- und Atmosphärendatenbank (GRAD) wurde erstellt um Bodenfeuchtigkeitsbeobachtungen von GNSS-R und Time Domain Reflectometry (TDR) sowie atmosphärische Parameter und Modelldaten zu archivieren.

Zwischen 2014-2019 wurde der VWC an zwei Messstationen (Marquardt und Fürstensee) in Deutschland mit speziell installierten hochwertigen sowie kostengünstigen GNSS-Antennen und -Empfängern überwacht. Die GNSS-R Messungen des VWC- werden mit Ergebnissen der TDR- sowie gravimetrischen Methoden verglichen. Im Vergleich zu den TDR Messungen des Bodenfeuchtegehalts weisen die kostengünstigen Empfänger eine geringere Korrelation (0,67) als die High-End-Empfänger (0,75) auf. Die gravimetrischen Messungen werden zur Kalibrierung der VWC-Restbodenfeuchte von GNSS-R verwendet. Eine Analyse des Fehlerbudgets der GNSS-R-Beobachtungen der Bodenfeuchte wird auf der Grundlage der Ergebnisse der High-End-Empfänger durchgeführt.

Alle Stationen im globalen Netzwerk des Internationalen GNSS-Dienstes (IGS) werden einzeln auf ihre Tauglichkeit zur Beobachtung der Bodenfeuchte getestet. Von den 506 Stationen in diesem globalen Netzwerk erfüllen nur 30 Stationen (6%) die Voraussetzung für GNSS-R Beobachtungen: die Reflexionen sollten von flachem Grasland kommen. Die Beobachtungen des volumetrischen Wassergehalts (VWC) werden mit den Ergebnissen der 5. Version des ECMWF-Reanalysemodells - ERA5 - verglichen. Die Vergleiche zeigen eine gute Korrelation zwischen beiden Datensätzen, wobei ERA5 den Restwassergehalt an den meisten Standorten überschätzt. Die Korrelationen werden in der Arbeit für jede Station separat diskutiert, wobei der Schwerpunkt auf dem Einfluss der Umgebungsbedingungen der Station und den klimatischen Bedingungen liegt.

Ein neues 1-dimensionales empirisches Bodenfeuchtemodell wird entwickelt, um die Beziehung zwischen der Bodenfeuchte und dem Wassergehalt der Atmosphäre zu quantifizieren. Verschiedene Modellversionen, die auf Temperatur, Wasserdampf und Niederschlag basieren, werden diskutiert und mit GNSS-R- und TDR-Bodenfeuchtigkeitsbeobachtungen in der Versuchsstation Marquardt verglichen. Das resultierende Modell wird zur weiteren Bewertung auf GNSS-Stationen aus dem IGS-Netz angewendet. Vergleiche mit der von GNSS-R abgeleiteten Bodenfeuchte zeigen eine höhere Korrelation (>0,6) als die aus ERA5 abgeleitete Bodenfeuchte. Im Gegensatz zum ERA5 überschätzt das neue Modell die Restbodenfeuchte in den Stationen nicht.

Eine neue Methode zur Schneehöhenmessung wird in einem GNSS-R-Aufbau in der Antarktisstation Neumayer III validiert. Diese neue Technik zeigt verbesserte Eigenschaften zu der klassischen bodengebundenen GNSS-R-Schneehöhenbestimmung mit einer einzigen Antenne. Die Validierung erfolgt in einer Umgebung mit konstanter Schneedecke. Die Ergebnisse der verschiedenen Messmethoden zeigen sehr ähnliche Ergebnisse mit einer

Korrelation von über 0,85 zwischen GNSS-R- und Schneebojenmessungen. Die Schneehöhe wird auch in den 7 IGS-Stationen innerhalb der kontinentalen Klimazonen bestimmt. Die Ergebnisse werden mit dem ERA5, den lokalen Schneehöhenmessungen und den klimatischen Mittelwerten verglichen.

Contents

Abstract v

Zusammenfassung vii

Motivation xvii

1 The Global Water Cycle 1

1.1 Atmospheric Water vapour . . . 3
1.2 Soil Moisture . . . 5
1.3 Snow cover . . . 7

2 Established techniques for monitoring the water cycle 9

2.1 Atmospheric Water Vapour . . . 9
2.1.1 Radiosounding . . . 9
2.1.2 Water Vapour Radiometers . . . 11
2.1.3 Satellite measurements . . . 12
2.2 Soil Moisture . . . 13
2.2.1 Time and Frequency Domain Reflectometry . . . 13
2.2.2 Gravimetric measurements . . . 14
2.2.3 Satellite measurements . . . 14
2.3 Snow cover . . . 15
2.3.1 Snow depth poles . . . 15
2.3.2 Snow buoys . . . 16
2.3.3 Satellite observations of snow depth . . . 16
2.4 Numerical modelling of atmospheric water vapour and soil moisture . . . 16
2.4.1 1D soil moisture bucket modelling . . . 17
2.4.2 The Weather Research and Forecasting (WRF) NWP model . . . 18
2.4.3 The ERA reanalysis . . . 19
2.5 Limitations of the established techniques . . . 20
2.5.1 IWV observations and modelling . . . 20
2.5.2 Soil moisture observations and modelling . . . 21
2.5.3 Snow height observations and modelling . . . 23

3 Water cycle monitoring with GNSS **25**
3.1 GNSS and selected basics of signal propagation 25
3.2 GNSS tropospheric delays 28
3.2.1 GNSS observation equations 28
3.2.2 Atmospheric refraction 29
3.2.3 Mapping functions 30
3.2.4 Zenith Tropospheric Delay 32
3.3 GNSS processing software 32
3.3.1 NAPEOS 33
3.3.2 EPOS 34
3.3.3 Bernese GNSS Software 35
3.4 Water vapour monitoring 36
3.5 Earth surface observation using GNSS reflected signals 39
3.5.1 Soil moisture 39
3.5.2 Snow height 45

4 GNSS water vapour measurements **47**
4.1 State-of-the-art of GNSS meteorology in Bulgaria 47
4.2 Sofia University Atmospheric Data Archive 49
4.2.1 2007 heat wave observations at IGS station Sofia 50
4.2.2 Long-term monitoring at IGS station Sofia. 52
4.3 SUGAC first processing campaign - 2013. 58
4.3.1 Evaluation of the WRF model 59
4.3.2 Seasonal variations 61
4.3.3 Diurnal cycle 64
4.3.4 Hailstorm events 65
4.3.5 Precipitation efficiency 67
4.3.6 Comparison between PPP and DGNSS processings 68

5 GNSS Reflectometry soil moisture measurements **71**
5.1 Data processing routine 72
5.1.1 GFZ soil moisture retrieval software 72
5.1.2 GFZ Reflectometry and Atmospheric Database (GRAD) 75
5.2 Validation of GFZ soil moisture retrieval software 75
5.3 Monitoring at stations Marquardt and Fürstensee 79
5.3.1 Station description Marquardt 79
5.3.2 Soil moisture at station Marquardt derived from L2C and L5 data . 81
5.3.3 Using low-cost single frequency receivers 88
5.3.4 Gravimetric measurements in station Marquardt 92
5.3.5 Station description Fürstensee 93

5.3.6 Monitoring soil moisture in station Fürstensee . . . 94
5.4 Soil moisture monitoring with the IGS network . . . 97
5.4.1 Visby, Sweden . . . 100
5.4.2 Fredericton, Canada . . . 103
5.4.3 Mbarara, Uganda . . . 107
5.4.4 Tsukuba, Japan . . . 108
5.4.5 Marlborough, New Zealand . . . 110
5.5 GNSS Reflectometry soil moisture error budget . . . 111
5.5.1 Effects influencing precision . . . 112
5.5.2 Effects influencing accuracy . . . 115
5.6 Recommendations to IGS network sites . . . 115

6 Empirical soil moisture model 117
6.1 Soil moisture model . . . 117
6.2 Soil moisture model design iterations . . . 119
6.3 Soil moisture model validation . . . 121

7 GNSS Reflectometry for snow height monitoring 125
7.1 Snow height monitoring at Antarctic station Neumayer III . . . 125
7.2 Snow height monitoring at IGS stations . . . 131
7.2.1 Visby, Sweden . . . 133
7.2.2 Metsahovi, Finland . . . 135
7.2.3 Olsztyn, Poland . . . 136
7.2.4 Calgary, Canada . . . 137
7.2.5 Pickle Lake, Canada . . . 139
7.2.6 Fredericton, Canada . . . 140
7.2.7 Shediac, Canada . . . 141

Conclusions and outlook 143

List of References 166

List of Figures 172

List of Tables 174

Abbreviations 175

Acknowledgements 179

A Used instruments **181**
A.1 Javad TRE_G3TH GNSS receiver . . . 181
A.2 Javad GrAnt GNSS antenna . . . 181
A.3 Antcom S67 GNSS antenna . . . 182
A.4 U-blox GNSS antenna and receiver . . . 182
A.5 Vaisala WXT520 combined meteorological sensor . . . 183
A.6 Vaisala radiosondes . . . 183
A.7 TDR sensor . . . 183

B Used software **185**
B.1 Sofia University Atmospheric Data Archive (SUADA) . . . 185
B.1.1 SUADA structure . . . 186
B.1.2 SUADA datasets . . . 189
B.2 GFZ Reflectometry and Atmospheric Database (GRAD) . . . 192
B.3 RINEX data format . . . 193

C Köppen climate classification **195**

D List of IGS stations and description **199**
D.1 List of stations . . . 199
D.2 Description of individual stations . . . 202
D.2.1 Metsahovi, Finland . . . 202
D.2.2 Olsztyn, Poland . . . 203
D.2.3 Redu, Belgium . . . 204
D.2.4 Nicosia, Cyprus . . . 205
D.2.5 Noto, Italy . . . 206
D.2.6 Mitchell, Australia . . . 207
D.2.7 Boolardy station, Australia . . . 208
D.2.8 Parkes, Australia . . . 209
D.2.9 Sydney, Australia . . . 210
D.2.10 Ascention Island . . . 211
D.2.11 Kourou, French Guiana . . . 212
D.2.12 Alofi, Niue . . . 213
D.2.13 Funafuti, Tuvalu . . . 214
D.2.14 Lombrum, Papua New Guinea . . . 215
D.2.15 Hartebeesthoek, South Africa . . . 216
D.2.16 Mafikeng, South Africa . . . 217
D.2.17 Thohoyandou, South Africa . . . 218
D.2.18 Sutherland, South Africa . . . 219
D.2.19 Calgary, Canada . . . 220

D.2.20 Pickle Lake, Canada 221
D.2.21 Shediac, Canada 222
D.2.22 Torrance, USA 223
D.2.23 Curitiba, Brazil 224

Motivation

Currently there are more than 20 000 ground-based GNSS stations, installed worldwide. They belong to private networks, government agencies and research institutes. Each one of these stations has the potential to provide data for environmental monitoring but this potential has been exploited mainly for monitoring tropospheric water vapour.

The motivation to start this research is to demonstrate, that the data from the available GNSS sites can be utilized beyond their direct purpose of deriving differential corrections and positioning applications. All of these stations are affected by two distinct error sources: tropospheric delays and multipath. These error sources for the positioning applications can be used as signals for environmental research. In this thesis available European and global GNSS networks are used to analyse the state of the atmosphere and soils in the surroundings of more than 500 stations. These stations provide the opportunity to monitor atmospheric water vapour, soil moisture and snow height globally, systematically and homogeneously in order to contribute to global climate studies, as well as the analysis of severe weather events and natural hazards. The ability to measure multiple environmental parameters with the same hardware is the main advantage of GNSS environmental measurements over other observation techniques.

The aim of this work is the derivation and analysis of hydrological parameters from ground-based GNSS stations. To achieve this aim, the three distinct and related objectives are formulated. The first objective is the derivation and analysis of GNSS derived atmospheric water vapour. The second objective is to develop and apply the GNSS Reflectometry (GNSS-R) method for short- and long-term monitoring of soil moisture and snow height. The third objective is to quantify the relation between atmospheric water vapour and soil moisture and develop an empirical model for soil moisture using GNSS water vapour observations.

GNSS Meteorology is an established field in meteorological research in the past more than 20 years. Integrated Water Vapour IWV observations with high spatial and temporal resolution are widely used in weather forecasting, analysis of severe weather events and are assimilated operationally into numerous Numerical Weather Prediction NWP models throughout the world. The areas, covered by GNSS Meteorology observations are spreading further throughout the globe, but still large regional gaps need to be filled.

GNSS Reflectormetry is a relatively new approach for observing properties of reflective surfaces. Soil moisture derivation from ground-based GNSS stations is an emerging topic in the last 12 years. This approach for soil moisture monitoring is not as mature and wide spread, as GNSS Meteorology, although both methods use the same basic infrastructure. The opportunity to observe more than water vapour with a large GNSS network on a global scale has not yet been exploited. The observation methodology of GNSS-R is very challenging, giving large opportunities for incorporating previously unchallenged large global networks of stations. The benefits of expanding the derivation of products from such global networks are significant. With the spread of low-cost GNSS solutions, this opportunity shows an even larger potential. Additionally the same methodology can be applied to stations in higher latitudes for the derivation of snow height in the winter periods in parallel to the soil moisture observations during summer.

The GNSS Meteorology and GNSS-R fields will benefit greatly from the deployment of new GNSS satellites and constellations. The application of the methodologies, used in this thesis will be expanded with the commissioning of the Galileo constellation and of the next generation of satellites from GPS and GLONASS, providing denser observations with higher temporal resolutions and better observation accuracy. The software packages, developed for this thesis, can serve as a basis for these future developments.

In this thesis measurement techniques for these three different components (atmospheric water vapour, soil moisture and snow) of the water cycle on the Earth are discussed. In chapter 2 the established techniques of measuring atmospheric water vapour and soil moisture will are summarized. New techniques, such as the innovative GNSS ground-based techniques, described in chapter 3 can contribute to a more complete understanding of the observed processes. In chapter 4 the results form the GNSS Meteorology studies are summarized. Chapter 5 is dedicated to the GNSS-R soil moisture retrievals. The focus in chapter 6 falls on the interaction between the atmospheric water vapour and liquid water in soils. Snow height observations with GNSS-R are presented in chapter 7.

Chapter 1

The Global Water Cycle

Water is the only substance on the planet Earth, which in naturally occurring conditions exists in major quantities in all three phases: solid - ice, liquid - liquid water and gas - water vapour. These water phases can be found in the Atmosphere, Biosphere, Cryosphere and Geosphere, forming its own sphere - the Hydrosphere. Water is essential to life on Earth due to its biochemical and physical properties.

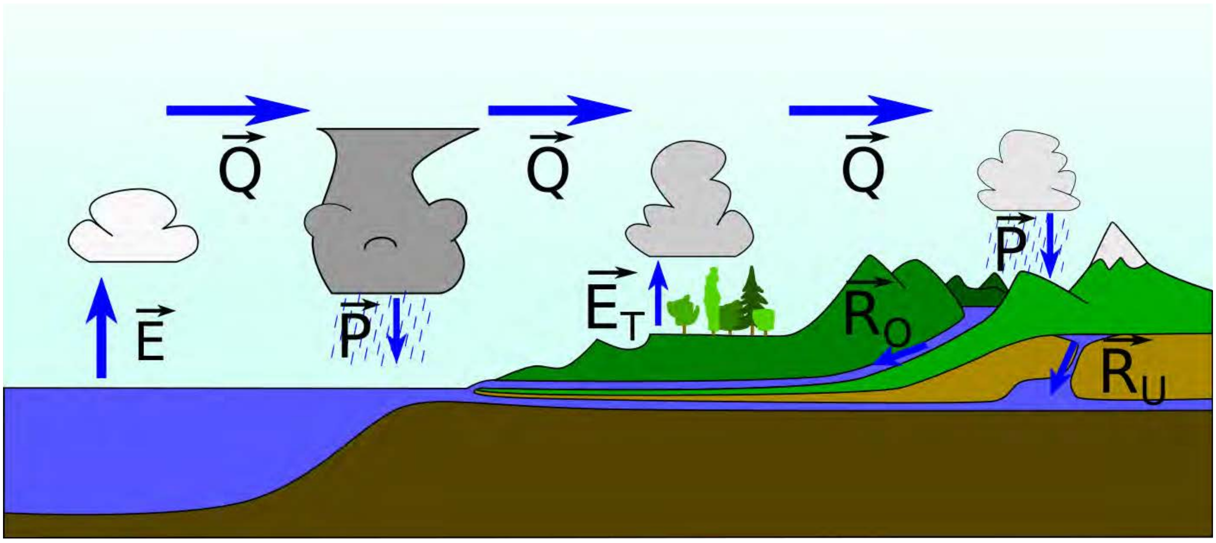

Figure 1.1: Water cycle diagram, showing the sinks and sources of water in every water reservoir - oceans, atmosphere, cryosphere, surface and ground water ($\vec{E}$ - evaporation, $\vec{E_T}$ - evapotranspiration, $\vec{P}$ - precipitation, $\vec{R_O}$ - surface runoff, $\vec{R_U}$ - groundwater runoff, $\vec{Q}$ - advection of water vapour in the atmosphere).

Water vapour is one of the major gases in the troposphere (lower 12 km of the atmosphere). Its quantity is between 0 and 7% of the volume of the dry air (4% on average). It is the most important greenhouse gas, contributing to a positive feedback loop, increasing the strength of the greenhouse effect (*Raval and Ramanathan*, 1989). It is also an important carrier of latent heat, transporting energy between ocean and land in the atmosphere. Water vapour is the most mobile form of water in Earth's water cycle. There are three major sources of water vapour in the atmosphere: soils and water bodies (oceans, seas, lakes and rivers) through evaporation, ice/snow cover through sublimation and vegetation through evapotranspiration.

Water in its liquid form is the most prominent variable in Earth's soils. Soil moisture is the third most dynamic storage of water in the hydrological cycle of the Earth, after water vapour in the atmosphere and surface runoff water in rivers and lakes. Although soil moisture is one of the smallest water reservoirs (shown in figure 1.2), it is crucial for the water cycle. Soils, rivers and lakes are the interface of interaction between the atmosphere and the ground water. Liquid water is the most efficient and abundant solvent on Earth, thus being essential to the transportation of minerals, organic chemicals and nutrients for the biosphere (*Brady and Weil*, 2013).

Earth ice caps, together with ice crystals in the upper troposphere contribute to the positive feedback loop of increasing the Earth's surface albedo, thus balancing the greenhouse effect, caused by the water vapour and other greenhouse gases in the atmosphere. Moreover, the interaction between all these water reservoirs plays a key role in the weather and climate on the Earth's surface. While being distinct, the dynamics of the water storages are interconnected (shown in figure 1.2).

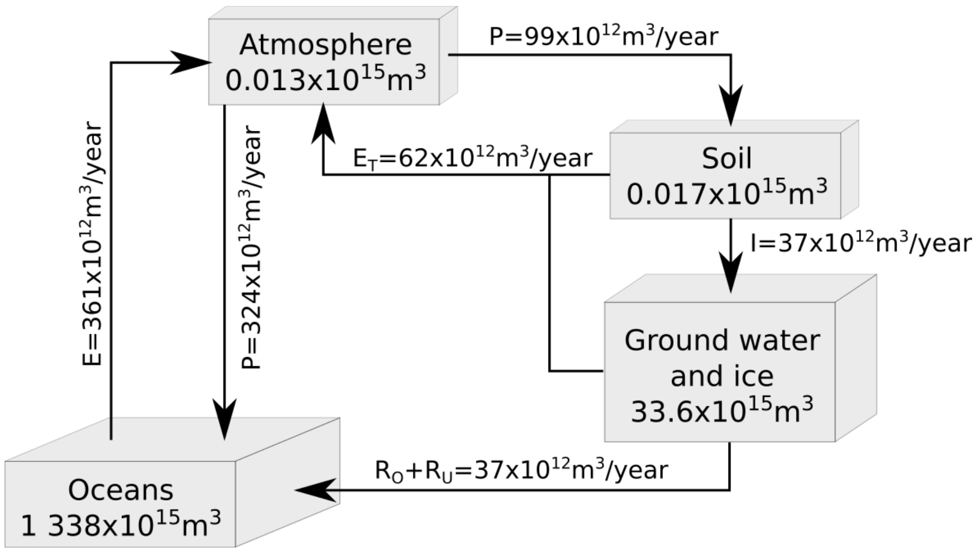

Figure 1.2: Water balance and storages in the oceans, land and atmosphere and absolute values of fluxes between these media on a yearly basis (E - evaporation, E_T - evapotranspiration, P - precipitation, R_O - surface runoff, R_U - groundwater runoff, I - infiltration) (*Oki and Kanae*, 2006).

Form of water	Total Volume (km^3)	Mean Depth (m)	Share (%)	Residence Time
World ocean	1 338 000 000	3700	96.539	2500 years
Ice and snow	24 364 000	2160	1.757	50 years
Ground water	23 400 000	174	1.688	1400 years
Lakes	176 400	42	0.013	5 years
Soil moisture	16 500	0.2	0.0012	1 year
Atmospheric water	12 900	0.025	0.0009	8 days

Table 1.1: World water reserves (*Anderson and McDonnell*, 2005, p.14).

1.1 Atmospheric Water vapour

The most dynamic water reservoir on the Earth is the atmosphere. Water vapour has relatively short lifetime in the atmosphere - between 7-10 days, which means that all water molecules in the atmosphere are fully renewed on average 45 times in a year (table 1.1). The atmosphere's water capacity is smallest, but since the density is smallest as well, it allows water to be transported faster than in any other medium. Water resides far longer in rivers, lakes, the soil and underground (see table 1.1), while the world ocean and the cryosphere are the most inert water storages (*Anderson and McDonnell*, 2005).

Apart from transport of mass, the water cycle is also a means of transporting latent heat. The specific latent heat capacity of water is very high, meaning that $1.996kJ$ of energy is required for heating $1g$ of water by $1K$, while $4.1J$ of energy is necessary for evaporating $1g$ of water. This energy during evaporation is consumed and during condensation is released back into the atmosphere, thus transferring heat energy from the place of evaporation to the place of condensation (*Speight et al.*, 2005).

In the recent decades the water cycle in the atmosphere has intensified, as a result of the changes in the global climate (*Huntington*, 2006). As the temperature of the Earth's surface and atmosphere increases, so does the moisture holding capacity of the atmosphere. Atmospheric water vapour is expected to increase in the warming climate by between 5 and 12% per $1K$, according to the latest evidence, based on the Clausius Clapeyron equation (*O'Gorman and Muller*, 2010). Water vapour released into the atmosphere contributes to a positive feedback loop in increasing global temperature, which leads to higher amounts of evaporation and higher water vapour holding capacity of air (*Raval and Ramanathan*, 1989). Water vapour released into the atmosphere adds $1K$ to global warming for every $1K$ contributed by man through greenhouse gas emissions (*Dessler and Sherwood*, 2009). The contribution of water vapour to the greenhouse effect can be observed indisputably through the troposphere (*Sinha and Harries*, 1995). Additionally with the global increase of temperature it has been proven, that the tropopause height is increasing by several meters per year (*Schmidt et al.*, 2008) and that the amount of water vapour increases not only in the troposphere, but also in the lower stratosphere (*Oltmans and Hofmann*, 1995).

Clouds consist of tiny droplets of liquid water, ice crystals and water vapour. The droplets and crystals make clouds visible to the naked eye, while water vapour is a transparent gas. The existence of water droplets and ice crystals in clouds is dependent on the temperature and water vapour pressure inside the cloud. The balance between droplets and crystals is managed through the difference in the saturation water vapour pressure over water and ice in the cloud, described by the Wegener–Bergeron–Findeisen process (*Bergeron*, 1935).

The methods, which are described in this thesis can be applied for measurement of the water vapour content only. In the literature there are two metrics for the measurement of the total amount of water vapour in a vertical column of air, namely Integrated Water Vapour (IWV) (*Ware et al.*, 1997) and Precipitable Water Vapour (PWV), or Precipitable Water (PW) (*Tregoning et al.*, 1998). The difference between these three definitions can be described by the following equation:

$$PWV = PW = \frac{IWV}{\rho_{lw}} \tag{1.1}$$

where $\rho_{lw} \approx 1000[kg/m^3]$ is the density of liquid water. The density is dependent on the temperature of the water with maximum density at 4^oC. IWV by definition is measured in $[kg/m^2]$, representing the mass of the water vapour in a column of air with base of 1 square meter, while PWV is measured in $[mm]$, indicating the height of the condensed water vapour, precipitated as liquid water. The absolute values of IWV and PWV are approximately equal, since $\frac{\mathbf{1}[kg/m^2]}{1000[kg/m^3]} = \mathbf{1}[mm]$. The terms PW or PWV can lead to the wrong assumption, that liquid water is also included into this integrated quantity. This is the reason why IWV exclusively is used in this work.

The dynamics of water vapour in the atmosphere is defined by the following processes: evapotranspiration, condensation and transportation (shown in figure 1.3). These three parameters change their significance due to the irregularities of the Earth's surface. For example, evaporation is larger over water surfaces, such as oceans, rivers and lakes. And while precipitation over the world ocean is far greater than over the land, there is a water vapour transport flux from water surfaces to the land (figure 1.2) (*Anderson and McDonnell*, 2005). The differences between the sources and sinks of water in the atmosphere are balanced by the transfer of water from places with more evaporation to places with less evaporation. Thus over a single point the input and output of water will be balanced between the horizontal and vertical fluxes (*Sellers et al.*, 1997). This property of the atmosphere to exchange horizontally energy and mass is the primary reason for the existence of weather.

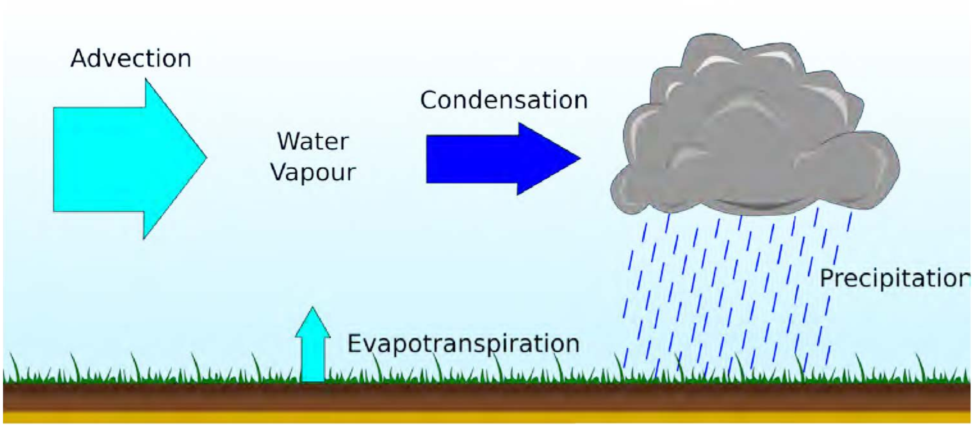

Figure 1.3: Water vapour balance. The sources and sinks of water in the atmosphere are not collocated. The advection of water vapour for a specific region can be a much more significant factor, than local evaporation, unlike condensation and precipitation, which are more localized.

1.2 Soil Moisture

For the purpose of this thesis, soil moisture is the amount of liquid water in the top 20cm of the soil, also known as the O-horizon (O stands for Organic). This quantity is also known in literature as Surface Soil Moisture, or SSM. It is clearly distinguishable from the Ground water, which is contained above the bedrock, between 2-5 m below surface (*Brady and Weil*, 2013). Water in the A and B-horizons (figure 1.4) is frequently also referred to as soil moisture, but in this work the focus is on measuring and estimating of surface soil moisture in the O-horizon only.

This thesis tackles the problems of measuring soil moisture in flat areas. Effects of tilted soil are not considered and are excluded from the observations as well as from the modelling efforts in this work. The dynamics of the soil moisture is influenced by the atmosphere and the soil properties. The evaporation from the soil surface to the atmosphere and the infiltration of water to lower horizons due to gravity are the main sinks of soil moisture. The main source of water in the top soil surface is precipitation. In some cases direct condensation of water (also known as horizontal precipitation) and surface runoff can also contribute to a soil moisture increase (*Rushton et al.*, 2006). The latter two factors happen very rarely, but their contribution can be significant. The infiltration of water in the soils is governed mainly by gravity, thus for homogeneous unbroken soils the horizontal fluxes of soil moisture are not essential to its dynamics, therefore the vertical movements of water in the soil are dominant. When the surface of the soil is tilted, or inhomogeneities in the soil are present, gravity driven horizontal fluxes are observed. In any case on large scales, the horizontal fluxes can be considered insignificant, which leads to a far simpler modelling of the soil moisture variation using

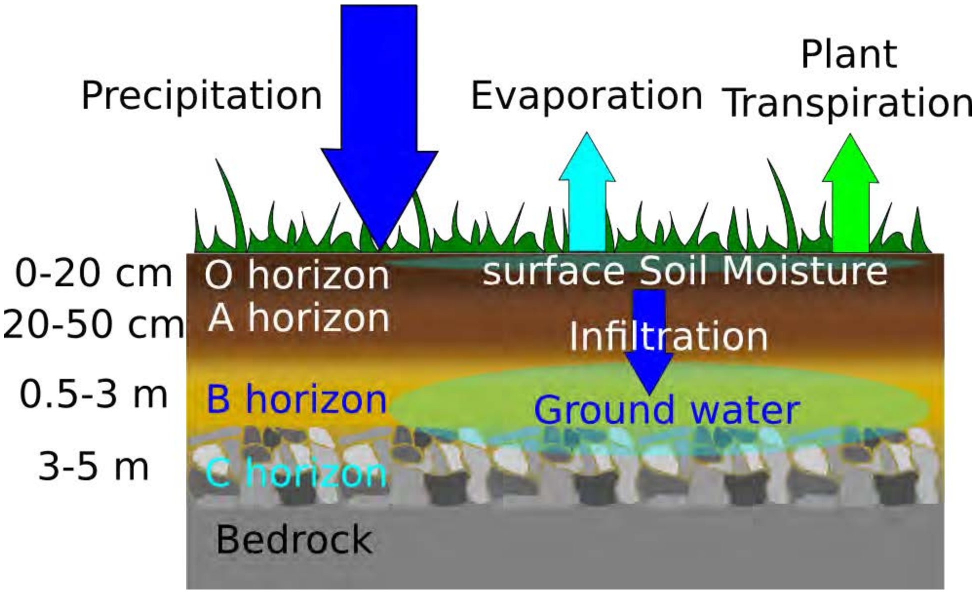

Figure 1.4: Soil water balance. The vertical fluxes of water in flat soil areas are dominant with hardly any horizontal transportation of water.

1D or bucket models, unlike the 3D case with water vapour (*Guswa et al.*, 2002).

Soil moisture can be represented in several metrics: Specific Water Content (SWC), which is the fraction of the water mass from the mass of a confined amount of soil, or as Volumetric Water Content (VWC), which is the fraction of the water volume in a confined volume of soil. VWC can be measured in both $[\frac{cm^3\ H_2O}{cm^3\ soil}]$ or in $[Vol\%]$, where the absolute values have the following relation: $1[\frac{cm^3\ H_2O}{cm^3\ soil}] = 100[Vol\%]$. Another soil moisture metric is the Relative Water Content (RWC), which represents the volume of water present in the soil as a fraction of the saturated water amount in the soil. RWC is measured in [%]. The soil moisture metric, used in this work is VWC with units of measurement $[Vol\%]$.

Soil moisture quantities are primarily dependent on the soil type, orography, as well as atmospheric humidity and temperature. The yearly cycle for mid latitudes is characterised by high values in the winter season, due to lack of evaporation, and large variability during the summer, due to summer rain events and strong evaporation (*Brady and Weil*, 2013). This behaviour is opposite to the behaviour of the water vapour in the atmosphere, where the capacity of the air to hold water is exponentially proportionate to the temperature.

1.3 Snow cover

Currently around 10% of the Earth's land surface is covered by glaciers, ice caps and snow cover. Snow and ice cover play important role in the Earth's climate by reflecting solar radiation and thus decreasing the average Earth temperature. The albedo of a given surface is the percentage of solar energy, reflected by it back into space, compared to the radiation initially striking that surface. The albedo of snow and ice (as shown in table 1.2) is larger than the albedo of bare ground. Glaciers and ice caps participate in a positive feedback loop in the Earth's climate. By contracting due to increasing temperatures, they reflect less solar radiation, further contributing to the global temperatures increase (*Kargel et al.*, 2014).

Surface	Albedo [%]
Fresh snow	75 - 95
Ice	30 - 40
Sand	15 - 45
Earth average	29
Grassy field	10 - 30
Ploughed field	5 - 20
Forest	3 - 10

Table 1.2: Albedo of different surfaces (*Ahrens*, 2012, p.48). Higher albedo indicates higher reflectivity of the surfaces.

Accumulation of snow over the ground though is a specific phenomenon, occurring at atmospheric and ground temperatures below $0°C$. Most of the precipitation, reaching the ground, starts as snow, even in the summer periods. When either the atmosphere, or the ground is warmer, the snowflakes, fallen on ground melt. Similar to soil moisture snow accumulation is also much more influenced by the local precipitation. Unlike soil moisture, the snow cover can drift with wind after the snow has precipitated and accumulate unevenly (*Ahrens*, 2012).

There are several snow cover properties, which are known and used in the scientific community. The one, which will be briefly addressed in this work is snow height. Snow height is the same as snow depth, or accumulated snow cover. It is the total height of snow, accumulated over the underlying ground. Snow height is different from snowfall rate. Meteorological stations usually report both snowfall rate and snow cover, but snowfall is more frequently used. Both of these properties are measured in meters or centimetres.

Chapter 2

Established techniques for monitoring the water cycle

2.1 Atmospheric Water Vapour

2.1.1 Radiosounding

The first attempts of measuring a vertical profile of the atmosphere were conveyed in the end of the XIX - beginning of the XX centuries. The carrier platforms for meteorological equipment varied - experiments with kites and balloons were carried out and the balloons proved to be the more efficient platform. The first measurements were carried out using termographs and barographs - devices designed to record changes of temperature and pressure over time. With the development of measuring technologies and the invention of the radio and radars, the current radiosondes (like the one shown in figure 2.1) provide measurements of temperature, pressure, humidity, wind speed and wind direction as standard. Some advanced radiosondes are equipped also with gas detectors for various atmosphere compounds, such as pollens, aerosols, trace gases or air pollution (*Adam et al.*, 2005).

Figure 2.1: The RS92 radiosonde from Vaisala.

The classical weather balloons go through the Troposphere and penetrate the Tropopause (10-15km above sea level). Depending on the weather conditions, these standard measurements are extended into the Stratosphere with the usual balloon flight terminated at around 30-35km. In parallel Stratospheric balloons are used for experiments in the Stratosphere, at heights up to 50km. All of these measurements are recognized as standard and approved by the World Meteorological Organization

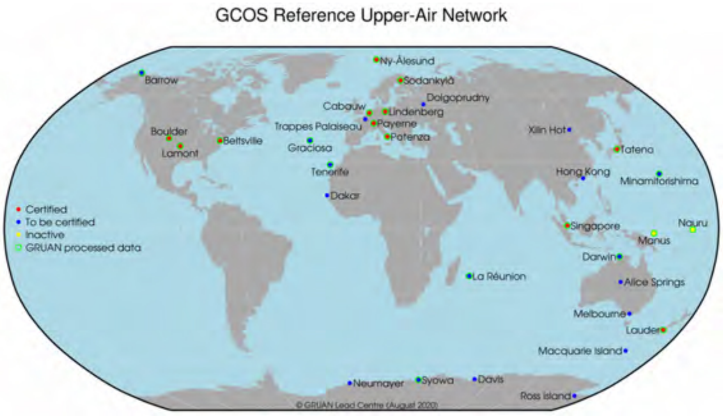

Figure 2.2: Map of the GRUAN network.

(WMO). Regular radiosounding of the atmosphere is performed in more than 1000 meteorological stations worldwide with measurements taking place on a daily or sub-daily intervals.

In this work radiosonde measurements from standard weather balloons are used for validation of the IWV measurements, described in chapter 3.4. For computing the IWV from the radiosonde profiles (RS-IWV) the following equation is used:

$$IWV = \frac{R_d}{m_{H_2O}} \sum_{i=0}^{N} \frac{p_{wv}(T_i).RH_i}{T_i} \tag{2.1}$$

where $R_d = 287.04 Jkg^{-1}K^{-1}$ is the gas constant of dry air, $m_{H_2O} = 18 gmol^{-1}$ is the molar mass of water, p_{wv} is the saturation vapour pressure in hPa and T is the temperature in K (*Dirksen et al.*, 2014).

The collection of radiosonde data incurs substantial operational cost. Most of the radiosounding systems are not reusable, limiting the spatial coverage and number of launches per day. A specialized GCOS Reference Upper-Air Network (GRUAN, see figure 2.2) has been established in the late 1990s with 28 stations world-wide as part of the Global Climate Observing System (GCOS), where a variety of higher atmosphere parameters measurements is undertaken (*Ladstädter et al.*, 2015). These observatories operate Radiosoundings and GNSS water vapour measurements and often use lidars and microwave radiometers as additional techniques for observation (*Thorne et al.*, 2013).

The radiosoundings, analysed in this thesis, are launched from meteorological station Sofia. The sondes used before 2001 in this station are the Russian produced MARZ. Between 2001-2005 the Vaisala RS80 system was used for the routine soundings. In the period between 2005-2014 the RS92 sonde was on duty and since 2014 the latest Vaisala sonde, the RS41 is deployed for operational observations. The radiosounding data cover the time periods when the RS80, RS92 and RS41 are launched. The radiosondes between 2001 and 2019 are launched once per day in 12 UTC. The radiosonde data spans from

1955.

2.1.2 Water Vapour Radiometers

Water Vapour Radiometers are a relatively new ground-based remote sensing device for measuring water vapour in the atmosphere. First developed in the middle of the XX century, by the beginning of the XXI they are developed into a powerful atmospheric sensing tool. Microwave radiometers (Radiometrics MP3000-A microwave radiometer shown on figure 2.3) use electromagnetic waves in the spectrum between 20-35 GHz (K-band and K_a-band). They rely on measuring the absorption of microwaves in water vapour, as well as in liquid water droplets. Thus they can determine with good precision the amount of water vapour in different regions of the atmosphere from lower troposphere (*Morland*, 2002), up to the mesosphere (*Straub et al.*, 2010). Similar to radiosounding (see figure 2.4), water vapour radiometers provide information about the profile of water vapour (*Shangguan et al.*, 2015; *Heise et al.*, 2013). Similar to weather radars, the radiometers can be mounted on rotating mounts, providing measurements in 360° azimuth and at various elevation angles, thus giving a more detailed scan of the atmosphere and providing data about water vapour gradients.

Figure 2.3: Microwave radiometer on the roof of A17 building at GFZ. Photo by *Torsten Schmidt*

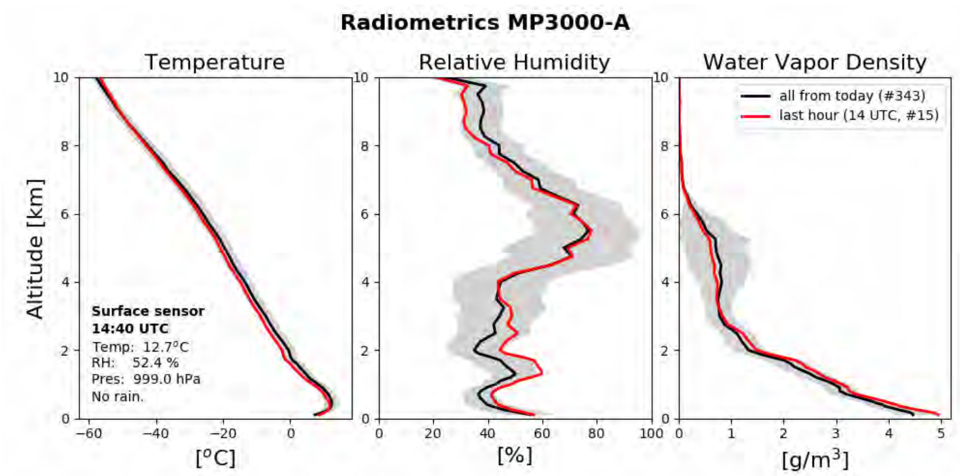

Figure 2.4: Radiometrics MP3000-A microwave radiometer profiles of the atmosphere for March 1st 2019. Figure taken from GFZ portal `http://www-app2.gfz-potsdam.de/pb1/GASP/GASP2/CHAMP/RO_EXPERIMENT/index_radiometer.html`. Red curves represent the accumulated measurements over the last hour, while the black curves - over the last 24 hours of temperature, relative humidity and water vapour density.

2.1.3 Satellite measurements

Water vapour measurements from space are one of the first applications of meteorological satellites. The first meteorological satellite mission, scanning the Earth's surface was launched in 1960. The TIROS-1 satellite, designed by NASA, was in orbit for 78 days and provided images of the Earth in the visible spectrum. The following satellites of the TIROS programme included infrared imagers in parallel to the visible part of the spectrum and was followed by the NIMBUS programme, which widened the possibilities of these LEO systems for providing all-weather meteorological data for weather forecasting. The current programs of the Earth Science Enterprise (ESE) of NASA include JASON, CALIPSO, OCO, AQUARIUS and HYDROS among others (*Neeck et al.*, 2005). The latest meteorological satellite missions, launched in the US are the GOES-17 GEO and the NOAA-20 LEO satellites.

The European Space Agency (ESA) launched their first meteorological satellite, the METEOSAT-1 in 1972. The first generation of the Meteosat programme included 7 satellites, while until today 11 of these GEO satellites are launched in 2 generations. The imaging sensors aboard the Meteosat satellites are integrated into the MVIRI - Meteosat Visible and Infrared Imager, working in thermal infrared region (TIR), in the water vapour absorption bands (WV), and in the visible range (VIS) (*Desbois et al.*, 1982). The second generation of Meteosat satellites improved on the resolution and added additional scanning bands to the MVIRI system. Currently SEVIRI, the second generation of MVIRI, provides 15 minutes temporal resolution data from 12 different channels, among which the high-resolution visible (HRV) channel with 1km spatial resolution, and multiple IR channels at 2.5 and 5 km resolutions (*Schmetz et al.*, 2002). The third generation of Meteosat satellites (MTG) is currently under development with the new Flexible Combined Imager (FCI) proposed as a replacement of the SEVIRI sensors, providing higher temporal (10-2.5 minutes), spatial (0.5-2km) and spectral (16 spectral channels between 0.44-13.3μm) resolution (*Durand et al.*, 2015). In parallel the MetOp series of satellites are developed, utilizing LEO orbits and equipped with the Infrared Atmospheric Sounding Interferometers (IASI) (*Schlüssel et al.*, 2005). Using these satellites the water vapour is measured in 6.2 and 7.3 micrometer channels, peaking at different levels in the troposphere, thus enabling differentiation between lower and higher troposphere (*Zinner et al.*, 2008). What the satellites are effectively measuring is the water vapour absorption of close infrared radiation, coming from the surface of the Earth at different altitudes above ground, thus creating water vapour profiles. These measurements provide, total water vapour column measurements, which are comparable to radiosonde measurements in terms of accuracy and representativeness (*Schroedter-Homscheidt et al.*, 2008).

2.2 Soil Moisture

2.2.1 Time and Frequency Domain Reflectometry

Time Domain Reflectometry (TDR) and Frequency Domain Reflectometry (FDR) are standard methods of measuring soil properties, such as soil moisture. TDR and FDR have many similarities, which is why both methods are described together. The equipment for measuring soil moisture with these methods comprises of sondes, inserted into the soil (see figure 2.5) and an emitter/receiver device (*Rajkai and Rydén*, 1992). The TDR method is used in this thesis to provide a reference dataset for accessing the quality of the GNSS Reflectometry GNSS-R soil moisture retrievals in chapter 5.

Figure 2.5: TDR probe.

Propagation constants for electromagnetic (EM) waves in soil, such as velocity and attenuation, depend on soil properties (water content and electrical conductivity), which determine dielectric permittivity from the velocity of an EM wave that is emitted by a pulse generator and passed along the rods of the TDR probe (*Robinson et al.*, 2003). The dielectric constant (K_a) of the soil, measured by TDR, can provide information about the soil water content:

$$K_a = \left(c\frac{t}{2L}\right)^2 \tag{2.2}$$

where c is the speed of light in vacuum, t is transit time for an electromagnetic pulse to travel the length of a transmission line and L is the length of the probe. The TDR measurements are sensitive to soil moisture and, to a lesser degree, dependent on soil texture and salinity. This technique provides automated long-term *in-situ* measurements (*Zazueta and Xin*, 1994; *Hernández et al.*, 2018). The accuracy of the TDR measurements have been estimated to be within $2[Vol\%]$ (*Evett et al.*, 2002).

The Frequency Domain Reflectometry (FDR) technique is similar to TDR. Instead of measuring the time delay of a signal in the soil, the primary observable is the change in frequency of the transmitted signal, which is altered by, among others, soil moisture of the ground. Apart from using the capacitance of the soil, rather than conductivity, the two methods provide very similar results and are used in a very similar way (*Leib et al.*, 2003).

TDR is used in this work as reference for the GNSS-R soil moisture retrievals in two stations in Germany - Marquardt and Fürstensee (stations described in section 5.3).

2.2.2 Gravimetric measurements

Gravimetric soil moisture measurements are the most simple and traditional VWC measurements. The procedure of obtaining data starts with the extraction of soil samples directly in the field. Metal rings of different sizes are used for the soil extraction. Directly after the extraction, the weight of the sample is measured. Afterwards the soil sample is dried and weighted again. The difference in mass between the wet and dry samples gives the amount of water in the soil. In order to prevent any burn or disturbance of the soil sample, the drying is done at temperatures between 60 and 90 degrees over 24-48 hours (shown on figure 2.6). The big advantage of the gravimetric measurement is the direct measurement of soil moisture with very high accuracy and precision. The precision of the method depends on the precision of measuring scales and the handling of the soil samples and is less than $1[Vol\%]$. High accuracy is achieved by multiple samplings with a larger area coverage. This direct method is the only method used, which presents absolute measurements directly, without any further processing (*Reynolds*, 1970).

Figure 2.6: Gravimetric soil moisture measurements - drying of soil samples.

Gravimetric measurements are carried out in this thesis in section 5.3. The results from these measurements are used for validation and calibration of TDR and GNSS-R (GNSS-R defined in chapter 3) soil moisture observations.

2.2.3 Satellite measurements

Various satellite-based active and passive microwave sensors are used to retrieve surface soil moisture from the measured surface backscatter and brightness temperature signals *Botteron et al.* (2013). These include measurements from the European Remote Sensing (ERS) satellite scatterometer of microwave backscatter with a spatial resolution of 50 by 50 km (*Wagner et al.*, 1999), and inference from the surface energy balance, such as the Advanced Microwave Scanning Radiometer for the Earth observing system (AMSR-E). Currently two specialized satellite soil moisture missions are operational, namely the Soil Moisture and Ocean Salinity (SMOS), launched by ESA, and the Soil Moisture Active Passive (SMAP), launched by NASA.

The European Soil Moisture and Ocean Salinity (SMOS) mission was successfully launched into LEO in early 2 November 2009 and provides global L-band radiometric observations for soil moisture and ocean salinity. The SMOS Microwave Imaging Radiometer using Aperture Synthesis (MIRAS) radiometer measures at L-band for optimum sensitivity to soil moisture and ocean salinity. SMOS is the first satellite specifically dedicated to monitoring soil moisture with an accuracy of 0.04 m^3/m^3 over continental surfaces. The wide swath provides two to three day global revisit. The SMOS instrument uses a synthetic aperture antenna that provides 40-km horizontal resolution globally (*Kerr et al.*, 2010; *Al-Yaari et al.*, 2016). The second soil moisture observing mission of the EUMETSAT is the Active Scatterometer ASCAT on-board the 3 MetOp satellites. These satellites also provide global coverage on LEO orbits with revisit of 5 days and horizontal resolution of 0.1°, or $11km$.

SMAP is NASA's first Earth-observing satellite designed to collect global observations of surface soil moisture. SMAP was launched on 31 January 2015 with expected mission duration of minimum 3 years. Its primary goal is to map global soil moisture and detect whether soils are frozen or thawed. The orbit of the satellite is polar sun-synchronous LEO at 685 km altitude. The swath coverage from successive orbits provides for global coverage in 2-3 days depending on latitude. The orbit track repeats exactly every 8 days. SMAP is designed to provide high spatial resolution global measurements of soil moisture from space. The satellite is planned to work in two different modes - active and passive. The active mode is enabled through an L-band active radar, providing 10km resolution, while the passive system is comprised of an L-band radiometer, providing $36km$ resolution (*Entekhabi et al.*, 2010). The active radar aboard the satellite should have provided much higher resolution and accuracy of soil moisture estimation, but was defunct only 3 months after the mission launch. Thus SMAP provides similar to SMOS resolution and coverage.

2.3 Snow cover

2.3.1 Snow depth poles

Snow depth is an environmental measurement, which has been performed since the earliest days of meteorological observations. Snow poles are the earliest method to determine snow depth and are still widely used. Snow depth poles, or sticks, are robust rudimentary devices, designed to measure the thickness of the snow cover. They are secured into a fundament in the ground and marked with distinct patterns of equally spaced bands. The accuracy of these measurements is half the size of one band. The snow poles are prone in strong winds to higher snow accumulation around them, than their premises.

2.3.2 Snow buoys

Snow buoys, or snow height beacons, are devices, measuring relative changes in the snow cover height (seen in figure 2.7). They consist of 4 ultra-sonic snow depth sensors. The devices are mounted on a 2.5 meter mast in direction nadir. The design to use 4 sensors is required in order to correct for forced snow accumulation on the windward side and snow drift on the leeward side of the mast. The buoy is calibrated against snow depths during installation and during sensor height changes. Snow height is estimated as the average from the four sensors. The accuracy of snow height estimation is 1cm with sampling rate of 10 minutes (*Nicolaus et al.*, 2016).

Figure 2.7: Snow buoy. Picture from `https://www.awi.de/`

Snow buoys data is used in this thesis in chapter 7 for validation of snow height measurements with GNSS reflected signals at station Neumayer.

2.3.3 Satellite observations of snow depth

Snow cover is one of the earliest satellite observations, derived from visual images from satellites, such as the ESA Meteosat and NASA Landsat missions. Snow cover describes, if snow is present or not, but is not indicative of other snow parameters, such as snow depth (*Gascoin et al.*, 2019). Another satellite-observed snow parameter is the Snow Wet Equivalence (SWE). Both SWE and snow height can be measured using Interferometric Synthetic Aperture Radar (InSAR) in C-band, but the measurements are highly dependent on the type of snow cover. The measurements show highest agreement for dry snow and are representative only for single layer snow cover (*Li et al.*, 2017). Thus multiple snow layers, accumulated over time are an open topic. (InSAR) data, derived from the ESA Sentinel mission is used to observe snow depth over the northern hemisphere with a $1km^2$ spatial and weekly temporal resolution. The methodology is applicable mainly to mountainous regions whith longer residing snow cover and is comparable to auxiliary observations (*Lievens et al.*, 2019).

2.4 Numerical modelling of atmospheric water vapour and soil moisture

In this thesis three different models are used:

- 1-Dimensional empirical soil moisture bucket model (1D-ESMM), developed for this thesis,

model	1D-ESMM	WRF	ERA5
modelled parameters	VWC	IWV	IWV, VWC
spatial resolution	1D	9km(0.09°)	31km(0.28°)
temporal resolution	1 day	30 minutes	1 hour
data assimilation	-	no	4D-Var
domain	-	regional	global
application	local environment	weather forecast	climate research

Table 2.1: General characteristics of the numerical models, used in this thesis. The results from the 1D-ESMM model are discussed in chapter 6, the results from the WRF are incorporated in the analysis in chapter 4 and the ERA5 datasets are used in the studies in chapters 5 and 7.

- Mesoscale NWP model of the atmosphere (WRF),
- ECMWF 5th generation land and atmosphere re-analysis (ERA5).

A summary of the models is presented in table 2.1. The setup of the models is presented in sections 2.4.1, 2.4.2 and 2.4.3.

The local model is used for specific stations only. The regional models are used for weather forecasting. The global reanalysis models are used for climatological studies.

2.4.1 1D soil moisture bucket modelling

As discussed in chapter 1.2, the dynamics of the water in the surface soil horizons is dependent mainly on three processes: precipitation, evapotranspiration and infiltration. Both precipitation and evaporation are directly linked to the atmosphere. The infiltration is a process, dependent on the soil type and the amount of soil moisture.

The most widely used 1D soil moisture model is the HYDRUS-1D. The software package is designed for simulating water, heat and solute movement in 1D variably saturated media. The model consists of a set of equations, each designated to solve a particular problem: a flow equation, based on the Richards equation, for the water fluxes in the soil and the soil-plant interaction, a heat transport equation for the propagation of heat between the soil layers and solute transport equations for the chemical reactions and dispersion of the water soluble soil compounds. The model is designed to simulate the flows of CO_2, Ca, Mg, Na, K, SO_4, Cl and NO_3 among others, as well as the general soil alkalinity. The model is fed with several groups of data, including soil properties (soil type, composition, structure, water flow), vegetation parameters (root water uptake, root depth) and meteorological data (relative humidity, temperature, wind direction and speed) (*Šimøunek et al.*, 2008).

Soil and vegetation parameters are the key factor, affecting the soil moisture dynamics in HYDRUS-1D (*Chen et al.*, 2014). The HYDROS-1D model requires a lot of environmental parameters, which are not within the scope of this thesis. Thus a simplistic one-dimensional (1D) single layer empirical model is developed to estimate the amounts of water in the soil, based purely on meteorological observations. Data from station Marquardt, described in detail in section 5.3, is used for the development of this model. Further details about the model setup are given in chapter 6.

2.4.2 The Weather Research and Forecasting (WRF) NWP model

The Weather Research and Forecasting (WRF) model is developed in the USA by a collaboration of groups at National Center for Atmospheric Research (NCAR), Mesoscale and Microscale Meteorology Division, the National Oceanic and Atmospheric Administration (NOAA), National Center for Environmental Prediction (NCEP), Earth System Research Laboratory (ESRL), Department of Defence Air Force Weather Agency (AFWA), Naval Research Laboratory (NRL), Center for Analysis and Prediction of Storms (CAPS), Federal Aviation Administration (FAA) and the University of Oklahoma. WRF is a free-to-use NWP used by countless universities and research centers all around the world. It relies on a strong support from both its developers in NCAR, as well as from a large community of independent university developers. The model can be run with a spatial resolution between 1 and 10 km. Numerous specific models, such as the Hurricane Weather Research and Forecasting (HWRF) have been created upon WRF. From the first release in 1990 until now the model has evolved (*Michalakes*, 1999) and additional packages have been developed for interactive nesting, upgraded physics, 3D-Var data assimilation and simplified parallelization (*Michalakes et al.*, 2005). WRF has large worldwide community with over 20,000 users in over 130 countries.

The WRF v3.4.1 (*Skamarock et al.*, 2008) is computed for a domain covering Bulgaria with a horizontal resolution of 9 km and a vertical resolution of 44 levels and initial and boundary conditions from the Global Forecast System (GFS) model with horizontal resolution 0.5°. No assimilation is carried out, thus the model acts as a downscaling tool for the GFS analysis. The following parametrizations schemes for the model physics are selected:

- Unified Noah land-surface model for the land surface (*Barlage et al.*, 2010),
- Yonsei University (YSU) scheme for the planetary boundary layer (*Hong et al.*, 2006),
- WRF Single moment Microphysics (WSM) 6-class graupel scheme for the microphysics (*Hong et al.*, 2010),
- Rapid Radiative Transfer Model (RRTM) for the long/short-wave radiation (*Mlawer et al.*, 1997).

Two types of WRF model parameters are analysed in this thesis in chapter 4, namely surface parameters (pressure and temperature) and profiles (pressure, temperature, water vapour mixing ratio and the model level height). The profiles from WRF are used to compute the water vapour density at each model level ($\rho_{wv}(z)$) and then by integration over the model levels the WRF-IWV is obtained using the following equation:

$$IWV = \frac{1}{\rho_w} \int_{z}^{z_n} \rho_{wv}(z)\, \mathrm{d}z \tag{2.3}$$

where ρ_w is density of liquid water, n is the number of model levels.

2.4.3 The ERA reanalysis

The reanalysis datasets, used in this work are the ERA-Interim and the ERA5. The initiative to start the re-analysis of atmospheric data on a global scale is conceived in the 1990's by the European Center for Medium-Range Weather Forecasts (ECMWF). The first re-analysis campaign, called ERA-15 (ERA standing for ECMWF Re-Analysis), is an attempt to create a homogeneous dataset of all measurable atmospheric parameters, using every available ground and space-based atmospheric observation between 1978 and 1994. The goal is to access the weather on the Earth globally and homogenize the datasets for further climate studies. The following implementations of the ERA datasets are using the latest versions of the ECMWF model, while looking further back into the past. The latest dataset, known as ERA5, incorporates data since 2000 with hourly temporal and 0.28 degrees (31km) horizontal resolutions and 137 vertical levels from the Earth's surface to 80km, or 0.1hPa. The longest ERA dataset is the ERA-20C (ERA XXth century), incorporating atmospheric measurements between 1900-2010 (*Poli et al.*, 2016).

A re-analysis dataset is produced using a single version of the assimilation system. In case of ERA-Interim and ERA5 the assimilation is done using a **4**-**D**imentional **Var**iational assimilation (4D-Var) technique for the atmosphere and using Land Data Assimilation System (LDAS) for the soil. All available observations are first combined with prior information from the model forecast. The products of this combination are subsequently used as initial conditions for the next model run, which on the next step is, again, combined with meteorological observations (*Dee et al.*, 2011). The assimilated observations include surface measurements, upper-air observations, as well as satellite imagery. Most importantly for this work, the ERA5 and ERA-Interim datasets include assimilation of MetOp-A/B ASCAT soil moisture, as well as SMOS and SMAP brightness temperatures data (*Poli*, 2010).

The soil moisture analysis system in the ERA is based upon a point-wise Extended Kalman Filtering (EKF) as part of the LDAS. The observations, used in the system, include measurements from satellites, such as SMOS, SMAP and ASCAT, as well as surface temperature and pressure observations. The core of the system is a Jacobian cost function minimization procedure, using model previous state and observations from current step of the model. This procedure is repeated daily at 00, 06, 12 and 18 UTC (*Drusch et al.*, 2009). The indicated correlations between the EKF in the ERA and ASCAT observations for a case study in Southern France is higher than 0.78 (*Rosnay et al.*, 2011).

Data from the satellite-based NOAA Snow Cover Extent daily products, as well as in-situ snow depth data is assimilated into the ERA5 throuth the LDAS. An evaluation of the ERA5 snow depth product shows large positive bias (up to a factor of 10), compared to in-situ measurements in the Tibetian plateau (*Orsolini et al.*, 2019). This bias is related to the excessive precipitation, observed in the ERA5 data.

2.5 Limitations of the established techniques

2.5.1 IWV observations and modelling

Radiosondes are the most accurate and the only direct method of water vapour measurement in the atmosphere. They are used as calibration datasets for the satellite and ground-based remote-sensting observation techniques. The main disadvantage of the radiosondes is the lower temporal and spatial resolution due to the elaborate methodology of their launching. Additionally the price of a single radiosonde can be as high as 3000 Euro with the standard routine sondes costing between 50-250 Euro. Executing radiosonde measurements is further complicated by the requirements of the necessary infrastructure.

The microwave radiometers, compared to the radiosondes, are priced at around 100 000 euro, which costs less than the worth of 2 years of daily radiosondes. Microwave radiometers can provide much higher temporal resolution, since they are a remote sensing technique and the observations have no additional cost. However the radiometers are sensitive not only to water vapour, but also to liquid water, which limits their observation capacity in cloudy conditions.

Satellites provide global coverage of water vapour measurements, but, similar to microwave radiometers, are limited to clear sky observations only. They provide very high spatial resolution as well, but are dependent on calibrations from in-situ measurements. Numerical weather models and reanalyses assimilate the observations from all available platforms, providing a compromised observation fields in terms of resolution and accuracy (see figure 2.8). Numerical weather models, though, cannot work without data to assimilate.

Precision, accuracy and footprint are not the only parameters, which have to be estimated when evaluating these techniques. Satellite missions are extremely expensive and some of the ground-based techniques can be not only expensive, but also elaborate to work with. The complexity of the economy of the measurement is added to the complexity of

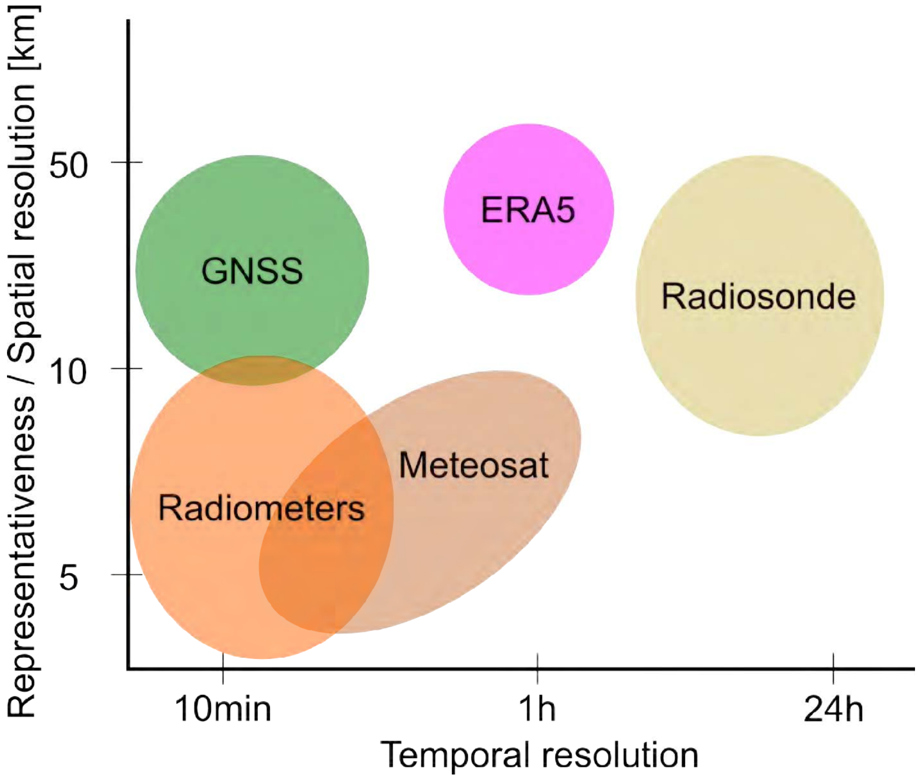

Figure 2.8: Water vapour measurement techniques spatio-temporal resolution. The figure schematically represents the highest spatio-temporal resolutions of the water vapour measurement techniques. GNSS Meteorology (discussed in chapter 3.4) is a gap-filling technique with superior capabilities under certain conditions.

the accuracy and representativeness, making the choice of a measurement technique even harder. Moreover the atmospheric sounding capabilities of microwave radiometers can be replicated for the 10th of the cost using a ground-based GNSS station with the added value of providing invaluable information about the state of the soil.

Thus there is a gap for an all-weather remote sensing observation technique, which is cost-efficient to operate and can provide highly accurate near real time water vapour observations. The GNSS Meteorology technique (discussed in chapter 3.4) fulfills all of these requirements.

2.5.2 Soil moisture observations and modelling

The classical gravimetric soil moisture measurements provide very robust and accurate direct observation of the soil moisture, which require minimal infrastructure and investment. These measurements, although very accurate, have several very significant drawbacks - the collected samples are representative of very small volumes of soil, the samples cannot be reused and continual measurements are very labour intensive. Thus these measurements are used for calibration of other observation techniques, such as TDR and FDR. Both TDR and FDR can provide data with high temporal resolution and high accuracy, but they are representative of very small volumes of soil, similar to gravimetry.

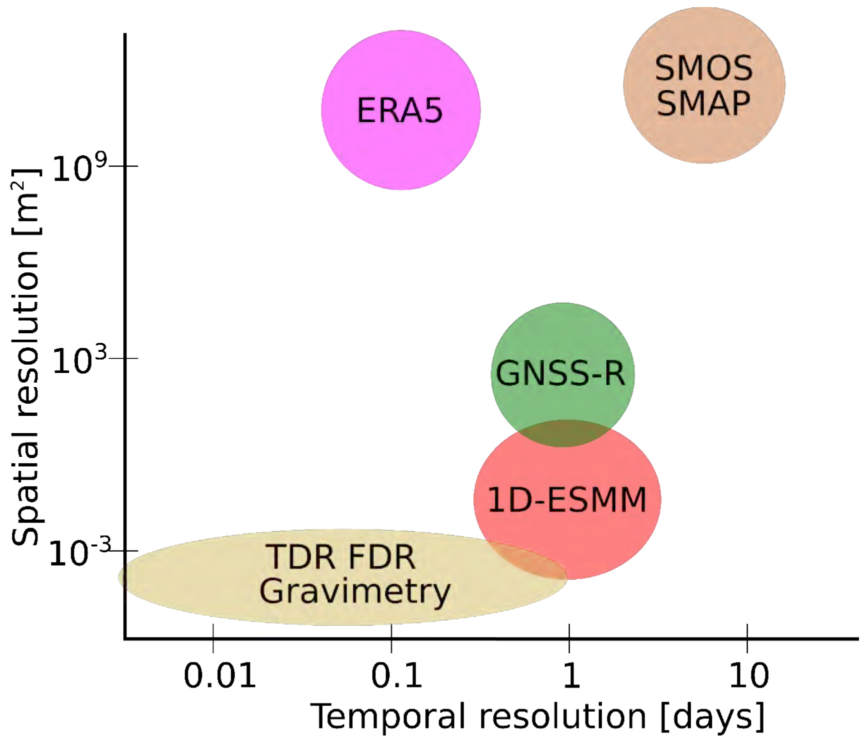

Figure 2.9: Soil moisture measurement techniques spatio-temporal resolution. The figure schematically represents the highest spatio-temporal resolutions of the soil moisture measurement techniques, discussed in this chapter. In chapter 3.5 GNSS-R is presented as a gap-filling observation technique with superior capabilities under certain conditions. In chapter 6 the developed 1D-ESMM is presented as a supplementary model for soil moisture.

Satellite measurements of soil moisture, such as SMOS and SMAP provide global coverage of homogeneous soil moisture measurements, a product, which no other technique provides. Spatially their resolution is 10-50 km^2, while their temporal resolution is between 2-10 days for the different satellite missions. Ground-based in-situ measurements are essential for the calibration of these satellite measurements and provide much higher precision, accuracy, as well as better temporal resolution (see figure 2.9).

Numerical weather models and reanalysis provide soil moisture data, based on assimilation of satellite measurements, with similar to satellites resolution. Local soil models, coupled with weather models can provide a much better representation of soil moisture, especially when in-situ data is assimilated.

The in-situ measurements are not representative for larger areas and are prone to local inhomogeneity and biases, while the satellite measurements excel in large area coverage. The gap in between these methods is challenging and can be fulfilled with newer observation and modelling techniques, based on emerging scientific methods. The GNSS Reflectometry soil moisture observations technique is presented in chapter 3.5 and a newly developed soil moisture local model is presented in chapter 6. While comparable in price to a standard TDR/FDR set-up, GNSS-R provides data with much larger area footprint. Unlike TDR/FDR, GNSS-R needs a bespoke software, tailored to the particular application and system, which involves much more manpower to develop and to implement. Every GNSS-R station has to be evaluated separately, thus increasing the manpower costs with every application.

2.5.3 Snow height observations and modelling

The easiest method to measure snow height or snow depth is through snow poles. This rudimentary observation technique uses very basic infrastructire, but relies on manual data record. The ultra-sonic snow buoys provide automatic snow depth measurements, thus increasing the temporal resolution and lowering the operational costs. Both snow buoys and snow poles are representative of a relative small area and are prone to local snow accumulation, which may alter the snow records significantly.

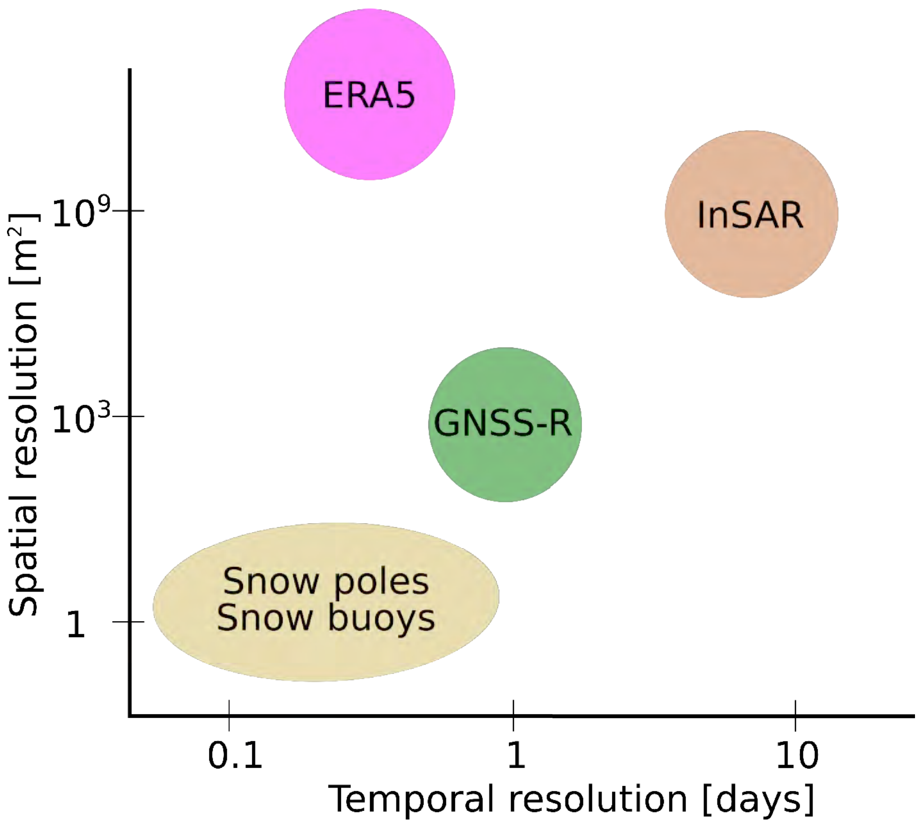

Figure 2.10: Snow height measurement techniques spatio-temporal resolution. The figure schematically represents the highest spatio-temporal resolutions of the snow height measurement techniques. GNSS Reflectometry is a gap-filling technique between classical and satellite observations.

Satellite observations of snow depth are an emerging topic with the latest generation of InSAR satellites. They can provide snow measurements with large footprint and low temporal resolution and are relient on many assuptions regarding the state of the snow cover. The ERA5 reanalysis provides snow cover data with similar spatial resolution to satellite measurements, but the snow depth data is significantly overestimated, when compared to in-situ measurements.

Snow height observations using GNSS Reflectometry, described in section 3.5.2, can provide gap-filling observations between the in-situ and space-based observations, providing field-sized measurement footprint with daily frequency (see figure 2.10). Every GNSS-R station has to be evaluated separately, similar to the GNSS-R application for soil moisture.

Chapter 3

Water cycle monitoring with GNSS

3.1 GNSS and selected basics of signal propagation

The term Global Navigation Satellite System, or GNSS, has recently been introduced. It incorporates all navigation systems with a space segment: the United States of America's Global Positioning System (GPS), the Russian Federation's GLObal'naya NAvigatzionnaya Sputnikovaya Sistema (from Russian - Global Navigation Satellite System, GLONASS), the European Union - Galileo, the People's Republic of China - BeiDou and the regional Japanese Quasi-Zenith Satellite System (QZSS) along with the Indian Regional Navigation Satellite System (IRNSS). These systems share similar technical parameters, such as L-band carrier frequencies and multiple inclined Medium Earth Orbits (MEO) (combined with Geostationary Orbits (GEO) for the regional systems), of their space segments. All of these systems provide a spectrum of capabilities for the whole GNSS constellation, which cannot be achieved by any of these systems separately (*Hoffmann-Wellenhof et al.*, 2008).

Although this work is entitled "Derivation and analysis of atmospheric water vapour and soil moisture from ground-based GNSS stations", most of the presented results are performed using the GPS system only. Since the system was developed and available before the other competing GNSS, environmental measurements are historically clustered around GPS data. The details in the development of this system's signals is important for the better understanding of the results and used methods in this work.

The first GPS satellite was launched in 1978. Together with the following 9 satellites they are from the first generation of GPS, commonly known as "Block I". The Block I satellites are using slightly different orbits from the following generations at inclination angle of 63^o. They are transmitting signals in the L1 ($f = 1575.42\ MHz,\ \lambda \approx 19\ cm$) and L2 ($f = 1227.60\ MHz,\ \lambda \approx 24.4\ cm$). The satellites are controlled using S-band communications and are powered by a solar array, outputting over 400W. The initial Block I constellation was transmitting L1 signals in a Coarse/Acquisition (C/A) coding, which is freely available to the public and L2 signals in a special Precision, or P-code, which is only available to the US military (*Parkinson et al.*, 2005).

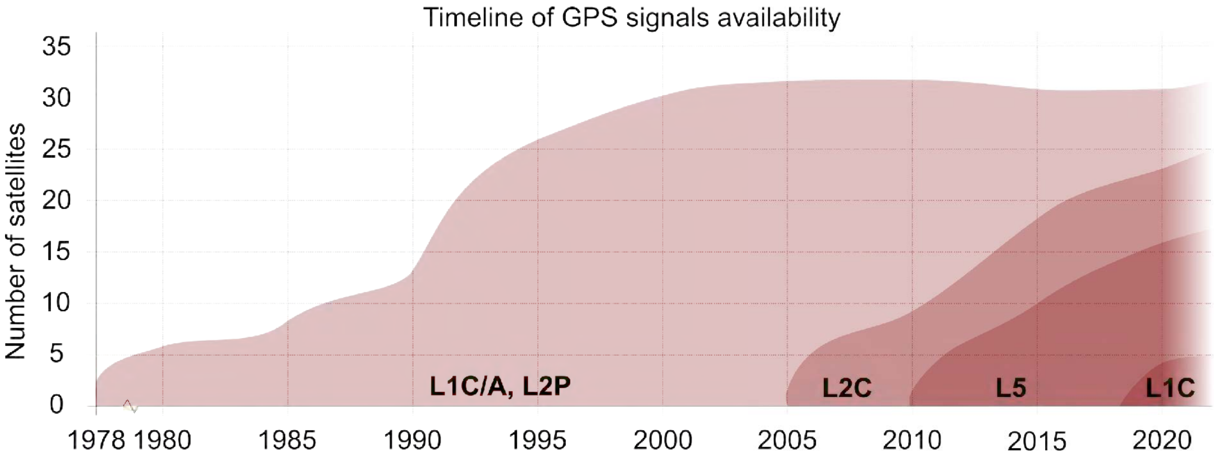

Figure 3.1: Timeline of the introduction of GPS signals. Since the lifetime of GPS satellites is over 10 years, new codes and frequencies have gradually been implemented throughout the system.

The second generation of GPS satellites, also known as Block II saw a major upgrade over the Block I with higher power of the solar array, more precise atomic clocks and higher power of the output signals. They are launched in several upgraded versions from 1989, until 2016. During the development of the satellites new frequencies and new encodings are developed for civilian use. In 2005 the first satellite of the Block IIR-M was launched, which transmits L2C (C for civilian) signals. These signals are freely available for civilians, but are also transmitted with higher power, compared to the L2P signals. L5 ($f = 1176.45\ MHz,\ \lambda \approx 25.5\ cm$) signals are first transmitted by a Block IIF satellite in 2009 and are designed for search and rescue, as well as for better ionospheric corrections (*Hofmann-Wellenhof et al.*, 2012; *Teunissen and Montenbruck*, 2017).

As stated above, the GNSS satellites continuously broadcast microwave L-band signals towards the Earth with ground-based GNSS antennas passively capturing the incoming signal. GNSS signals can be received at any time (day and night), and at any environmental condition, including through clouds and during heavy precipitation events (*Gleason and Gebre-Egziabher*, 2009). Every satellite has its own space vehicle number (or SVN), which is serial numbers assigned to each GPS satellite. Each satellite is recognized by the unique "pseudo-random noise" sequences (PRN's), or Gold codes, associated with the specific position of the satellite in the constellation. Thus over time when a new satellite replaces an old one in the constellation, it has a new, unique SVN, but it inherits the PRN of the satellite it replaces.

The GNSS signals on their way through the atmosphere are affected in several different ways by the atmosphere. The higher layers of the atmosphere, between 60 and 600 km above ground contain significant amounts of ionized gases and free electrons, compared to the neutral atmosphere. In total 0.1% of the mass of this layer is ionized. The GNSS signals, like any electromagnetic wave, are bent when passing through the Ionosphere. The bending of the signals is frequency-dependent, so the effect of the Ionosphere on the signal bending can be calculated using the difference between the GNSS signal's frequencies (*Petrie et al.*, 2010). Thus GNSS signals can be used for Total Electron Content (TEC) measurements in the higher atmosphere (*Arras et al.*, 2008). Secondly the GNSS signals are being delayed due to the changing optical density of the atmosphere with altitude (*Tralli and Lichten*, 1990). This delay is used for atmospheric water vapour observation, a method which is described in more details in chapter 3.4. The space-based GNSS applications are used in radio occultation missions for ionospheric and tropospheric retrievals (CHAMP (*Wickert et al.*, 2001), FORMOSAT-3/COSMIC (*Wickert et al.*, 2009), gravimetry missions (GRACE, GOCE, GRACE-FO (*Flury and Rummel*, 2005)), reflectometry missions (UK-DMC (*Gleason*, 2006), TDS-1, CYGNSS, G-TERN GEROS-ISS (*Wickert et al.*, 2016)) for sea ice coverage (*Zhu et al.*, 2017; *Cardellach et al.*, 2018), wind speed retrievals and rain effects (*Foti et al.*, 2015; *Asgarimehr et al.*, 2018). In this work ground-based geodetic stations are exclusively used for the monitoring of atmospheric water vapour and soil moisture (*Bevis et al.*, 1992; *Guerova et al.*, 2016a; *Georgiadou and Kleusberg*, 1988).

In chapter 5, which is devoted to GPS reflectometry, L1, L2C and L5 signals are used for the estimation of the soil moisture and in chapter 7 for snow height observation from the reflected GPS signals. Unlike GLONASS, Galileo and BeiDou, GPS orbits are chosen at such altitude, that the satellites repeat their position every sidereal day (23h 56m 4s). This orbit period ensures that each GPS satellite rises and sets from the same direction in regards to a static GNSS receiver every day consistently. Thus the GPS orbits enable ground reflections from each satellite to be located in the same area continuously over long periods of time, enabling daily observations. GLONASS satellite orbits provide such continuity not on a daily basis, but every 8 days. Galileo provides orbit repeatability every 10 days and BeiDou - every 7 days. Thus creating reflections time series over the same reflection points from Galileo, GLONASS and BeiDou can be performed at worse than weekly data rate, compared to the daily rate from GPS.

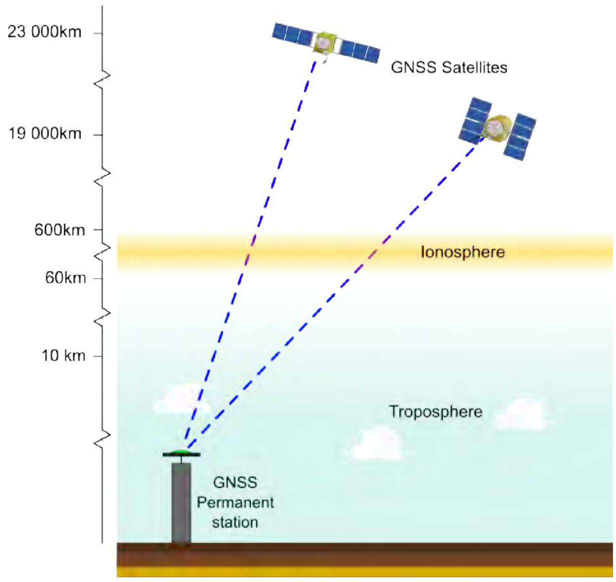

Figure 3.2: GNSS signals and the layers of the atmosphere.

3.2 GNSS tropospheric delays

3.2.1 GNSS observation equations

There are several GNSS observables, which can be provided by a GNSS receiver. These observations are:

- Pseudorange,
- Carrier-phase,
- Doppler.

All definitions and equations in this section are taken from *Teunissen and Montenbruck* (2017); *Blewitt* (1997).

The pseudorange measurements represent the apparent signal travel time between the GNSS satellite and the receiver. The receiver generates a replica of the transmitted satellite code and aligns it with the received signal. The time shift between the two codes is the apparent transit time of the signal. It is then combined with additional information from the satellite's navigation data to obtain the actual travel time from the satellite to the receiver. This time is then multiplied with the speed of light to obtain the pseudorange between the satellite and the receiver. These measurements differ from the actual distance, since the signal is subject to delays and the receiver's and satellite's clock offsets are unknown.

The pseudorange equation, describing the distance between the satellite and receiver takes the following form:

$$p_r^s(t) = \rho_r^s(t) + \xi_r^s(t) + c(d_r + d^s) + c(dt_r + dt^s + \delta t^{rel}(t)) + I_r^s(t) + T_r^s(t) + \epsilon_r^s(t), \quad (3.1)$$

where $p_r^s(t)$ is the pseudorange, $\rho_r^s(t)$ is the actual distance between the satellite and the receiver, $\xi_r^s(t)$ is the correction of the phase-center offsets of the transmitting and receiving atennae, d_r and d^s are the receiver and satellite instrumental delays, dt_r and dt^s are the clock offsets, $\delta t^{rel}(t)$ are relativistic corrections, I and T are the ionospheric and tropospheric delays and $\epsilon_r^s(t)$ are residuals, such as noise and multipath.

The receiver also records the carrier phase form. It creates a replica of the carrier signal, aligns it with the observed messages from the satellite and then measures the phase shift between the two. Since the wave lengths of the GNSS signals are in the range between 15-30cm, each full phase cycle indicates a change in the distance between the satellite and receiver equal to the wave length. The carrier phase measurements are more precise, than the pseudorange measurements, because they are relative to one another. On the downside the carrier-phase observations cannot be used to calculate the distance between receiver and satellites - only relative distance changes. The carrier-phase observations equation is:

$$\phi_r^s = \rho_r^s(t)+\xi_r^s(t)+c(\delta_r+\delta^s)+c(dt_r+dt^s+\delta t^{rel}(t))-I_r^s(t)+T_r^s(t)+\lambda(\omega(t)+N)+\epsilon_r^s(t), \quad (3.2)$$

where λ is the wave length of the signal, ω is the relative angular rotation between the receiver and transmitter antennae and N is the number of phase cycles, called ambiguities. Different level of positioning accuracy is achieved through the treatment of the ambiguities: firstly float ambiguities are retrieved through least-square estimations, secondly the ambiguities are mapped from $\mathbb{R} \rightarrow \mathbb{Z}$ into integers and lastly the integer ambiguities are fixed and a second least-square adjustment is carried out for the final positioning.

Another observable by the receiver characteristic is the Doppler shift of the received frequency. The Doppler shift is caused by the relative movement between the satellite and the receiver and can be expressed by the following equation:

$$D_r^s = \frac{1}{\lambda}\left(\frac{\vec{v^s}}{c} - \vec{e}\right).(\vec{v^s} - \vec{v_r}) + (df_r + df^s) + \frac{c}{\lambda}\delta f_{clk}^{rel}, \quad (3.3)$$

where D is the observed Doppler shift, df_r and df^s are the frequency deviations of the receiver and satellite, c is the speed of light, $\vec{v_r}$ and $\vec{v^s}$ are the relative movement speeds of the receiver and the satellite, respectively, $\vec{e}$ is the unit line of sight between the satellite and receiver and δf_{clk}^{rel} are the clock related relativistic effects.

3.2.2 Atmospheric refraction

The atmosphere is a medium with changing density. In lower altitudes the density of the atmosphere is higher, than in higher altitudes. The electromagnetic waves travelling through such medium with changing density are subject to decrease in their speed, according to the optical density of the atmosphere. Following Snell's law, the optical density (also known as refractive index) of a medium is described through the speed of electromagnetic waves, passing through it:

$$n_m = \frac{Speed\ of\ light\ in\ vacuum}{Speed\ of\ light\ in\ the\ medium} = \frac{c}{v}. \quad (3.4)$$

Snell's law postulates, that an electromagnetic wave, penetrating the border between two media with different optical density, changes the direction of its propagation:

$$n_1 sin\alpha_1 = n_2 sin\alpha_2 \quad (3.5)$$

where α_1 is the angle of propagation to the border between the two media of the wave in the first medium, α_2 is the same angle in the second medium and n_1 and n_2 are the refractive indices of the media, respectively (see figure 3.3). The Fermat's principle is the integrated form of Snell's law for medium with gradually changing optical density:

$$S = \int_a^b n(s)ds \tag{3.6}$$

where S is the optical path of the wave through the medium with changing density ($n(s)$), a and b are the start and the end of this path. For the atmosphere this equation can be modified to the following:

$$S = \int_{h_0}^{h_{top}} n(h)dh \tag{3.7}$$

where h_{top} is the top of the atmosphere and h_0 is the Earth's surface.

The optical density of the atmosphere (n) is dependent on its pressure (p - pressure, p_0 - pressure at sea level), temperature (T - temperature, $T_0 = 273.15K$ - melting point of water) and properties of the molecules of air (N_a - Avogadro constant, V_0 - molar volume of an ideal gas under standard conditions, α - scalar atomic polarizability and ϵ_0 - the absolute dielectric permittivity of vacuum) and can be described by the following equation (*Foelsche*, 1999):

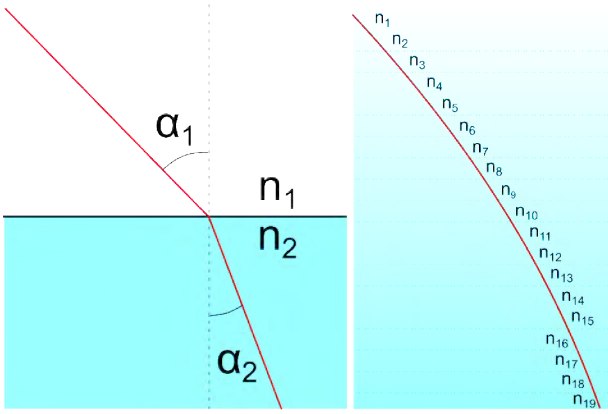

Figure 3.3: Visualization of Snell's law and Fermat's principle.

$$n = \frac{10^6 N_a T_0}{2\epsilon_0 V_0 p_0} \alpha \frac{p}{T} \tag{3.8}$$

Optical density is a measure of the ratio between the speed of propagation in vacuum and the speed of light in a certain medium. The difference between the time needed for the signal to travel in vacuum and the signal to travel in the medium is referred to as delay.

3.2.3 Mapping functions

GNSS receivers receive positioning messages from the satellites from elevation angles close to the horizon up to zenith. Thus the signals travel through longer or shorter slanted paths to the receiver, depending on the angle and the thickness of the atmosphere at the specific locations, so that each signal is delayed differently. In this work tropospheric delays, mapped to zenith using mapping functions, such as the one, described by *Niell* (1996) are examined.

The mapping function is a projection of the tropospheric wet and dry delays to zenith (as seen on figure 3.4). The projection is dependent on the elevation angle of the satellite.

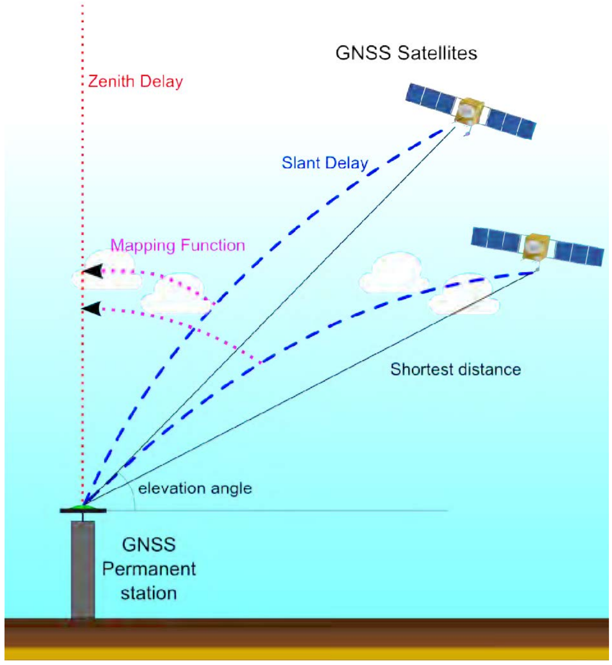

Figure 3.4: Effect of the neutral atmosphere on the GNSS signals. The electromagnetic waves follow the optical path, defined by the Fermat's principle. The tropospheric delays are then mapped to zenith.

The simplest mapping function can be derived as:

$$m(\epsilon) = \frac{1}{sin(\epsilon)}, \tag{3.9}$$

but thus approximation is far from perfect. *Marini* (1972) developed a more complex and accurate mapping function:

$$m(\epsilon) = \frac{1}{sin(\epsilon) + \frac{a}{sin(\epsilon) + \frac{b}{sin(\epsilon)+...}}}, \tag{3.10}$$

where a, b, c... are coefficients, defined differently by different authors. Later *Niell* (1996) developed a set of mapping functions (Niel Mapping Function, NMF) through the following equation:

$$m(\epsilon) = \frac{\frac{1}{1+\frac{a}{1+\frac{b}{1+c}}}}{sin(\epsilon) + \frac{a}{sin(\epsilon)+\frac{b}{sin(\epsilon.)+c}}}. \tag{3.11}$$

The mapping function, used in this work is the Global Mapping Function (GMF), in which b and c are empirically derived values, while a has the following structure (*Boehm et al.*, 2006):

$$a = a_0 + A\cos\left(\frac{doy - 28}{365} 2\pi\right), \tag{3.12}$$

where a_0 is a global grid of mean values, A is a global grid of amplitudes for both hydrostatic and wet coefficients and doy is day of year. The differences between GMF , Vienna Mapping Function (VMF) (*Kouba*, 2008) and NMF can reach up to 10mm vertically (*Boehm et al.*, 2006).

3.2.4 Zenith Tropospheric Delay

The atmosphere is composited of different gases, each with its own optical density. Based on the optical density of the wet and dry constituents of the atmosphere, delays for dry (Z^{dry}) and wet (Z^{wet}) atmosphere can be postulated:

$$d_{trop}^{dry} = \int_{h_0}^{h_{top}} (n^{dry}(h) - 1)dh, \tag{3.13}$$

$$d_{trop}^{wet} = \int_{h_0}^{h_{top}} (n^{wet}(h) - 1)dh. \tag{3.14}$$

These factors represent how the dry gases and water vapour differ from ideal gas. The full tropospheric delay, as defined in equations 3.1 and 3.2, is a product of the dry and wet delays:

$$d_{trop} = d_{trop}^{wet} + d_{trop}^{dry}. \tag{3.15}$$

The accuracy of the used mapping functions is very important for the accuracy of the computed ZTD:

$$ZTD = m^{wet}(\epsilon)d_{trop}^{wet} + m^{dry}(\epsilon)d_{trop}^{dry}, \tag{3.16}$$

where d_{trop}^{dry} is the hydrostatic tropospheric delay in direction of the satellite, computed from equation 3.13 and the d_{trop}^{wet} is the wet tropospheric delay, computed from equation 3.14. $m^{wet}(\epsilon)$ and $m^{dry}(\epsilon)$ are the wet and dry mapping functions for elevation angle ϵ. In order to compute the ZTD, the GNSS processing software has to assimilate pressure and temperature measurements from the GNSS station. Earlier the values for pressure and temperature are introduced with empirical equations, based on the station's altitude. The precision of such empirical methods is not sufficient for modern millimetre accuracy of GNSS coordinate solutions, thus data from NWP models is used by the processing software to estimate the ZTD more precisely (*Hobiger and Jakowski*, 2017).

3.3 GNSS processing software

All software and techniques, mentioned in this section relate to processing GNSS data for positioning and tropospheric parameters. The bespoke software, developed for reflectometry is discussed in section 5.1.

There are two approaches to processing GNSS observables: Precise Point Positioning (PPP) and Differential Processing (DGNSS). The DGNSS technique is the older approach of the two. DGNSS relies on the availability of many GNSS stations, which are processed together. From the direct pseudorange and carrier-phase observations each station is producing, position differences between the stations (usually referred to as baseline coordinates) are estimated (*Hatch*, 1989). The pseudorange differences are used in standard DGNSS processing, while the more accurate carrier-phase differential observations enable Real-Time Kinematic solutions (RTK). Satellite parameters, such as frequency deviations, clock offsets, orbits can be calculated with higher precision when large networks of stations with long baselines are processed together in differential mode (*Teunissen and Montenbruck*, 2017).

A recent development in GNSS processing is use of the PPP strategy (*Zumberge et al.*, 1997). In contrast to DGNSS, PPP uses data only from the station of interest, as well as GNSS satellite orbits and clocks, products of DGNSS processing. PPP is preferable for individual stations, or small dense network, since it uses preprocessed clocks. Since 2013, the International GNSS Service (IGS, *Dow et al.* (2007); *Caissy et al.* (2012)) provides ultra-fast or real-time precise satellite orbit and clock corrections in support of PPP processing (*Douša and Vaclavovic*, 2014; *Li et al.*, 2015b; *Yuan et al.*, 2014; *Ahmed et al.*, 2016). The PPP strategy has the advantage of being computationally much more efficient than DGNSS and hence can provide estimates for large networks of stations with high temporal resolution (every 5 min). This task can be achieved by the conventional DGNSS strategies only by using superior IT infrastructure.

3.3.1 NAPEOS

NAPEOS (NAvigation Package for Earth Orbiting Satellites, `http://www.esa.int/Our_Activities/Operations/NAPEOS`) is developed by the European Space Agency (ESA) for the processing of GNSS data. NAPEOS is developed and maintained by the European Space Operations Centre (ESOC) of the European Space Agency (ESA). NAPEOS is used at ESOC since January 2008. NAPEOS has several key features:

- Multi-GNSS processing, incorporating GPS, GLONASS and the European GALILEO,
- Can be used both for network solution undifferenced processing, as well as for PPP,
- User-friendly interface,
- The license is free of charge for institutions in ESA member countries.

The NAPEOS software requires stations coordinates and dynamic parameters (station speed, ocean loading displacement) in order to process the GNSS data. The processing sequence of NAPEOS in PPP mode is shown in the scheme on figure 3.5:

The input files for processing in PPP mode are:

- Uncompressed RINEX files

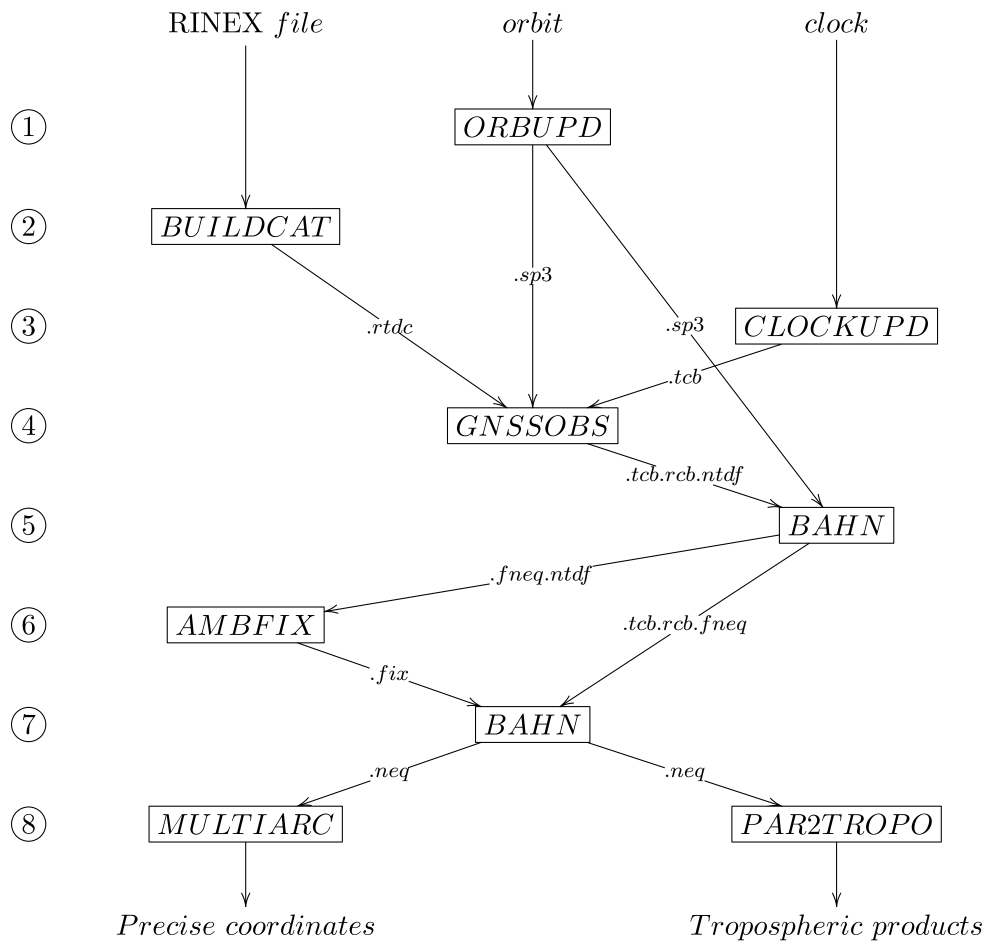

Figure 3.5: NAPEOS processing scheme for PPP processing, used in this thesis in section 4.3. The inputs to the software are the RINEX files, together with orbit and clock files. In the intermediate steps of the processing files are generated with synchronized orbits (.rcb), clocks (.tcb) ambiguities fixing (.fix), normal equations (.neq, .fneq) as well as catalogue files for internal use.

- Orbit files (.sp3), obtained from IGS
- Clock files (.clk), obtained from IGS
- Dynamic parameters (station speed, ocean loading displacement)

The NAPEOS version 3.3.1 is used for the processing in this study. The processing is performed using the GMF and 10° elevation cut-off angle. The data is processed using the PPP strategy with fixed ambiguities and employing IGS satellite orbits and clocks. The computed ZTDs are with a temporal resolution of $300s$ ($5min$).

3.3.2 EPOS

Earth Parameter and Orbit System (EPOS) is a GNSS processing software, developed in GFZ. The development of the software was started in the 1990's by the IGS group in GFZ

(*Gendt et al.*, 2004). The software has since been developed into several generations, the latest being EPOS8. As a first step in the processing (the "Base cluster analysis" in figure 3.6), EPOS employs a network solution least squares adjusted undifferenced strategy for calculating precise satellite orbits and clocks. In the second step the processed network or stations are divided into clusters and handled in PPP. The ZTD's and gradients can be produced with very high temporal resolution. The clustering and the PPP strategy allow for processing of vast networks, since every station is handled independently.

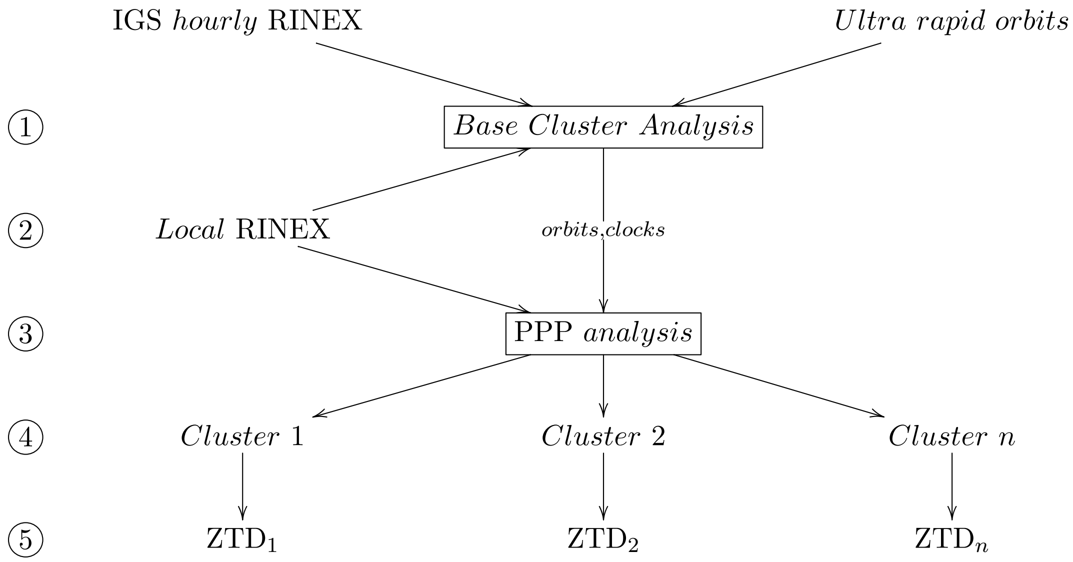

Figure 3.6: EPOS processing scheme.

3.3.3 Bernese GNSS Software

The Bernese GNSS Software (BSW) is developed in the Astronomical Institute of the University of Bern (AIUB), Switzerland. Bernese is one of the most widely used GNSS processing software packages in the world, especially in Europe. The software operates using a double differencing network solution processing approach, where multiple ground-based GNSS stations with long baselines are necessary for accurate positioning solutions. The software can also use a PPP strategy. Bernese in its current version 5.2 supports fully both GPS and GLONASS. The analysis of dual–frequency data for the upcoming new systems, like European Galileo, Chinese BeiDou, or Japanese Quasi-Zenith Satellite System (QZSS), is prepared but not yet fully developed for an operational processing (*Dach and Walser*, 2015).

Bernese is a software with wide range of scientific applications, including positioning, monitoring of earth crust movements, estimation of tropospheric delays and gradients and ionospheric effects for both GNSS and Satellite Laser Ranging (SLR) applications. The software can also be used for correction of receiver and antenna biases. Both GMF and VMF can be used for the estimation of the tropospheric delays.

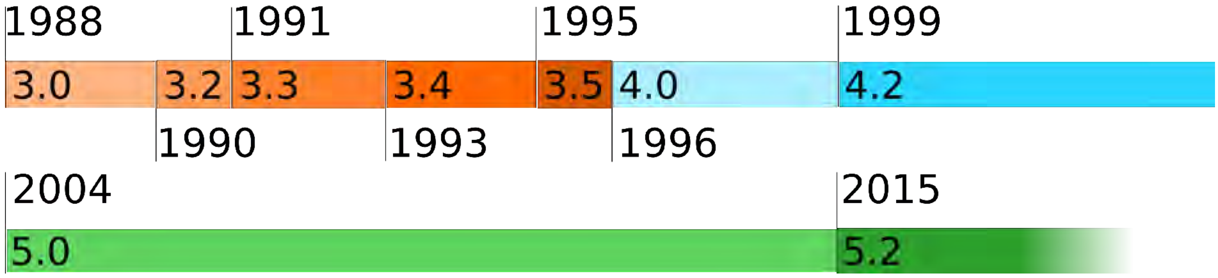

Figure 3.7: Evolution of the Bernese GNSS processing software.

3.4 Water vapour monitoring

The concept of GNSS Meteorology is suggested by *Bevis et al.* (1992). The propagation of the GNSS signal through the atmosphere is affected by the atmospheric gases (*Tralli and Lichten*, 1990; *Elgered and Wickert*, 2017). The magnitude of the tropospheric effects depends on several factors: the composition of the atmosphere; the elevation of the receiver (thus on the thickness of the atmosphere); the elevation angle of the satellite and the amount of water vapour, which is mostly dependent on the atmospheric conditions.

There are two contributing factors for the ZTD. They are the Zenith Hydrostatic Delay (ZHD and the Zenith Wet Delay (ZWD):

$$\mathrm{ZTD} = \mathrm{ZHD} + \mathrm{ZWD}. \tag{3.17}$$

The hydrostatic delay is caused by all the gases in the atmosphere, except the water vapour. They are the main contributor to the positioning uncertainty. The hydrostatic delay is relatively stable on a daily time scale. It can be derived, using its dependency on the local atmospheric pressure:

$$ZHD = (2.2768 + 0.0024)\frac{p_s}{f(h,\theta)} \tag{3.18}$$

$$f(h,\theta) = 1 - 0.00266cos(2\theta) - 0.00028h \tag{3.19}$$

where p_s is local surface pressure and $f(h,\theta)$ is a factor, dependent on height h and the latitude variation of the gravitational acceleration θ.

The second contributing factor to the ZTD is the ZWD. It is caused by the water vapour in the atmosphere. The ZWD has a large temporal variation in a hourly time scale. This is the reason, why the GNSS derived IWV is so valuable with its high temporal resolution. The ZWD contributes less then 10% of the ZTD. ZWD and IWV can be calculated with the use of these expressions:

$$IWV = \frac{10^6}{(k_3/T_m + k_2')R_v}ZWD, \tag{3.20}$$

$$T_m = 70.2 + 0.72 t_s, \tag{3.21}$$

where $k_2' = (17 \pm 10)[\text{K hPa}^{-1}]$, $k_3 = (3.776 \pm 0.004)10^5[\text{K}^2\ \text{hPa}^{-1}]$ are constants derived first by *Thayer* (1974) and $R_v = 461.51[\text{J kg}^{-1}\text{K}^{-1}]$ is the gas constant for water vapour and T_m [K] is the weighted mean atmospheric temperature.

Ground-based GNSS water vapour estimations are first derived in the beginning of the 1990s. Some of the first studies are carried out in the US, with a European COST 716 (*Elgered et al.*, 2005) project channelling the efforts of scientists from the UK, France, Germany (*Gendt et al.*, 2001), Switzerland (*Guerova et al.*, 2003), the Netherlands, Belgium, Sweden and other countries. The initial research combined the GPS networks of France, Italy and Spain (*Haase et al.*, 2002). The first contributions of GFZ as the German GNSS analysis center for water vapour monitoring date back to the year 2001 (*Dick et al.*, 2001), when 10 GNSS stations, collocated with meteorological stations, are established to prove the concept of GNSS Meteorology for the German weather service (Deutscher Wetterdienst, DWD). This cooperation is further expanded through the GASP project (*Reigber et al.*, 2004). Operational provision of ground-based GPS tropospheric products in Near Real Time (NRT) was first attempted during the COST 716 project in 2001 (*Elgered et al.*, 2005). These studies are followed by the establishment of the E-GVAP project in 2005 (*Pacione et al.*, 2008; *http://egvap.dmi.dk/*) within the EUMETNET network. This project has 17 contributing processing centers who continuously provide operationally processed IWV data to 18 weather services throughout Europe. GFZ is also one of these operational centers (*Bender et al.*, 2008; *Li et al.*, 2014). Most of these centers perform double differencing network solutions for estimating station positions and, subsequently, tropospheric delays.

The first attempt to process GPS stations individually using the Precise Point Positioning (PPP) technique is performed by *Zumberge et al.* (1997). GFZ together with NGAA (processing center of Chalmers University, Sweden), developed a global product for GNSS orbits and clocks to foster the PPP processing technique (*Gendt et al.*, 2004). Building upon these investigations, IGS launched near-real time (NRT) estimations of GNSS orbits and clocks (*Caissy et al.*, 2012) for PPP processing. *Douša and Vaclavovic* (2014) found the PPP processing with IGS NRT products to be accurate for meteorological observations. Since, PPP has been proven reliable and is used in more and more GNSS analysis centers (*Li et al.*, 2015a; *Yuan et al.*, 2014; *Li et al.*, 2015b).

In recent years the research in the field of GNSS meteorology is further fostered by the COST ES1206 "Advanced Global Navigation Satellite Systems tropospheric products for monitoring Severe Weather Events and Climate" (GNSS4SWEC) project (*Jones et al.*, 2020), focused on meteorological applications, nowcasting (*Haan et al.*, 2020) and climate (*Bock et al.*, 2020). Subsequent studies involved experiments in 3D profile reconstruction of the atmospheric water vapour through tomography (*Bender et al.*, 2011; *Bosy et al.*, 2010). While in Europe, application of GNSS in Meteorology is well established, in East Europe it is an emerging research field. Since the start of the GNSS4SWEC project, new GNSS processing centers emerged in Eastern Europe (*Dousa et al.*, 2020).

GNSS tropospheric products from the BULgarian intelligent POsitioning System (BULiPOS, *http://www.bulipos.eu/* (2013)) GNSS network in Bulgaria are used in this thesis. The BULiPOS network of reference stations is established in 2008 and has 26 stations mainly used for navigation and geodetic applications.

The pressure at the GNSS station altitude is calculated using the model pressure at the nearest model grid point. The pressure difference between the GNSS station altitude and the nearest NWP model grid point is calculated using the polytropic barometric formula (*Sissenwine et al.*, 1962):

$$P_g = P_m \left(\frac{T}{T - L(H_g - H_m)} \right)^{(\frac{g_0}{R}\frac{M_0}{L})} \tag{3.22}$$

where P_g [hPa] is the pressure at the GNSS station altitude, P_m [hPa] is the pressure at meteorological station altitude, T [K] is the temperature in meteorological station, $L = 6.5 \frac{K}{km}$ is tropospheric lapse rate, H_m [km] is the altitude of the meteorological station, H_g [km] is the altitude of the GNSS station, $g_0 = 9.806 \frac{m}{s^2}$ is the gravitational acceleration, $M_0 = 28.9644 \frac{g}{mol}$ is the molar mass of air and $R = 8.31432 \frac{Nm}{(molK)}$ is the universal gas constant.

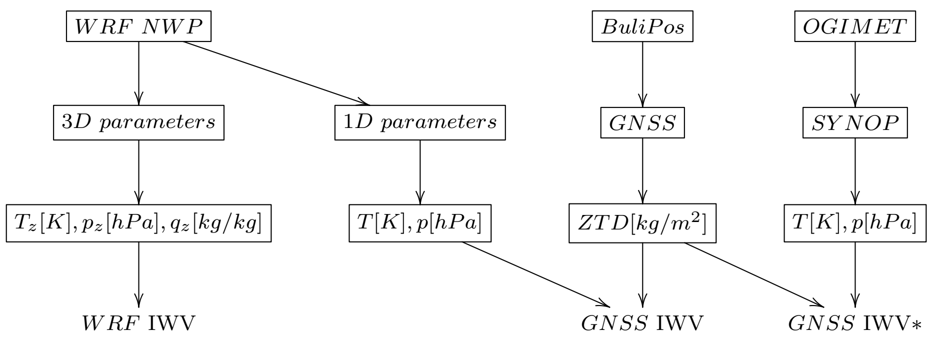

Figure 3.8: IWV processing data flow and data sets.

Presented in figure 3.8 is the processing data flow, used in chapter 4. The source of meteorological information are the measurements are from the surface observation network (SYNOP) of the National Institute of Meteorology and Hydrology (NIMH) in Bulgaria. Observations of temperature (T), pressure (p), precipitation (PP) and other parameters of the atmosphere are collected manually every 3 hours (00, 03, 06, 09, 12, 15, 18 and 21 UTC) throughout the Bulgarian observation network. The data are available from the OGIMET weather information server (*http://www.ogimet.com/*). The surface pressure and temperature are used for derivation of IWV from the GNSS tropospheric products. Using surface observations the IWV is derived every 3 hours and is referred to as IWV* (seen in figure 3.8). The WRF simulations from the nearest to the GNSS station grid point are used to compute the GNSS IWV.

3.5 Earth surface observation using GNSS reflected signals

3.5.1 Soil moisture

Since the establishment of the GNSS ground-based networks multipath effects have been considered inferior to the accuracy of coordinate estimations in the stations. Thus techniques are developed to map and estimate the influence of reflected signals in order to decrease their influence on geodetic measurements (*Hannah*, 2001). *Masters et al.* (2004) for the first time proposed to use these reflections as opportunistic signals to estimate properties of the reflective surfaces. Since then the use of Signal-to-Noise Ratio (SNR) from ground-based receivers is implemented by many GNSS processing centers in USA (*Katzberg et al.*, 2006; *Larson et al.*, 2008b), Luxembourg (*Tabibi et al.*, 2015), France (*Zhang et al.*, 2018), Spain (*Egido et al.*, 2012; *Rodriguez-Alvarez et al.*, 2012) and Germany (*Vey et al.*, 2016a). The Planetary Boundary Observatory (PBO) GNSS network is currently used operationally to provide data for the amount of soil moisture in the western US (*Larson*, 2016).

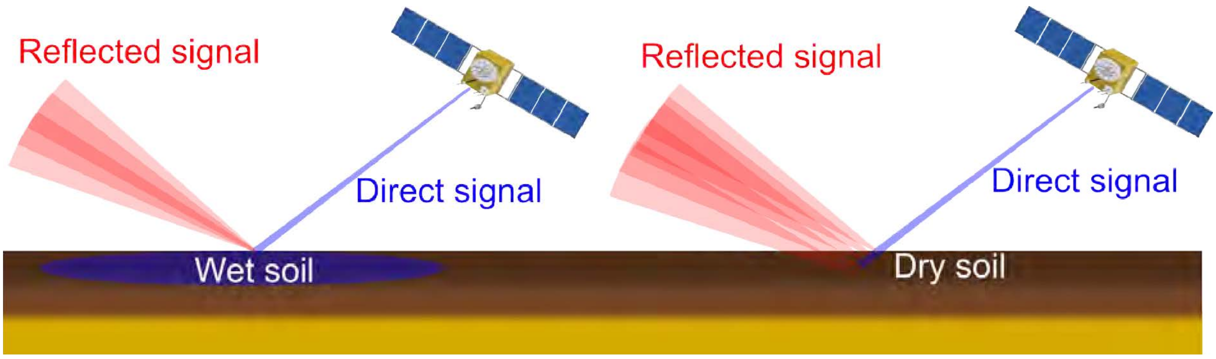

Figure 3.9: GNSS signal penetration in wet (left) and dry (right) soils is dependent on the dielectric constant of soils and water. The more water, the smaller the penetration of the signal.

When GNSS signals are received by a ground-based station, several of their properties are recorded: code, phase, Doppler shift and signal strength observations. The code and phase contain the navigation messages from the GNSS satellite modulated with lower frequency into the carrier signal. Using these observations the position of the receiver can be determined in relation to the positions of the GNSS satellites. The signal strength

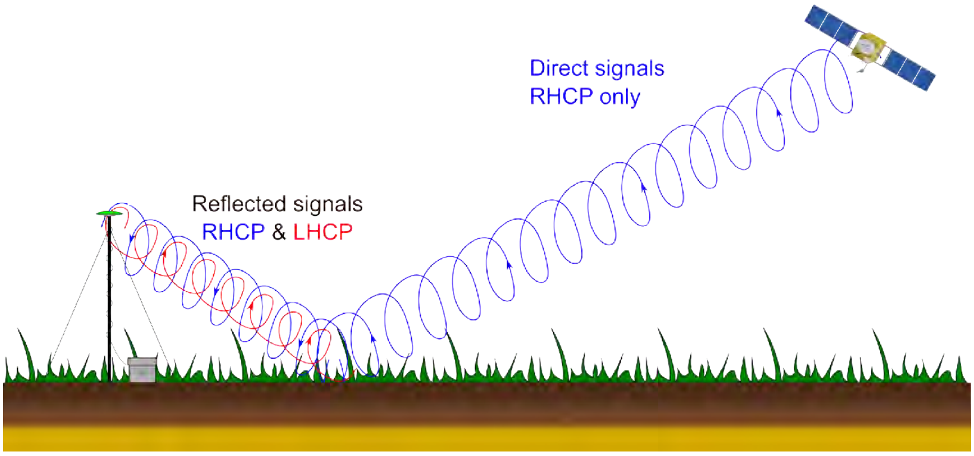

Figure 3.10: Change of the GNSS signal polarization during reflection.

observations show the power of the signal from each satellite from the direction of emitting. It depends on the elevation angle of the satellite and is highest in angles closest to zenith. The strength of the received signal is also a function of the emitting power of the satellite antennas and of the gain pattern of the antenna, connected to the receiver. Finally reflections from nearby obstacles can also contribute to the power of the signal received. Thus the area and position of the reflective surface can be determined *Chew et al.* (2016).

The dielectric permittivity of a medium is the physical property, describing the way it is interacting with electromagnetic fields. The dielectric constant (ϵ) of a dielectric medium is a frequency-dependent parameter, which determines the way in which electromagnetic waves are reflected from a surface with higher permittivity materials having stronger reflections (*Fuks and Voronovich*, 2000). For microwave frequencies (such as GNSS L-band), the dielectric constant of water is 78.4, while for dry soil its value is 3.5 (*Hallikainen et al.*, 1985). This large difference is the reason why GNSS reflected signals are sensible to water in the soil (*Katzberg et al.*, 2006). The difference in the dielectric properties of wet and dry soils also influences the penetration depth of the signal (see figure 3.9). The higher the dielectric constant, the closer to the surface of the soil the reflection happens.

The GNSS signals are Right Hand Circular Polarized (RHCP). According to the Brewster's law, when a circular polarized signal is being reflected, the reflected signal under a certain critical angle (Brewster angle, θ_B), changes its polarization (*Trizna*, 1997). The Brewster angle is different for different reflective surfaces and is dependent on the dielectric constant of the medium (ϵ_m):

$$\theta_B = \arctan \frac{\epsilon_m}{\epsilon_{air}} \tag{3.23}$$

Water, for example, has a very low Brewster angle ($\approx 5°$ elevation[1]), thus any RHCP

[1]Elevation angle is the angle between the horizon and the line of sight.

signal reflected at higher elevation angles, is predominantly polarized with Left Hand Circular Polarization (LHCP). The Brewster angle for soil is much higher, than for water, thus a significant part of the reflected signal retains its RHCP polarization (visualized in figure 3.10). Since the standard GNSS receivers, used in this work, are sensible to RHCP only, they are not sensible to the LHCP part of the reflected signal.

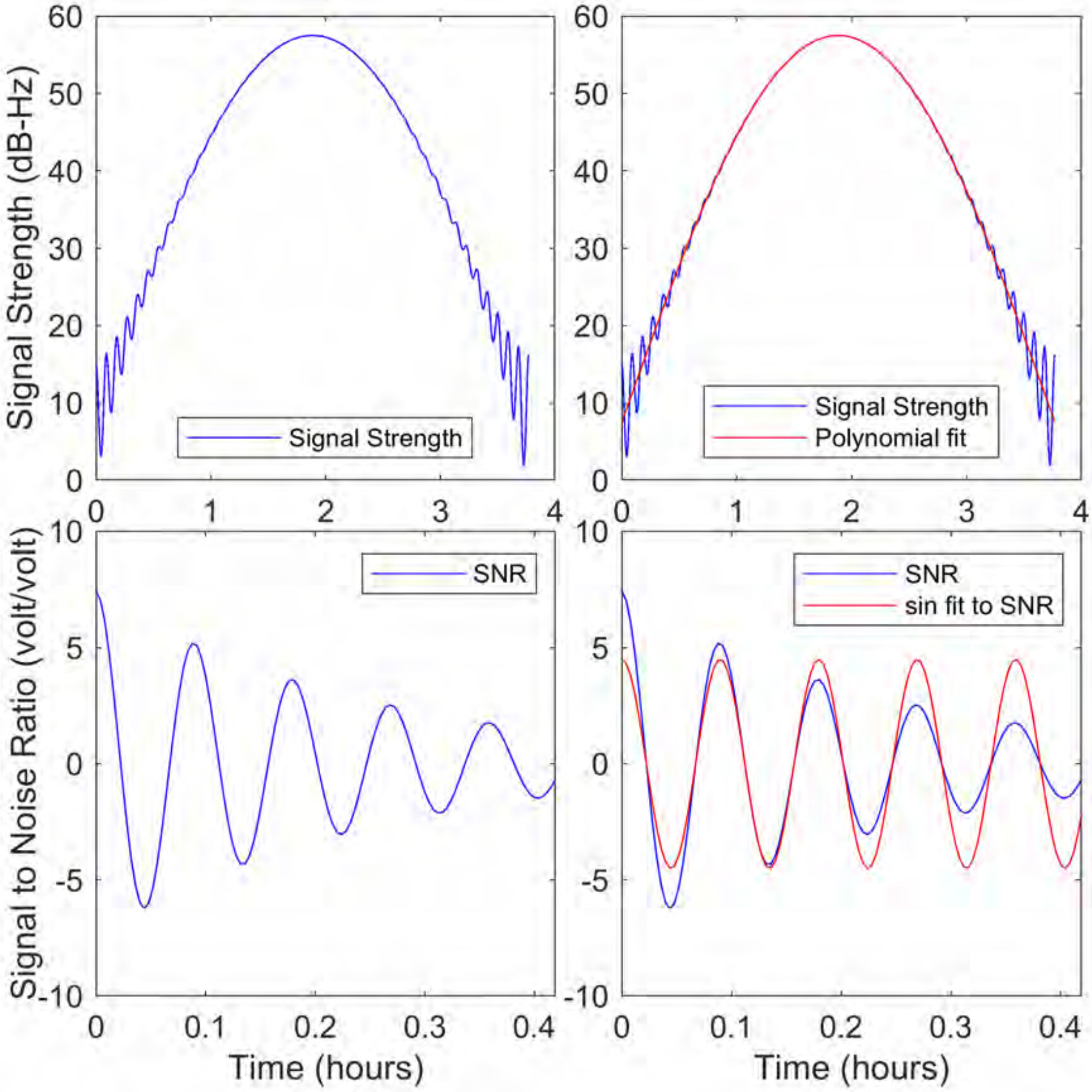

Figure 3.11: Interference patterns in the GNSS signal strength data at low elevations can be described by the antenna height, as well as the reflective surface properties. On this simulation example the process of acquiring the amplitude and phase of the interference pattern is shown.

When the direct and reflected signals reach the GNSS antenna, both of them are detected. The signal strength of the direct and the reflected signal, as received by the antenna are dependent on the elevation angle of the GNSS satellite (through the Brewster law dependence) and on the GNSS antenna gain pattern (*Larson et al.*, 2008a). Since reflected signals are usually regarded as noise, geodetic antennae are equipped with noise-cancelling choke rings (specially designed metal collars, which create shadow from the reflected signals). The antenna can't distinguish the direct signal from the reflected, the recorded signal strength shows the interference pattern between these two signals (as shown on figure 3.11). The reason for the occurrence of the interference pattern is that there is a periodicity in the phase difference between the direct and reflected signals (figure 3.12). When the direct and reflected signals are in-phase, the resulting amplitude of the received signal strength is amplified, while when the two signals are in counter phase, the signal strength, as received by the antenna is dampened. In this thesis the term signal strength is used as a description of the directly measured by the receiver signal in units of $dB - Hz$.

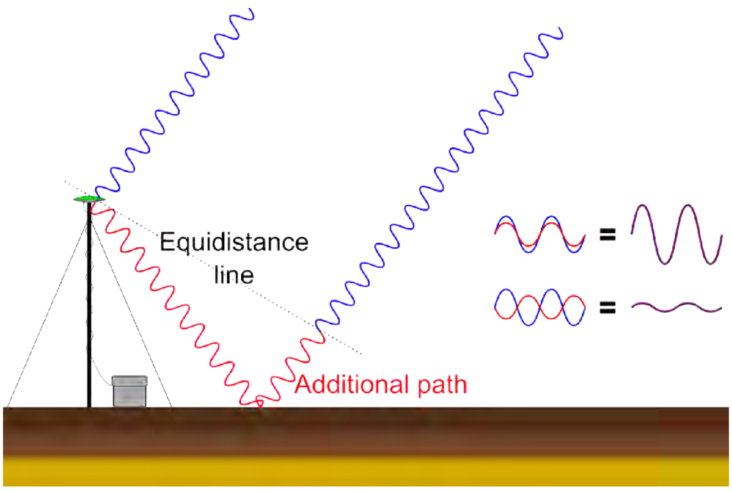

Figure 3.12: GNSS direct and reflected signals as received by a permanent GNSS station. The reflected signal travels a longer distance. The strength of the reflected signal is smaller than the strength of the direct. The phase difference between the direct and reflected signals influences the recorded signal strength. Figure inspired by *K. Larson*.

The resulting signal strength interference pattern is polynomially de-trended and subsequently the low elevation angles of the signal to noise ratio (SNR) is acquired and analysed. The SNR can be modelled with the following equation:

$$SNR = A \cos\left(\frac{4\pi h_0}{\lambda} \sin e + \phi\right) \tag{3.24}$$

where A is the average amplitude of the interference pattern, h_0 is the hight difference between the antenna and the reflective surface, λ is the frequency of the signal, e is the elevation angle of the satellite, ϕ is a phase shift and the SNR is the result of the de-trending of the signal strength and is measured in $\frac{volt}{volt}$. The units of the SNR are Figure 3.11 (bottom left and right) show that the amplitude is dependent on the elevation angle.

The amplitude and phase shift of the SNR are estimated using a Lomb-Scargle Least Square Adjustment (LSA). The Lomb-Scargle method is developed for finding weak periodic signals in random and unevenly sampled data and test their significance (*Press and Rybicki*, 1989; *Lomb*, 1976; *Scargle*, 1982). The method applies sampling of frequencies in predefined interval and uses LSA, comparing the original data with the fitted sinusoidal curves. Every sampled frequency is represented in the spectrum of significance, where the highest significance is given to the lowest least-square difference between the sample and the fitted curve.

The soil moisture estimations are extracted from the phase shifts of the SNR data. *Chew et al.* (2014) estimated that the change of 0.65° in the phase shift of the SNR is equivalent to a $1Vol\%$ change of soil moisture. Since the relation between the two parameters is linear, a dataset with the phase changes can be created:

$$\Delta\phi = \phi - \phi_0 \tag{3.25}$$

where ϕ_0 is the minimum phase shift of the SNR for the entire dataset. From this the volumetric water content (VWC) of the soils can be estimated:

$$VWC = \frac{\Delta\phi}{\gamma} + c_{min} \tag{3.26}$$

where c_{min} is a constant, equal to the minimum soil moisture, measured in the station, also known as residual soil moisture. The value of c_{min} has to be estimated for each station individually. In this thesis this value is set at $c_{min} = 3.5Vol\%$, which is a value, described in more details in chapter 5.3. *Chew et al.* (2014) determined the slope of $\gamma = \frac{0.65°}{1Vol\%}$ theoretically, but also mention that this slope is not applicable for all stations, claiming a 20% higher slope from field studies. Apart from a minimum possible value for soil moisture, there is also a saturation soil moisture value. This value is estimated in section 5.3 to be equal to $50Vol\%$, which physically means, that half the volume of the soil is composed of water. The saturation soil moisture value in ERA5 is also set to be $50Vol\%$. *Brady and Weil* (2013) estimate the saturation soil moisture to be $60 \pm 10Vol\%$, depending on the type of soil. In any case VWC can't exceed these thresholds, which is the reason why the scaling coefficient γ is changed to $\frac{1°}{1Vol\%}$, so that the maximum estimated soil moisture values for these stations does not exceed these thresholds. In the cases of these stations, the true scaling coefficient γ cannot be estimated, since no other soil moisture measurements are available in the area.

Standard geodetic GNSS receivers are equipped with RHCP zenith-oriented antennas only. These antennas are capable of detecting both direct and reflected signals and are the main focus of this thesis. There are systems, incorporating dual antennas - RHCP and LHCP. In this case the LHCP antennas are tilted to the horizon for optimal acquisition of reflected LHCP signals. In these systems the reflectometry-related observable is not the interference pattern in the SNR, but the difference in received signal strength between the upward and downward looking antennae. Such systems can also be used for soil moisture monitoring, but are not used in this work (*Masters et al.*, 2004).

The GNSS signals are usually described as geometrical lines. In reality the signal propagation between the GNSS satellite and the receiver forms a wave front. The prolate spheroid volume, encapsulating semi-coherent signals with phase shifts up to 90° from the direct optical path is the first Fresnel zone (visualized in figure 3.13). This is the reason why if an object stands in the direct optical path of the signal, the data transmission is not obstructed. The subsequent 2nd Fresnel zone is a similarly shaped volume, encapsulating the counter-phased wave fronts. The section of the first Fresnel zone of a reflected signal has elliptical shape and is calculated for each elevation angle using the following expressions:

$$a = \frac{\sqrt{\lambda h \sin e}}{(\sin e)^2}; b = \frac{\sqrt{\lambda h \sin e}}{\sin e} \qquad (3.27)$$

where a and b are the semi-major and semi-minor axes of an ellipse. Since the elevation

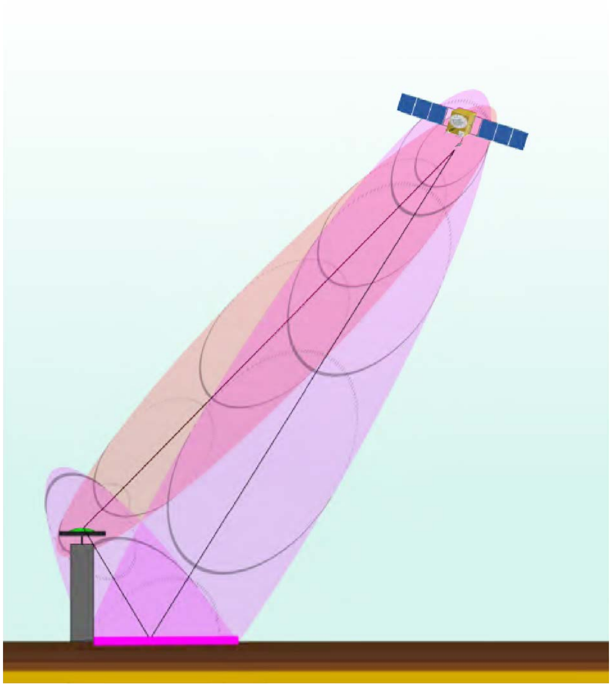

Figure 3.13: First Fresnel zones of a direct and reflected signal, reaching a GNSS receiver. The purple line on the ground represents the section of the first Fresnel zone of the reflected signal.

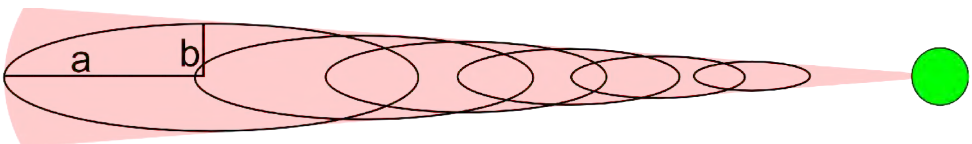

Figure 3.14: Schematic visualization of first Fresnel zone reflections from different elevation angles, stacked on a wedge-shaped track. View from above. The green circle illustrates the GNSS antenna. a and b are the semi-major and semi-minor axes of the Fresnel zones.

angles are an unbroken continuum, the Fresnel zones from the different elevation angles overlap in a wedge-shaped footprint of the reflection, as seen in figure 3.14. For a 1.5m high antenna the ellipse of the 5° elevation angle has dimensions of $a \approx 21m$ and $b \approx 2m$ and for 20° elevation angle $a \approx 2.7m$ and $b \approx 0.9m$.

3.5.2 Snow height

Soil moisture is not the only hydrological property, which can be obtained from the GNSS reflections. Accumulated snow reduces the reflector height in equation 3.24. Thus, from the time series of the height estimates from the SNR data, the snow height (SH) in GNSS stations can be measured (*Larson and Nievinski*, 2013):

$$SH = h_0 - h_e \tag{3.28}$$

where h_0 is the average reflection height without snow and h_e is the reflection height estimate. Observations from all GPS frequencies can be used for the derivation of snow height with higher accuracy of the reflector height estimation in cases of low reflector heights for the L1 signals, compared to L2 and L5, due to the L1 higher frequency (*Tabibi et al.*, 2015).

Nievinski and Larson (2014a) describe a similar approach to measuring the snow height using GPS phase observations, instead of the signal strength. This approach has been referred to as phase interference. The phase observations (described in section 3.2.1) show similar interference pattern with comparable or superior accuracy to the signal strength observations (*Nievinski and Larson*, 2014b). This approach has not been exploited in this work.

Another way of measuring the snow height in a station is using phase changes of the SNR, described in equations 3.24 and 3.25, which can be interpreted as reflector height changes. Following this assumption, the snow height changes can be detected using not only the reflector height estimations which are dependent on the frequency of the interference pattern, but also using phase estimations. Since such a measurement is not absolute, observation series have to be calibrated to a pre-known value (Φ_N). This approach uses the following equation:

$$SH = (\phi - \Phi_N)\frac{\lambda\pi}{360^o} \tag{3.29}$$

where SH is the snow height estimation, $\lambda/2$ is half the GPS frequency and $\frac{2\pi}{360^o}$ is conversion from degrees to radians. Φ_N is calculated as the average phase in snow-free environment. This approach is effective for small snow depths (*Vey et al.*, 2016b).

Chapter 4

GNSS water vapour measurements

This chapter describes the unique work carried out for this thesis in GNSS Meteorology. It is a first effort to derive high sampling frequency GNSS tropospheric products with the PPP processing strategy for validation of NWP models. The work is a Bulgarian contribution to Working Group 1 of the COST Action ES1206 GNSS4SWEC (*Dousa et al.*, 2020) with SUGAC being among the newly established Analysis Centers (AC's) within the project (*Simeonov and Guerova*, 2020).

Firstly, in section 4.2, a database for meteorological and GNSS observations is developed to comprise tropospheric products from leading GNSS Analysis Centers (AC's), meteorological observations and Numerical Weather Prediction (NWP) models simulations. In section 4.2.1 the effects of the 2007 heat wave over the Balkan peninsula are discussed in the context of GNSS station Sofia. Additionally, in section 4.2.2, a climatological study for station Sofia is carried out with comparisons between the tropospheric products from 5 different GNSS processing AC's.

Secondly, in section 4.3, a GNSS processing of a network of 7 stations in Bulgaria is performed with the NAPEOS software and the data is converted and analysed both for seasonal variations, as well as extreme meteorological events. The results of the data processing are compared to the results from a processing with the Bernese software.

4.1 State-of-the-art of GNSS meteorology in Bulgaria

Remote sensing of the troposphere with GNSS is a well-established method in western Europe (*Guerova et al.*, 2016a). The use of this method in South-Eastern Europe started in 2011 at Sofia University "St. Kliment Ohridski" with the FP7 project "Exploitation of ground-based global navigation satellite systems (GNSS) for meteorology and climate studies in Bulgaria/South-East Europe" `https://cordis.europa.eu/result/rcn/164029_en.html`. As a part of the project, a regional database Sofia University Atmospheric Data Archive (SUADA) is established. Within this thesis the first paper (*Guerova et al.*, 2014), presenting the SUADA database and two case studies of short- and long-term variation of IWV are conducted and presented in section 4.2. The work continues with the establishment of the Sofia University GNSS Analysis Center (SUGAC). Its first data processing campaign (2014) involves 7 Bulgarian GNSS stations in PPP mode with a temporal resolution of the tropospheric products of 5 minutes (see section 4.3). The resulting tropospheric products are used to evaluate a numerical weather forecasting model (WRF Weather Research and Forecasting) for 2013 (*Simeonov and Guerova*, 2020).

GNSS water vapour measurements in Bulgaria is a recently established topic of research. The only GNSS station, which has continuously been operated for water vapour retrievals is the IGS station SOFI. It is located in the Plana mountain, $1120m\ asl$, about $20km$ from Sofia. The station is equipped with Leica antenna and multi-frequency receiver. It is established by the Bundesamt für Kartographie und Geodäsie - the German Federal Agency for Cartography and Geodesy (BKG) and is in operation since 1998 for their global GNSS network positioning products. As of 2019, SOFI is also the only station on the territory of Bulgaria, which has been included in the EUMETNET EIG GNSS water vapour programme (EGVAP). EGVAP is a network, providing IWV measurements to the European national operational meteorological services. The station was not functional between the springs of 2013 and 2014, so all GNSS datasets have gaps in this period. Additionally the data density in 2018 is reduced due to communication problems. The Sofia meteorological station (WMO 15614) is located $15km$ away from the GNSS site at an altitude of $595m\ asl$ Surface observations are carried out in all synoptic periods (every 3 hours, starting 00 UTC), together with radiosoundings, performed daily at 12 UTC. The station is established in the 1950's, then outside the city borders. Nowadays the station is located within one of the large residential districts of the city. A study of data from the 2007 heat wave for Sofia is presented in section 4.2.1, followed by an analysis of the historical datasets since 1999 in section 4.2.2.

There are more then 4 operational private GNSS networks in Bulgaria, operating in total more than 100 GNSS sites. BuliPOS is one of them, part of the European EUPOS network. Data from 7 stations for a period of 1 year are provided from this network for the study of the water vapour over the territory of Bulgaria. This study is summarized in section 4.3.

The work in this thesis has served as basis for several peer-reviewed scientific articles: *Mircheva et al.* (2017), *Stoycheva et al.* (2017), conference proceeding and research reports: *Haralambous et al.* (2018), *Guerova et al.* (2016b), *Simeonov and Guerova* (2020) and more.

4.2 Sofia University Atmospheric Data Archive

Part of this section is published in AMT, 7/p2683–2694, 2014 (*Guerova et al.*, 2014). Currently SUADA has 5 GNSS datasets processed with different software and strategies. As seen in table 4.1 the GNSS data offer high temporal resolution from 5 min to 6 hours and the IGS station in Sofia Bulgaria (SOFI, marked by red pointer in figure B.2) is available since 1997. The GNSS datasets are discussed bellow.

The SUADA is a regional database aiming at: 1) achieving atmospheric water vapour observations from different techniques and 2) using the data for meteorological and climatic studies in Bulgaria/South-East Europe. Similar to the STARTWAVE database (*Morland et al.*, 2006), SUADA is designed to enhance and facilitate the atmospheric research at the Sofia University, but also to provide online data access, via a web portal, for interested researchers in Bulgaria and the neighbouring countries. SUADA is developed using the My Structured Query Language (MySQL) for a relational database management system (*Codd*, 1970).

dataset name	tropos. product	available yyyy - yyyy	number of stations	observation frequency	number of observations
IGS repro 1	ZTD	1995 - 2019	9	5 min	8 262 322
IGS repro 1	IWV	2000 - 2019	1	3 hours	42 554
CODE repro 2	ZTD	1996 - 2019	7	5 min	613 527
CODE repro 2	IWV	2003 - 2019	1	3 hours	27 022
EUREF	ZTD	1997 - 2019	8	5 min	507 002
EUREF	IWV	1999 - 2019	1	3 hours	47 481
ZenitGEO	ZTD	2011 - 2013	30	5 min	26 043 846
ZenitGEO	IWV	2012	30	3 hours	299 598
SUGAC	ZTD	2013	7	5 min	581 003
SUGAC	IWV	2013	7	30 min	104 812
Balkan	ZTD	2007 - 2014	23	5 min	21 607
Balkan	IWV	2011 - 2014	10	3 hours	6 480
GFZ	ZTD	2010 - 2019	1	5 min	217 748
GFZ	IWV	2010 - 2019	1	3 hours	16 665
Radiosonde	Profiles	1980 - 2019	1	1 day	18 989
SYNOP	surface P, T	1999 - 2019	26	3 hours	437 865
WRF	Profiles	2010 - 2019	139	30 min	6 086 961
WRF	IWV	2011 - 2019	139	30 min	640 245

Table 4.1: A summary of the GNSS, meteorological and NWP datasets present in the SUADA database as of 1.09.2019. More information on the datasets can be found in appendix B.1.2.

Datasets from multiple sources are incorporated into SUADA, including GNSS routine and post-processed data (as seen in table 4.2), as well as data from meteorological

name	scale	method	strategy	source
IGS repro 1	Global	PPP	Post-processed	1
CODE repro 2	Global	Network Solution, double-differenced	Post-processed	2
EUREF datasets	Europe	Network Solution, double-differenced	Routine	3
GFZ	Global	Network Solution, un-differenced	Post-processed	4
SUGAC	Bulgaria	PPP	Post-processed	5
Balkan	Balkan	Network Solution, double-differenced	Post-processed	6
ZenitGEO	Bulgaria	Network Solution, double-differenced	Post-processed	6

Table 4.2: Used datasets processing strategies and methods, as described in (*Guerova et al.*, 2016a). 1. `ftp://cddis.gsfc.nasa.gov/pub/gps/products/troposphere/zpd/` 2. `ftp://gssc.esa.int/gnss/products/` 3. `http://igs.bkg.bund.de/root_ftp/EUREF/products/` 4. `ftp://ftp.gfz-potsdam.de/GNSS/products/nrttrop/product_COST_EPOS8/` 5. described in section 3.4. 6. described in appendix B.1.2.

surface observations, radiosoundings and NWP models (see table 4.1). A comprehensive description of the datasets is provided in appendix B.1.2.

4.2.1 2007 heat wave observations at IGS station Sofia

Heat waves have become a common summer feature in the South-East Europe region (*Matzarakis et al.*, 2007). The July 2007 heat wave has the largest geographical extension reaching Bulgaria. The atmospheric circulation leading to the heat wave is characterized by northerly displacement of the subtropical jet stream (flow at 200 hPa) that allowed subtropical African air to reach South-East Europe as far as 50^oN. The GNSS-IWV from the IGS repro2 and RS-IWV are used to study the 2007 heat wave. The annual and seasonal mean GNSS-IWV for the period 2001-2010 is compared to the 2007 and is presented in table 4.3.

As seen in table 4.3, the annual GNSS-IWV in 2007 is 14.0 kg/m^2 and is similar to the 2001-2010 mean. The seasonal values show that in 2007 the GNSS-IWV is larger in winter (+5 %) and smaller for summer and autumn (-5 and -6 % correspondingly). For comparison the IWV from radiosonde (RS-IWV) station in Sofia is also presented in table 4.3. The RS-IWV annual, winter, summer and autumn seasonal mean in 2007 have the same tendency as GNSS-IWV.

In addition, the monthly IWV anomalies are studied. In figure 4.2 GNSS-IWV and RS-IWV anomalies are plotted. When GNSS-IWV in 2007 (solid line in figure 4.2a) is compared to 2001-2010 (dashed line in figure 4.2a), the following features stand out: i.)

	IWV-IGS repro2 SOFI		IWV-RS Sofia	
Time period	mean	change	mean	change
2001 - 2010 2007	14.3 kg/m^2 14.0 kg/m^2	 -2%	15.5 kg/m^2 15.1 kg/m^2	 -3%
2001 - 2010 DJF 2007 DJF	8.0 kg/m^2 8.4 kg/m^2	 +5%	8.8 kg/m^2 9.1 kg/m^2	 +3%
2001 - 2010 MAM 2007 MAM	12.7 kg/m^2 12.7 kg/m^2	 0%	13.6 kg/m^2 13.2 kg/m^2	 -3%
2001 - 2010 JJA 2007 JJA	21.8 kg/m^2 20.6 kg/m^2	 -5%	23.9 kg/m^2 22.5 kg/m^2	 -6%
2001 - 2010 SON 2007 SON	14.8 kg/m^2 14.0 kg/m^2	 -6%	16.0 kg/m^2 15.5 kg/m^2	 -3%

Table 4.3: Comparison of meteorological parameters for year 2007 with the 2001-2010 period for station Sofia, Bulgaria. Rows 2-3 are annual mean for 2001-2010 and 2007 accordingly; row 4-5: winter DJF (December, January and February) mean for 2001-2010 and 2007; row 6-7: spring MAM (March, April and May) mean for 2001-2010 and 2007; column 8-9: summer JJA (June, July and August) mean for 2001-2010 and 2007; row 10-11: autumn SON (September, October and November) mean for 2001-2010 and 2007. The 2007 departure from 2001-2010 mean is given in % in the "change" columns (*Guerova et al.*, 2014).

	Temperature		Precipitation	
Time period	mean	change	mean	change
2001 - 2010 2007	8.4^oC 8.8^oC	 $+0.4^oC$	$55mm/month$ $69mm/month$	 +25%
2001 - 2010 DJF 2007 DJF	0.2^oC 2.6^oC	 $+2.4^oC$	$40mm/month$ $34mm/month$	 -15%
2001 - 2010 MAM 2007 MAM	10.7^oC 11.7^oC	 $+1.0^oC$	$55mm/month$ $66mm/month$	 +20%
2001 - 2010 JJA 2007 JJA	20.4^oC 21.8^oC	 $+1.4^oC$	$73mm/month$ $86mm/month$	 +17%
2001 - 2010 SON 2007 SON	11.3^oC 9.5^oC	 -1.8^oC	$50mm/month$ $91mm/month$	 +82%

Table 4.4: Annual and seasonal mean of temperature and precipitation for station Sofia, Bulgaria for winter (DJF), spring (MAM), summer (JJA) and autumn (SON) for 2001-2010 and 2007 (*Guerova et al.*, 2014).

IWV decrease in April, ii.) IWV increase in May and iii.) a sharp IWV decrease in July. Clearly seen from figure 4.2b is that the largest negative IWV anomaly is in July about -4kg/m^2 from GNSS-IWV and -5kg/m^2 from RS-IWV. There is very good correlation of the anomaly from the two techniques despite the different sampling rate and location. The difference between the GNSS-IWV and RS-IWV anomaly is under 0.5kg/m^2 in 7 months, between 0.5 and 1kg/m^2 in 2 months and about 1kg/m^2 in 3 months.

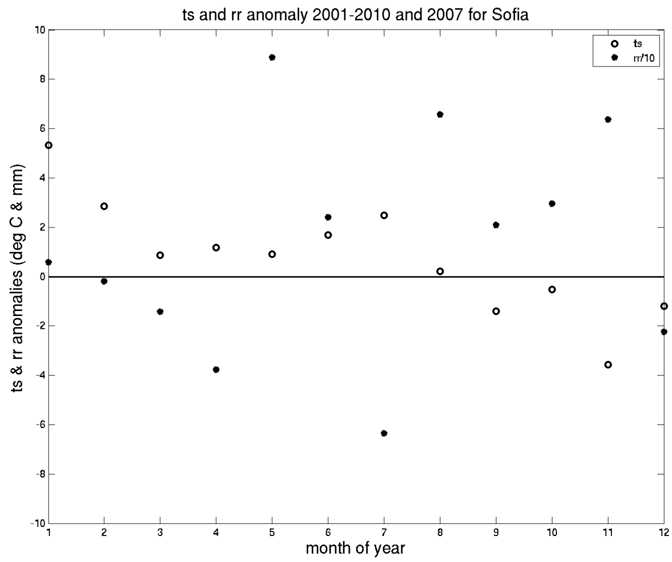

Figure 4.1: Monthly anomaly of temperature (open circles) and precipitation (filled circles) for Sofia, Bulgaria (*Guerova et al.*, 2014).

The 2007 winter is 2.4°C warmer than the 2001-2010 (row 5 in table 4.4). The 2007 spring and summer are with 1.0 and 1.4°C warmer. In particular, July 2007 is +3.7°C warmer (figure 4.1) and with less IWV than the 2001-2010 with -16 % and -19 % correspondingly for the GNSS-IWV and RS-IWV. It is to be noted that the annual precipitation amount in 2007 is 25 % higher than the 2001-2010. However the winter is 15% drier (row 5 in table 4.4) and from spring only the month of May has positive precipitation anomaly over $80kg/m^2$ as seen in figure 4.1. In the summer 2007 the month of July is very dry (about $60kg/m^2$ less that the 2001-2010 mean).

4.2.2 Long-term monitoring at IGS station Sofia.

The data used in this section covers the interval between 2000-2019 and has a gap in 2000 (seen on figure 4.3) and has not been homogenized.

To derive tropospheric product from GNSS data in Sofia synoptic data from meteorological station in Sofia is used. For this the temperature and pressure are interpolated to the altitude of the GNSS site using the polytropic barometric formula (equation 3.22). This dataset of temperature and pressure is used for the calculation of all GNSS IWV data.

The earliest data available for the station are from 2000, as part of the first IGS reprocessing, followed by the BKG and the Bayerische Erdmessung Komission (BEK) processing centers of EUREF. Additionally the station is included in the second IGS reprocessing campaign of the Center for Orbit Determination (CODE) of the University

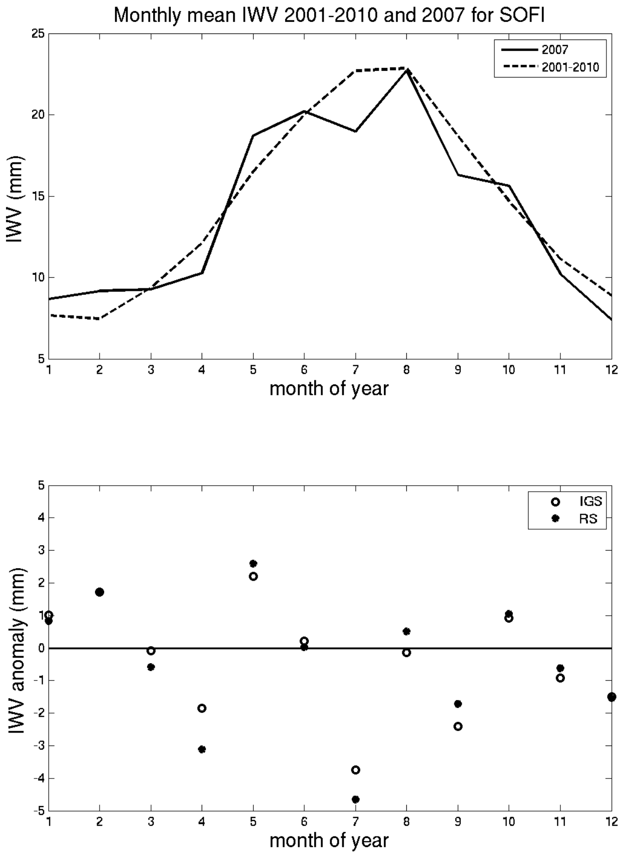

Figure 4.2: Top figure: monthly mean IWV for SOFI, Bulgaria (thick line 2007, dashed line 2001-2010). Bottom figure: monthly anomaly (difference 2007 mean and 2001-2010 mean) from GNSS (open circles) and Radiosonde (filled circles) (*Guerova et al.*, 2014).

of Bern. All of these processing centers are using the Bernese software (see more in section 3.3.3). The reprocessing campaigns are performed with a single stable version of the software, while the EUREF routine processings used the most up-to-date versions - from 4.2 to 5.2 through time. The time scale of using the different versions of the software is presented in figure 3.7.

The IGS center in GFZ has also processed the SOFI dataset with the in-house developed EPOS software. In this work a reprocessed 10 year period from 2010 until 2019 is analysed. The GFZ dataset has significant gaps, spread throughout the dataset (seen in figure 4.4).

The GNSS datasets can be divided into two significant groups. The first group comprises of the BKG and BEK datasets. Both of these datasets are routine processings, meaning that the tropospheric products are calculated using the latest available versions of the Bernese software. Thus with the data from the EUREF processing centers is not homogeneous, because of the evolution and changes to the processing software. The sec-

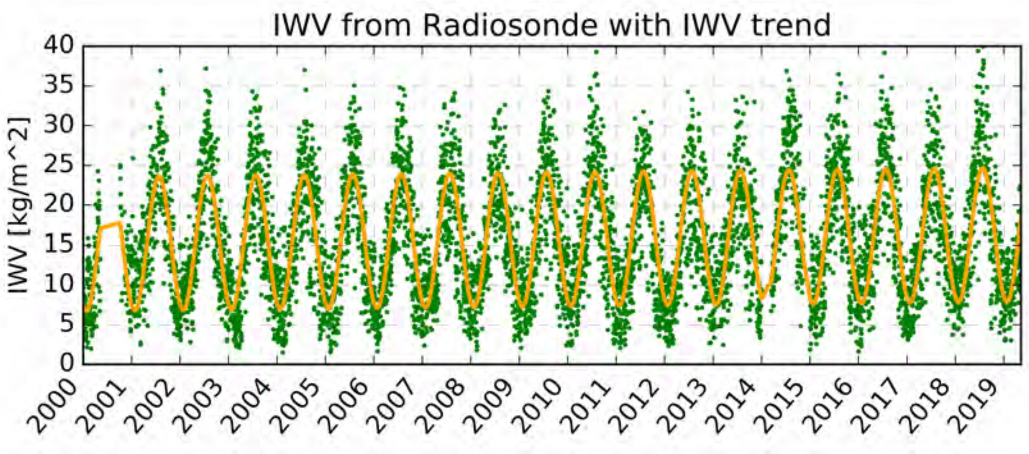

Figure 4.3: Observed IWV and estimated trend for station Sofia from the Aerological observatory of the National Institute of Meteorology and Hydrology (NIMH), using radiosondes.

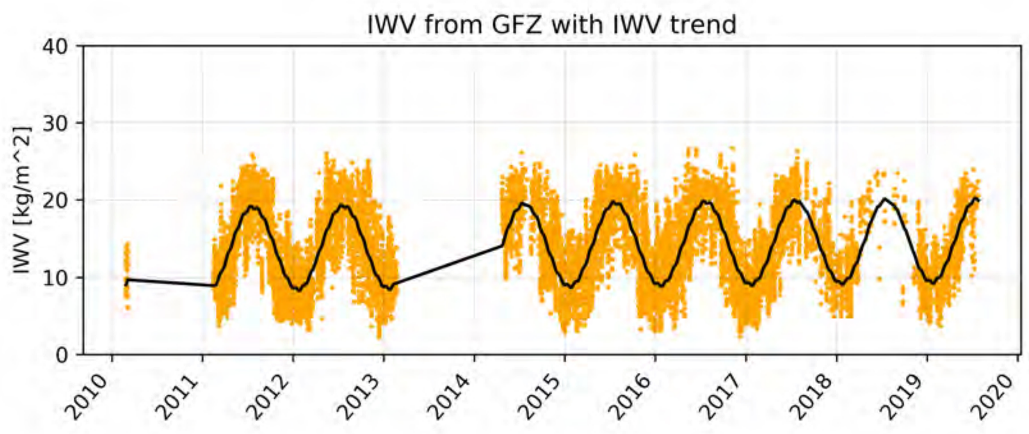

Figure 4.4: Observed IWV and estimated trend for station Sofia from the GFZ processing center.

ond group are the GFZ, IGS repro 1 and the CODE repro 2 datasets. These datasets are reprocessed, meaning that each center uses a certain stable version of the processing software to calculate the tropospheric products for the entire available period. In the case of GFZ, the reprocessing is performed using EPOS8. Bernese software is used for both the IGS repro 1 and the CODE repro 2 datasets, but while the IGS repro 1 is performed in a PPP mode, the CODE repro 2 is performed in a double differencing mode. A short comparison of the processing approaches is presented in table 4.2. This processing approach guaranties the homogeneity of the datasets and is more appropriate for climate research and trend analysis. The differences between both approaches in terms of IWV results are significant, as can be seen from table 4.5.

The correlations in table 4.5 show, that the EUREF datasets have lower correlation to the radiosonde observation, than the reprocessed data. Moreover, the CODE repro

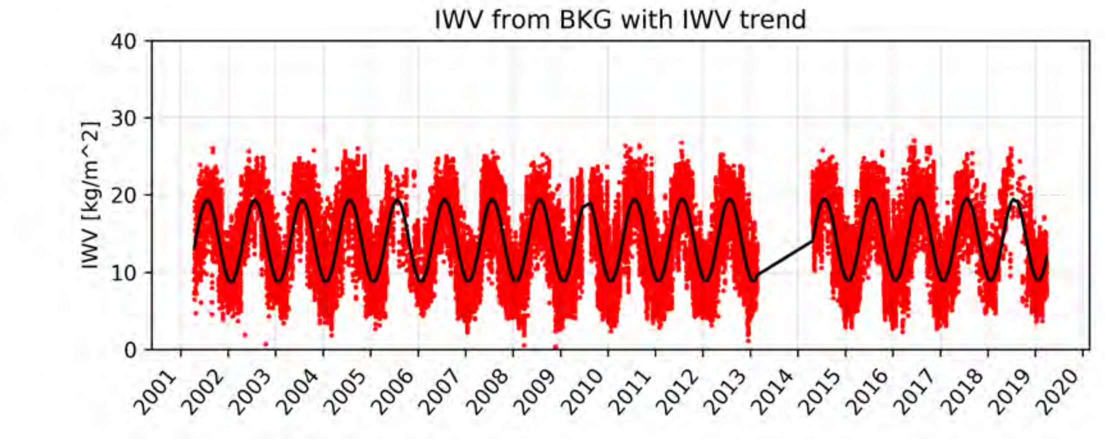

Figure 4.5: Observed IWV and estimated trend for station Sofia from the BKG processing center.

Sensor/Source	1.	2.	3.	4.	5.	6.
1. Radiosonde	-	0.89	0.88	0.93	0.98	0.91
2. EUREF-BKG	0.89	-	0.99	0.96	0.92	0.93
3. EUREF-BEK	0.88	0.99	-	0.96	0.91	0.93
4. IGS repro 1	0.93	0.96	0.96	-	0.94	0.99
5. CODE repro 2	0.98	0.92	0.91	0.94	-	0.99
6. GFZ	0.91	0.93	0.93	0.99	0.99	-
Average	0.92	0.94	0.93	0.96	0.95	0.95

Table 4.5: Correlations between IWV sources for IGS station Sofia. The correlations cover the full period when each pair of datasets is available.

2 shows highest correlation to the radiosondes, than any other GNSS processing. This can be explained with the fact, that compared to the IGS repro 1, the CODE repro 2 is started later with a more advanced version of the Bernese software. Moreover since BEK and BKG are using the same software and the same processing strategy, the correlation between the two datasets is very high, as well as the correlation between the GFZ dataset and the other two reprocessings.

A spectral analysis of the most dominant frequencies is carried out for all datasets. Using the Lomb-Scargle LSA (described in section 3.5.1), the power spectra of all datasets are determined. As expected, the most dominant periodicity in all datasets is the seasonal cycle (365.25 days, seen in figure 4.6). The half-year cycle does not show significant dominance in any of the analysed datasets, but monthly and bi-monthly cycles appear in most of the GNSS processings. The periodicity in the radiosonde data has only one dominant frequency - the seasonal cycle.

In order to determine the trends of all datasets, a modified *Ning* (2012) fitting function

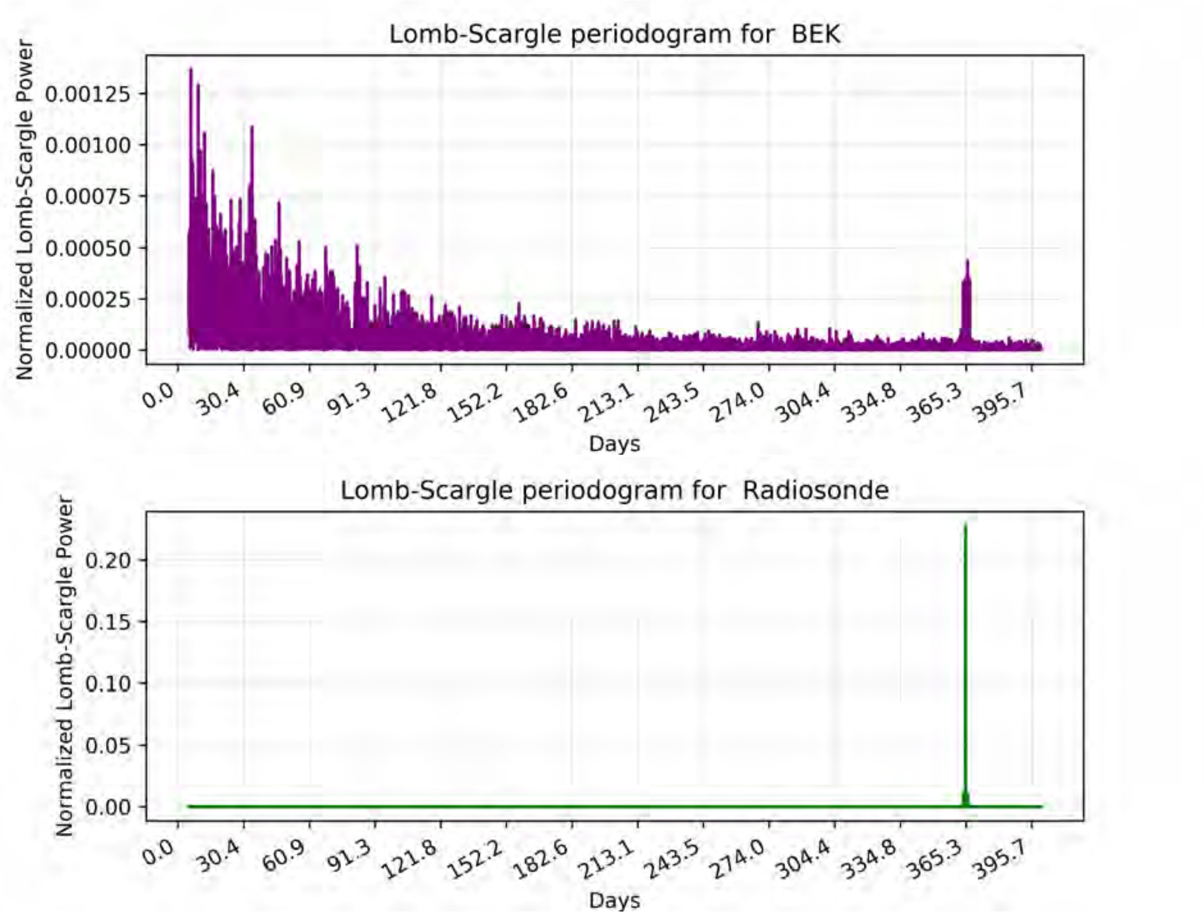

Figure 4.6: Power spectra of frequencies of the BEK GNSS tropospheric products and Radiosounding. The multiple frequencies in the BEK dataset can be explained with the shorter dataset, as well as with the sub-daily observation frequency. Both datasets show a strong yearly cycle.

is used:

$$y = at + b\cos(2\pi t) + c\sin(2\pi t) + d\cos(24\pi t) + e\sin(24\pi t) + f \tag{4.1}$$

While *Ning* (2012) uses seasonal and semi-seasonal periodical signals, the power spectra of the GNSS datasets suggest a higher dominance of seasonal and monthly periodicities. The calculated linear trends (the a in formula 4.1) show very different behaviours in the datasets. For the 2000-2009 decade the trends vary between -1.44 - 0.85$\frac{kg}{m^2}/decade$ (displayed in table 4.6). The tropospheric products from the routine processings from the EUREF centers show similar behaviour to each other, as do the IGS reprocessings. For the second decade, observed by GNSS (2010-2019), the situation is similar with the GFZ processing center reprocessing showing the highest trend over the period of 1.33$\frac{kg}{m^2}/decade$.

This large difference within the estimated trends from each AC can be influenced by several factors:

- the datasets are not homogenized,

Years/Source	'00-09	'10-19	full time series
1. Radiosonde	-0.64	2.04	0.61
2. EUREF-BKG	-1.44	0.93	0.14
3. EUREF-BEK	-1.12	0.75	0.03
4. IGS repro 1	0.81	0.86	0.83
5. CODE repro 2	0.85	0.45	0.75
6. GFZ	-	1.33	1.33

Table 4.6: IWV $\frac{kg}{m^2}/decade$ trends for station Sofia from all discussed sources.

Years/Source	'00-09	'10-19	full time series
1. Radiosonde	15.18	16.01	15.58
2. EUREF-BKG	13.31	13.21	13.26
3. EUREF-BEK	13.33	13.16	13.25
4. IGS repro 1	13.26	13.03	13.16
5. CODE repro 2	12.86	12.92	12.89
6. GFZ	-	13.35	13.35

Table 4.7: IWV mean values for station Sofia from all discussed sources. All values are in $\frac{kg}{m^2}$.

- the locations of the radiosonde launches and the GNSS site are approx. 15km apart.

There are two aspects of the lack of homogenization problem, which can be discussed. Firstly from the GNSS side there have been several updates to the station hardware over time. But these updates would influence all GNSS datasets, not just one of them. There is another argument, that the analysis is done over two routine and two reprocessing datasets, and they have to show a similar behaviour pair by pair. When comparing the derived trends, as well as the mean values (in table 4.7) and the standard deviations (in table 4.8), conclusions on the similarity between the BEK and BKG pair and the IGS repro 1 and CODE repro 2 pair can be drawn.

The radiosonde dataset is influenced by the changes of used equipment, but more im-

Years/Source	'00-09	'10-19	full time series
1. Radiosonde	4.63	4.87	4.77
2. EUREF-BKG	3.51	3.59	3.57
3. EUREF-BEK	3.62	3.57	3.61
4. IGS repro 1	3.58	3.58	3.58
5. CODE repro 2	3.51	3.53	3.53
6. GFZ	-	3.51	3.51

Table 4.8: IWV standard deviation for station Sofia from the de-trended water vapour observations from all sources. All values are in $\frac{kg}{m^2}$.

portantly by the different dynamics in the Sofia valley. While the GNSS site is situated on a mountain plateau next to the city, the launch site for the radiosonde is some 500m below the GNSS station and 15km to the North. The altitude difference presents itself through the large difference in the water vapour mean values (see table 4.7). The variability in the water vapour in the Sofia valley is far larger, than in the Plana mountain plateau, thus the standard deviation, calculated from the de-trended datasets is far larger for the radiosondes. Additionally the radiosonde dataset comprises of midday observations only, while the GNSS datasets have between 8-12 observations daily.

The analysis of these datasets shows the influence the processing approach has on the analysed tropospheric products. The reprocessed datasets, which are predominantly envisaged for climate studies show very similar results to each other. The routine processings, although replicating the reprocessed data with high correlation coefficients, show very different trend estimates. The final analysis of these datasets can be performed only after homogenization of the results from each individual source. Thus only reprocessed homogeneous datasets can be used for climate studies and can be applied into global monitoring and reference networks, such as GRUAN.

4.3 SUGAC first processing campaign - 2013.

Results from the first PPP GNSS processing for seven stations in Bulgaria (seen in figure 4.7) is presented, together with results from the WRF NWP model. The aim of this work is to evaluate the IWV from GNSS and the WRF NWP model for Bulgaria in 2013. The working steps are:

- processing GNSS RINEX[1] data for 7 stations in Bulgaria in PPP mode using the NAPEOS GNSS processing software,
- deriving GNSS IWV for Bulgaria using surface pressure and temperature from synoptic observations and the WRF model,
- evaluating the WRF model IWV:
  - seasonal variations
  - diurnal cycle
  - behaviour during severe weather events
- evaluating the Precipitation Efficiency (PE) (*Bordi et al.*, 2015) of the WRF model for Bulgaria in 2013,
- comparing between PPP and DGNSS processings.

The PPP processing and derivation of the GNSS IWV data is described in section 3.4.

[1]Receiver Independent Exchange data format - RINEX, read more in appendix B.3

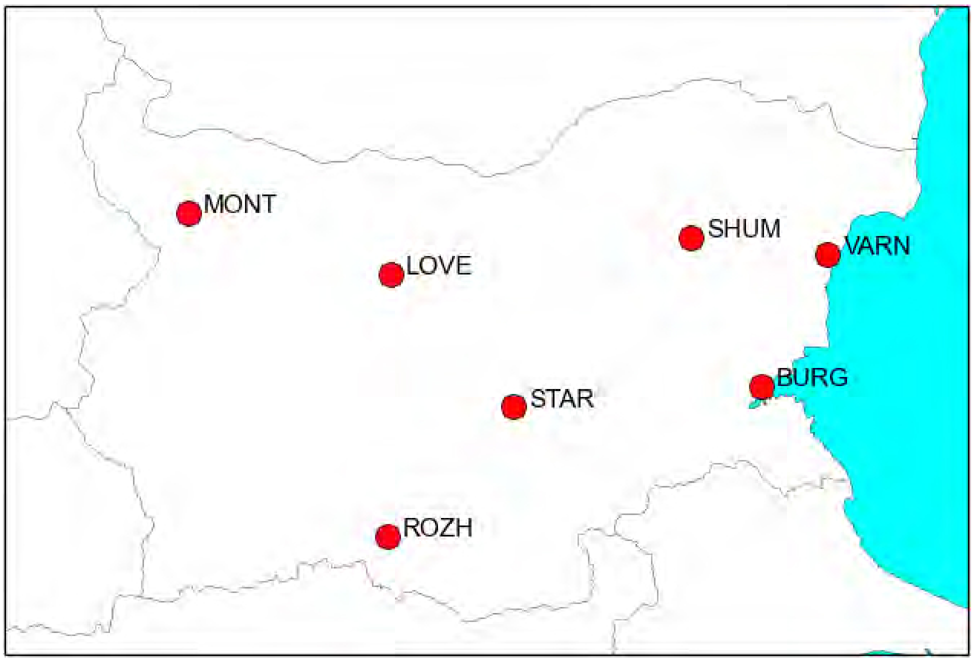

Figure 4.7: Map of the ground-based stations of the Bulipos GNSS network. The red markers show the station locations. The marked stations are: Montana (MONT), Lovech (LOVE), Shumen (SHUM), Varna (VARN), Burgas (BURG), Stara Zagora (STAR) and Rozhen (ROZH).

Station	GNSS altitude [m]	SYNOP altitude [m]	WRF altitude [m]	GNSS Longitude	GNSS Latitude
Varna	62	43	12	27^o 55'	43^o 12'
Burgas	71	28	5	27^o 28'	42^o 29'
Lovech	191	221	298	24^o 43'	43^o 09'
Montana	167	-	136	23^o 15'	43^o 26'
Rozhen	1779	-	1560	24^o 45'	41^o 40'
Shumen	268	-	217	26^o 52'	43^o 16'
Stara Zagora	227	-	186	25^o 36'	42^o 24'

Table 4.9: GNSS, meteorological stations and WRF nodes coordinates of the stations, used in the SUGAC first processing campaign.

4.3.1 Evaluation of the WRF model

The annual mean, standard deviation and correlation between the surface pressure and temperature from WRF and SYNOP are presented in Table 4.10. For this the WRF pressure and temperature are extracted with the temporal resolution of the SYNOP i.e. every 3 hours. The correlation coefficient between the two data sets for atmospheric pressure for station Lovech (LOVE) is 0.99 with the mean difference $0.5hPa$. The correlation coefficient for the temperature is 0.96. The largest differences in the two data sets are observed for December 2013. For station Varna (VARN) the correlation coefficient for the pressure is 1.00 and for the temperature 0.96 with a mean difference between the SYNOP and NWP-WRF of $0.2hPa$ for the pressure and 0.2° C for the temperature. For station Burgas (BURG) the correlation coefficient for the pressure is 1.00 and for the temperature 0.96. The mean difference for the pressure is $0.1hPa$ and 0.2° C for the temperature. The NWP-WRF surface pressure shows an agreement of $0.5hPa$ or better with the SYNOP dataset. Thus using the WRF surface pressure allows to take advantage of deriving IWV with temporal resolution of 30 minutes, instead of 3 hours. A comparison between IWV and IWV* for station Burgas is seen in figure 4.8.

Station	Pressure WRF mean	Pressure SYNOP mean	Pressure WRF σ	Pressure SYNOP σ	Correlation coefficient
Lovech	1015.4	1015.9	7.4	7.4	0.989
Burgas	1015.6	1015.8	7.3	7.4	0.995
Varna	1015.6	1015.8	7.2	7.4	0.996
Station	Temperature WRF mean	Temperature SYNOP mean	Temperature WRF σ	Temperature SYNOP σ	Correlation coefficient
Lovech	15.1	14.0	8.7	9.6	0.957
Burgas	13.9	14.2	8.3	8.3	0.960
Varna	13.7	13.9	8.1	8.3	0.975
Station	IWV mean	IWV* mean	GNSS IWV σ	IWV* std	Correlation coefficient
Lovech	18.2	17.0	7.6	7.3	0.999
Burgas	19.6	19.4	7.5	7.5	0.996
Varna	17.4	17.3	6.9	7.0	0.999

Table 4.10: Comparison between parameters derived from SYNOP and WRF. Mean values (column 2 and 3), standard deviation (column 4 and 5) and correlation between the datasets (column 6) for Surface pressure (lines 2-4), Temperature (lines 6-8) and derived IWV with WRF pressure and temperature and IWV* derived with SYNOP pressure and temperature.

A comparison between the GNSS and WRF IWV for Burgas, Lovech, Montana, Shumen and Stara Zagora gives a correlation coefficient of between 0.95 and 0.96. The RMSE of IWV is between 0.5 and $1.8kg/m^2$. The smallest mean difference is obtained for Shumen and Burgas and is a consequence of the small altitude difference between the GNSS stations and the WRF model height (see table 4.9). The altitude difference for station Lovech is 107 m and there the largest mean difference of $1.8kg/m^2$ is obtained. For Varna and Rozhen the correlation coefficient is 0.9 and 0.76, and the mean IWV difference is negative with -0.9 and -$3.2kg/m^2$ respectively. When the year is split into seasons, the smallest RMSE's are observed during the first quarter of the year (Q1 in figure 4.9) for

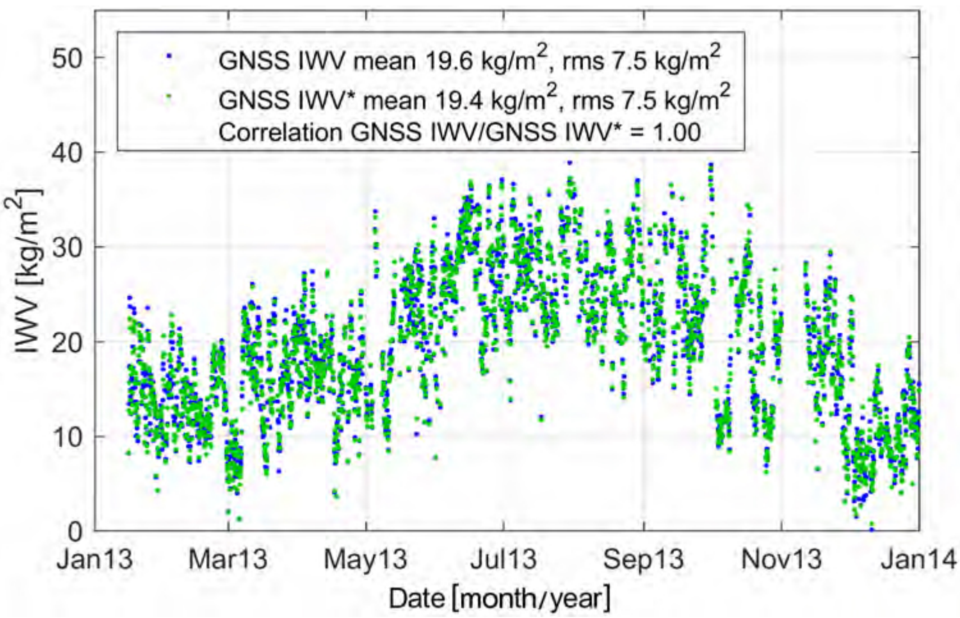

Figure 4.8: GNSS IWV and IWV* for station Burgas in 2013. The GNSS IWV is derived using temperature and pressure from the WRF model and the GNSS IWV* is derived using SYNOP ground observations.

all stations, while the largest - during Q2 and Q3. The correlations on the other hand are highest during Q4, between October and December. These high correlations can be explained with the relatively monotonous decrease during Q4 of IWV.

4.3.2 Seasonal variations

The comparison between the GNSS and WRF monthly mean IWV for 2013 is presented in figure 4.11. At all stations with exception of Rozhen the monthly mean IWV minimum is $10 kg/m^2$ in December 2013 and the maximum is $25 kg/m^2$ in June 2013. The GNSS and WRF IWV for station Burgas is shown in figure 4.11a. It can be seen that there is good agreement between the monthly mean IWV from GNSS and WRF. The correlation coefficient varies between 0.84 and 0.96. The maximum and minimum correlation is seen in winter and autumn, and spring and summer, respectively. Stations Shumen (figure 4.11b) and Stara Zagora (figure 4.11c) show similarities in the IWV. The values indicate again a maximum in June and a minimum in December. For Shumen the lowest correlation is observed in April and it stays low during the spring months. For Stara Zagora the correlation coefficient stays low in with minimum from April till August. Montana (figure 4.11d) is in Northwest Bulgaria where the influence of the Balkan mountains is significant and the interaction with synoptic flows plays a major role for the IWV distribution. The lowest GNSS and WRF IWV values are seen for December $12 kg/m^2$ and the highest for June with $27 kg/m^2$. For Varna (figure 4.11e) of interest is the difference between GNSS and WRF, which is seen during the months April and May. From January to April the

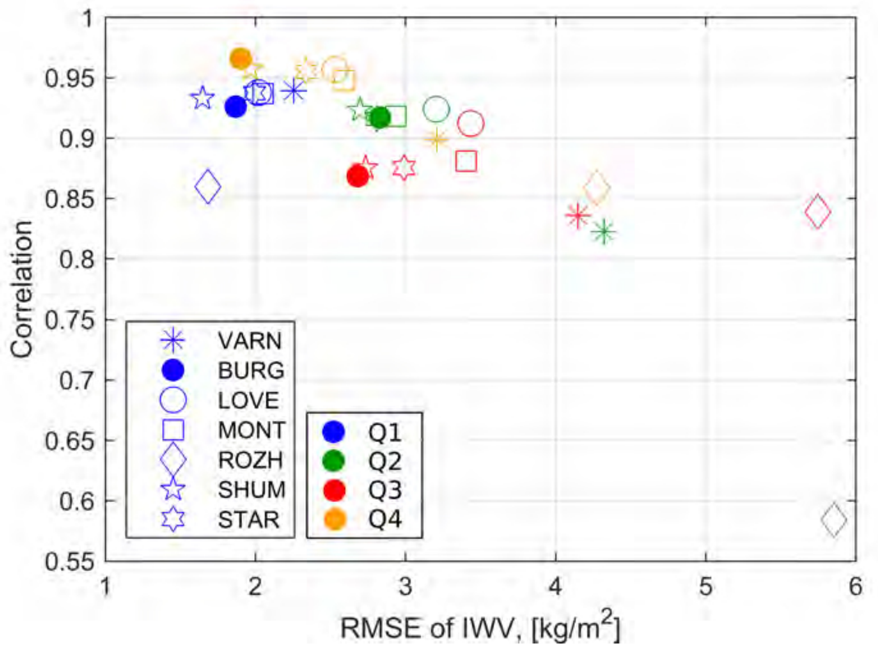

Figure 4.9: Correlation and RMSE between WRF and GNSS IWV for all Bulgarian stations for each season. Q1, Q2, Q3 and Q4 stand for the first, second, third and fourth quarters of the year (*Simeonov and Guerova*, 2020).

IWV in the WRF is lower than the GNSS and from May to December it is the opposite. Similar GNSS IWV jump between April and May is seen at Rozhen (figure 4.11f).

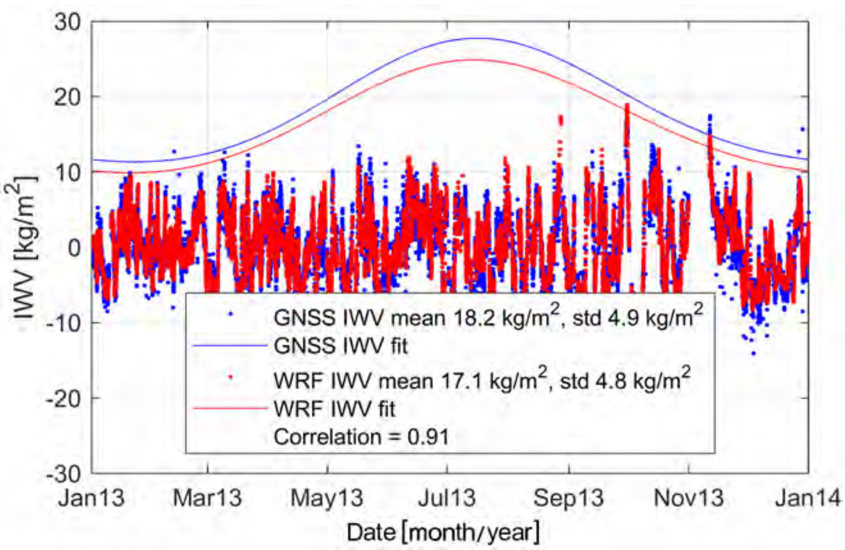

Figure 4.10: Comparison of de-trended WRF and GNSS IWV for station Lovech. The lines represent the seasonal trend, while the points show the scatter of the de-trended values. The systematic bias of $0.2kg/m^2$ can clearly be seen in the trends.

The datasets of Lovech and Shumen have the shortest gaps among the studied stations.

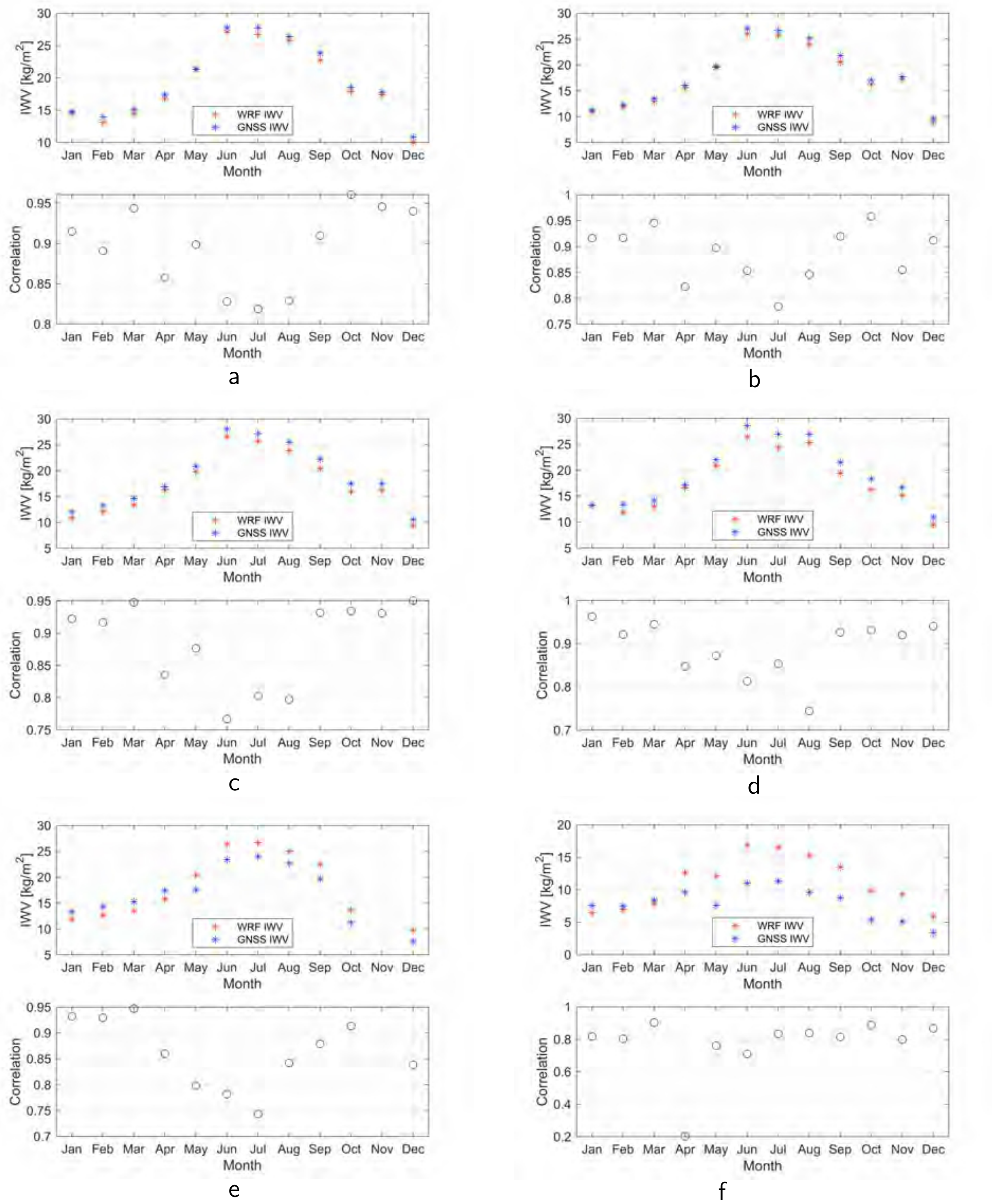

Figure 4.11: Monthly average water vapour from WRF and GNSS (top figures) and monthly correlations (bottom figures) for stations a) Burgas, b) Shumen, c) Stara Zagora, d) Montana, e) Varna, f) Rozhen.

These two stations are de-trended using the following annual fitting function, as proposed by *Ning* (2012) :

$$y = at + b\cos(2\pi t) + c\sin(2\pi t) + d\cos(4\pi t) + e\sin(4\pi t) + f \tag{4.2}$$

where b and c are the annual coefficients and d and e - the semi-annual, while a is a linear trend component. These coefficients are determined using least-square analysis. The correlation between the datasets is high - 0.91 for Lovech (as seen in figure 4.10 and 0.90 for Shumen after subtracting the seasonal variation. This analysis could not be performed for the other 5 stations, because of the gaps in the datasets, which influence the trend analysis of both the annual variation and the monthly change in IWV.

4.3.3 Diurnal cycle

The diurnal cycle of IWV for Burgas is presented in figure 4.12a. The WRF IWV is between 0.5 and $1.0kg/m^2$ lower than for GNSS. The mean difference between the two data sets is around $0.5kg/m^2$ up to 10 UTC. Between 10 and 20 UTC the difference is larger at around $1kg/m^2$. For Lovech (figure 4.12b) the difference between GNSS and WRF IWV is between 1.0 and $1.5kg/m^2$. This however is expected and is due to the discussed altitude difference (107 m) between the WRF grid point and the GNSS station. It is to be noted that the GNSS, WRF altitude difference is under 40 m for the other 4 stations. For Montana, Shumen and Stara Zagora WRF has a dry bias relative to the GNSS. For Montana (figure 4.12c) the estimated difference is between 1.2 and $1.7kg/m^2$. Larger differences between datasets are seen in the afternoon after 13 UTC (top plots in figure 4.12c). The mean difference in the diurnal IWV variation at Shumen (figure 4.12d) and Stara Zagora (figure 4.12e) between GNSS IWV and WRF IWV is in the range of between 0.5 and $1.0kg/m^2$. At all stations between 00 and 01 UTC the GNSS has a tendency to underestimate IWV. In the beginning of each processing the GNSS solution is unstable due to lack of initial conditions. The PPP processing uses daily IGS orbits files with jumps in the orbits on the day boundaries. These jumps influence the IWV values.

The WRF model has an underestimation of diurnal IWV cycle at all stations in the range of 0.5-$1.5kg/m^2$, which agrees with results from studies with the COSMO model for Germany (*Guerova and Tomassini*, 2003). WRF-MM5 *Behrend et al.* (2002) finds an IWV bias up to 6 kg/m^2 between GPS and non-hydrostatic MM5 numerical weather prediction model. *Schwitalla et al.* (2008) compares IWV from MM5 and GPS in a mountainous region and finds a systematic model overestimation by about 15–20%. This is believed to be due to a too moist boundary layer parametrization scheme. It is not possible to link our study with the one done with COSMO model as each NWP model has its own characteristics (*Guerova et al.*, 2016a). NWP models are set up differently, and have different performance, depending on selected region, resolution, season and parametrisation schemes. Our experience with simulation of intense summer precipitation in Bulgaria during 2012 has shown that the WRF model has high sensitivity to the convective parametrization scheme used.

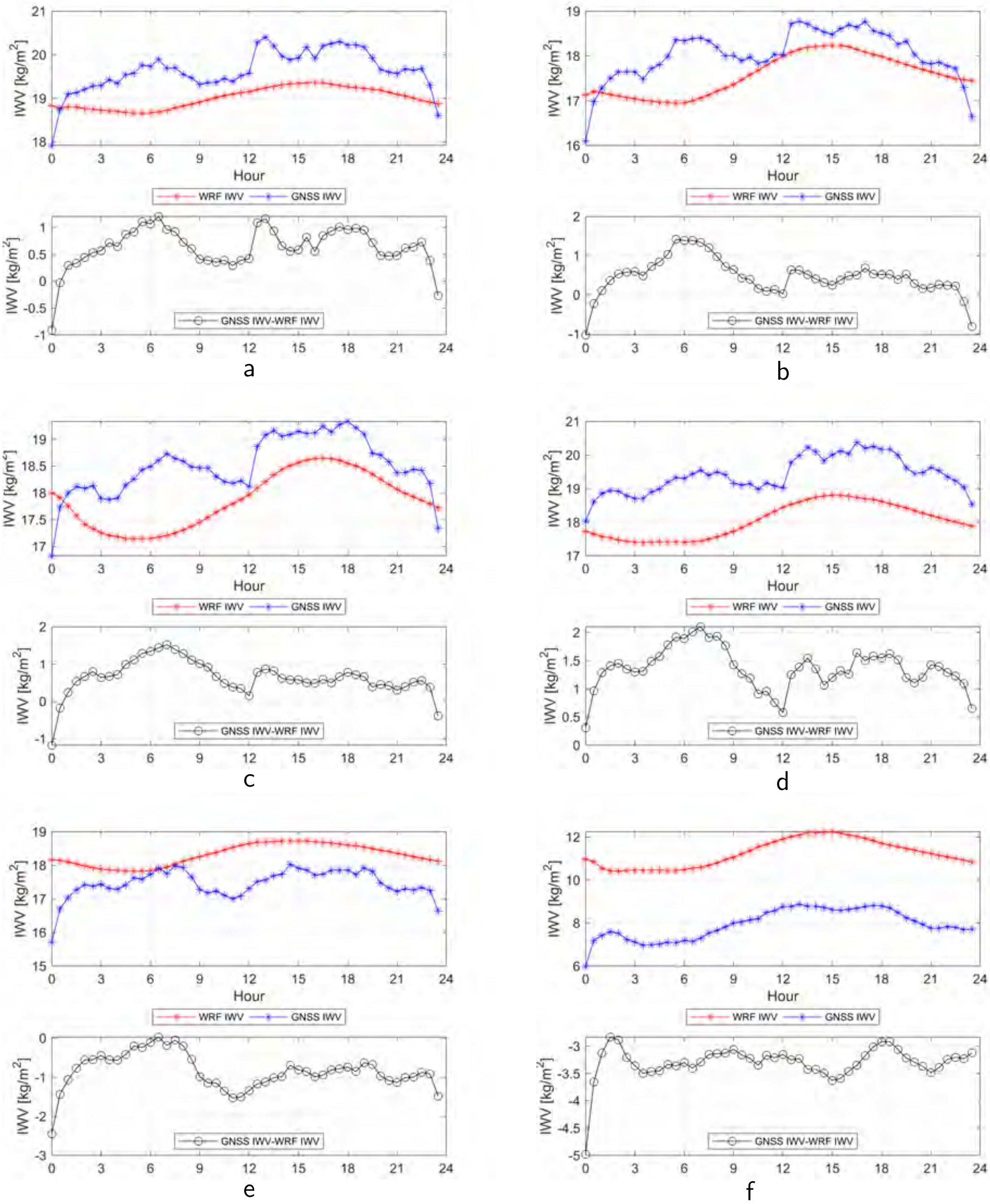

Figure 4.12: Daily cycle with half-hourly resolution of IWV from GNSS and WRF for stations a) Burgas, b) Shumen, c) Stara Zagora, d) Montana, e) Varna, f) Rozhen.

4.3.4 Hailstorm events

During 2013 several hailstorm events are detected within 30km from stations Montana and Stara Zagora. In most of these cases the WRF model fails to predict the sudden increase in water vapour preceding the events. In table 4.11 the dates and duration of the precipitation events are shown, as well as the correlation for these particular days. Despite the good agreement over summer months, the model is not predicting well the daily IWV cycle during these extreme events. This suggests that assimilation of GNSS IWV likely has a positive impact at those conditions.

Date	Time (UTC)	GNSS station	IWV/IWV* correlation
17 May	12:27 - 12:47	Montana	0.46
24 May	10:22 - 11:57	Stara Zagora	0.69
31 May	12:04 - 12:16	Stara Zagora	0.76
4 June	11:25 - 11:44	Stara Zagora	0.48
10 June	12:24 - 12:24	Montana	0.54
11 June	20:33 - 20:57	Stara Zagora	0.55
13 June	13:04 - 13:09	Montana	0.35
6 July	15:12 - 15:26	Stara Zagora	-0.05

Table 4.11: IWV correlations between WRF and GNSS during 8 days with hailstorm precipitation events for the summer of 2013.

The hailstorm on the 17th of May in the vicinity of Montana is caused by a passing cold weather front of a Mediterranean cyclone. The storm approached from West and reached the polygon for hail suppression in the village of Mala Kutlovitza at 15:27 local time (12:27 UTC). The clouds are seeded with Silver Iodite (AgI).

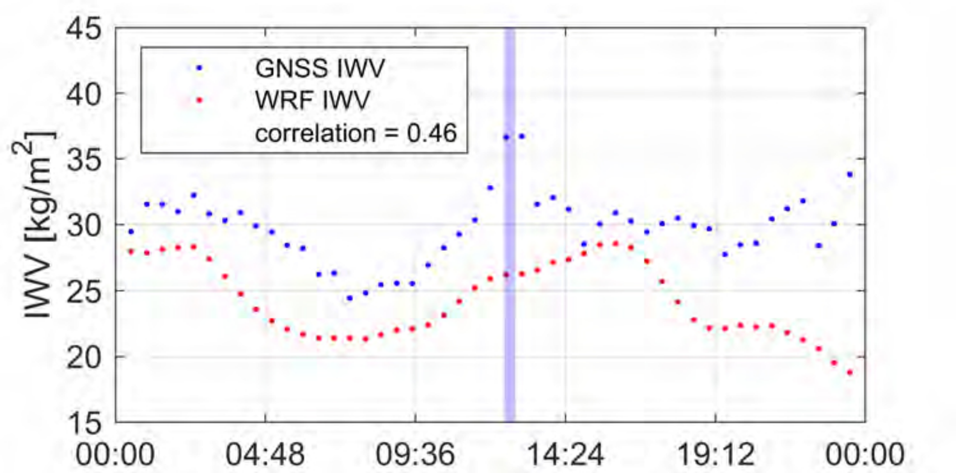

Figure 4.13: IWV during May 17th, 2013 hail storm near Montana. During the duration of the hailstorm (marked with the blue line), IWV from GNSS approached its maximum values for the day, while WRF shows no response to the event.

The development and approach of the hail cloud is clearly visible in the IWV record from GNSS station Montana (as seen in figure 4.13). The IWV increased by more than 30% from the morning hours before the storm, reaching its maximum value of $37kg/m^2$ during the hailstorm event. After the event the GNSS IWV drops back. The WRF IWV shows no increases and misses completely the approach of the convective system. Since the size of the mesoscale convective system is around 15km and the resolution of the model is only 9km in this instance, the storm can be viewed as a sub-grid event from the model perspective. It is important to mention, that in these occasions, when severe storm is approaching a monitoring station, only GNSS Meteorology and Weather Radars can produce accurate measurements. In these conditions microwave radiometers would not be able to show the correct amount of water vapour and radiosounding could only provide a single profile, while GNSS and radar are scanning continuously.

In the other cases of hailstorms around the GNSS sites the maximum of IWV also occurs at the time of the pass of the storm, or within 30 minutes from it. This behaviour can be explained by the fact, that convective clouds, producing hail have very tall structure, along which the relative humidity is 100%, meaning not only a lot of liquid water and ice crystals, but also high amounts of water vapour.

4.3.5 Precipitation efficiency

The Precipitation Efficiency (PE) is a value, calculated for each station, which is descriptive for air masses in two time scales: Cloud Microphysics Precipitation Efficiency (CMPE) (*Braham Jr*, 1952) and Large-Scale Precipitation Efficiency (LSPE) (*Tuller*, 1971). In this study LSPE is assessed. It is representative for the regional climate and climate variations. PE is expressed as percentage of the IWV that is converted and measured as precipitation. *Bordi et al.* (2015) proposed to use GNSS IWV to compute PE. In this work the daily PE is computed as following:

$$PE = \frac{PP}{IWV} 100\% \tag{4.3}$$

where PP and IWV are daily averaged precipitation and IWV at the station. Precipitation efficiency gives a long-term indication of stability of the atmosphere. In this study the analysed stations for PE are in low altitudes; PE computed from GNSS IWV and observed PP is entitled GNSS PE and from WRF IWV and PP is entitled WRF PE. In all stations, apart from Varna and Rozhen (as seen on figure 4.14), the PE is overestimated by WRF, as compared to GNSS. At Burgas (figure 4.14a) the PE has minimum in August less than 1 % and maximum in May 14 %. For Lovech (figure 4.14b) the maximum PE is in May but is slightly smaller than in Burgas (12 %) and the minimum is in September of about 1 %. The PE at those two stations also shows differences which are expected as the two stations are located in different climatic regions in Bulgaria. While Burgas is in south-east Bulgaria close to the Black Sea, Lovech is in north-west Bulgaria. The atmospheric circulation in Bulgaria is dependent on the Balkan mountains in middle of the country i.e. south of the mountain range the Mediterranean cyclones are the main source of precipitation, while the north of the mountain range their influence is largely

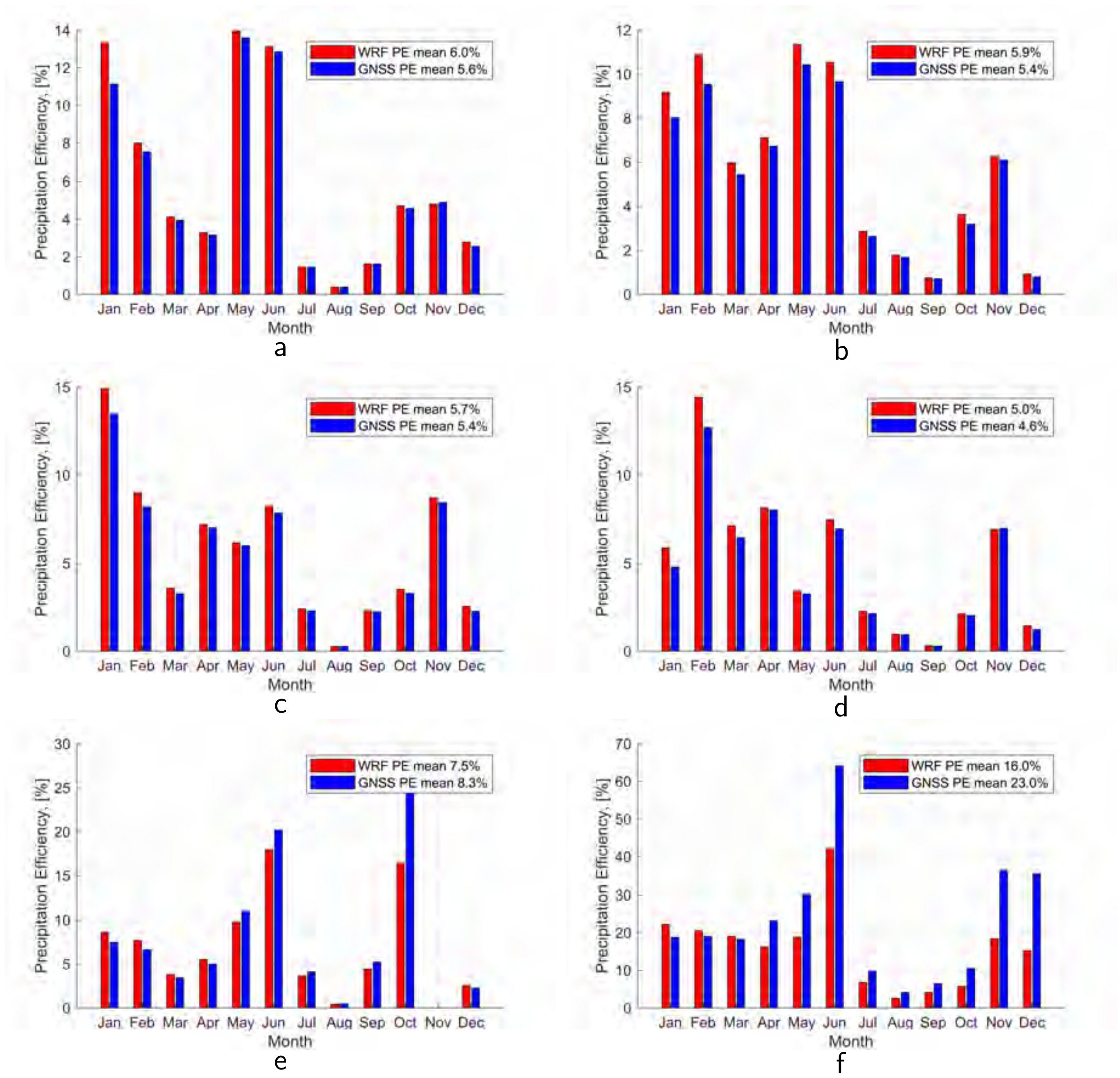

Figure 4.14: Precipitation efficiency from WRF and GNSS for stations a) Burgas, b) Lovech, c) Stara Zagora, d) Montana, e) Varna, f) Rozhen.

reduced. The annual PE in both stations is in the range of 5.5-5.8 % from GNSS and 5.9-6.0 % from WRF, which is in agreement with the range of 5-10 % for the region reported by *Tuller* (1971).

4.3.6 Comparison between PPP and DGNSS processings

Further work is carried out to investigate the possible reasons for the reported drop in GNSS-IWV values at station Varna and Rozhen. The manual screening of the raw GNSS data showed that at station Varna an incorrect antenna model was reported in the raw data. After the antenna model correction the processing resulted to an IWV increase by $2kg/m^2$ in December 2013. For station Rozhen the manual investigation does not show any errors.

Station	PPP IWV mean	DP IWV mean	DP - PPP IWV mean	DP - PPP IWV std	Correlation
Burgas	10.8	10.9	0.0	1.2	0.96
Shumen	9.9	9.8	-0.1	1.1	0.95
Stara Zagora	10.4	10.6	0.2	1.1	0.97
Montana	10.9	11.0	0.0	1.4	0.95
Varna	6.5	8.7	2.2	1.2	0.93
Rozhen	2.4	4.3	1.9	1.9	0.86

Table 4.12: IWV comparison between PPP and network solution processings for the period of 15-31 December 2013. All IWV values in kg/m^2.

The data from the network is also processed with the Bernese 5.0 software in double differenced mode. The observed breakpoints from the PPP processing in stations Rozhen and Varna are not detected. The results show (figure 4.15) clearly, that the biases for all stations, accept Rozhen and Varna are insignificant. Moreover the double difference processing shows significantly less outliers, compared to the PPP.

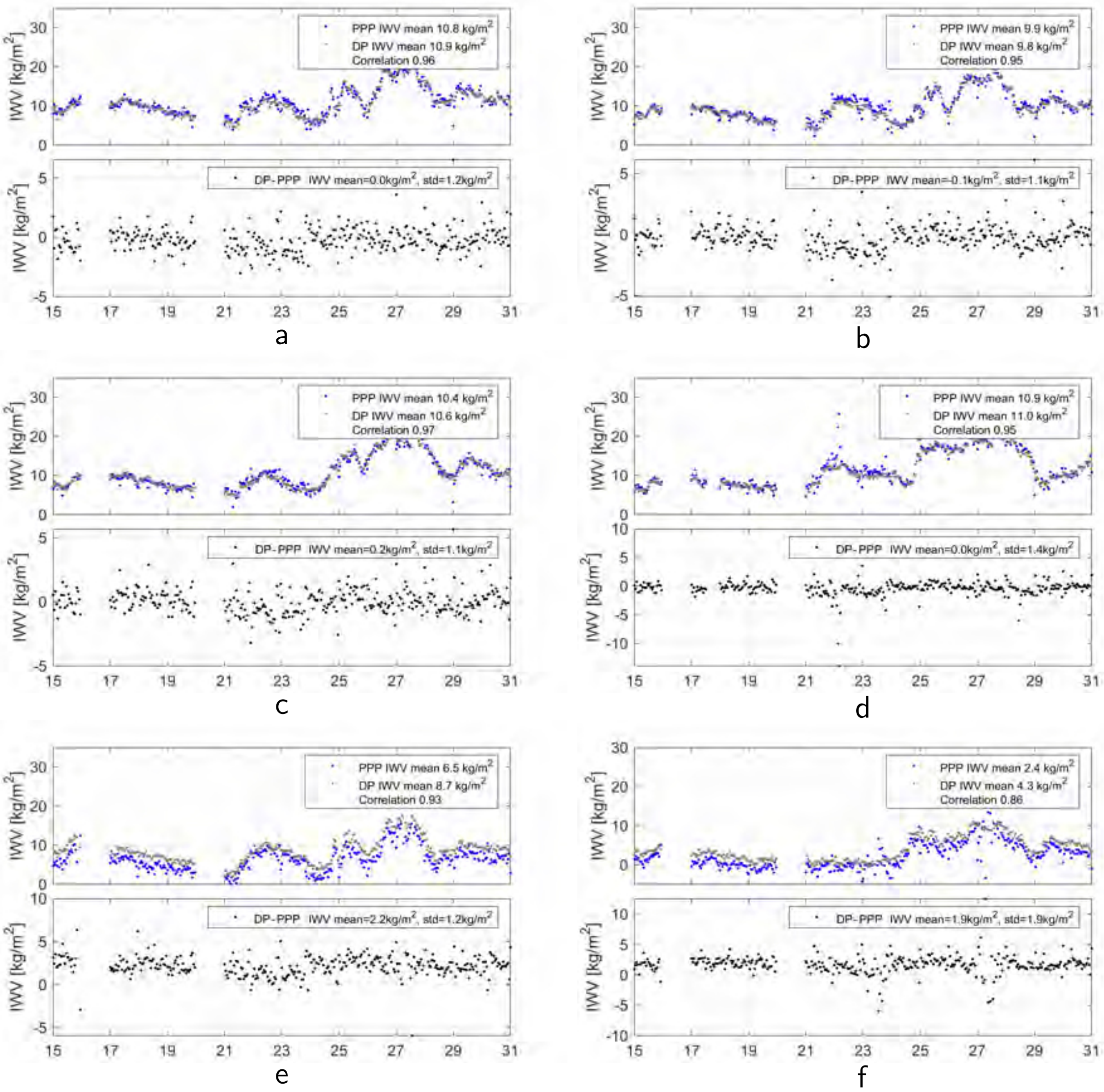

Figure 4.15: IWV comparison between PPP and network solution processings for the period of 15-31 December 2013 for stations: a) Burgas, b) Shumen, c) Stara Zagora, d) Montana, e) Varna, f) Rozhen. The results for Varna and Rozhen clearly show the bias in the PPP processing, resulting from problems in the stations.

Chapter 5

GNSS Reflectometry soil moisture measurements

This chapter describes the unique work carried out for this thesis in GNSS Reflectometry for soil moisture observation.

Firstly, in section 5.1, an available bespoke software for detecting reflections from adjacent surfaces next to GNSS stations is further developed. A database for meteorological, GNSS-R and TDR observations is also developed to comprise soil moisture measurements, as well as meteorological reanalysis datasets (ERA5). The developed software is also validated against available datasets from another data processing center (described in section 5.2). A set of unique soil moisture coefficients is developed to evaluate the quality of the GNSS-R soil moisture retrievals.

Secondly, in section 5.3, a series of parallel measurements in two experimental GNSS-R site is carried out. Comparisons between state-of-the-art GNSS receivers and low-cost counterparts is carried out. The produced soil moisture datasets are compared to available TDR and meteorological data. Two gravimetric measurements are carried out to further validate the TDR and GNSS-R observations.

Thirdly, in section 5.4, a complete screening of 506 stations, part of the IGS GNSS network is performed. 30 of the 506 stations are evaluated as suitable for GNSS-R observations for soil moisture determination. Soil moisture estimations from these stations are carried out with comparison to meteorological data and the ERA5 reanalysis. The results from this work are also presented in appendix D.

Fourthly, in section 5.5, the effects influencing the precision and accuracy of GNSS-R derived soil moisture is discussed. Data processing experiments are carried out to visualize the robustness of the GNSS-R technique for soil moisture observation.

5.1 Data processing routine

5.1.1 GFZ soil moisture retrieval software

A dedicated GFZ soil moisture retrieval software for processing GNSS reflected signals from ground-based GNSS stations is in development since 2013. At the beginning of 2016 the software produces phase, amplitude and height observations and stores them into Matlab data format. For this thesis the available software is further upgraded with more consistent date formatting, more robust data processing, as well as the possibility to export the data into the GFZ Reflectometry and Atmospheric Database (GRAD) database. This allowed the assignment of processing numbers to further allow comparison of changing parameters and different observation techniques. The soil moisture extraction routine is enhanced with filtering of vegetation effects. In the older versions of the software the final soil moisture values are calculated as means from 4 different sectors, rather than as means of all observed satellites. This approach is changed to give equal weight in the soil moisture derivation to each reflection. Alteration of the phase observations calculation output is also made to improve the phase estimations and the visualization of the estimated phases on the standard output plots for internal use.

The GNSS signals, processed in this chapter, are exclusively from GPS. GPS signals, namely L1, L2C and L5, are used for the estimation of the soil moisture and in chapter 7 for snow height observation from the reflected GPS signals. Unlike GLONASS, Galileo and BeiDou, GPS orbits are chosen at such altitude, that the satellites repeat their position every sidereal day (23h 56m 4s). This orbit period ensures that each GPS satellite rises and sets from the same direction in regards to a static GNSS receiver every day. Thus the GPS orbits enable ground reflections from each satellite to be located in the same area continuously over long periods of time, enabling daily observations. GLONASS satellite orbits provide such continuity not on a daily basis, but every 8 days. Galileo provides orbit repeatability every 10 days and BeiDou - every 7 days. Thus creating reflections time series over the same reflection points from Galileo, GLONASS and BeiDou satellites can be performed at worse than weekly data rate, compared to the daily rate from GPS. This characteristic of the constellations is a limiting factor for the single antenna GNSS-R setups, which are used in this thesis.

The processing of the GNSS data in order to acquire soil moisture and snow height data (scheme seen on figure 5.1) starts with the RINEX data files, provided from each station. Some stations provide the more modern RINEX v3 format, some the older RINEX v2. The transition is being performed, using *gfzrnx* - a specially developed GFZ software by *Nischan* (2016). The RINEX v2 file is then parsed through a program, which extracts the signal strength (SS) data and records them in an observation file (*Roesler and Larson*, 2018). The rest of the processing is done in the in-house developed Matlab-based reflectometry retrieval software. First is the de-trending of the SS data in order to acquire the SNR. The first reflector height estimation (h_{est}) is done using LSA with a pre-known reflection height from the log file of the GNSS station. The second estimation of reflector height h is done using the Lomb-Scargle frequency spectrum. The subsequent amplitude A and phase ϕ estimations are performed using the average reflector height estimation h from the Lomb-Scargle Fast Fourier transform. This two-step process is devised so that the height estimate is as precise as possible with the phase changes only being dependent on the soil conditions.

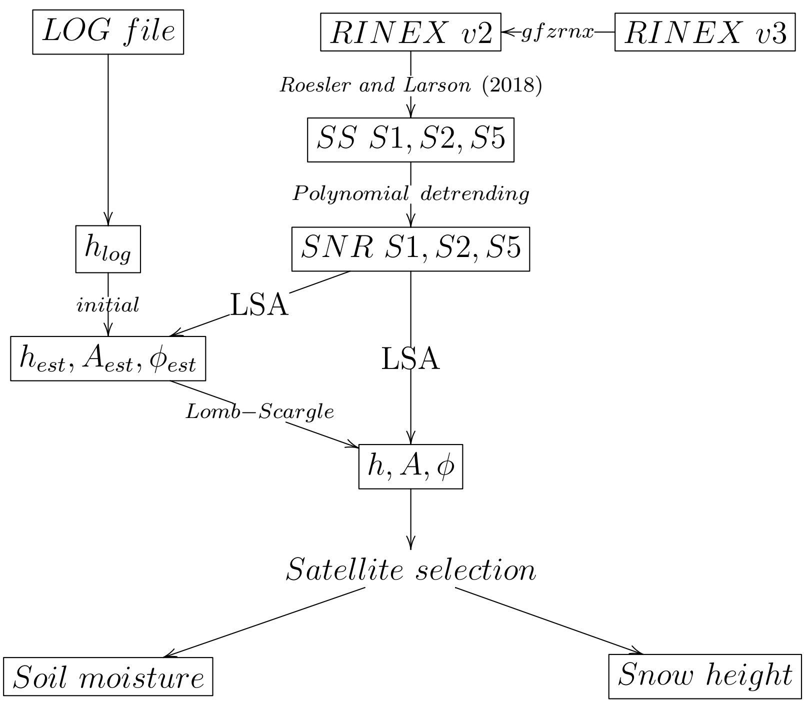

Figure 5.1: GNSS-R data flow in the GFZ soil moisture retrieval software. SS stands for Signal Strength, SNR - Signal to Noise Ratio, S1, S2 & S5 are the SS measurements on L1, L2 & L5. The final step from satellite selection to soil moisture is explained in chapter 3.5.

The surrounding of the GNSS station is divided into 4 sectors, each 100^o wide: sector I covers reflections between $[-95^o; 5^o]$ azimuth (NW), sector II covers $[-5^o; 95^o]$ azimuth (NE), sector III covers $[175^o; -85^o]$ azimuth (SW) and sector IV covers $[-175^o; 85^o]$ azimuth (SE). The overlap between the sectors is necessary to accommodate any reflections, happening on the borders between the sectors.

After the height h, amplitude A and phase ϕ of the SNR pattern have been calculated for each satellite and each sector. Since GPS satellites make two passes over a GPS station a day (orbital period of 11h 58m), and during each pass they appear from different directions, each satellite contributes with 4 reflections per day, which are located in each of the sectors. Thus 32 satellites in orbit can provide up to 128 reflections per sidereal day. Not all of these reflections, though, are sensible to soil moisture. Reflections from buildings and roads cannot be used for soil moisture determination. Moreover, since the model of the reflections, presented in chapter 3.5 relies on horizontal, flat surfaces, only stations with level surroundings are suitable for this type of reflectometry measurements. Thus the not suitable reflections have to be manually disregarded from further processing.

The selection of suitable reflections is done in two steps:

- check the stability of the height and phase estimations over time,
- check the response of the reflections to precipitation events.

The stability of the height estimates is checked through the standard deviation of the height estimates over the years. The check of the stability of the phase estimates is done on an yearly basis for each satellite with the phase changes required to be within 100^o of that time. Any outliers are cleaned in this step.

The next step in the processing is a screening of the reflection amplitude estimates. According to *Chew et al.* (2016), if the estimated amplitude is less than $0.78A_{norm}$[1] for an extended period of time, then most likely, vegetation changes are occurring in the station surroundings. This screening has been performed for all stations and if the values of the amplitude are lower, the observations are ignored. The change of receiver, antenna and GNSS satellite influences the amplitude magnitude, thus for stations with longer datasets, these changes have to be taken into account.

After the appropriate reflections are selected, a soil moisture dataset from each satellite for each year is calculated with the lowest 5% of all estimates from each satellite for each year of measurements assigned to a predefined minimum value. The assignment is done on an yearly basis to avoid the influence of any soil erosion, or other changes leading to a trend in the estimates. Then the estimates from all reflections from all sectors are averaged to produce the final soil moisture dataset from the GNSS station. The final dataset is calibrated again to the lowest 5%, as it is done for the individual reflections. This procedure differs from the procedure, used by *Chew et al.* (2016), where the mean phase from the bottom 15% is used as a calibration setting for the residual soil moisture. By performing the procedure twice, first on a satellite level and then on combined estimated soil moisture level gives very close results to the 15% threshold applied once, as can be seen in the following section.

The final manipulation to the dataset is a smoothing procedure, which eliminates the noise in the data. This smoothing is the reason why the soil moisture values start rising the day before the precipitation occurs. On the other hand the soil moisture datasets have maximums exactly when they are supposed to be, so no information is lost during this procedure. This procedure is employed mainly because of the high daily variations

[1] A_{norm} is the value of the top 20th percentile of the amplitude data series from all reflections for each satellite

in the IGS stations, described in 5.4 and appendix D. Such data manipulation has been used by *Vey et al.* (2016a).

5.1.2 GFZ Reflectometry and Atmospheric Database (GRAD)

The GRAD database is developed for the storage and analysis of soil moisture data. It contains all of the above mentioned data and is designed to enable the comparison of processings with different settings for each station. Data both with and without the final smoothing are stored in the GRAD database.

Similarly to the SUADA database a parallel database, oriented to soil products is created. The reasons to create the database are:

- to store all data from all different sources,
- to enable comparisons between different processing schemes of the same dataset,
- to create a more robust storage space, less vulnerable to data loss,
- to allow several scientists to work on the same dataset in its latest version.

The GRAD database is only used internally in GFZ. More technical details on the GRAD database can be found in appendix B.2.

5.2 Validation of GFZ soil moisture retrieval software

In order to validate the available soil moisture retrieval software a comparison validation campaign is initiated using a GNSS station in USA. The selected station (p038, Latitude 34.1473^o North, Longitude 103.4073^o West) is part of the Plate Boundary Observatory (PBO, `https://www.kristinelarson.net/portfolio/pbo-h2o/`) permanent GNSS network in the west part of North America and is situated in the Eastern part of the state of New Mexico, on the territory of Portales Municipal Airport (as shown on figure 5.2). The station receiver is TRIMBLE NetRS double frequency with 10 Hz sampling rate (10 observations per second) coupled with a TRM29659.00 antenna and a SCIT radome. This station is part of the network, used for soil moisture retrieval on the PBO H_2O data portal. This GNSS station is chosen because of the 360^o azimuth overview without obstacles, low vegetation due to the warm and relatively dry climate and the flat reflective surface without changes in height. The antenna is placed on a tripod approximately 2 meters above surface.

The settings of the software for this campaign are:

- low constraint on reflective surface height between 1 and 4 meters

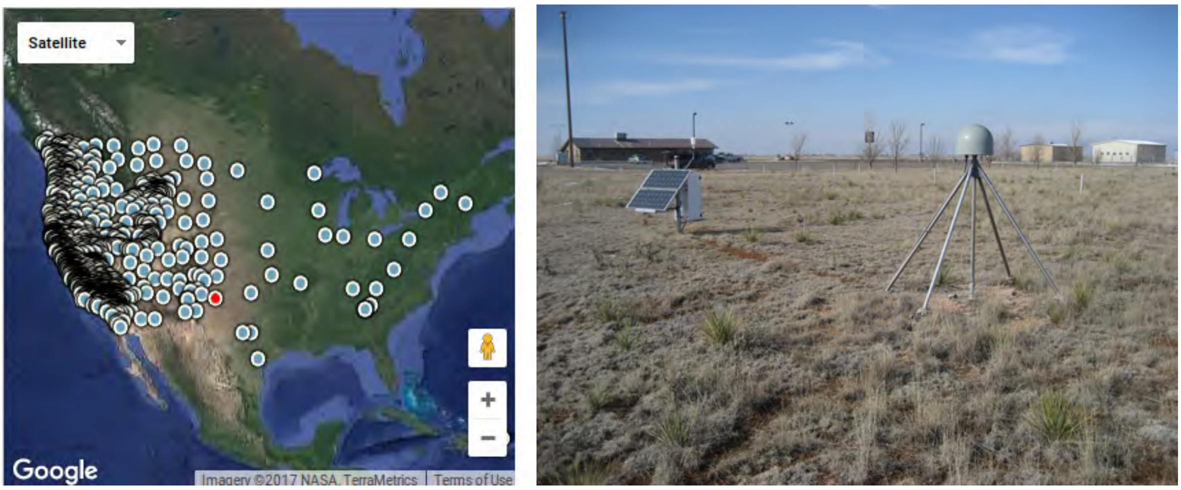

Figure 5.2: Position of station p038 from Unavco web site on the map of North America (left) and a picture of the station surroundings (right).

- elevation angles between 5^o and 30^o
- minimum spectral power difference between the first and second most prominent frequencies from the Lomb-Scargle periodogram of 1.5 times.

The results presented in figure 5.3 are plotted against the rainfall record of the station, which is measured by Vaisala WXT520. The agreement between the two retrievals is very high with correlation (see figure 5.4) between the two datasets of soil moisture of 0.98 and only marginal differences in the magnitude of the soil moisture response.

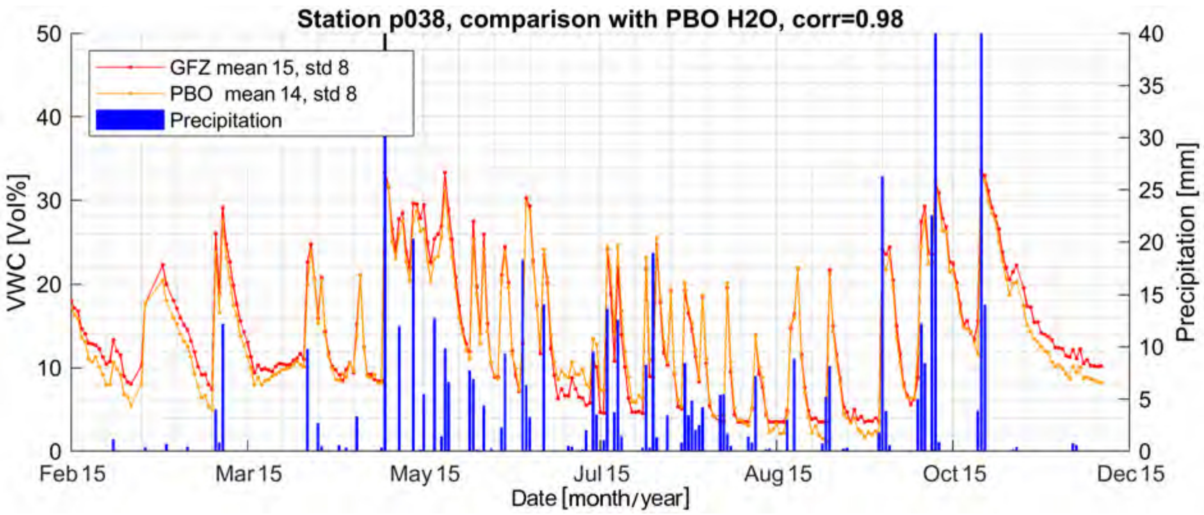

Figure 5.3: Soil moisture retrievals for 2015: comparison between GFZ and PBO for station Portales.

Station p038, can also be used to do an initial validation of ERA5 soil moisture data. ERA5 is a global reference meteorological model reanalysis dataset, created by ECMWF with 0.25 degrees horizontal resolution and hourly temporal resolution. It provides data about the atmosphere, as well as about the soil moisture in 4 depth levels. The first soil level from ERA5 is representing the top 7 centimetres of soil, which is within the range of GNSS-R retrievals. Thus comparison of the two datasets (in figure 5.5) shows significantly higher soil moisture values, than the measurements from GNSS-R. Apart from this systematic bias, the data correlate very well with correlation 0.81.

Using this station as a good comparison benchmark, several coefficients of assessing the quality of soil moisture retrievals have been created. In the following chapters these coefficients are referred to as SMC$_x$ (number x Soil Moisture Coefficient). In order to create these coefficients, the soil moisture dataset is divided into 4 subsets, dependent on the soil moisture daily tendency and on the precipitation. The subsets are the following:

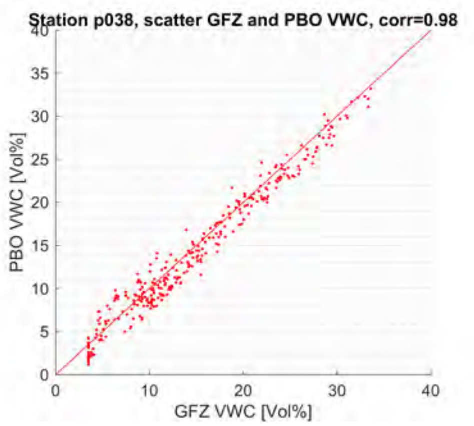

Figure 5.4: Soil moisture retrievals comparison between GFZ and PBO.

- positive (pos) - VWC $\nearrow$, precipitation > 0
- not positive (nop) - VWC $\nearrow$, precipitation $= 0$
- negative (neg) - VWC $\searrow$, precipitation $= 0$
- not negative (non) - VWC $\searrow$, precipitation > 0

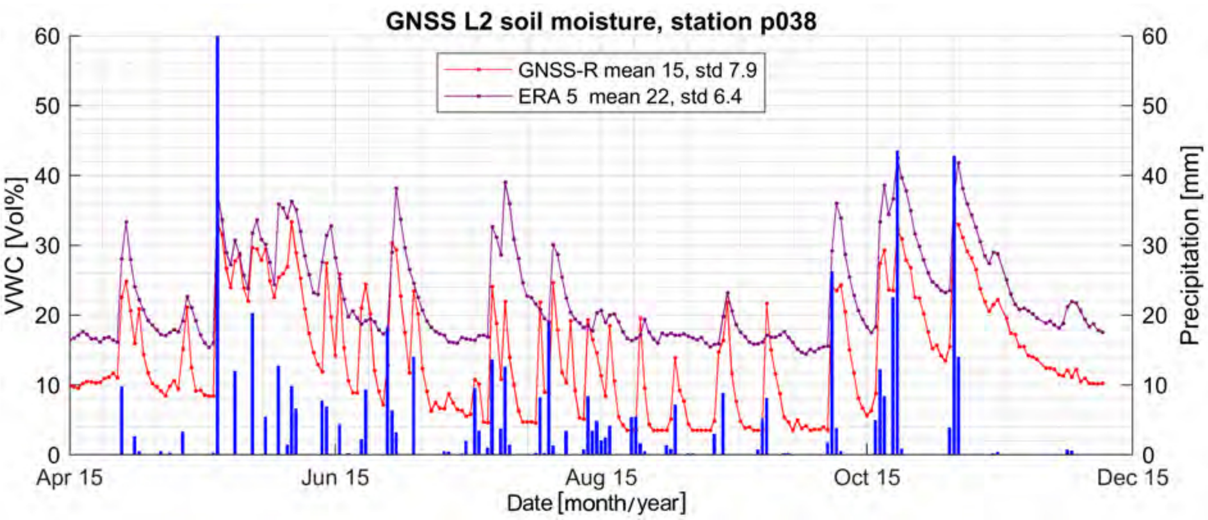

Figure 5.5: Soil moisture retrievals for 2015: comparison between GNSS-R and ERA5 for station Portales.

Physically the behaviour of VWC should follow the logic of increasing during precipitation and decreasing, when there is no precipitation. These two cases are represented with the "positive" and "negative" subsets. The "not positive" and "not negative" subsets represent irregular behaviour, increasing the soil moisture without precipitation or decreasing it, when precipitation is available. In nature the "not negative" behaviour can be observed in a series of precipitations several days in a row. Then, in general, soil moisture can increase or decrease, depending on the intensity of the precipitation. The "not positive" behaviour of soil moisture is the least expected, as far as the main source of soil moisture is precipitation and the increase of VWC should be directly linked to precipitation.

The coefficients use the following logic:

$$\mathrm{SMC}_1 = \frac{N_{pos}}{N_{pos} + N_{nop}} \tag{5.1}$$

where N_{pos} represents the number of days in the dataset, when the soil moisture and precipitation observations belonged to the "positive" subset and N_{nop} - to the "not negative" respectively.

$$\mathrm{SMC}_2 = \frac{mean_{pos}}{mean_{nop}} \tag{5.2}$$

$$\mathrm{SMC}_3 = \frac{N_{pos} + N_{neg}}{N_{all}} \tag{5.3}$$

$$\mathrm{SMC}_4 = \frac{N_{neg}}{N_{neg} + N_{non}} \tag{5.4}$$

$$\mathrm{SMC}_5 = R^2(VWC \nearrow, Precip) \tag{5.5}$$

	SMC_1	SMC_2	SMC_3	SMC_4	SMC_5
Values	0.84	6.0	0.67	0.62	0.20

Table 5.1: Soil moisture coefficients for station Portales.

The values for coefficients SMC_1, SMC_3, SMC_4 and SMC_5 are designed to be in the range between 0 and 1 with higher values indicating better observation of the soil moisture, compared to the expected environment. The SMC_2 coefficient has possible values between 0 and ∞, with well performing stations showing values bigger than 1. Although theoretically expected, the value of SMC_5 cannot exceed 0.5, since the increase of soil moisture is governed not only by the amount of precipitation, but also by the soil conditions, which are not taken into account in this coefficient.

5.3 Monitoring at stations Marquardt and Fürstensee

5.3.1 Station description Marquardt

Experimental station Marquardt is situated in the North-East Germany, circa 20 km to the west of Berlin. It is installed in a research experimental field (shown in figure 5.6) of the Leibnitz Institute for Agriculture Potsdam-Bornim, Forschungsstandort Marquardt. The permanent sensors in the station include multiple GNSS antennae and receivers, an array of TDR sensors and a meteorological station. Since Marquardt is situated in close proximity to GFZ Potsdam, sporadic vegetation and soil moisture measurements are performed in the station in parallel.

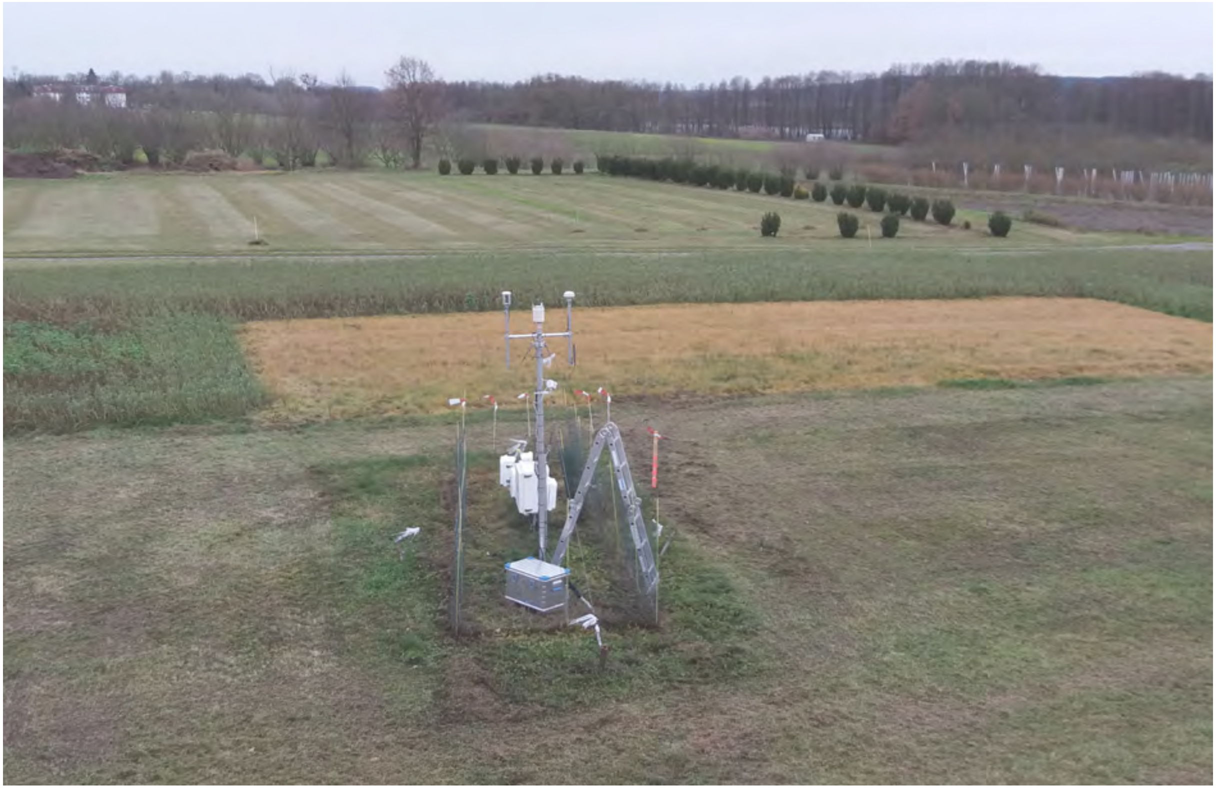

Figure 5.6: The GNSS station MARQ in station Marquardt is located on a 3 meter long pole, where the antennae and the meteorological sensors are mounted. The picture is taken looking in direction South.

There are 4 GNSS antenna/receiver sets: the MARQ set is a multi-frequency Javad TRE_G3TH receiver coupled with a Antcom S67 antenna; the MAR1 set is a single-frequency Novatel NOVSMART-V1 antenna coupled with a NOV OEMV1 receiver in a single housing, the MAR3 is a u-blox antenna and receiver and MAR4 is a u-blox receiver, connected to the same Antcom S67 antenna as MARQ via a passive splitter (all receivers shown in a schematic figure 5.7). All antennae are installed on a 3 meter pole together with a Vaisala WTX520 meteorological sensor cluster. The technical specifications of all sensors can be found in the appendix to the thesis.

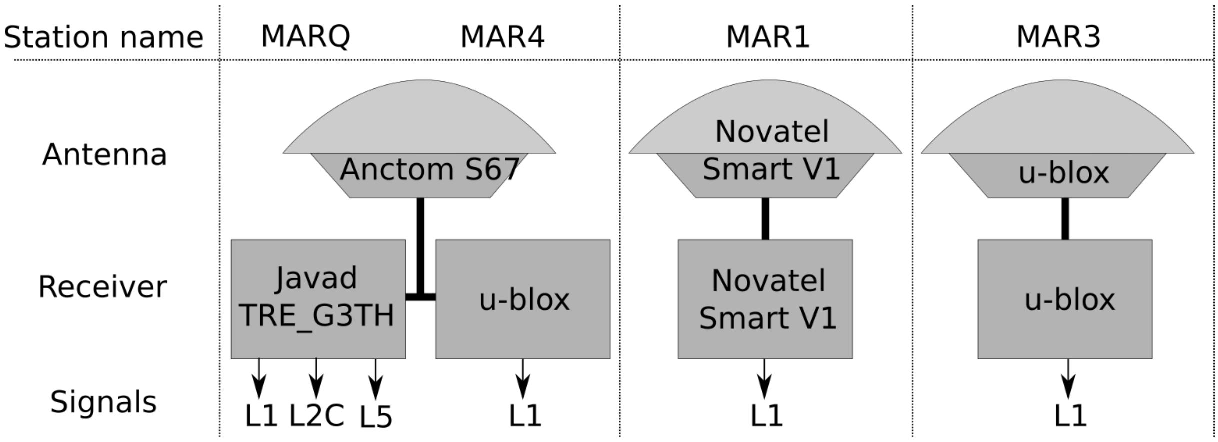

Figure 5.7: GNSS setups in station Marquardt. The four symbol abbreviations of the stations are used to identify the unique combinations of antennae and receivers.

A TDR sensors array is installed 4 meters south from the GNSS mast. The TDR sensors array has the following layout: there are several depths at which the sensors are situated for Marquardt they are 8: at 1, 3, 5, 9, 11, 25, 45 and 75 cm. The TDR sensors are also organized to take profile data. There are 6 profiles with sensors at every of the above mentioned depths. This means there are 48 TDR sensors in Marquardt. The GNSS-R results are compared to the average values from TDR sensors at each of the depths in all profiles. The TDR profiles are connected to a Multiplex device, which reads the sensors one at a time. This allows high temporal resolution for the data with minimum amount of data loggers. After grass mowing in the autumn of 2017 the top TDR sensors at 1cm depth are destroyed. This incident does not influence the lower sensors, which continued providing soil moisture data.

The GNSS stations MARQ and MAR1 were established on 23rd of June 2014 (day of year 174). Station MAR3 is added later, on 15th of September 2015 (day of year 258). In August 2017 the MAR4 receiver is installed. Since their establishment, all receivers have recorded data every second ($1Hz$ sampling rate).

Agricultural activities in this experimental station are performed since September 2015 and have influenced the GNSS measurements. The datasets can be divided into several periods. Since the start of the experiments the field south of the GNSS array is not used for agriculture and is covered by low grass, which is regularly mowed. On the 20th September 2015 the field south of the array is ploughed with fur in East-West direction. The ploughing increased the roughness of the field and soil moisture retrieval from the GNSS reflected signals is impossible until the surface is grubbed the following spring on the 14th March 2016 and then partially seeded with crops. The crops are collected in July 2016. On figure 5.8 the area of agricultural activities is shown together with the Fresnel zones (described in chapter 3.5) of the reflected signals and the position of paved area and buildings in the premises of the GNSS stations.

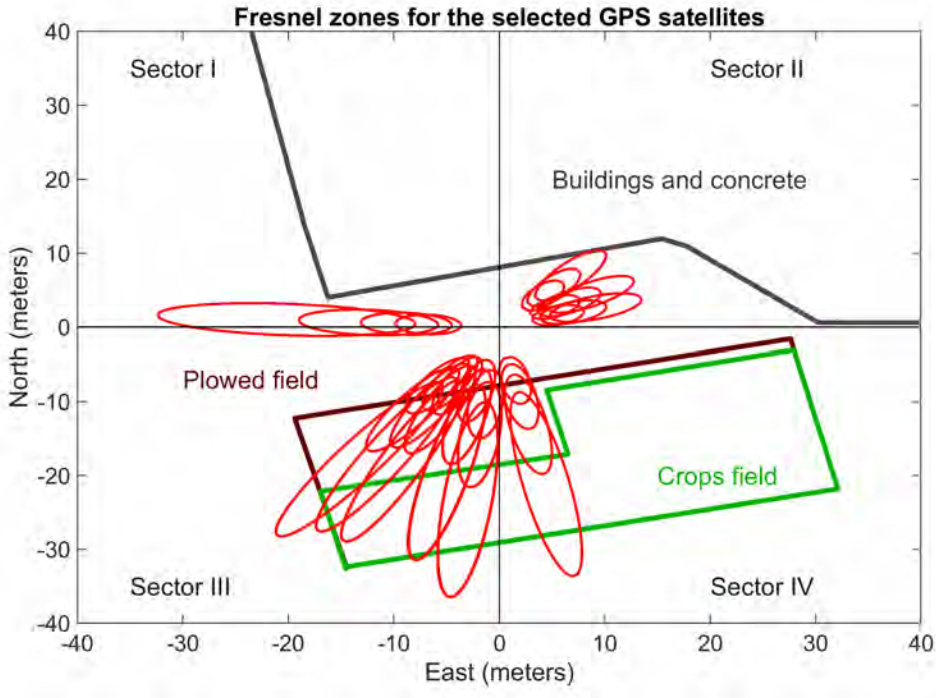

Figure 5.8: Fresnel zones of all GNSS stations in Marquardt. The chosen satellites are the same for all sensors. MARQ L5 dataset uses fewer reflections, because not all L2C satellites are L5 capabile. The selected satellites are the following: Sector I: PRN 27, Sector II: PRN 7,10,17, Sector III: PRN 9,15,27,29,30,31, Sector IV: PRN 7,10.

5.3.2 Soil moisture at station Marquardt derived from L2C and L5 data

Soil moisture is the final product of the analysis of the time series of the interference patterns between the direct and reflected signals at elevation angles below 30 degrees. For these measurements from the MARQ receiver for the L2C signals 13 satellite paths are selected for analysis and divided into four sectors (shown in figure 5.9). The indicated soil moisture estimates in each of the four sectors is different. The differences between the sectors can be explained with the lack of homogeneity in the soils around the GNSS site. Figure 5.8 shows that the reflection in sector 1 comes from a grassland area, in sector 2 the reflections are very close to a concrete surface, in sector 3 the reflections are coming from mostly bare soil, similar to the reflection from sector 4. The results show that the grass covered soil retains more moisture, compared to bare soil during dry periods. Similar results are achieved using the same receiver, antenna and reflections for the L5 GPS signal.

Both final calibrated sets of soil moisture measurements from the L2C and L5 signals show good correlation with the collocated TDR measurements at different depths (shown in figures 5.10). The 1cm sondes are most sensitive to any changes in the atmosphere -

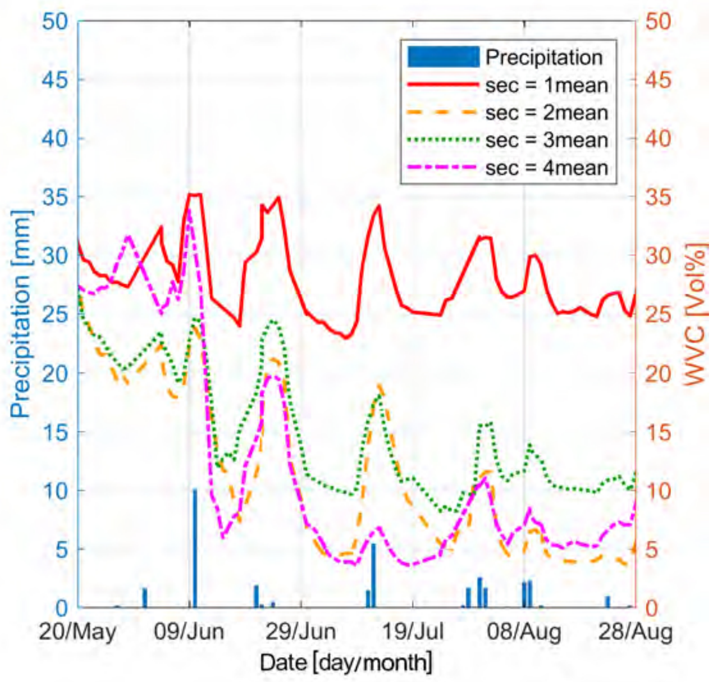

Figure 5.9: Sector soil moisture retreivals for L2C signals. The 4 sectors show slightly different behaviour in soil moisture. The presented data are before final outliers removal and calibration.

the response to precipitation and morning due are the highest at this layer. The deeper layers at 3 and 5cm show slower responses to precipitation. These layers are less exposed to the atmosphere and evaporate less water. The lowest layer at 9cm is much more inert, then the layers closer to the surface. It conserves much more water and usually disposes of it through infiltration.

The RMSE of the soil moisture comparisons between the L2C signals products and TDR shows highest values for the 1cm layer. The deeper layers show lower RMSE's with the lowest of 4.3$Vol\%$ for the 9cm TDR's (see figure 5.11). The seasonal analysis shows different behaviour for each season. The season with the highest RMSE is autumn (September, October, November (SON)), while the season with the lowest is spring (March, April and May (MAM)). The average RMSE between GNSS-R and 5cm TDR from these experiments is 4.5$Vol\%$.

The soil moisture datasets can be divided into cases season by season, based on the difference in correlation between winter and the rest of the year (see figure 5.11). This seasonal analysis shows a slightly different situation for each period. During the colder months the soil moisture estimations from the GNSS differ greatly from the TDR measurements. One of the reasons for this discrepancy is the fact, that it is not possible to distinguish snow cover from bare soil in the winter period. Whenever there is snow in the region of Marquardt, the total snow cover is in the range of between 0-5cm, which

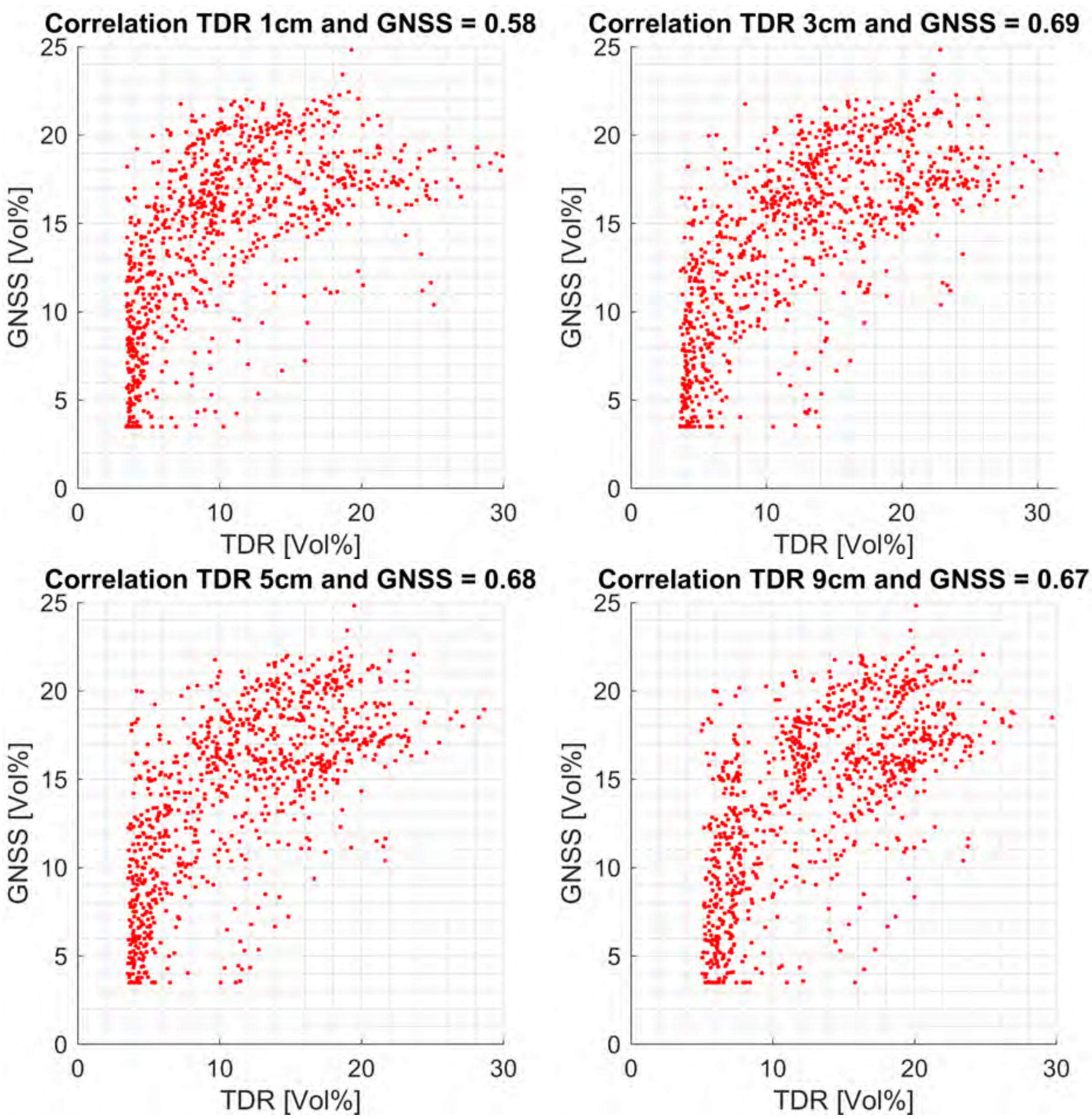

Figure 5.10: Scatter plots of TDR measurements at different depths and GNSS soil moisture. The GNSS-R retrievals show a wet bias when compared to the TDR measurements. The correlations between TDR at 3, 5 and 9*cm* and GNSS-R are very similar.

is within the reflection height estimation standard deviation. Thus soil moisture is the GNSS-R observable even when the bare soil is covered, which leads to additional uncertainty during the winter. Moreover winter is a season with much lower variation of the soil moisture, thus correlation can be a misleading metric. The expected correlation between the datasets is highest during spring, summer and autumn, because of the large variety of soil moisture values and the trends during these seasons.

Since the seasonal correlation (in figure 5.11) suggests two different modes in the behaviour of soil moisture, the winter cases are discussed separately from the warmer periods of the year. The winter soil moisture retrievals not only show lower correlation

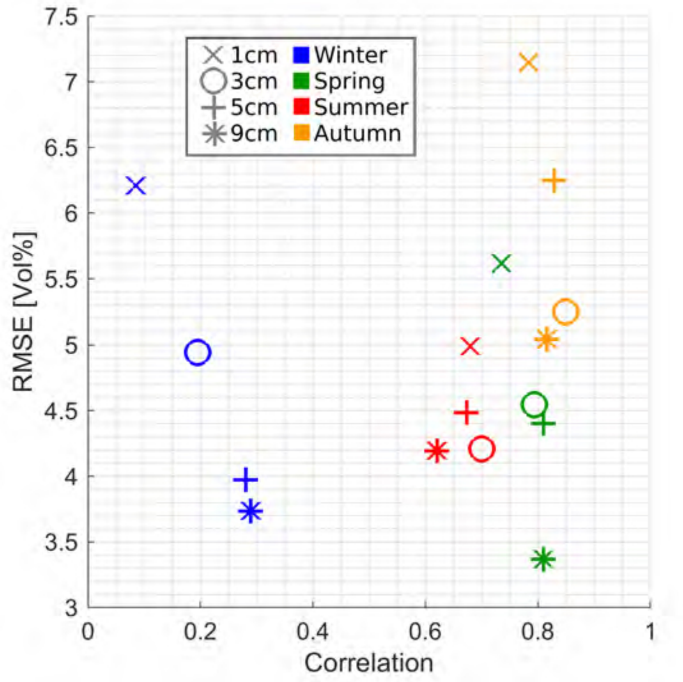

Figure 5.11: Seasonal comparrisson of correlation and RMSE for station MARQ L2C signals and TDR. Seasons are defined as DJF for winter, MAM for spring, JJA for summer and SON for autumn.

with TDR, but also their response to precipitation is not as significant. Temperature of 10^oC is the threshold below which this transition from lower to higher correlation occurs. Plots with the comparison between the two datasets can be seen in figures 5.12. These figures show two modes in the soil moisture measurements from GNSS, depending on $2m$ air temperature.

First winter case is when the air temperature is in the interval between 0 and 10^oC. The average values, recorded by the method are very close to the TDR measurements, thus GNSS is able to show high amounts of soil moisture during the winter season. This is expected, due to the lower evaporation when the temperatures are low. The precipitation amounts during winter are characterised with much lower precipitation rate and longer precipitation periods.

Second winter case is when the air temperature is below 0^oC. These are periods with conditions for water to freeze in the soil. Such conditions are available during every winter in NE Germany. The GNSS reflection model, developed by *Zavorotny et al.* (2010) is applicable only to liquid water in soils, rather than frozen water. Thus only the decrease of liquid water in the soil (which is referred to as soil moisture) is apparent in our measurements, while the frozen water can't be measured with this technique. The drop in soil moisture is present in both GNSS and TDR measurements, thus suggesting, that in these low temperatures, the GNSS reflections are indeed detecting soil moisture.

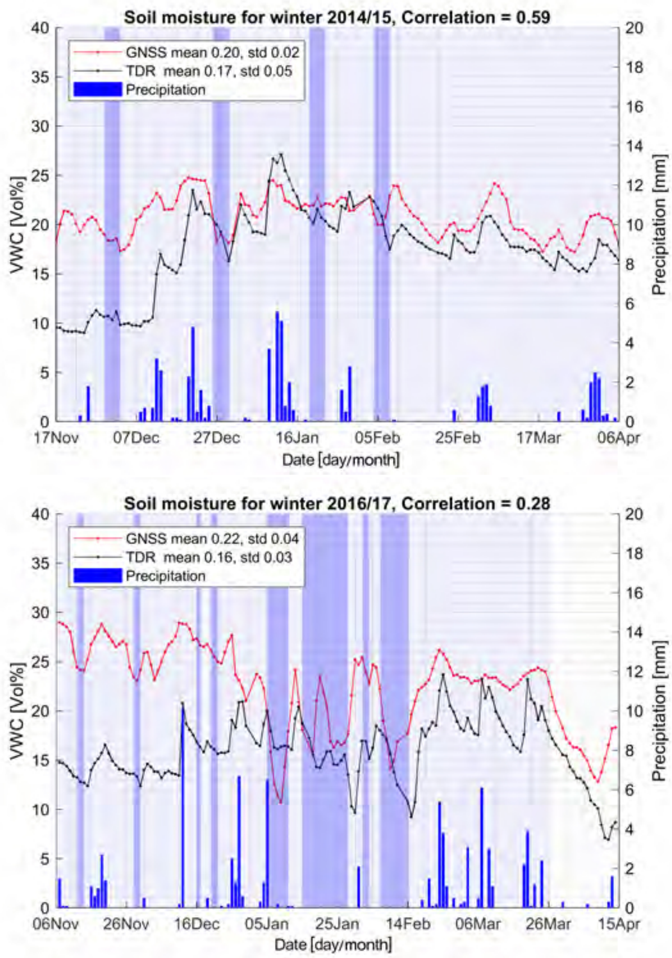

Figure 5.12: Winter soil moisture in Marquardt. Figure on the top is for winter 2014-2015, while on the bottom - 2016-2017. Light blue color indicates temperatures in the interval between 0 and 10^oC, while dark blue indicates temperatures below 0^oC.

The second winter case shows, that during winter time, the measured phase changes from the reflections are indeed dependent on the amount of soil moisture in the soil. The difference in the measured values by the two methods can be explained by the following differences in the methods themselves:

- TDR measures confined volume around the probes, while GNSS has large footprint, in case of Marquardt - more than $300m^2$,
- TDR measures at specific depths, while the penetration of the GNSS signal depends on the VWC in the soil,
- TDR is independent on above-ground vegetation, while GNSS is dependent on both above-ground vegetation and on roots
- GNSS signals get reflected from the snow cover, when one is present, thus corrupting the soil moisture retrieval.

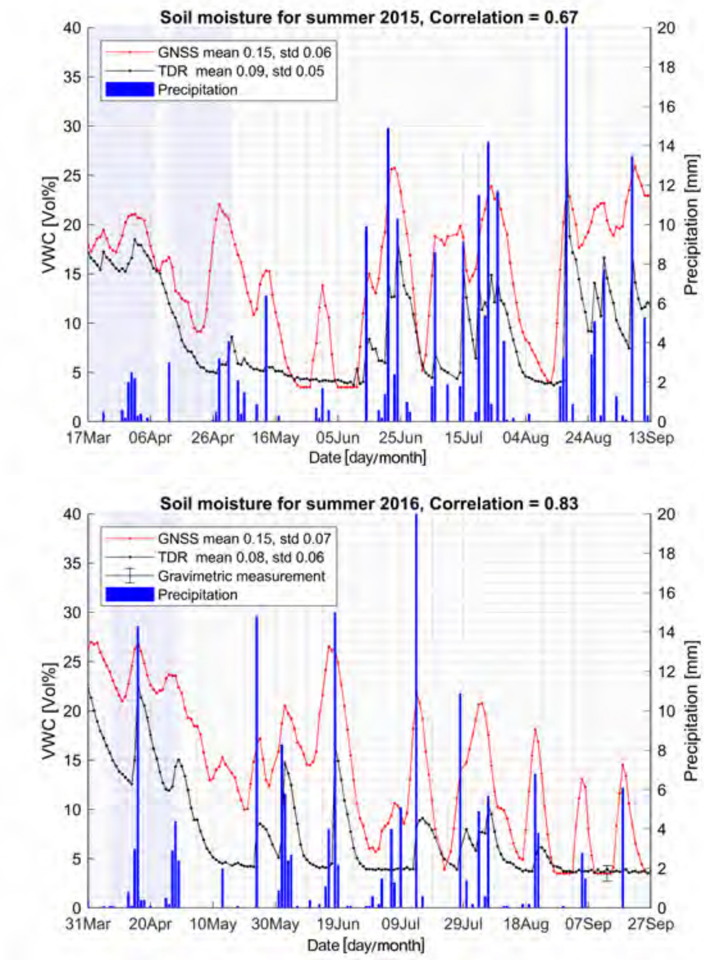

Figure 5.13: Summer soil moisture in Marquardt. Figure on the top is for the warm season ($2m$ temperature above 10^oC) of 2015, while on the bottom - 2016. Light blue color indicates temperatures in the interval between 0 and 10^oC.

These differences contribute to an entirely different measurement between the two methods, thus explaining partly the biases and not very high correlation between the datasets.

The differences between TDR and GNSS as soil moisture measuring techniques can be observed in the summer variation of both datasets as well (seen in figure 5.13). Several precipitation events occur between 20th August and the end of September 2016 in the premises of Marquardt. TDR shows very low to non-existing response to these precipitation events, while the response of GNSS can clearly be seen. One of the main reasons why TDR is not sensible to these precipitation events is lack of infiltration in the soil. The lack of infiltration could be triggered by the high temperatures during this part of the year (daily high temperatures in the range of 30^oC). All of the precipitation events are recorded in the afternoon hours, when the soil is most heated and the potential for evaporation from it is highest. This hypothesis is also supported by the response of the $1cm$ TDR probes, which indicate a short increase in measured VWC.

The GNSS estimates of soil moisture are done by averaging the soil moisture retrievals from each individual satellite. Since the reflections are happening non-uniformly throughout the day, some of the satellites contribute to the daily soil moisture values with through morning reflections, while some satellites contribute with evening reflections. This is the reason why in some cases the VWC, calculated using GNSS, shows local maximum values one day after the precipitation. Since precipitation events are more often an afternoon event, than a morning event, the dryer morning reflections contribute with much smaller values. The TDR values are also daily averages and also shows such behaviour.

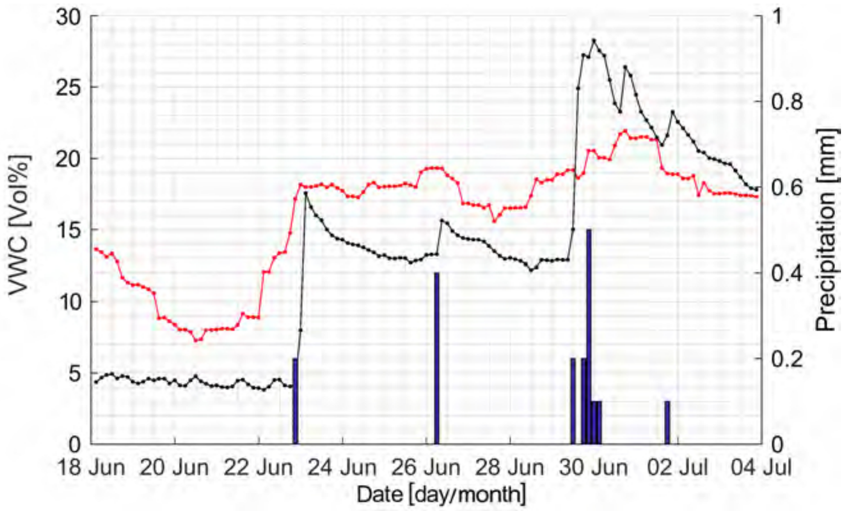

Figure 5.14: Severe summer rainfall - high resolution GNSS soil moisture experiment. This event happened in the end of June, beginning of July 2017 with recorded daily precipitation values of 35mm/day on the 29th of June. On the right axis 10 minutes precipitation rate plotted (blue bars). The red line indicates L2C derived soil moisture, while the black line is $5cm$ TDR.

In order to investigate the potential of GNSS to access soil moisture on a sub-daily scale, an experiment with several rainfall events is carried out. The averaging of the soil moisture is done using 24 hour sliding windows shown in figure 5.14). This small investigation showed that the local maximum in soil moisture coincides with the time of precipitation. The soil moisture retrieval with such high resolution of 3 hours in a sliding window configuration is unreasonable. The figure suggests an increase in soil moisture before the precipitation event, which physically is not possible. On the other hand creating an algorithm, which would sharpen the difference before and after rainfall without using the rainfall measurements themselves is going to be artificial and will not represent soil moisture correctly in many other cases. Follow up studies with this approach for high resolution GNSS-R soil moisture estimations are questionable, since such temporal resolution is not necessary neither for agriculture, nor for weather analysis.

5.3.3 Using low-cost single frequency receivers

Five different GNSS-R datasets are highlighted in this section: L1 retrievals from MARQ, MAR1 and MAR3, as well as L2C and L5 from MARQ. These retrievals have different properties and, although the antennae are at the same experimental site, on the same pole, at roughly the same height and the same position, the results from them are not the same. The most likely reasons for the differences are:

- the antennae are located on slightly different heights,
- the antennae have different gain patterns,
- the receivers have different signal strength resolutions (Javad has $\frac{1}{4}dB-Hz$ resolution, while the other receivers - $1dB-Hz$),
- the receivers have slightly different amplifying algorithms for the received signals, since the antennae are passive receivers,
- the antennae are located next to each other and shadow certain azimuth angles,
- the different signals interact with the reflective surface with dependence to their carrier frequency.

Some of these arguments have larger influence, than the others, but generally the expectation of having the same measurement with the different makes of antennae and receivers does not hold. The analysis of not only the soil moisture as a final product of the analysis of the signal strength would be incomplete when comparing the products of the receivers. Thus a more thorough screening of the recorded signal strength from the receivers has to be made.

In figure 5.15 the observed pattern of the signal strength of the L1C/A signals from PRN 14, recorded on the 19th of October 2017 by the MARQ, MAR3 and MAR4 stations can be seen. Since MARQ and MAR4 receivers are connected to the same antenna, it is clear, that the interference pattern between the direct and reflected signals is the same (as received by the antenna). But the peak power, the signal strength resolution and the average measured signal strength deviate. In general, the signal strength from the cheaper single-frequency u-blox receiver (MAR4) is lower by more than $1db-Hz$, than the same values, recorded by the Javad receiver. Moreover, the lower resolution makes it much harder to fit a sinusoidal curve to the rising and setting elevation angles of the recorded signal strength measurement of the satellite (as described in figure 3.11). This phenomena is occurring throughout all GPS satellites, at all elevation angles. There are several reasons why the signal strength from the different satellites reaches its peak far from the highest elevation angle and has variation over time when the maximum signal strength is reached. One of the reasons is, that the antennae, used in Marquardt are

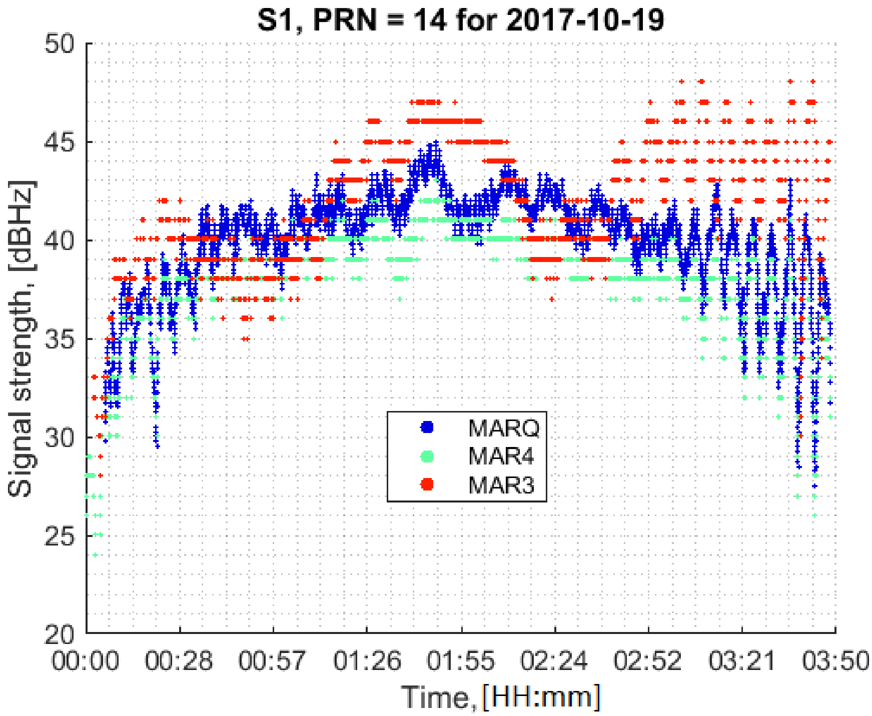

Figure 5.15: Comparison of the signal strength of the L1C/A signals from PRN 14, recorded on the 19th of October 2017 by the MARQ, MAR3 and MAR4 stations.

without choke rings, so none of the reflected signals from the ground get blocked. This allows the antennae to receive more power from the reflected signals, thus creating this flattened profile of the signal strength in higher elevation angles. The MAR1, MAR3 and MAR4 receivers also provide soil moisture retrievals, but the results from them are not satisfactory, compared to the standard geodetic MARQ receiver.

Since the GNSS Reflectometry derived soil moisture and TDR are not perfectly comparable, a much more adequate comparison is between the GNSS sensors. Apart from the previously discussed L2C and L5 signals from the MARQ station, L1 soil moisture retrievals are also possible using MARQ, MAR1, MAR3 and MAR4 receivers. The L1-only low-cost receivers do not show the expected performance, when comparing them to the MARQ L2C retrievals. The higher resolution of signal strength of the Javad receiver enables better agreement between L1 and L2C from MARQ than between the more cost-effective receivers, as shown in figure 5.16.

Since the low-cost receivers are introduced not all together at the same time, the comparison between the individual datasets cannot be carried out in a bulk format, but each pair of retrievals should be considered for comparisons. Thus in order to achieve consistency between the compared datasets, the selected satellites from the L2C retrievals in the previous sub-chapter, have been used for all L1 and L5 retrievals as well. These 13 reflections all come from L2C capable satellites with higher power output than the older Block II GPS generation. The availability of datasets is shown on figure 5.17.

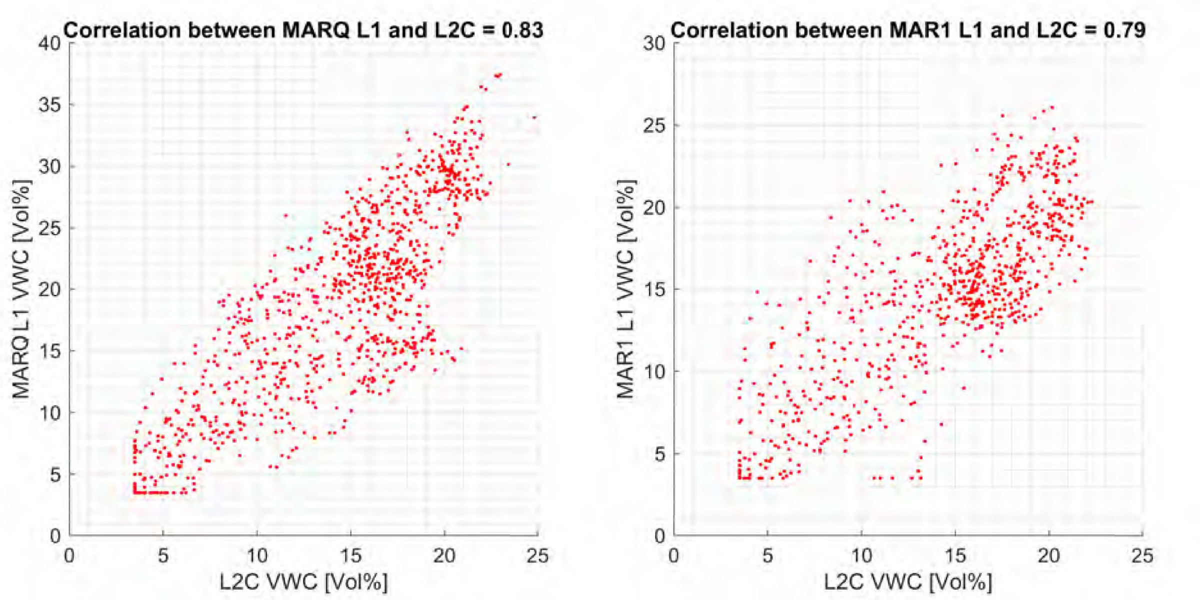

Figure 5.16: Scatter plot of soil moisture retrievals from GNSS stations MARQ and MAR1.

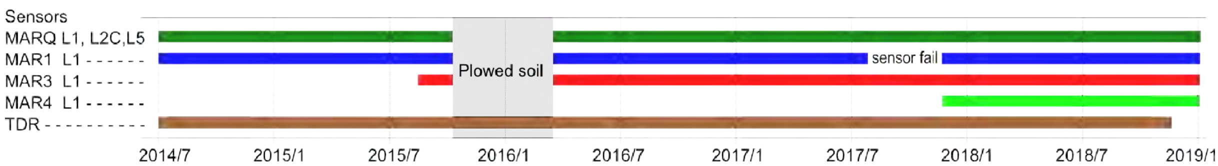

Figure 5.17: Data availability from all GNSS sensors in Marquardt. The datasets have small gaps in between observations with the larger gaps highlighted.

Station	1.	2.	3.	4.	5.	6.	7.
1. TDR	-	0.74	0.74	0.74	0.75	0.67	-
2. MARQ L1	0.74	-	0.83	0.71	0.77	0.39	0.72
3. MARQ L2	0.74	0.83	-	0.85	0.79	0.44	0.66
4. MARQ L5	0.74	0.71	0.85	-	0.62	0.41	0.79
5. MAR1 L1	0.75	0.77	0.79	0.62	-	0.50	0.75
6. MAR3 L1	0.67	0.39	0.44	0.41	0.50	-	0.37
7. MAR4 L1	-	0.72	0.66	0.79	0.75	0.37	-
Average	0.73	0.69	0.71	0.70	0.69	0.48	0.66

Table 5.2: Correlations between soil moisture estimations from all GNSS sensors and frequencies in Marquardt.

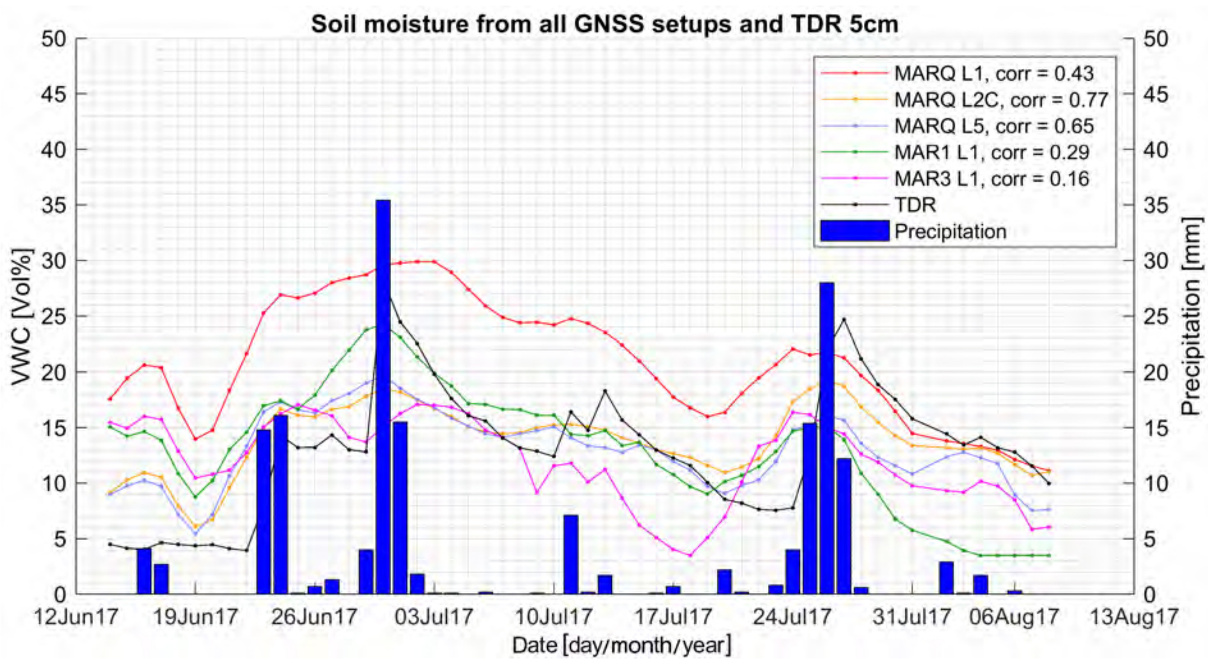

Figure 5.18: Soil moisture from all GNSS receivers from Marquardt. The correlation figures are comparisons to the TDR sensor from each GNSS antenna/signal.

The individual soil moisture datasets, compared to each other for the time periods when these observations are available (as shown on figure 5.17), are presented in table 5.2. The correlation coefficients agree with previous assumptions of good agreement between L2C and L5 measurements. Moreover the correlations show that L1, L2C and L5 frequencies do not stand out from each other and all of them are suitable for soil moisture determination. This is proved by the very close results of the L1, L2C and L5 derivations from the MARQ Javad receiver. The overlap period between MAR4 and MARQ datasets occurs during a half year, characterised by a naturally occurring decreasing trend from winter into summer. This trend may obscure the actual performance of the MAR4 dataset, as far as the soil moisture datasets are not de-trended for the seasonal variations. This is the reason for higher expected correlation between the MAR4 and MARQ datasets. MAR3 stands out from the group of retrievals with its lowest performance, as compared to the other GNSS receivers, scoring not only lowest correlation compared to MAR4, but also lowest average correlation. In total, if the MAR3 correlations are counted out from this comparison, all other sensors would score correlation coefficients above 0.66.

The low-cost receivers show not very high correlation with the benchmark L2C soil moisture retrievals. From this analysis of the soil moisture datasets it is apparent, that the cheaper sensors not always recognize precipitation events as well as L2C from MARQ (shown in figure 5.18). All GNSS datasets respond to the larger precipitation events, but the smaller rainfalls are omitted in the L1 dataset from the low-cost MAR1 and especially MAR3. The reason for this can be found in figure 5.15. As discussed previously, the low-cost GNSS receivers, used in this work have $1dB - Hz$ resolution of the signal strength of the GPS signals. Thus fitting a sinusoidal curve over interference pattern, represented by 5 equally distributed layers of data points is highly inaccurate, compared to a fit over 20 layers of data points.

5.3.4 Gravimetric measurements in station Marquardt

During the summer period in 2016, a gravimetric calibration of the sensors is initiated. 16 samples in total are extracted from the soil on the 13th of September in the afternoon. The day is chosen as to be hot and dry with previous precipitation event more then a week before the measurement. The whole month of September is unusually hot and dry for this area with daily temperatures exceeding 25 degrees.

The soil samples are taken from 4 sites, each less than 2m away from the TDR sensors. The sites are to the North-West, West, South and East of the sondes. The aluminium core cylinders, used for the sampling, are 100cm^3 in volume and 3cm high. In each of the 4 sites 2 vertical and 2 horizontal samples are taken. For both the horizontal and vertical samples the tops of the samples are situated at 1cm and at 3cm depth each. This approach enables the centers of the cores to be at around 3-6cm depth, which is comparable to the 5cm TDR.

Figure 5.19: Collecting gravimetric samples in Marquardt.

The core weights are measured the same day in the laboratory and are dried for 12 hours at 60^{o}C. After the drying process the samples are weighted again. The measured mean value from this measurement is $3.5 \pm 0.8 Vol\%$ of water in the soil. This value is used as the minimum possible measurement of soil moisture from the station for both GNSS and TDR.

Additional water saturation experiment is carried out with the soil samples. The samples are immersed in a water container in order to quantify the maximum water storage capacity of the soils in the area. The resulted value of $51 \pm 2 Vol\%$ is assumed as the highest possible value for station Marquardt. Such readings would only be possible in the event of a flood, when the surface is covered by run-off water. During the time of this experiment such an extreme event has not been recorded. Moreover, station Marquardt is located on a slight hill, dominating over the landscape, so such severe flooding events would be highly improbable for the close surroundings of the station.

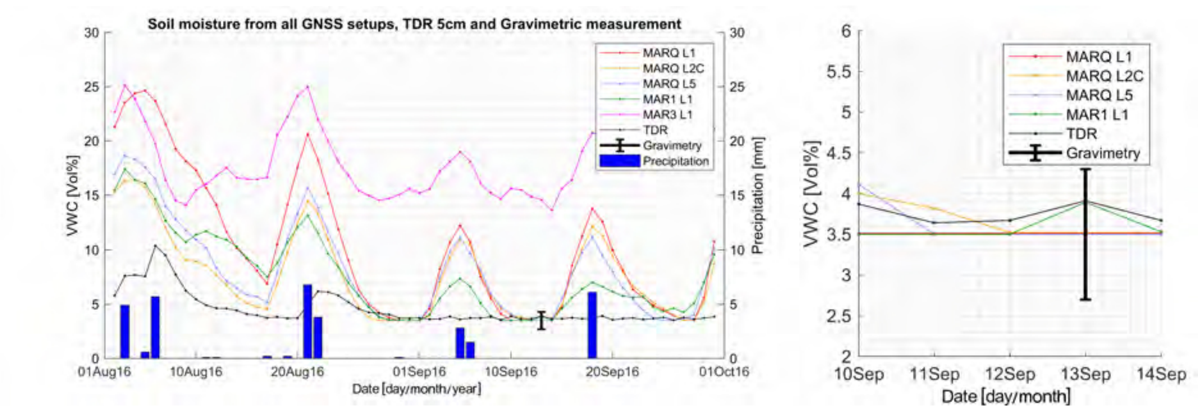

Figure 5.20: Gravimetric measurements, compared to GNSS and TDR for Marquardt. The left figure shows the good agreement between TDR, and all GNSS stations, except MAR3. The right figure shows the zoomed dynamics around the 13th of September when the measurements are taken. The error bars indicate the standard deviation of the gravimetric measurement.

5.3.5 Station description Fürstensee

Station Fürstensee is situated in North-East Germany, circa 100 km to the north of Berlin. Unlike Marquardt, this station is situated in an pasture field of a cow farm. The site is sitting on a small hill with no buildings around it. The station comprises a multi-frequency GNSS antenna and receiver (marked as TRFS), an array of TDR and FDR sensors, as well as a Vaisala WTX520 weather station. The Javad Grant-G3T GNSS antenna is elevated on a 4 meter pole above the top of the hill.

Soil erosion processes are occurring in close proximity to the station both in Northern and Eastern directions. A small forested area is also observable in direction North-East. Thus the reflections, used in the soil moisture derivation come from several distinguishable areas with different properties (seen on the Fresnel zones on figure 5.21).

The TDR array in Fürstensee consists of 5 profiles of sensors at 1, 3, 5, 7 and 9 cm depths. The profiles are located 2 meters to the south-west of the GNSS antenna. Since the TDR is located on the small hill, while most of the reflections, used for soil moisture determination are coming from the lower areas around the station, the measured soil moisture values by the two techniques do not represent the same soil conditions. Thus changes in the rate of infiltration of the water in the soil can be expected, especially since the reflections to the East are in the lowest point of the field (3 meters lower than the top of the hill), while the TDR sensors are at the highest local point. Nevertheless, the dynamics of the soil moisture is much more dependent on the atmospheric conditions, rather than on the positioning of the footprints of the measurements. The higher-positioned sensors indeed show faster water content depletion, than the lower areas around the station, as it can be expected.

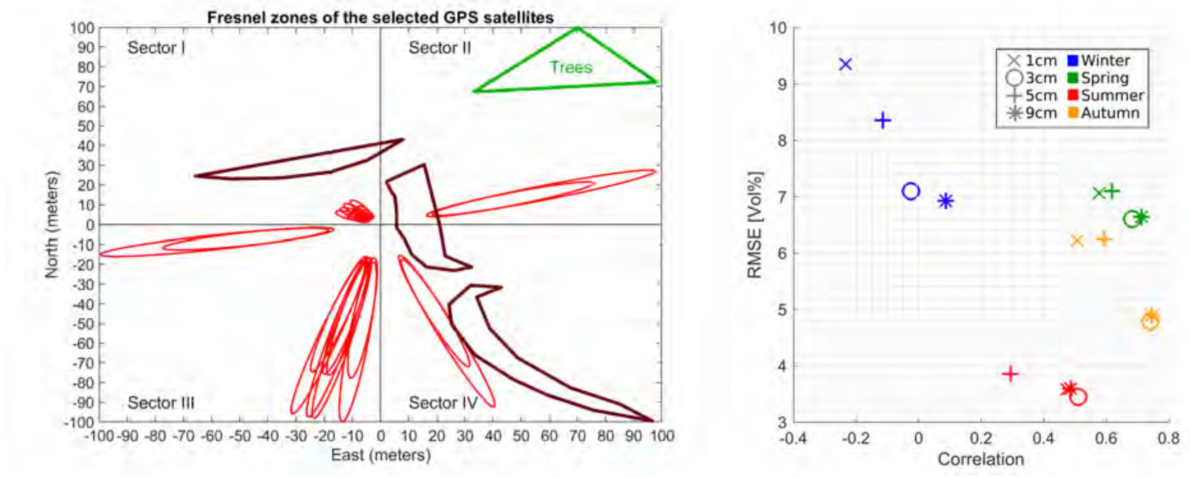

Figure 5.21: Fresnel zones of reflections, observed at GNSS station Fürstensee and seasonal comparison of correlation and RMSE. On the left figure the brown patches indicate areas with soil erosion, where soil moisture sensible reflections are impossible. The selected reflections in Sector II are closest to the TDR sensors, while in all other sectors the soil moisture retrievals come from lower ground. On the right figure seasons are defined as DJF for winter, MAM for spring, JJA for summer and SON for autumn.

5.3.6 Monitoring soil moisture in station Fürstensee

A gravimetric set of measurements is carried out on March 2nd 2017. Eight samples are taken on top of the hill, six other samples are taken 2 meters apart in a straight line away from the GNSS site in southern direction and four another measurements are taken in the lowest area to the east of the hill. The results from these measurements show VWC content of $13.5 Vol\%$ for the samples close to the TDR sondes, and $19.2 Vol\%$ in the lowest area to the East. The measurements, taken in southern direction show $16.2 Vol\%$ on average, with increasing values further away from the GNSS site. The average VWC from all measurements amounts to $15.7 Vol\%$. On the same day the average values from GNSS-R show $24.5 Vol\%$, while from TDR - $11.1 Vol\%$.

The correlation between the installed TDR and GNSS-R derived soil moisture is much lower, than in the case of station Marquardt, amounting to 0.65 for the whole period between 2015 and 2018. This can be explained not only by the differences between the two methods, as presented in station Marquardt, but also by the difference in the terrain, as explained in section 5.3.5. The RMSE between the two measurements are also higher ($5.9 Vol\%$), than in station Marquardt($4.9 Vol\%$).

Since the end of 2017, the TDR sensors at Fürstensee show significant deterioration in their performance. During the summer of 2018 (as shown on figure 5.22, bottom), the response of the TDR sondes is sporadic and inconsistent with the precipitation events recorded in the area. This behaviour is unlike the GNSS station, where the consistency in soil moisture retrievals is maintained. The mean yearly values of VWC for 2018 drop by $2 Vol\%$ compared to 2017. For this period the GNSS-R data can be used as reference

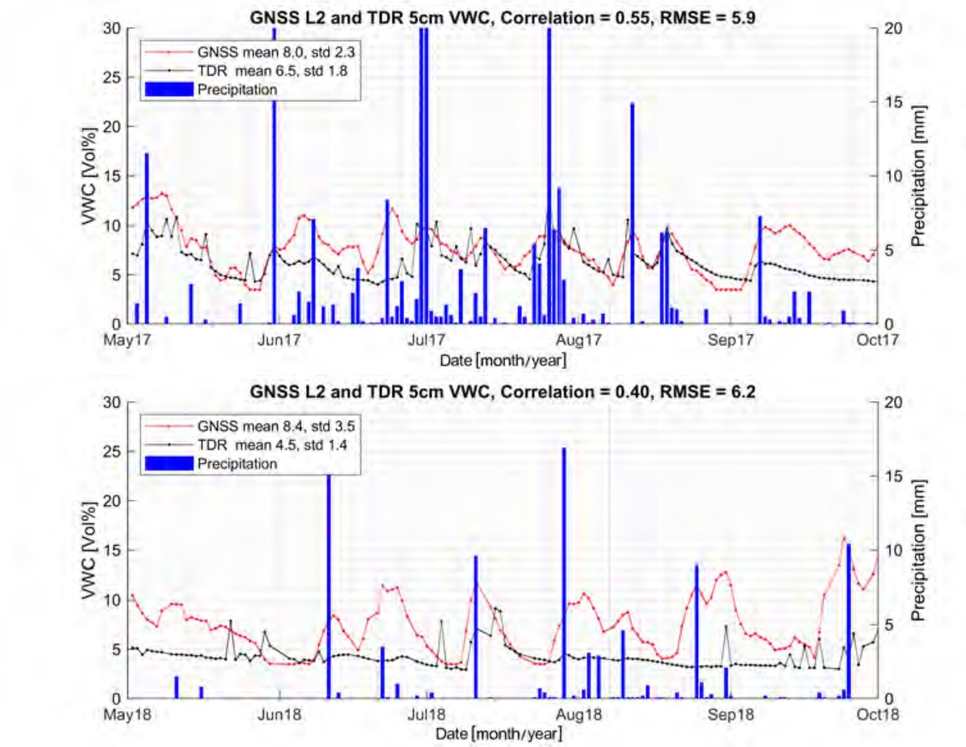

Figure 5.22: Soil moisture comparisons between GNSS and TDR at station Fürstensee for the summer of 2017 (top) and 2018 (bottom).

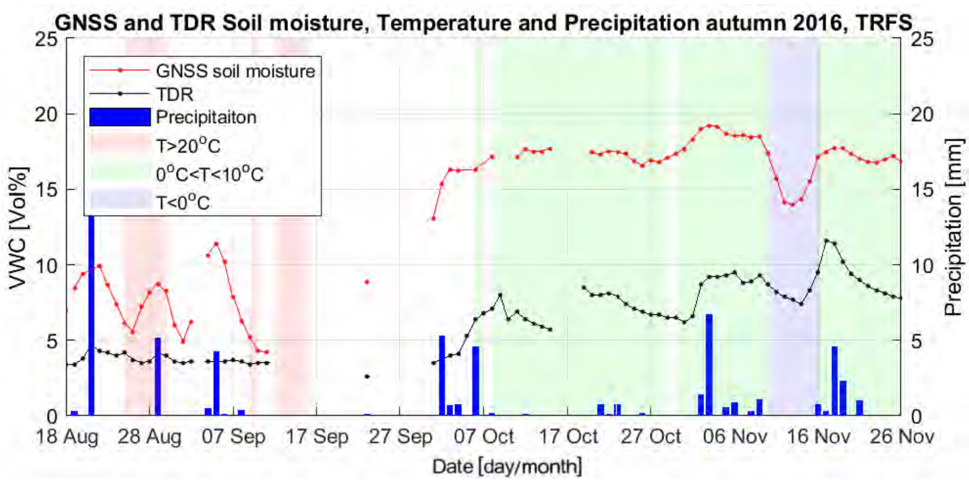

Figure 5.23: Soil moisture at station Fürstensee, autumn 2016. The increase in soil moisture in the autumn coincides with the coming of the lower temperatures in the area. The lower temperatures are associated with much lower evapotranspiration, meaning that soil moisture is not depleting to residual values until spring in 2017. GNSS-R soil moisture also responds to the temperatures below 0^oC, leading to soil freezing.

for soil moisture studies in this station.

During all precipitation events, the GNSS derived soil moisture consistently shows its dependence on precipitation. An interesting dynamics can be observed during the autumn of 2016 (seen on figure 5.23). With the arrival of the colder air masses over Germany in September, the air temperatures dropped below 10^{o}C. After the strong precipitation events, associated with the cold front which brought the lower temperatures, the evaporation potential dropped significantly, thus leaving the soil with higher amounts of water. This observation can not be obtained from the TDR sensors, because, as stated previously, they are situated above the reflection footprints and are subject to different infiltration conditions. Furthermore, with the lowering of temperatures below 0^{o}C, the water in the top soil freezes, decreasing the VWC. These observations show the importance not only of the precipitation events on the soil moisture, but of the air temperature as well.

The GNSS-R experiments and monitoring in Marquardt and Fürstensee showed that the environment around the GNSS stations is crucial for the analysis of soil moisture. The knowledge and experience derived from these investigations is to be applied to a larger network of GNSS stations.

5.4 Soil moisture monitoring with the IGS network

The International GNSS Service (IGS) is a collaboration of GNSS processing centers and the national geodetic and cartography agencies, which provides globally available high-precision data products for the GNSS orbits and clocks operationally and free of charge `https://www.igs.org/products` (*Johnston et al.*, 2017). In order to enable such monitoring and to provide the best estimates of satellite orbits and clocks, the IGS consolidates ground-based GNSS stations. As of February 2019, 506 GNSS sites are operated within the network of IGS stations (shown in figure 5.24). The oldest established stations in the IGS network date back to the end of the 1980's and stations are constantly being added to the network. Since the primary goal of this network is to establish the highest possible quality of positioning and navigation products, they have to be mounted on very stable platforms, which do not move in respect to the bedrock. Thus most of them are in seismically stable regions, mounted on buildings or on deep embedded concrete pillars. Reflectometry is not envisaged as a topic of interest during station installation, so only a few of them are located in interesting for GNSS-R environments. The screening of all these stations shows, that more than 80% of them are installed on buildings or in areas, where clear signal reflections from flat soil covered surfaces are impossible.

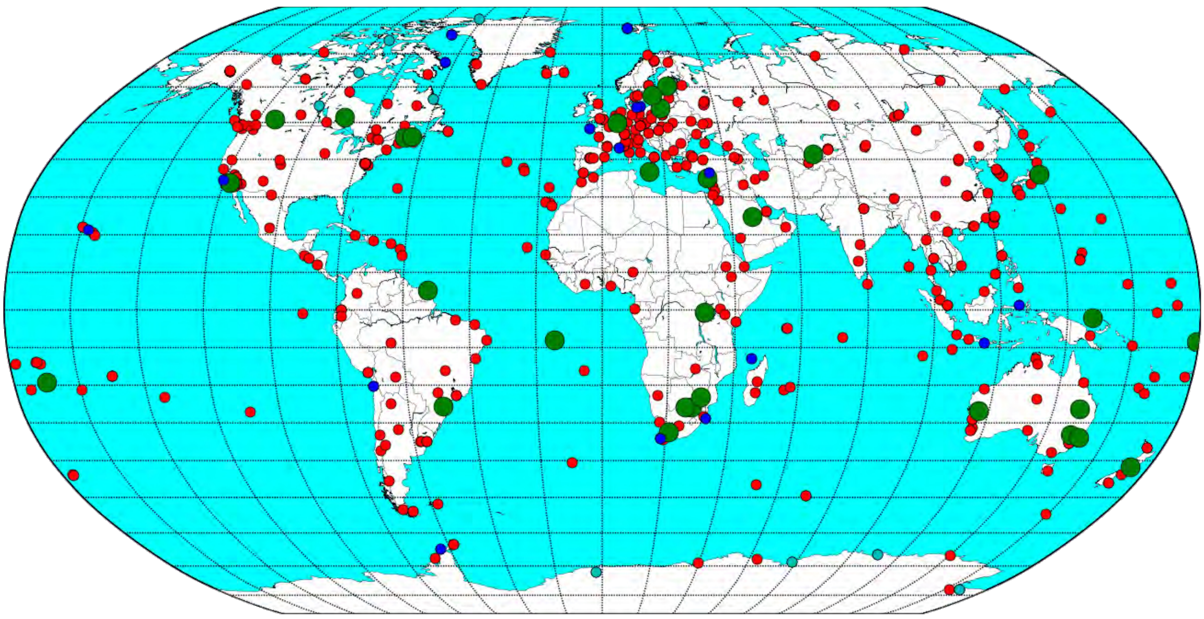

Figure 5.24: Map of all 506 IGS stations. Red markers indicate station, where no useful reflections from soils or water bodies are present, green indicate the stations, where soil moisture has already been retrieved, blue indicate stations with reflections from water bodies and cyan (3 stations in Antarctica) indicate stations, showing potential for snow studies. The stations in blue and cyan, although assessed during the GNSS stations screening, are not investigated in this work.

In order to estimate the possibility for soil moisture retrievals from each IGS station a multi-step analysis of the station surrounding is performed. These steps are:

- Screening of the log file. The log files of the IGS stations include information about the station fundament, if the station is installed on a roof or on the ground. Roof stations at this step are still not completely disregarded, because if they are mounted on the edge of the building might provide meaningful reflections.

- Reviewing the station pages on the IGS web site (*http://www.igs.org/*). Many of the IGS station's managing data centers provide pictures from the GNSS antenna and its surroundings. This is a most useful information source, but still many data centers do not provide such information.

- Observing the station on Google Maps (*https://maps.google.com/*) & Google Street View (*https://www.google.com/streetview/*). These sources provide the opportunity to visually observe most of the IGS stations (figure 5.30 is taken from Google Street View) and estimate the possibility for reflections from the ground surface.

- Processing the data and looking at reflections individually. Even if a station has passed all previous steps and checks all of them, the data might still not be available, or the reflections might come from rough terrain, which would compromise the resulted estimates of height, amplitude and phase.

Most stations in the IGS network are dropped out in steps 1 or 2, because they are situated either on roofs without sight of reflections from soil. The other reason to disregard stations on these steps is that the stations, being located on ground, are surrounded by obstacles (trees, buildings), or are situated on terrain with large alterations (hills, ditches, etc.). 110 stations passed the first 3 steps and are selected for final analysis. In the final selection process 2/3 of these stations are deemed not capable of providing soil moisture data. The final check for each station is the comparison of the phase changes with superimposed precipitation data. Thus 30 stations are selected for soil moisture analysis. Of these 30 stations 28 are described in this work with the 2 remaining being described in other independent studies. 5 of these 30 stations are IGS core stations.

It is to be noted that many of the selected stations have gaps in their datasets. These gaps are caused by RINEX version changes, or receiver/antenna changes at the stations. Still, these stations are included in the derivation processings, since the reflected signals indicate soil moisture dependency. If more complete datasets from these stations are available, further analysis can be done to describe the conditions in their regions. Until then, the data from them is recorded for further investigations.

The stations, processed in this work, are listed in figure 5.25. Their location varies from the tropical stations in the Pacific ocean, such as the once on the islands of Tuvalu and Nuie, to the cold continental climate of Canada and Northern Europe. The stations are not homogeneously distributed around the Globe, since the stations in Europe, China, Japan and North America are predominantly installed on roofs. And although the soil moisture

Stations	Number
Total number	506
Not suitable	447
Soil moisture reflections	30
Snow reflections only	10
Sea / lake reflections	19

Table 5.3: Statistics about the capabilities of the IGS network to provide data, suitable for GNSS retrievals of soil moisture, snow height and sea altimetry.

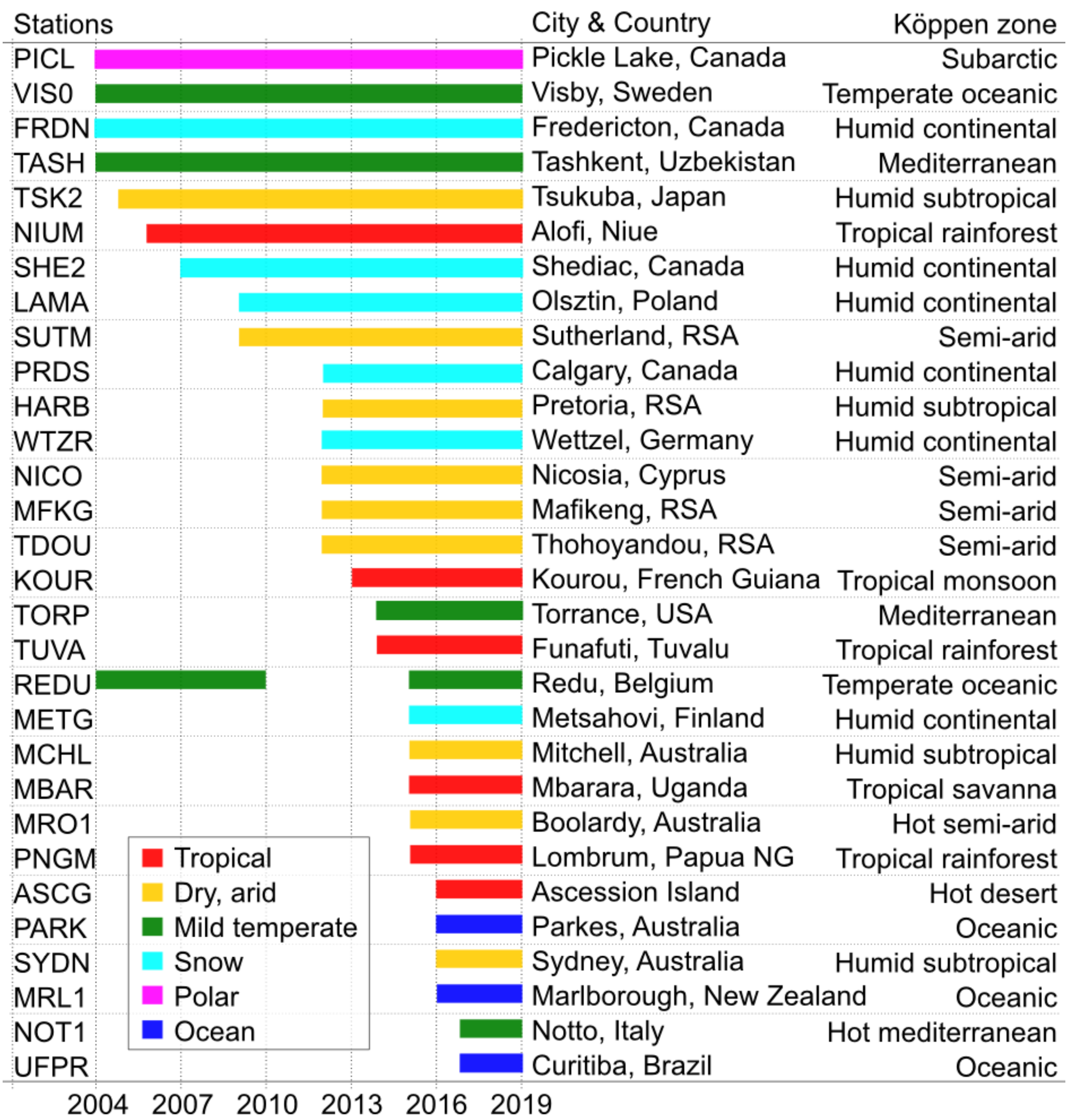

Figure 5.25: List of IGS stations for soil moisture retrieval, analysed in this work, ordered by longest datasets.

measurements on islands in the world ocean have questionable use for agriculture, or meteorology, they are a solid demonstration of the capabilities of the GNSS Reflectometry method.

As a result of this work set of recommendations, presented in section 5.6 is made to the IGS community on how to improve the information inside the station logs. The IGS station log guide is the most used GNSS station log guide and can improve the worldwide knowledge about GNSS stations in global and regional networks.

Short description of the observed soil moisture dynamics from some of the GNSS stations follows in the next sub-chapters. The description of the remaining GNSS stations can be found in Appendix D.

5.4.1 Visby, Sweden

Station Visby is located on the Gotland island in the Baltic sea. It is situated in a region, which is influenced by the Atlantic cyclones, coming from Iceland and the Siberian anticyclones. The position of the station is south of the Arctic circle. This region of Europe is characterised by relatively mild winters with average daily temperatures around 0^oC, cool summers and relatively low precipitation, around 500 $mm/year$. The land surface in winter is seldom covered with snow. The summer period is characterised by the long days with high evaporation potential, while the spring is the season with lowest amount of precipitation. The climate in the station can be described as mild oceanic with continental precipitation pattern.

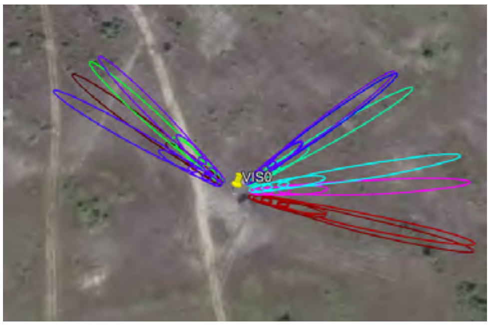

Figure 5.26: IGS station Visby - Fresnel zones.[3]

	SMC_1	SMC_2	SMC_3	SMC_4	SMC_5
SYNOP	0.37	1.13	0.59	0.82	0.04
ERA5	0.98	1.05	0.55	0.16	0.13

Table 5.4: Soil moisture coefficients for station Visby, according to definitions in chapter 5.2. The first row contains data comparison to SYNOP precipitation and the second to ERA5.

The analysis of the VWC, derived for station Visby shows a very good agreement between the increases of VWC and rainfall events (see figures 5.27 5.28). This tendency is confirmed also with the SMC's, presented in table 5.4. The maximum of VWC is achieved in the winter period. The dataset of soil moisture retrievals covers the time period since 2004. Since then the GPS constellation has been updated with newer satellites, capable of L2C signals, as well as L5. The satellite selection is PRN-based, not SRN and has

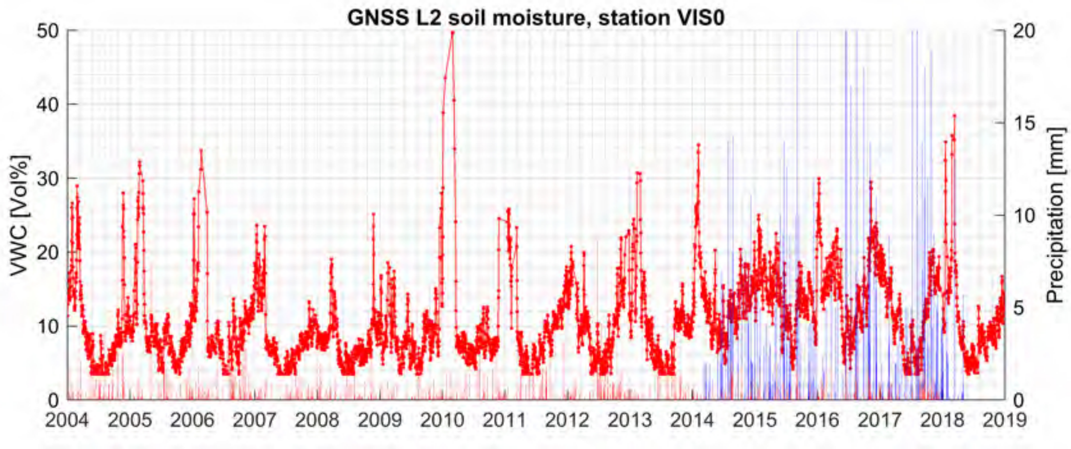

Figure 5.27: Soil moisture retrievals for 2004-2019 from IGS station Visby. The yearly cycle of the data is clearly visible with maximums in soil moisture in winter and minimums during summer. Blue bars indicate observed precipitation events, while red bars indicate ERA5 precipitation.

been carried out based on reflections from 2016. Thus the reflections before 2010 are less relevant, then the observations after 2010. The analysis does not take into account the change of the satellites in the same PRN, as well as the transition from L2P into L2C. All of the selected satellites in 2016 broadcast L2C signals.

Since Visby is situated on Gotland island, the global reanalysis model ERA-Interim does not provide soil moisture estimations for the station, but ERA5, the latest rerun of the ECMWF reprocessing campaigns does provide soil moisture estimations. Additionally, the observed with GPS reflections VWC can be compared with the soil moisture model, developed for this thesis and described in chapter 6.

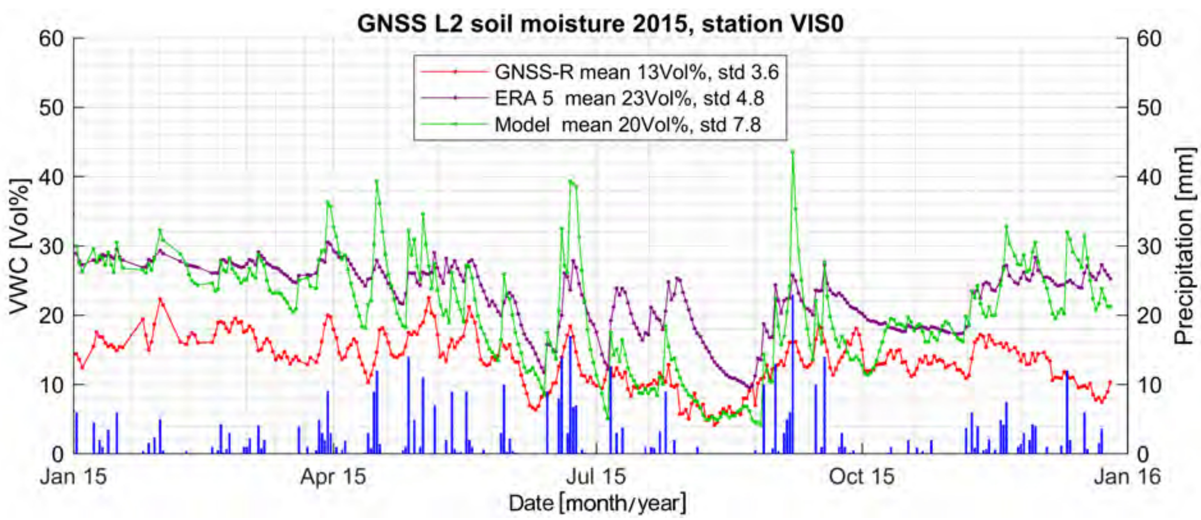

Figure 5.28: Soil moisture retrievals for 2015 from IGS station Visby. Precipitation in blue comes from SYNOP observations in nearby meteorological station.

ERA5 overestimates the summer soil moisture in the station (see figure 5.28), but still provides enough evidence for the soil moisture dynamics. The inconsistency between ERA5 and GNSS-R observations is reoccurring throughout this work. In general the correlation between ERA5 and GNSS-R is high at 0.77.

When comparing the precipitation records from ERA-Interim with the measurements at station Visby (see figure 5.29, the difference between the two datasets is clearly visible. The re-analysis dataset underestimates the amount of precipitation at the station 5-7 times. The soil moisture in the beginning of the year is clearly larger, than the precipitation, but in the second half of the year, precipitation accumulation is higher than the cumulative soil moisture dataset. This underestimation in ERA-Interim is not carried over in the ERA5 dataset, where the precipitation is only around 60-70% of the measurements in the meteorological network.

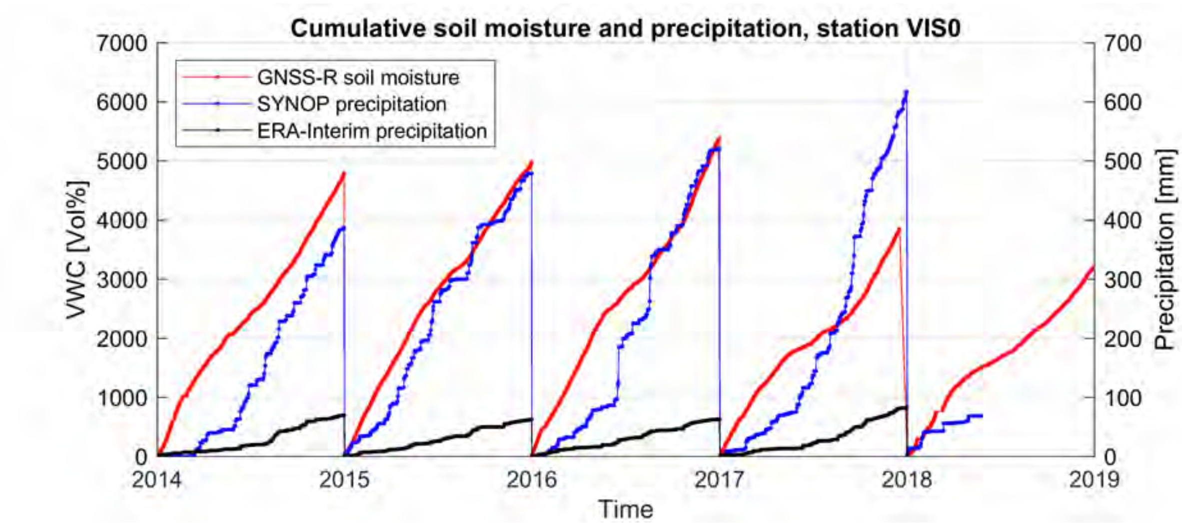

Figure 5.29: Cumulative soil moisture and precipitation for 2014-2019 from IGS station Visby. The yearly cycle of the data is clearly visible with maximums in soil moisture in winter and minimums during summer.

Another interesting pattern, which can be observed is the warm and humid 2017, when despite the large amount of precipitation, soil moisture during the summer period is very low, leading to lower than previous years cumulative soil moisture. The year 2018 is warmer than 2017 with heat waves occurring over Northern Europe, leading to even lower values of cumulative soil moisture.

5.4.2 Fredericton, Canada

Fredericton is a town, situated in the South-East corner of Canada, in the state New Brunswick, on Saint John river, about 100km west from the Bay of Fundy in the Atlantic ocean. This region of Canada is classified as Warm Summer Continental Climate according to Köppen classification (see appendix C). The mean monthly temperatures do not exceed 22°C in the summer, while the lowest monthly temperatures in winter reach below -3°C. The average precipitation for the region is more than 1000 $mm/year$ with highest precipitation amounts in October and the driest month is April. The climate in Fredericton is also characterised by snow precipitation during wither months with the snow cover reaching up to 60 cm in height. The analysis of the snow cover is presented in chapter 7.

Figure 5.30: IGS station Fredericton picture of surroundings. Image from *https://www.google.com/streetview/*.

The GNSS station FRDN has been installed in 2003 at an open field, covered with grass in one of the parks of the city. The antenna is mounted on a 1.5m concrete fundament (see fig 5.30) with the closes trees located more than 30 meters away from the station. The reflections, used for the soil moisture and snow height studies are coming from several different patches, mainly from south, east and north-west directions (seen on figure 5.31). The western direction is blocked by trees and slight alterations in the ground topography.

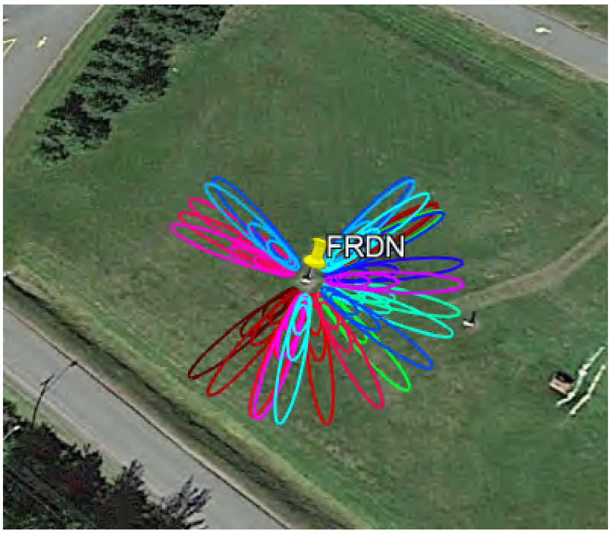

Figure 5.31: IGS station Fredericton - Fresnel zones.[5]

The VWC behaviour in the station follows the previously discussed pattern of increasing from precipitation and decreasing during dry days. 76% of all VWC increase events are related to precipitation (all SMC coefficients are presented in table 5.5). The remaining increase events can be attributed to snow melting. The correlation between precipitation amount and VWC increase is 0.11, which is positive, but insignificant (see figure 5.32 left). The maximum of soil moisture has been measured during early spring period. The limitations of GNSS reflectometry

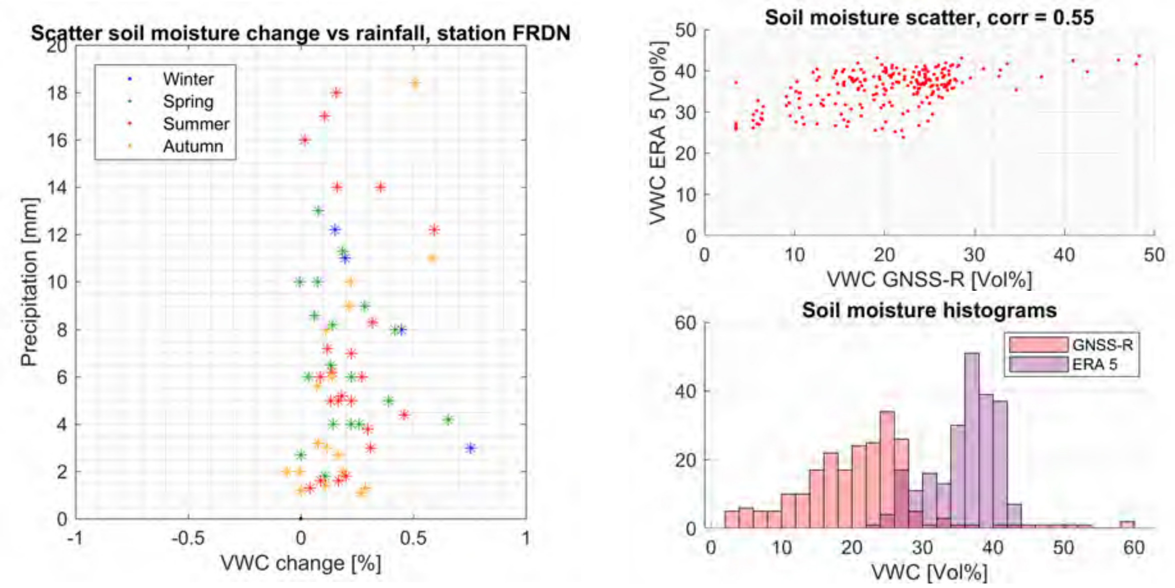

Figure 5.32: Soil moisture change, triggered by precipitation for IGS station Fredericton on the left. The data shows lack of correlation between the precipitation amount and the VWC relative change. Soil moisture scatter plot between ERA5 and GNSS-R in the top right. Soil moisture histogram from GNSS-R and ERA5 on the bottom right. The GNSS-R VWC observations are significantly different from ERA5 both in terms of mean and median, as well as range of values.

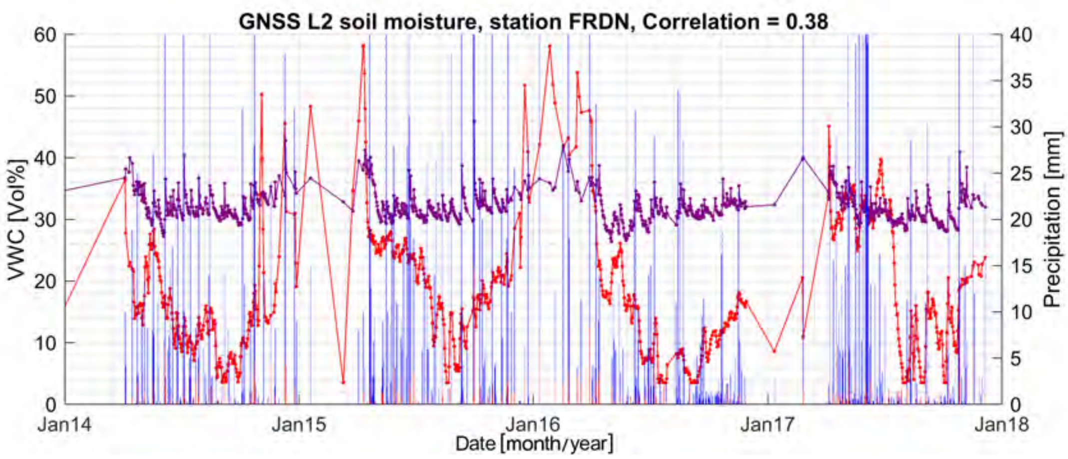

Figure 5.33: Soil moisture retrievals for 2014-2018 from IGS station Fredericton. The red line indicates GNSS-R derived soil moisture, while the purple - soil moisture from ERA5. The breaks in the winter season of soil moisture dataset indicate periods with snow cover (discussed in section 7.2.6). Blue bars indicate observed precipitation, while red bars show precipitation from ERA5.

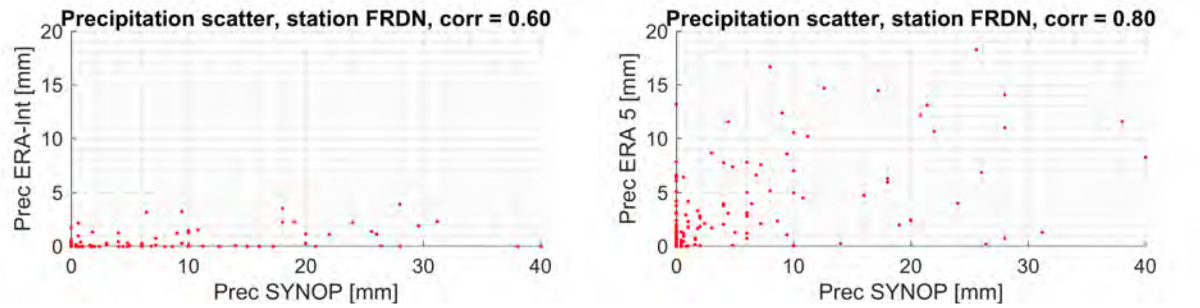

Figure 5.34: Precipitation measurements in Fredericton, compared to ERA-Interim (left) and ERA5 (right) precipitation estimates.

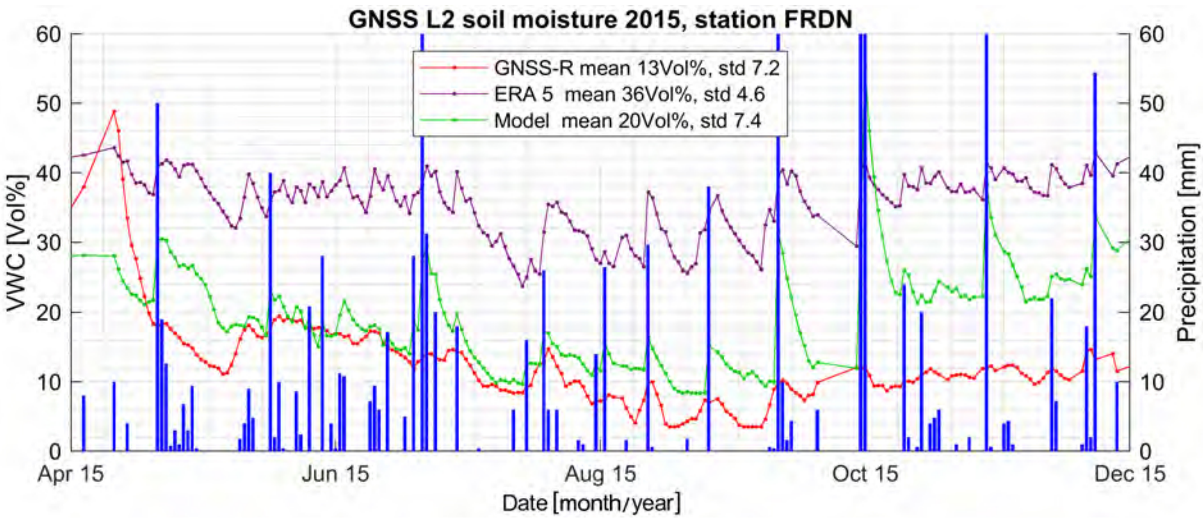

Figure 5.35: Soil moisture retrievals for 2015 from IGS station Fredericton. Precipitation in blue comes from SYNOP observations in nearby meteorological station. The soil moisture line in purple is from ERA5.

do not allow soil moisture measurements in the presence of snow (see gaps in fig 5.33). The snow melting period is clearly visible in the soil moisture data with the highest values measured after the snow has melted (see figure 5.36). GNSS Reflectometry snow measurements from station Fredericton are discussed further in chapter 7.2.

ERA-Interim and ERA5 misrepresent soil moisture significantly for station Fredericton. The annual cycle of soil moisture can not be observed in the data. Moreover the values of soil moisture are too high during summer, when the evaporation from ground is highest and VWC is lowest. Both ERA-Interim and ERA5 clearly overestimate soil moisture with its residual value above 20Vol% (seen on figure 5.32 right, bottom). This behaviour is systematic for almost all analysed stations.

These reanalyses do not provide accurate precipitation information as well (see figure 5.34). The ERA-Interim data shows significantly lower precipitation values, than meteorological station measurements. ERA5 performs better in representing the precipitation events. This behaviour of the ERA-Interim and ERA5 precipitation can be observed in all other IGS stations, thus the more detailed explanation of results for each station are

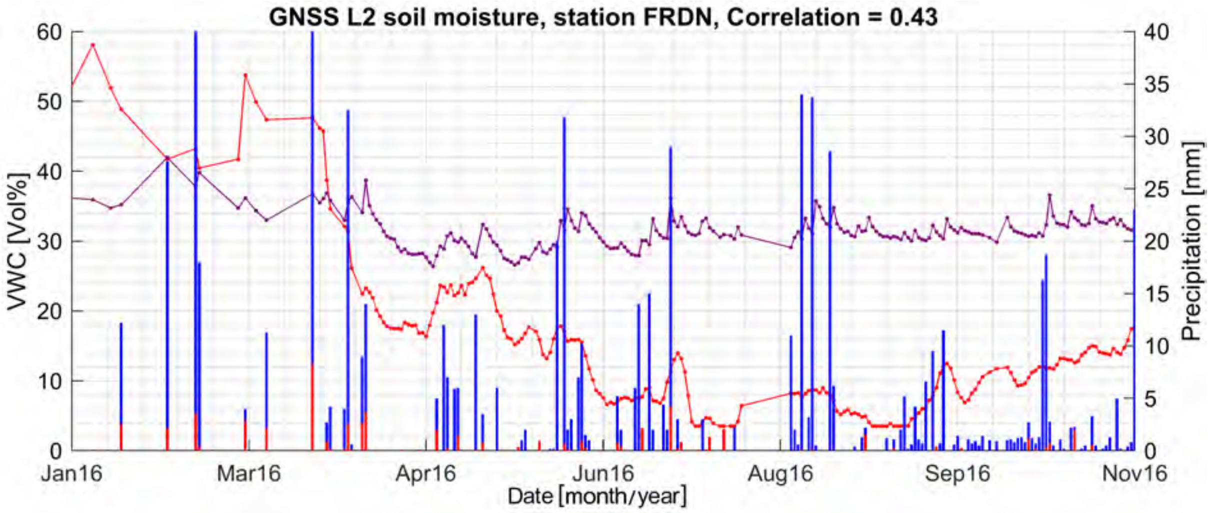

Figure 5.36: Soil moisture retrievals for 2016 from IGS station Fredericton. Precipitation in blue comes from SYNOP observations in nearby meteorological station, while precipitation in red is interpolated from ERA5. The soil moisture line in purple is from ERA5.

not mentioned.

	SMC_1	SMC_2	SMC_3	SMC_4	SMC_5
SYNOP	0.39	0.97	0.59	0.79	0.02
ERA5	0.99	1.04	0.57	0.22	0.04

Table 5.5: Soil moisture coefficients for station Fredericton, according to definitions in chapter 5.2. The first row contains data comparison to SYNOP precipitation and the second to ERA5.

Despite the inaccuracies in the precipitation estimates, both ERA5 and ERA-Interim respond to precipitation events. Curiously in some cases the reanalyses do not precipitate, but still show increase in soil moisture and this is in situations when precipitation events are occurring (seen in figures 5.35,5.36). This is most likely caused by the assimilation of SMAP and SMOS data through the LDAS, as discussed in section 2.4.3. Nevertheless the correlation between the model and the measurements is adequately representing the soil moisture dynamics.

5.4.3 Mbarara, Uganda

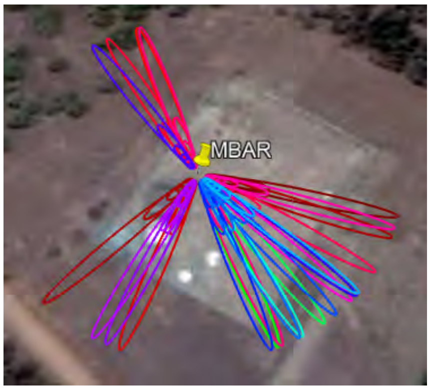

Figure 5.37: IGS station Mbarara - Fresnel zones. [7]

The GNSS station MBAR, near Mbarara, Uganda, is established in 2001 as a core IGS station. The station is fully surrounded by grass areas with the antenna situated at a 1.5m height above ground. Uganda is located in a tropical savannah climate, according to the Köppen climate classification (Aw , see appendix C)). This is a dryer climate from the tropical group. The seasonality in these climates is not driven by the difference in insolation throughout the year, but in the precipitation cycles. The climate in Mbarara is characterised by two precipitation maximums - during the boreal spring and autumn and dryer periods in January-February and June-July. The annual precipitation amounts to 1000 *mm/year* with average temperatures of 20°C throughout the year. The soil moisture dataset also shows the two maximums, observed in the precipitation records (see figure 5.38).

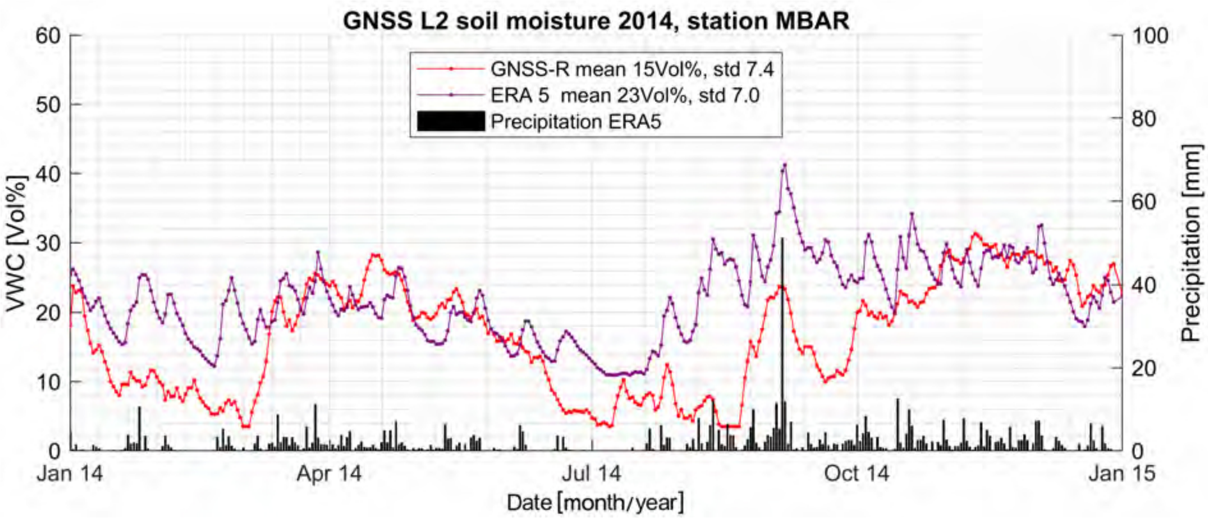

Figure 5.38: Soil moisture retrievals for 2014 from IGS station Mbarara. Precipitation is interpolated from ERA5. The soil moisture line in purple is from ERA5.

According to the criteria, presented in chapter 5.2, the performance of the soil moisture retrievals are close to the expectations. The coefficients for this station (as seen in table 5.6 are retrieved using ERA5 precipitation, instead of SYNOP, since SYNOP precipitation data is not available for this station. The closest WMO site does not provide precipitation records.

SNR data is available for station MBAR since 2004, providing a long dataset of soil moisture (seen on figure 5.39), obstructed by several periods, when data from the station is

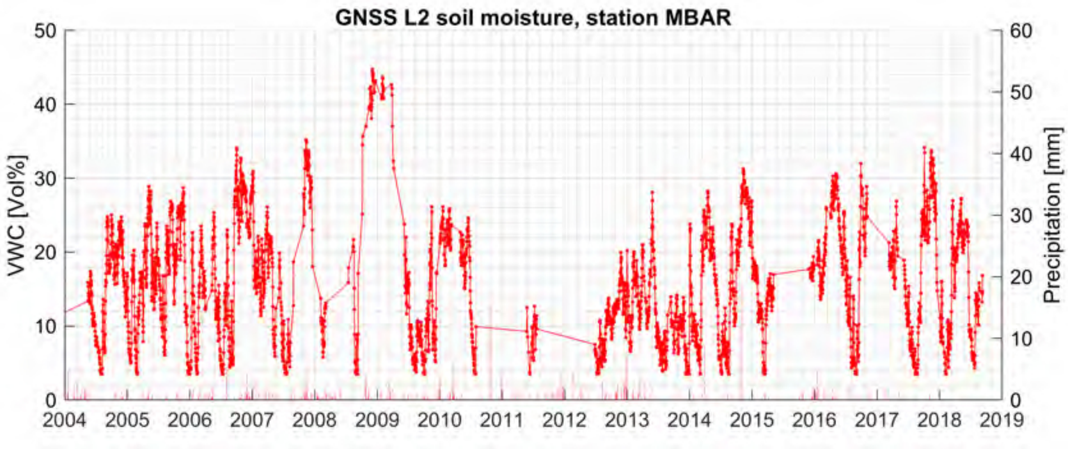

Figure 5.39: GNSS soil moisture for 2004-2019 from IGS station Mbarara. The clear seasonality is visible throughout the dataset.

	SMC_1	SMC_2	SMC_3	SMC_4	SMC_5
ERA5	0.99	0.76	0.52	0.10	0.11

Table 5.6: Soil moisture coefficients for station Mbarara, according to definitions in chapter 5.2. Since no SYNOP data for precipitation is available for station Mbarara, the coefficients are derived from ERA5.

not available. This soil moisture record is compliant with the expected seasonal variations, typical for tropical savannah climates.

5.4.4 Tsukuba, Japan

GNSS station TSK2 is situated in the town of Tsukuba, Ibaraki prefecture, Japan. Tsukuba is situated to the North the Greater Tokyo area. This GNSS site is established in 2003 with the first GNSS sensor, TSKB, founded in 1993. TSKB is placed on a pole 1m above the ground, but is not suitable for soil moisture studies due to obstructing buildings. TSK2 is mounted on a 5m pole, overlooking a large grass pitch and thus enabling soil moisture retrievals (as seen on figure 5.40). The station provides SNR data since its establishment, making it one of the longest GNSS Reflectometry soil moisture records (as seen on figure 5.43).

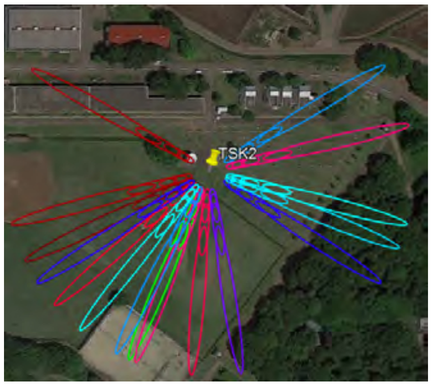

Figure 5.40: IGS station Tsukuba - Fresnel zones. [9]

According to the Köppen climate classification (see appendix C) Tsukuba is situated in a humid subtropical region with winter temperatures above 0°C and summer temperatures exceeding 22°C. The precipitation pattern throughout the year is seasonal with maximum in autumns and minimum in late winter. The average precipitation amount is above

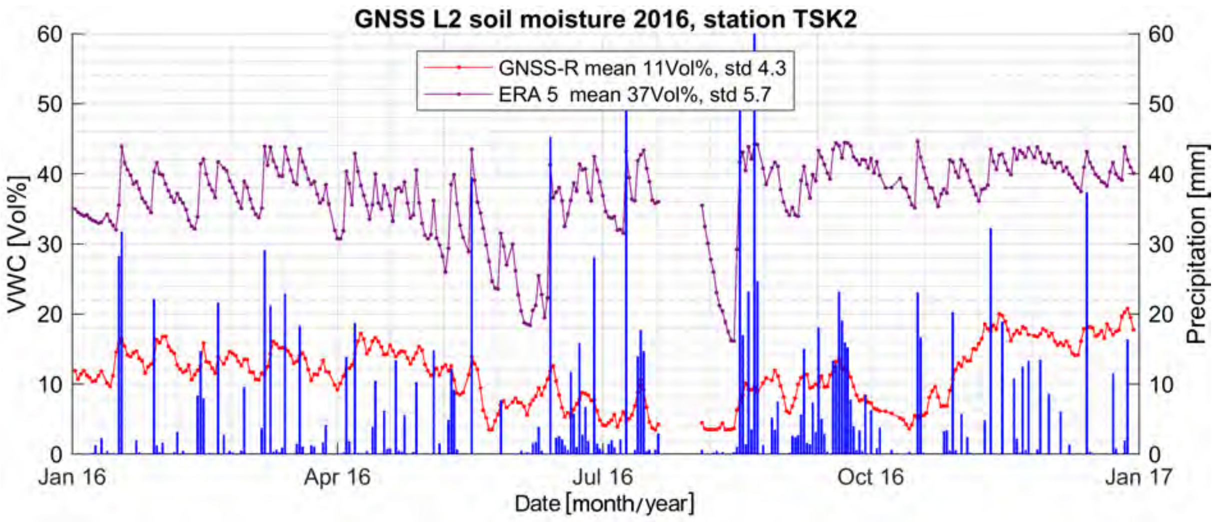

Figure 5.41: Soil moisture retrievals for 2016 from IGS station Tsukuba. Precipitation is interpolated from ERA5. The soil moisture line in purple is from ERA5.

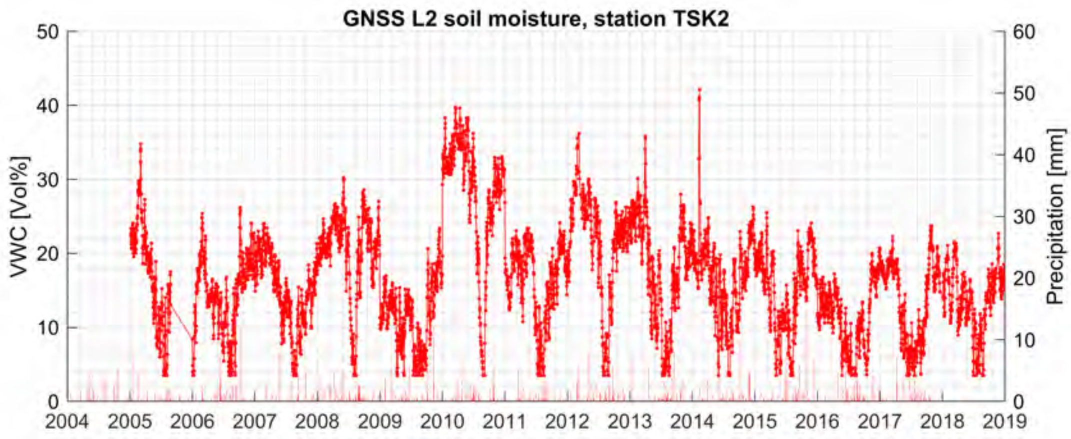

Figure 5.43: GNSS soil moisture for 2004-2019 from IGS station Tsukuba. The clear seasonality is visible trroughout the dataset.

1500mm/year.

Since the precipitation amounts are so large during the year, the calibration of the soil moisture retrievals, performed with the GNSS dataset is not adequate. This can be observed not only in station Tsukuba, but also throughout most of the subtropical stations with precipitation amounts above 1000 $mm/year$. The reason for this is that although the area has seasonality in the precipitation pattern, the soil moisture does not reach its minimum possible value. Having an accurate minimum value is necessary for proper calibration of the GNSS-R tech-

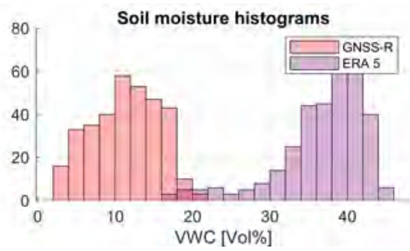

Figure 5.42: Soil moisture histogram from GNSS-R and ERA5 for station Tsukuba.

nique, since the retrieval is not of absolute values, but of relative changes in the phase behaviour of the interference patterns, thus soil moisture. This discrepancy between the GNSS and ERA5 can be seen on figure 5.42.

	SMC_1	SMC_2	SMC_3	SMC_4	SMC_5
SYNOP	0.76	1.23	0.72	0.71	0.18
ERA5	0.99	1.37	0.56	0.18	0.16

Table 5.7: Soil moisture coefficients for station Tsukuba, according to definitions in chapter 5.2. The first row contains data comparison to SYNOP precipitation and the second to ERA5.

5.4.5 Marlborough, New Zealand

The GNSS station MRL1 is located in the Marlborough region on the South island of New Zealand. The GNSS station is established relatively recently, in 2015 and is providing SNR data since. The antenna is mounted on a 4.5m pole in the middle of a open lawn in the premises of a VLBI station. The station surrounding is not obstructed by buildings in most of its northern azimuths providing a lot of reflections, sensible to soil moisture, seen on figure 5.44.

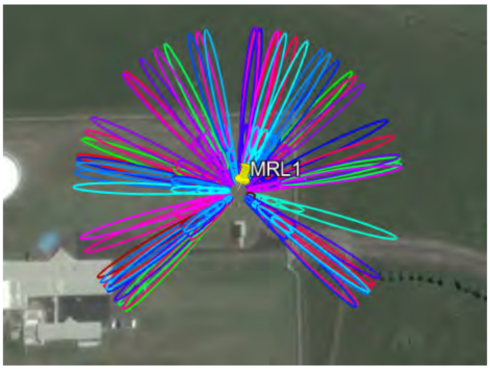

Figure 5.44: IGS station Marlborough - Fresnel zones. [11]

According to the Köppen climate classification the area is situated in Oceanic climate zone (see appendix C). This type of climate is characterised with temperatures above 0^oC year-round and precipitation maximum during Southern winter with annual total around 700 mm. Marlborough region is the key wine producing region in New Zealand, which indicates frequent precipitations, mild climate and absence of extreme temperatures. Since the region is located in the eastern shore of the South Island, its weather is dominated by Pacific cyclones, coming from the East and thus is regulated heavily by the temperature of the Pacific ocean. Changes in precipitation patterns are dependent on the El-Nino Southern Oscilation (ENSO).

The GNSS-R soil moisture coefficients in station MRL1 show that the station results are complying with the expected behaviour (as can be seen in table 5.8). The results in figure 5.45 show very good response of the soil moisture observations from GNSS-R to precipitation events, as modelled in ERA5. The distinct seasonality of the station can also be observed with the austral winter between July and October showing the highest soil moisture values, while the austral summer between December and April is the season

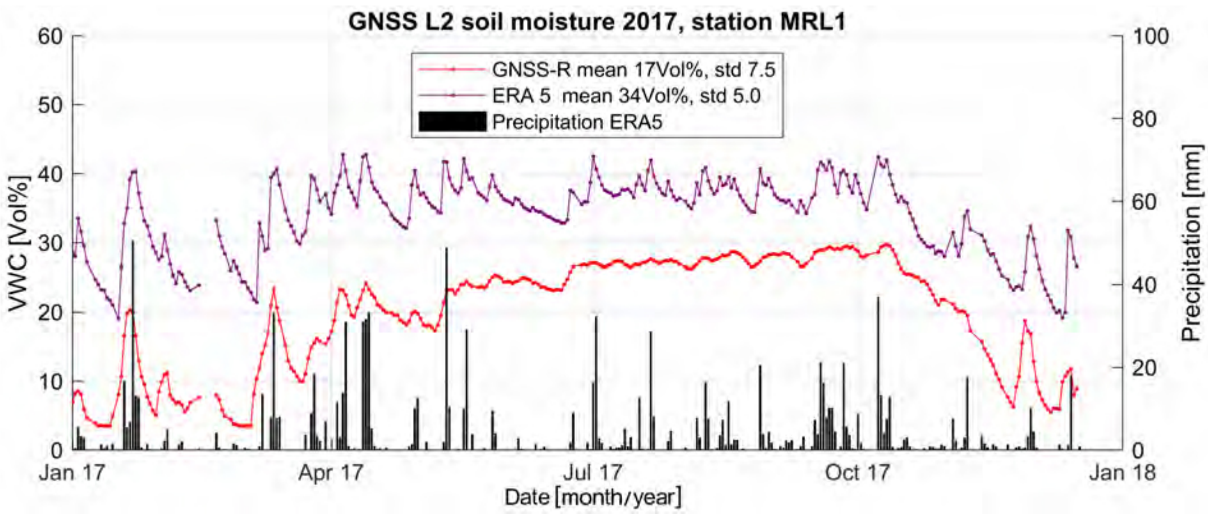

Figure 5.45: Soil moisture retrievals for 2017 from IGS station Marlborough. Precipitation is interpolated from ERA5. The soil moisture line in purple is from ERA5.

with the lowest VWC and highest amplitude, caused by the precipitation events and the higher evapotranspiration.

	SMC_1	SMC_2	SMC_3	SMC_4	SMC_5
ERA5	0.99	1.35	0.55	0.18	0.22

Table 5.8: Soil moisture coefficients for station Marlborough, according to definitions in chapter 5.2. Since no SYNOP data for precipitation is available for station Marlborough, the coefficients are derived from ERA5.

5.5 GNSS Reflectometry soil moisture error budget

The measurement technique, described in this thesis for soil moisture observation is relative and not absolute, which means, that in order to estimate the VWC in the soil, additional information, apart from the GNSS reflections, has to be supplied. The fact, that the approach is relative also means, that the accuracy and the precision of the measurements have to be estimated. Since different aspects of the data analysis contribute to the accuracy and precision in a different way, these two parameters are examined separately.

Apart from the effects, described below, which have influence on the accuracy and precision of the measurements, there are also parameters, which do not. One of these are the used GPS orbits. The whole study in this work on reflectometry has been convened using broadcast satellite orbits, instead of using final orbits. The broadcast orbit is a set of parameters, transmitted in the GNSS message from the satellite to the receiver and recorded locally. The final orbits are the same set of parameters, which are later on recalculated using a data processing software. The orbit data gives the precise position of each GPS satellite, thus enabling to determine the reflection direction and the elevation of the satellite. Although the signal strength is dependent on the elevation, the interference pattern is independent on the orbits message, and contains within itself the effect of the reflected signal. Thus the small differences between the broadcast and final orbits have no significance on the soil moisture estimation.

5.5.1 Effects influencing precision

Several experiments are carried out with data from station Marquardt. A base dataset is selected from the L2C results for 2016 from station MARQ. The data is then forcefully modified in order to estimate the sensitivity of the soil moisture derivation on different aspects of the processing procedure.

The first modification is to decrease the resolution of the signal strength data from $0.25dB - Hz$ to $1dB - Hz$. The signal strength resolution is known from literature to deteriorate the accuracy of the LSA and the Lomb-Scargle. The resulting dataset has 0.99 correlation and 1.8Vol% RMSE. The resulting response from this manipulation is negligible (seen on figure 5.47). The soil moisture dynamics is clearly visible and dependent on precipitation events.

The second modification carried out is to decrease the sampling rate of the data from 1 second to 10 and 30 seconds. This is done to estimate the significance of the sampling rate on the LSA. Theoretically, the lower amount of data points, the lower the accuracy of the LSA and the Lomb-Scargle. The difference between the initial dataset and the modified dataset is again very small - correlation 0.99 and RMSE of 1.2Vol% (seen on figure 5.47) for the 10 seconds and correlation of 0.99 and RMSE of 2.6Vol% for the 30 seconds sampling rate. The effect of changing the data sampling rate is distinguishable, but insignificant from the 1 second sampling rate dataset. This is further proved by the results, obtained in the IGS stations, where the sampling rates are 30 seconds and soil moisture can still be observed.

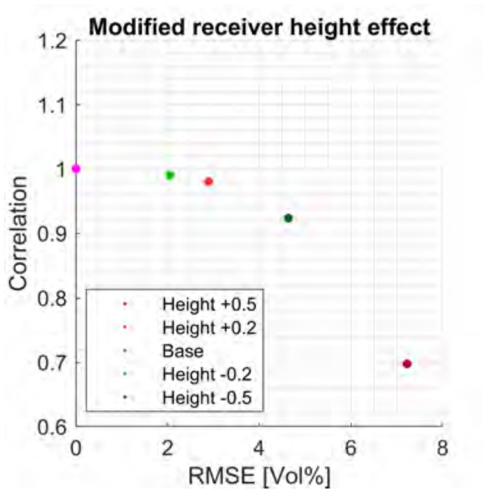

Figure 5.46: Reflector height modified correlation and RMSE.

Thirdly, the estimated reflector height of the average reflector height is both increased and decreased to observe the influence of the reflector height estimation accuracy on the final soil moisture. As discussed in the beginning of chapter 5, the reflector height is estimated for each individual satellite for each reflection. The reflector height over time

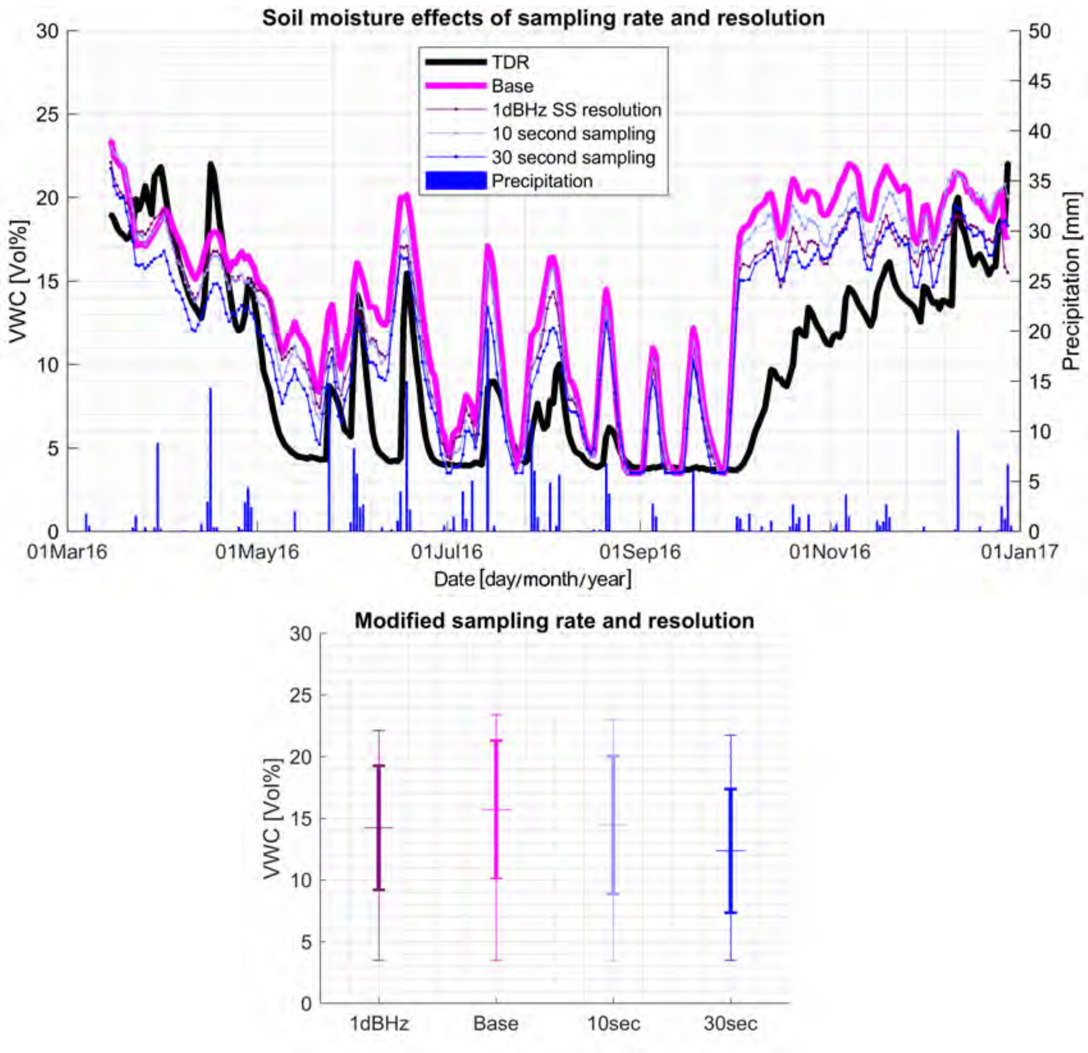

Figure 5.47: Effects of changing sampling rate and signal strength resolution on soil moisture retrievals. The Base sampling rate of 1 second is reduced to 10 seconds and the signal strength resolution is reduced from $0.25dB-Hz$ to $1dB-Hz$.

varies within 10 cm from the mean. The mean reflector height is then used to determine the phase and amplitude of the reflections. The reflector height is increased in two steps by 20cm and 50cm and decreased by the same amounts. Since the height of the pole, on which the antenna sits in Marquardt is 3 meters, the changes in the reflector height are by up to 17%. The height of the antenna is not physically changed for this experiment, only the estimated reflector height by the software.

All of the resulting datasets show clear deterioration, compared to the original results, but the soil moisture signature can still be observed in these datasets. A clear trend can be observed in the mean values and the distribution of the data in general. With the GFZ soil moisture retrieval software artificial lowering of the antenna height, the monitored soil moisture has smaller standard deviation and shows lower readings. With artificially increasing the reflector height the standard deviation, mean value and data range show

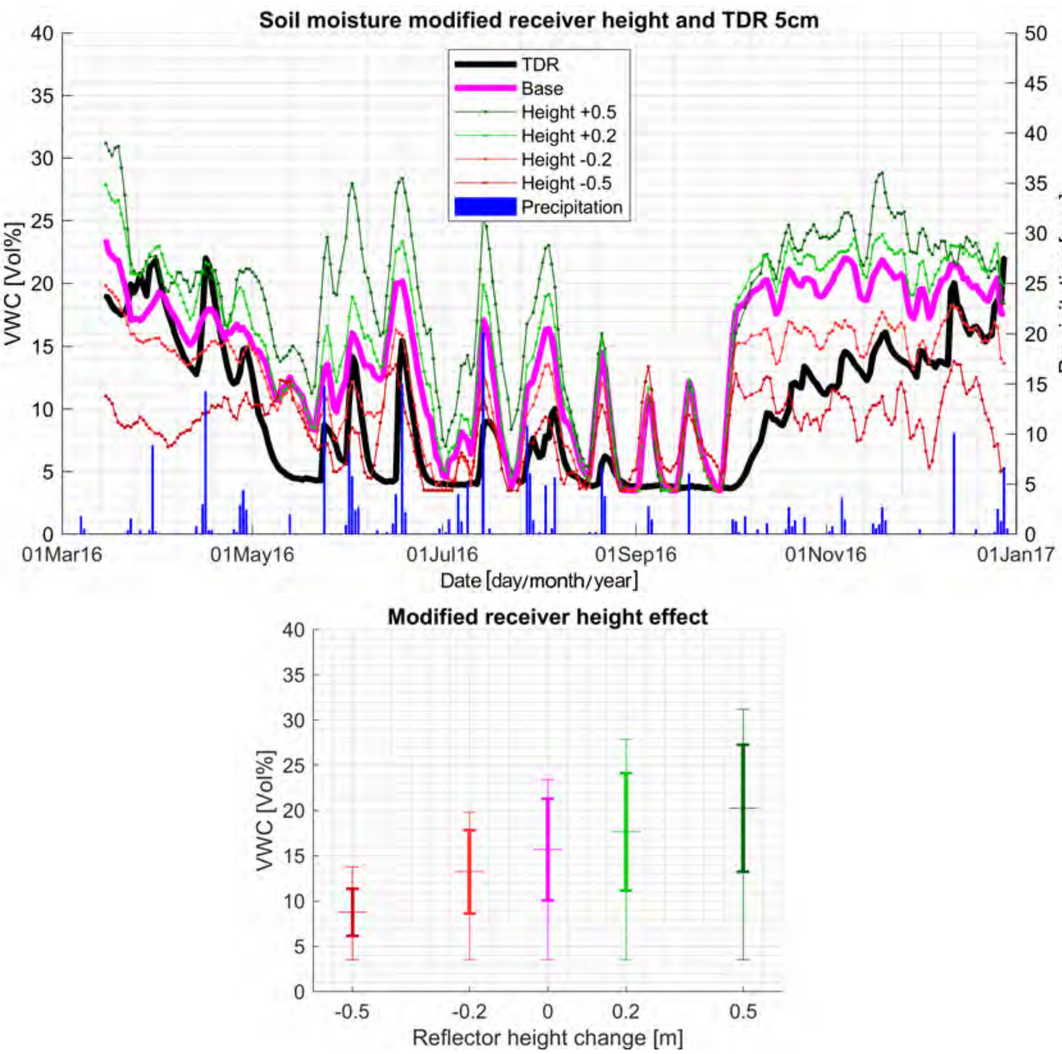

Figure 5.48: Reflector height modified value distribution. In the figure in the bottom, the thinner error bars mark the minimum and maximum values, the thicker error bars mark the standard deviation and the middle mark represents the mean value for the whole data series. These distributions describe the data, plotted on the top figure.

higher and wider range of values. This experiment shows, that if a station reflector height is miscalculated, the resulting soil moisture retrieval, although showing correct dynamics, shows inaccurate mean value and standard deviation.

Another source of biases to the soil moisture estimates is the scaling coefficient γ in equation 3.26. As discussed previously, theoretically, it should be equal to $\gamma = \frac{0.65°}{1Vol\%}$, but in practice this coefficient can vary greatly between stations, as discussed in page 43. The most likely explanation is, that γ is dependent on the soil composition. This is another effect, which is extremely hard to measure using the data sources in this thesis. The best way to examine the differences between soil types would be to install an experimental GNSS station with several different types of soils in the different sectors and examine the differences between them. Moreover soil composition can have large variability and soil samples from the IGS sites are not available for the analysis in this thesis.

5.5.2 Effects influencing accuracy

In the discussion for station Tsukuba (TSK2) in chapter 5.4, although the environment around the station is very wet, with more than 1000mm/year precipitation, the GNSS-R soil moisture estimates are surprisingly low. In fact all stations with humid climates, which do not have distinguishable rain season, but have significant amounts of precipitation throughout the year show similarly low estimates of VWC (Kourou (described in appendix D.2.11), Funafuti and Niue among others). It is reasonable to speculate, that in these stations the residual VWC is higher than the minimal possible VWC and cannot be achieved throughout the year, i.e. the soil is always wet, because it does not have time to dry out between precipitations. Since the GNSS method relies on calibrating the soil moisture estimates to the lowest possible soil moisture (c_{min} in equation 3.26), this amount has to be measured otherwise every year. Thus the VWC datasets are expected to show systematically drier conditions, than the reality. This means, that although the datasets show high correlation to ERA5, the absolute values of the estimations are systematically shifted. The errors, induced by this effect can not be estimated without supporting evidence from independent data sources.

5.6 Recommendations to IGS network sites

The highest standard of data quality and GNSS station stability is guaranteed with the IGS new site installation guidelines (`https://kb.igs.org/hc/en-us/articles/201433`). This guideline is the most detailed set of requirements for installing new GNSS stations and is followed as best practice in the GNSS community. Based on the research in this thesis several recommendations, concerning the guideline are proposed to improve the information regarding the station surroundings and sources of multipath.

Under section 2.1.7 of the guideline the "GNSS receiver shall be set to track satellites at least down to 5^o elevation" and in section 2.2.1 the "GNSS receiver should be set to track all satellites down to 0^o elevation." These low elevation angles may in some cases, like station VILL (Villanova, Spain), be obstructed by buildings and higher elevation angles mask may be necessary. Additionally under section 2.2.25 the guidelines recommend the station to be "expected to have low multipath (< 0.3 m)". The screening of the IGS network for this thesis shows, that the information regarding the obstacles in the premises of the GNSS sites is recommended to be logged into the station log files under section 2. "Site Location Information" or section 13. "More Information". Currently there are no strict rules regarding logging such information on the distance and the height of the obstacle. Such logging would not only contribute to better multipath mitigation from higher observation angles, but also provide more information if the conditions in the station are satisfactory for GNSS-R observations.

In section 1. "Site Identification of the GNSS Monument" under "Monument Description" of a IGS site log file (`ftp://igs.org/pub/station/general/sitelog_instr.txt`) the "Height of the Monument" of the site should be recorded. Many of the stations, situated on roofs mention the height above the building's roof (example: POTS, Potsdam, Germany), while others mention the height above ground (example: ISBA, Baghdad, Iraq). This duality in the logging is caused by the ambiguity of the "Height of the Monument" term. Based on the research in this thesis, it is proposed to add additional field "Height above ground", stating the vertical distance between the Earth surface and the GNSS antenna. Thus more details about the environment around the station can be obtained.

Under IGS new site installation guidelines section 2.2.8 it is stated that "providing SNR data from IGS stations is recommended, but not necessary." The observed SNR data can be used for multipath mapping around the GNSS site (*Strode and Groves*, 2016), as well as for soil moisture and snow height monitoring.

The inclusion of SNR data as compulsory RINEX messages and enhancing the station log files with more information regarding the elevation mask and obstacles around the GNSS antenna, a better understanding of the environment around the GNSS stations can be achieved.

Chapter 6

Empirical soil moisture model

This chapter describes a new approach for soil moisture modelling using atmospheric parameters. The newly developed model is then applied to available meteorological datasets and compared with TDR and GNSS-R observations of soil moisture.

6.1 Soil moisture model

Several important assumptions regarding soils have to be followed when constructing the basis of this new 1D empirical soil moisture model (1D-ESMM). The decrease in the soil moisture values can be achieved through evaporation and infiltration, which, in terns, are functions of the relative humidity, surface temperature and soil composition. The increase in the VWC is mainly dependent on precipitation and, rarely, on direct deposition due to low temperatures, or high relative humidity (simple diagram in figure 6.1). These dynamics have also inspired the soil moisture coefficients, described in chapter 5.2.

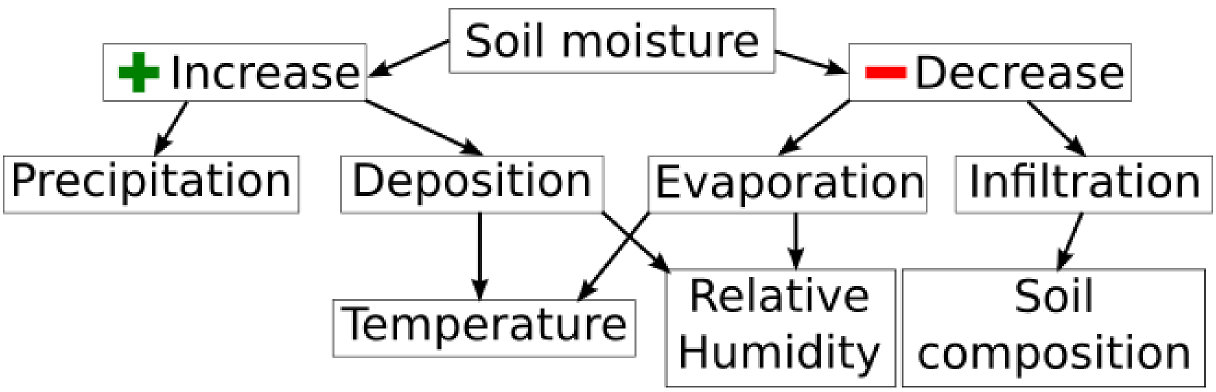

Figure 6.1: Simplified diagram of model soil dynamics.

All these factors are discussed independently with various levels of details. The general formulation of the model can be represented as follows:

$$VWC_i = \alpha(IWV, T)\mathrm{VWC}_{i-1} + \beta R + \gamma \tag{6.1}$$

where VWC_i is the value of soil moisture for the day of estimation, VWC_{i-1} marks the soil moisture from the previous day. $\alpha(IWV, T, I)$ is the evaporation and deposition parameter, dependent on water vapour (IWV) and temperature (T). It is envisaged as the main driver and balance parameter of the soil moisture model. β is a multiplier coefficient, introducing precipitation (R) into the equation. γ is a scaling coefficient, insuring positive values for soil moisture. In these investigations usually γ is set to be equal to the lowest possible amount of soil moisture in the station.

In order to construct the α parameter, several factors have to be acknowledged. These factors are the additives of the α parameter:

$$\alpha(IWV, T) = \alpha_n + \alpha_t(T_{thr} - T_{2m,C}) + \alpha_w RH(IWV) \tag{6.2}$$

The values of the arguments α_n, α_t, α_w are specific for each station and are adjusted according to the climate conditions. T_{thr} is a threshold temperature, further discussed in this chapter. Table 6.2 presents the specific arguments for each station.

The most interesting factor in equation 6.2 is the relative humidity. As discussed in chapter 3.4, the GNSS Meteorology is a well established technique of measuring the integrated water vapour column in ground-based GNSS stations. The relative humidity of the atmosphere has a direct connection to the integrated water vapour through the temperature of the atmosphere. In order to perform the transition from IWV into relative humidity, the dew point of the atmosphere has to be calculated, using *Reitan* (1963) formulation:

$$T_{d,F} = \frac{\frac{log(IWV)}{10} - a}{b}, T_{d,C} = \frac{T_{d,F} - 32}{1.8} \tag{6.3}$$

where $T_{d,F}$ is the dew point in Fahrenheit and $T_{d,C}$ is the dew point in Celsius. The coefficients a and b have been a matter of discussion among the meteorological community (*Reitan*, 1963; *Bolsenga*, 1965; *Smith*, 1966), but for these studies the values $a = -1.3098$ and $b = 0.0401$ are used (*Alshawaf et al.*, 2017). The transition from dew point to relative humidity is classically done using psychrometric tables (*Marvin*, 1900). In this work a more simplified approach for the calculation of relative humidity is used (*Lawrence*, 2005):

$$RH = \frac{100 - 5(T_{2m,C} - T_{d,C})}{100} \tag{6.4}$$

where $T_{2m,C}$ is the 2 meter surface temperature. This formula is using the empirical observation, that when the relative humidity RH is above 50%, the dew point decreases by 1^oC for every 5% decrease in RH (*Lawrence*, 2005). Thus relative humidity measurements can be obtained using 2m surface temperature and IWV.

The second contributing factor to the α parameter in equation 6.2 is the temperature. It is scaled with the α_t and T_{thr} constants. T_{thr} is a threshold temperature, above which evaporation is more rapid. In the case of Marquardt, $T_{thr} = 10°C$. Since the soil moisture is counter-correlated with temperature, the higher temperature values contribute to soil moisture reduction. The third constant, used in the α parameter is α_n. It is a scaling parameter, insuring that soil moisture decreases given the temperature and relative humidity contribute positively to the soil moisture change. This scaling parameter can be interpreted as representing the soil type, but for the sake of simplicity is kept constant.

The second and third parameters in equation 6.1, are β and γ. These are constants, derived for each station individually. The role of β is to introduce rainfall into the model. The estimation of β is made more complicated by the lack of correlation between the rainfall rate and the increase of soil moisture, as seen in the values of the SMC_5 values (in the range between 0 and 0.2) derived in chapter 5. Finally, the parameter γ is introduced into the model as a guarantee for positive values of soil moisture even during long droughts.

Parameter	Description
α_n	Scaling parameter representing infiltration and plant transpiration.
α_t	Scaling parameter representing evaporation, based on the temperature at the station. The higher the temperature, the higher the evaporation.
α_w	Scaling parameter representing evaporation or soil moisture deposition, based on the relative humidity at the station. At high relative humidity soil moisture deposition without precipitation is possible.
T_{thr}	Threshold temperature, above which evaporation is more rapid.
β	Precipitation scaling factor.
γ	Parameter, representing residual soil moisture.

Table 6.1: 1D-ESMM model parameters in equation 6.1.

6.2 Soil moisture model design iterations

For the development of this model (equation 6.1), several iterations are tested. The first iteration is a mathematical model, incorporating only rainfall as natural parameter:

$$VWC_i = \alpha \mathrm{VWC}_{i-1} + \beta R + \gamma + \delta \cos(time) \tag{6.5}$$

In it α is set as a non-variable parameter and the seasonality is achieved using trigonometric function, instead of temperature, humidity, or other atmosheric observables. The results from this modelling effort can be seen in figures 6.2 and 6.3 (orange). In the first physical model (figures 6.2 and 6.4, blue), temperature is implemented as a substitution

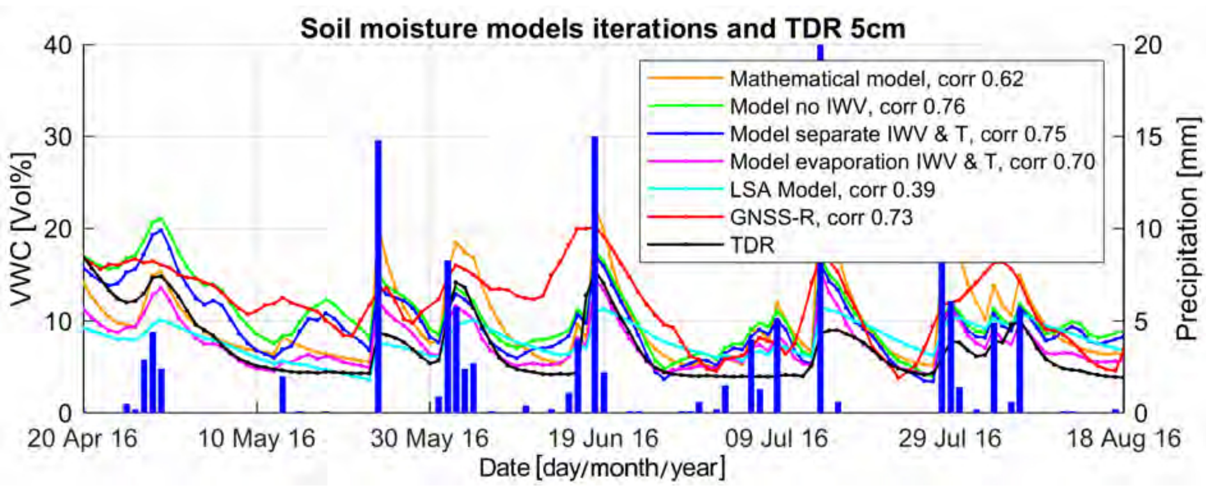

Figure 6.2: Soil moisture model variations for summer of 2016 for station Marquardt. These are the different implementations of the modelling strategy. With the increase of complexity of the models, their performance changes.

for the trigonometric time variable through a new parameter δ:

$$VWC_i = \alpha(IWV)\text{VWC}_{i-1} + \beta R + \gamma + \delta(T_{thr} - T) \tag{6.6}$$

The final variant of the model, as presented in equation 6.1, is conceived under the assumption, that the temperature should be included into α and should be dependent on the amount of soil moisture in the previous epoch. The results from this variation can be seen in figures 6.2 and 6.5 (magenta).

As an initial step to develop these models, a Least Square Adjustment approach is used. After many manipulations with the previous states of the model, as well as with the addition of further coefficients, the most adequate result is achieved using the following formulation of the model:

$$VWC_i = \alpha(IWV, T)\text{VWC}_{i-1} + \beta R \tag{6.7}$$

The LSA is based on TDR data, obtained in the station. The result of this LSA model are less satisfactory (figures 6.2, 6.6, cyan), than the results from the previous empirical attempts. Additionally, when the LSA is run with GNSS-R data, the correlations and the seasonal behaviour of the model is even less satisfying. Since the LSA parameters rely on the existence of TDR in the GNSS stations, which is not the case for most stations, the LSA approach is not used.

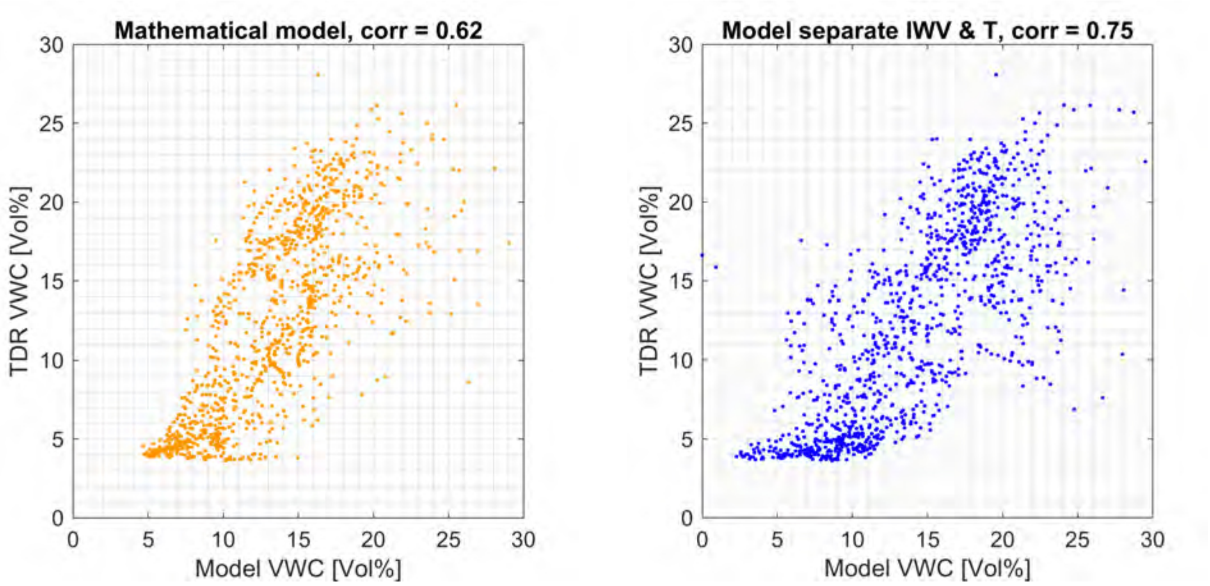

Figure 6.3: Mathematical model for soil moisture, using formulation 6.5.

Figure 6.4: First physical model for soil moisture, using formulation 6.6.

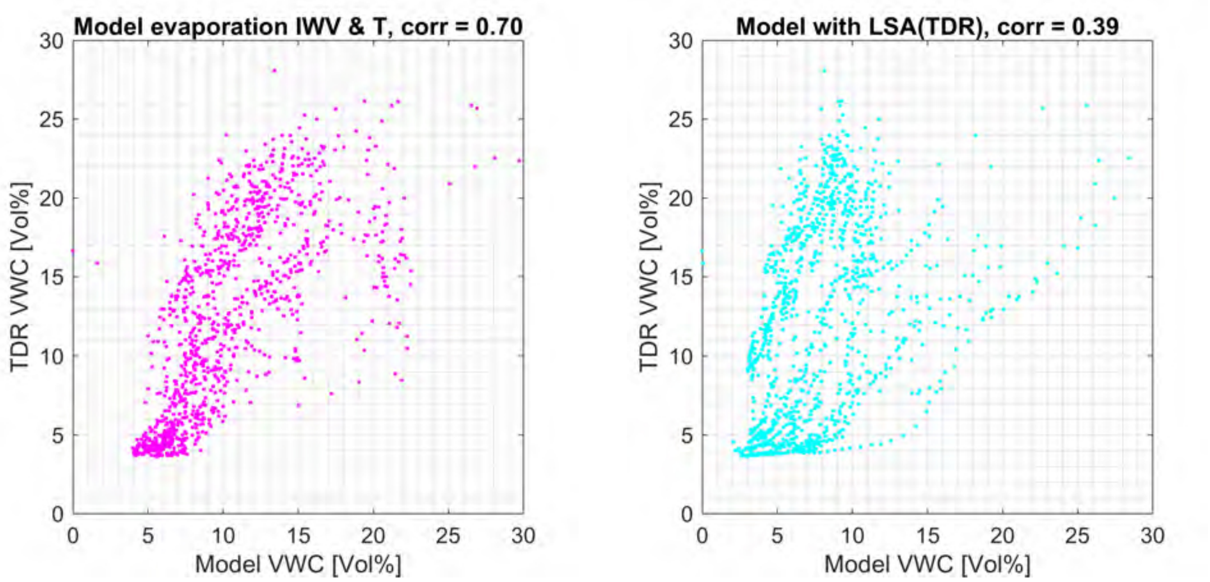

Figure 6.5: Final physical model for soil moisture, using formulation 6.1.

Figure 6.6: LSA model for soil moisture, using formulation 6.7.

6.3 Soil moisture model validation

A detailed simulation, covering 3 cold front passages through the station in Marquardt is presented in figure 6.7. Peaks in the IWV and in the soil moisture during the frontal passages are observed. The peaks in the IWV on 22 August, 6 and 19 September are caused by the large amounts of water vapour in convective clouds, which are typical for cold fronts, as well as by the subsequent evaporation after the precipitation events. The maxima in the soil moisture in the days of the cold front passages are caused by the precipitation from the convective clouds. In this series of cyclones, after the cold fronts

Station	α_n	α_t	α_w	T_{thr}	β	γ
Marquardt	0.65	0.01	0.12	10^{o}C	1/200	0.015
Visby	0.4	0.028	0.2	8^{o}C	1/300	0.05
Olsztyn	0.4	0.04	0.2	10^{o}C	1/300	0.04
Fredericton	0.4	0.04	0.2	10^{o}C	1/400	0.04
Redu	0.4	0.035	0.15	10^{o}C	1/300	0.035
Calgary	0.5	0.04	0.05	8^{o}C	1/400	0.05
Tsukuba	0.5	0.04	0.02	10^{o}C	1/300	0.07
Sutherland	0.6	0.02	0.2	7^{o}C	1/200	0.04
Mafikeng	0.6	0.005	0.6	15^{o}C	1/80	0.015

Table 6.2: Model coefficients from equation 6.1 at all GNSS stations.

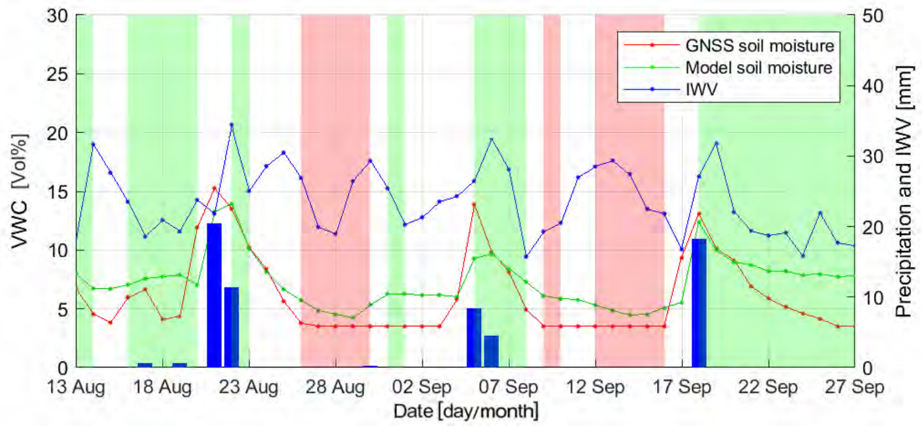

Figure 6.7: Soil moisture model compared to observations for station Marquardt for the end of summer of 2016. The red background indicates average daily temperatures above 22^{o}C, while the green background - temperatures below 18^{o}C.

passes, the warm fronts of the following cyclones advance over the area, bringing little to no precipitation, thus depleting the soil moisture storage in the soil.

The developed model shows very similar behaviour to the observed GNSS-R soil moisture observations, with a steeper depletion curve during warmer weather and peaks during the precipitation events. The lowest readings from the model are achieved during the warmest days, but the model does not evaporate enough water during the warm periods with high IWV (and relative humidity). The lack of correlation between the soil moisture increase and the precipitation amounts is the primary reason why the model cannot represent well the peak soil moisture values, observed from GNSS-R, seen clearly in figure 5.32.

Results from the soil moisture model implementation can be seen on figures 5.28, 5.35 and 6.8. These figures show, that the model:

- shows very similar average values to the actual observations,

- shows similar/stronger responses to recorded precipitation events than observations and ERA5,
- follows the seasonal variations of the GNSS-R observations.

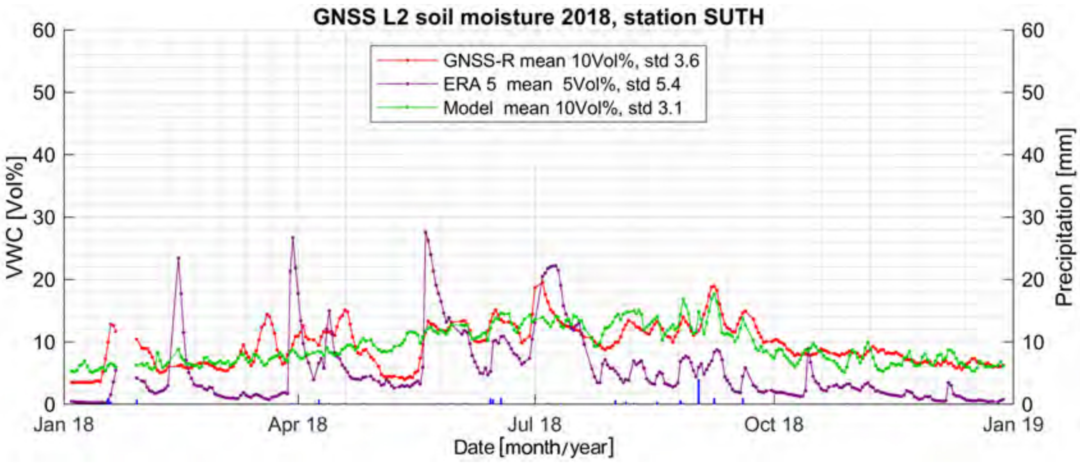

Figure 6.8: Soil moisture comparison between model and GNSS-R at IGS station Sutherland in 2018.

Chapter 7

GNSS Reflectometry for snow height monitoring

This chapter describes the unique work carried out for this thesis in GNSS Reflectometry for snow height determination.

Firstly, in section 7.1, snow height observations using the GNSS-R technique are compared to snow buoy measurements at the German Antarctic station Neumayer III. A classical and a new approach for snow height determination from GNSS-R are compared with detailed analysis of the results from the new proposed approach.

Secondly, in section 7.2, the snow height at 7 IGS stations is estimated and compared to data from locally available observations, as well as from ERA5.

7.1 Snow height monitoring at Antarctic station Neumayer III

A GNSS receiver is installed next to the Antarctic station Neumayer-III, as part of a collaboration between the GFZ and Alfred-Wegener-Institute (AWI), which is the Helmholtz center for polar and marine research, based in Bremerhaven and Potsdam. Neumayer-III is assembled in 2009 on the Ekström Ice Shelf in Queen Maud Land, continental Antarctica. The exact coordinates of the station are 70.7^{o}S 8.3^{o}W. The Spuso on the figure is the chemical observatory Spurenstoff, which is also part of the now defunct Neumayer-II station.

The GNSS station, established in the Antarctic station is called NMSH. It comprises Javad TR_G3TH receiver with a Javad Grant G3T antenna without a choke ring. This is a classical GFZ set-up for reflectometry, also implemented in station Fürstensee (see chapter 5.3.6). The GNSS station is installed in February 2015. Collocated with the GNSS sensor is a set-up of 4 snow buoys.

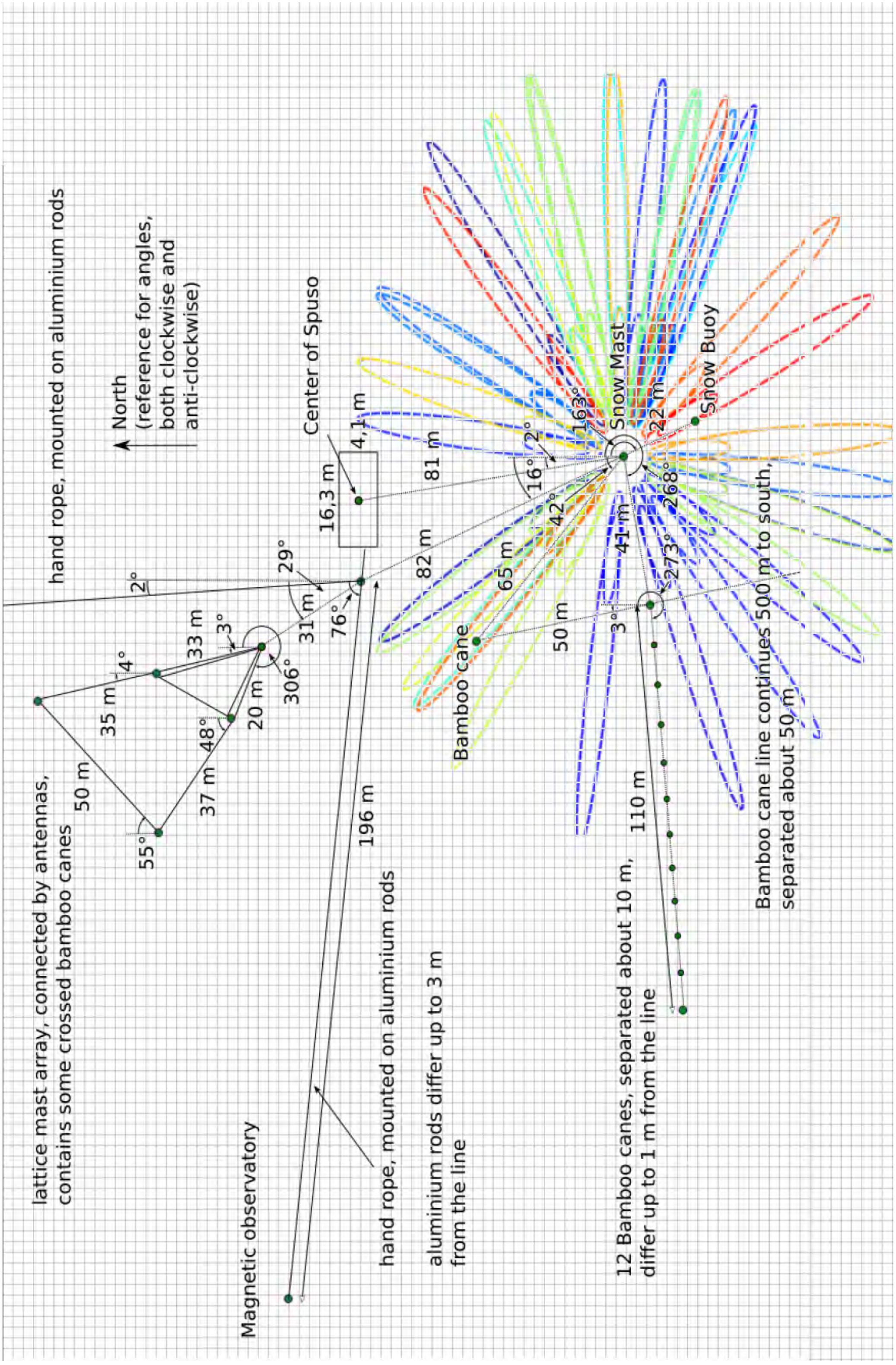

Figure 7.1: Position of the Snow Height mast in the vicinity of Neumayer. The scheme is produced by AWI with imposed Fresnel zones of the GNSS antenna added by GFZ.

The GNSS site is lifted twice during the observation period. The first one occurred on 6 October 2016, lifting the station by 145cm, while the second one is on the 11 February 2017 with a lift of 44cm (antenna mounting can be seen on figure 7.2). For the retrieval a set of 37 reflections is used, coming from all directions (seen on figure 7.1). The retrieval is set loosely to allow the changes in height to be recorded. Thus the GFZ soil moisture retrieval software allows maximum recorded changes in height within 2 meters per year. The resulting average yearly trends vary between the two datasets. For the snow buoys the trend is 96cm/year, while for GNSS-R the trend is recorded at 86cm/year. The 10cm/year difference can be caused by several factors, such as snow compression on the base of the GNSS antenna pillar, or concentration of snow around the buoys. The GNSS measurement is more independent on snow accumulation around objects, as far as the snow height is measured remotely.

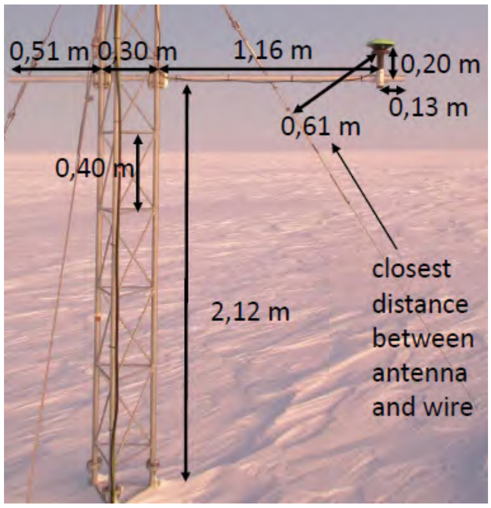

Figure 7.2: Position of the GNSS antenna, mounted on a pillar in Neumayer-III.

The elevation angles of the retrieval are varying. When the antenna is high above the snow, the elevation angles are 13-19 degrees, while when the antenna is getting closer to the reflective surface, the elevation angles are gradually lowered with the lowest interval of between 5-10 degrees. This is done in order to ensure that the sensed area in the retrieval is the same (as shown on figure 7.3).

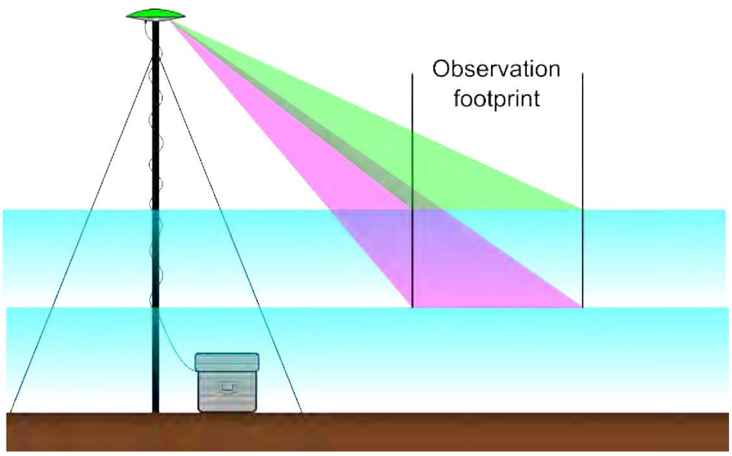

Figure 7.3: Changes of elevation angle to sense the same observation footprint. With the increase of the snow depth the elevation angles for observing the same footprint are shifted.

As discussed previously, the phase changes of the SNR, described in equations 3.24 and

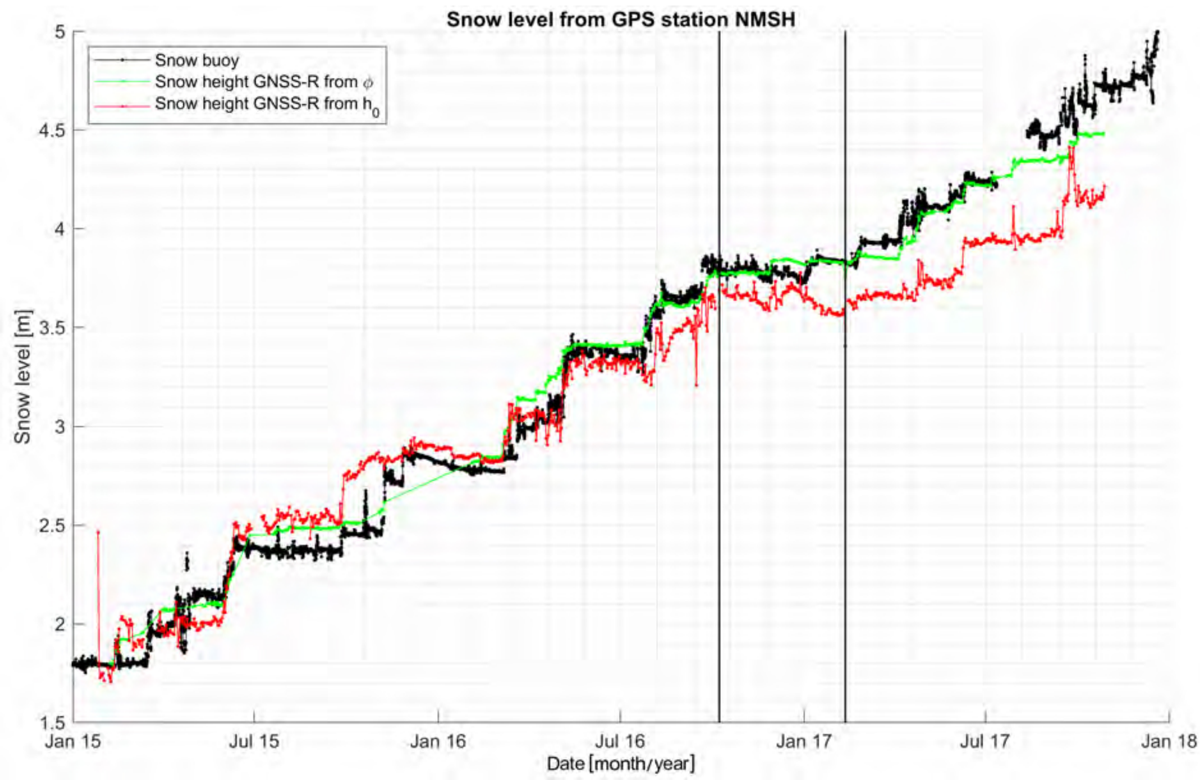

Figure 7.4: Snow height observations from Neumayer-III station in Antarctica. The black line indicates measurements from nearby-installed snow buoys. The red line indicates the snow height using the SNR height estimations with fixed breakpoints of the antenna height changes and excluded outliers. The cyan line indicates the snow height using the SNR phase estimations with fixed breakpoints.

3.25 can be interpreted as reflector height changes. Following this assumption, the snow height changes can be detected using not only the reflector height estimations, but also using phase estimations. Since such a measurement is not absolute, the first snow height record in the series has to be sourced from independent observations. This approach uses the following equation:

$$SH_i = SH_{i-1} + C\delta\phi\frac{2\pi}{360} \tag{7.1}$$

where SH_i is the current snow height estimation, SH_{i-1} is the previously measured snow height, $\delta\phi = \phi_i - \phi_{i-1}$ is the change in the phase of the interference pattern, $\frac{2\pi}{360}$ is the transition from degrees into radians and C is a scaling coefficient. Using this approach an independent dataset of height changes has been created for GNSS station Neumayer (seen on figure 7.4). This approach is very similar to the approach proposed by *Vey et al.* (2016b), but modified with the introduction of the scaling coefficient C, which has units of length. Through LSA analysis the C coefficient has been estimated to be equal to 0.172m with accumulation rate of 90cm/year.

The snow height retrievals from the phase estimations show a higher correlation of 0.996, than the retrievals from the interference frequency 0.98 (see figure 7.5). This can

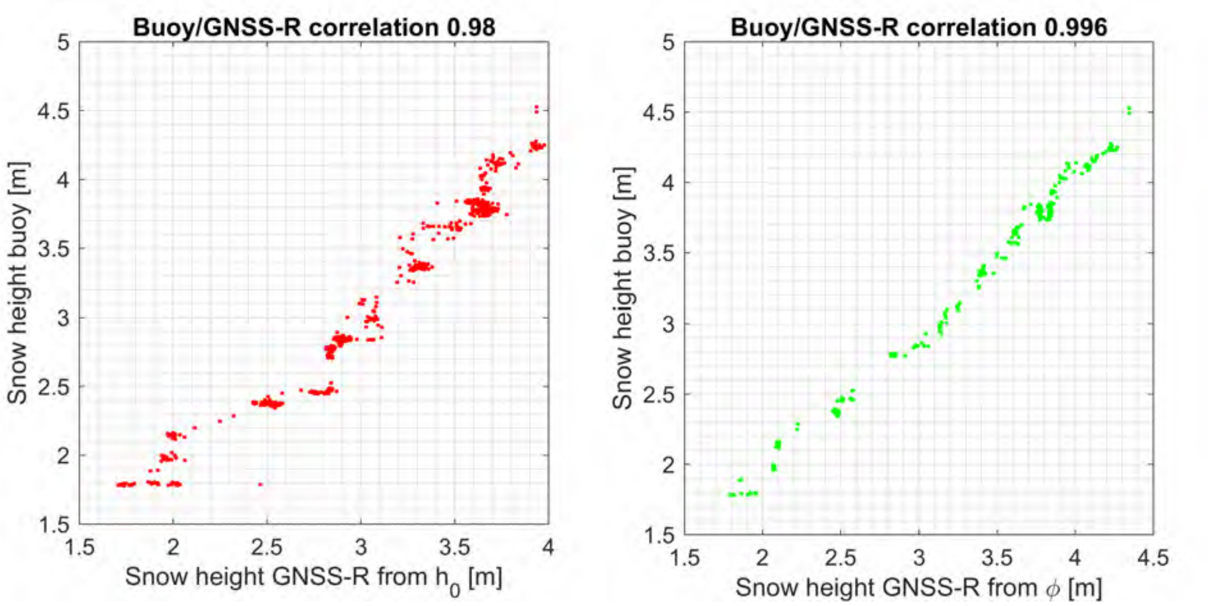

Figure 7.5: Snow height retrieval correlations from Neumayer-III station in Antarctica. Snow height using the SNR height estimations on the left, snow height using the SNR phase estimations on the right.

be explained by the fact that the estimation of the phase of the interference pattern of the SNR is far more accurate, than the estimation of the frequency of the interference pattern. This result is achieved using the same reflections datasets for the two retrievals and the same satellite selection. The data gaps in the phase dataset can be explained by the difference in the processing. The interference frequency estimations are averaged over any available data, with the exclusion of outliers beyond 1σ, while the phase dataset contains data points, where all reflections are recorded, without exclusion of outliers. The same result is achieved using several different settings of the processing software.

For a more comprehensive analysis of the data the de-trended datasets of all measurements also have to be assessed. The correlations between the de-trended snow height values of the GNSS-R and GNSS-R ϕ approaches are very significant, as shown in figure 7.7. The Root Mean Square Errors (RMSE) of the two measurements are 19.7cm and 7.7cm accordingly.

The better performance of the GNSS-R ϕ can be explained with the high reliability of phase estimates even when the reflector height is not estimated correctly. This effect is already observed in chapter 5.5 in the experiment with wrongly estimated reflector height.

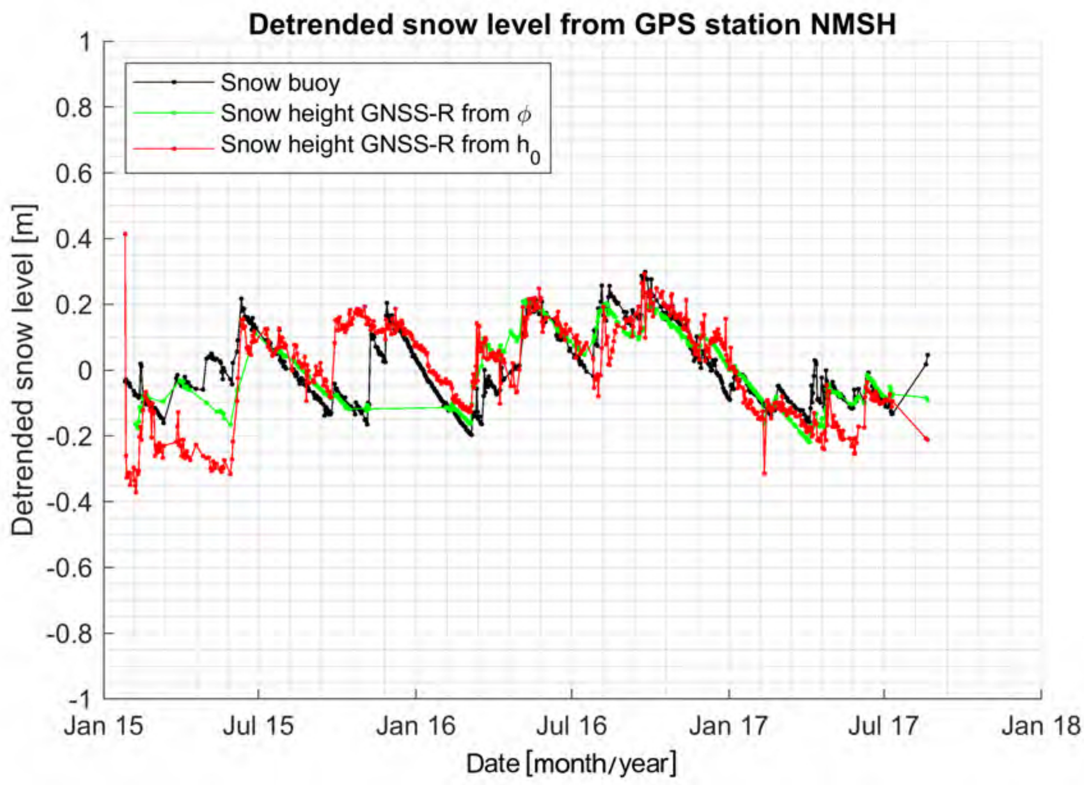

Figure 7.6: De-trended snow retrieval from Neumayer-III station in Antarctica. The black line indicates measurements from nearby-installed snow buoys. The red line indicates the snow height using the SNR height estimations with fixed breakpoints of the antenna height changes and excluded outliers. The cyan line indicates the snow height using the SNR phase estimations with fixed breakpoints.

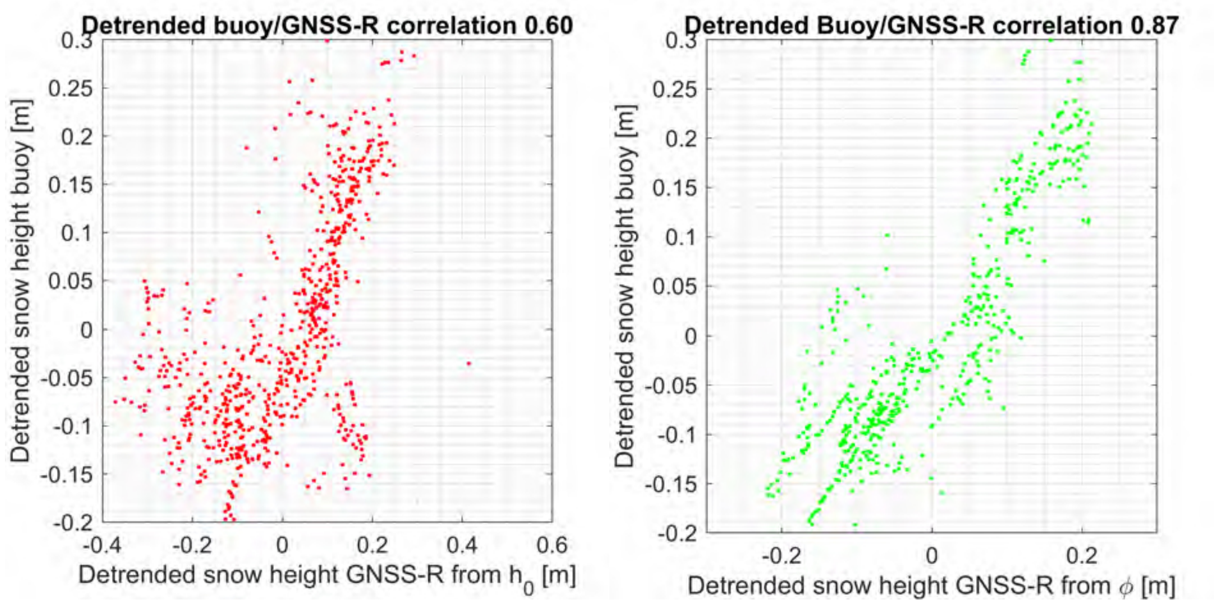

Figure 7.7: De-trended snow retrieval correlations from Neumayer-III station in Antarctica. Snow height using the SNR height estimations on the left, snow height using the SNR phase estimations on the right.

7.2 Snow height monitoring at IGS stations

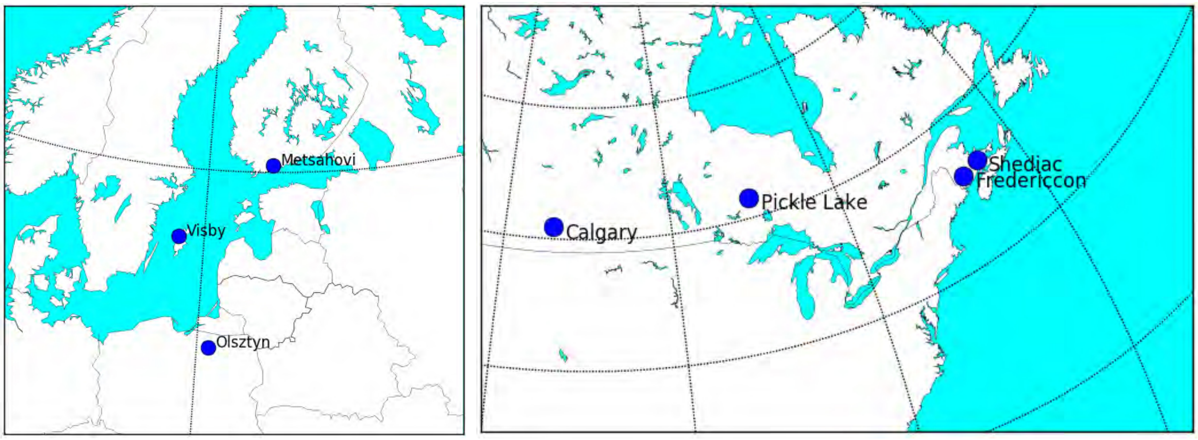

Figure 7.8: Maps of IGS stations capable of detecting snow height in Europe (left) and North America (right).

Several IGS stations, located in the northern regions of the globe provide not only opportunities for soil moisture measurements (as shown in section 5.4), but also for snow height determination. Table 7.1 shows the stations, used for such studies. The stations are located in Northern Europe as well as in Canada (see maps on figures 7.8). The European stations from north to south are Metsahovi, Visby and Olsztyn. The Canadian are from west to east Calgary, Pickle Lake, Fredericton and Shediac (seen on map 7.8 (right)). All of the stations in Canada are located between 45^o and 52^o northern latitude. It is highly unlikely that any other IGS station can be used for such retrievals. Station Kiruna in Sweden is deemed unsuitable for such investigations due to rough terrain and the availability of trees, closely surrounding the GNSS site. Stations Alert, Baker Lake, Nain, CFS Flin Flon and Resolute in Canada, as well as Vesleskarvet in Antarctica might also provide suitable reflections, but their surroundings are mostly rocky and, for most of them, the stations antenna height is 1.5 meters above ground. Additionally 3 stations in Antarctica, namely Davis, Casey and Ross Island are situated directly on the ground. These three stations might be interesting for the research of signal attenuation under snow cover.

The retrieval of the snow height has been performed using the following equation:

$$SH = h_0 - h_e \tag{7.2}$$

as previously described in chapter 3.5. In order to clear the signal of the snow change from the noise of the reflector height change, occurring due to changes in soils and environment around the station, every year in the stations datasets has been treated separately. For every year the average reflector height has been determined, as well as the standard

City	Station name	Country	Coordinates
Fredericton	FRDN	Canada	45.9^{o}N 66.6^{o}W
Shediac	SHE2	Canada	46.2^{o}N 64.5^{o}W
Calgary	PRDS	Canada	50.8^{o}N 114.2^{o}W
Pickle Lake	PICL	Canada	51.5^{o}N 90.1^{o}W
Metsahovi	METG	Finland	60.2^{o}N 24.3^{o}E
Olsztyn	LAMA	Poland	53.8^{o}N 20.7^{o}E
Visby	VIS0	Sweden	57.6^{o}N 18.4^{o}E

Table 7.1: Names of IGS stations for snow depth retrieval, their country and position.

deviation of all reflector heights for each satellite individually. Then the height of the snow is determined using:

$$SH = (h_0 - \sigma_h) - h_e \tag{7.3}$$

where σ_h is the standard deviation of the dataset. In cases when SH is below 0, the measurement is disregarded. This procedure is done, due to the fact that for each satellite for each year the standard deviation can reach up to 15cm. Thus the final measurement for the snow height is determined by averaging all reflections for the same day. This approach is effective when the station has experienced significant snowfall. When no snow is detected using the GNSS-R approach, the dataset is double checked using temperature records for the area. The snow height datasets are compared with ERA5 reanalysis. The snow height records for the European stations cover 3 stations with 4 more station in Canada.

The second methodology used for snow detection is also described in chapter 3.5. Similarly to the monitoring in station Neumayer, this dataset is calculated using the phase changes of the interference patterns of each satellite:

$$SH = C(\phi - \Phi_N)\frac{2\pi}{360^o} \tag{7.4}$$

where ϕ is the measured phase of the SNR interference pattern and Φ_N is the median phase for each year. The median is used instead of the mean in order to neglect the effect of the snow cover on the dataset. Since snow is present in the stations for less than 6 months during the year, the median always gives values, representing bare soil. This approach creates a dataset, which promotes positive snow height estimates throughout the year. The snow height is estimated for each satellite reflection individually and then combined from all satellites to create an unified data set.

The final value of the GNSS-R snow height estimates is determined from a linear combination of the above mentioned two methods. The strength of this approach is the availability of more data for each data point. The strengths of both methods are also acknowledged - one is more sensible for higher snow covers, the other for lower. When no snow is detected with this approach, the dataset is double checked using temperature records for the area. The snow height datasets are compared with ERA5 reanalysis.

7.2.1 Visby, Sweden

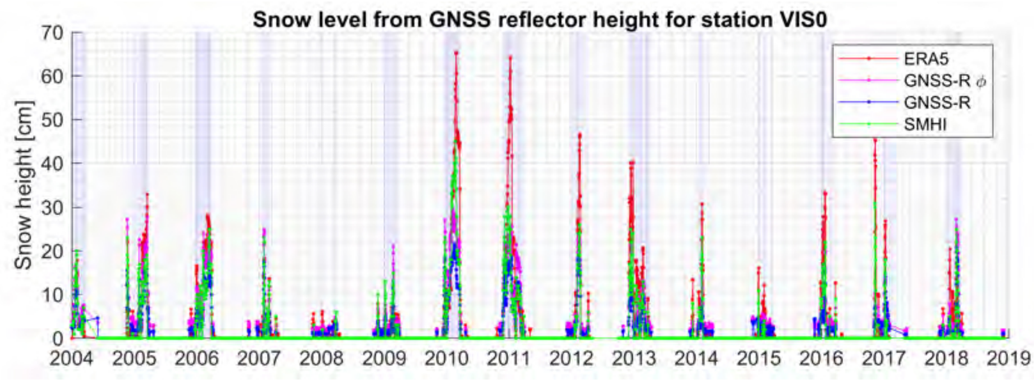

Figure 7.9: Snow height retrievals from IGS station Visby. The time periods, marked with light blue background indicate temperatures below 0^oC.

Visby, as discussed in chapter 5.4, is situated in a temperate oceanic climate. The GNSS station is situated 1.3km away from the station of the Swedish Meteorological and Hydrological Institute (SMHI), where daily snow height measurements have been performed regularly since 1946 (*Larsson et al.*, 2012). The whole historical dataset is digitalized and available to download from general public `https://www.smhi.se/en/weather/sweden-weather/observations`. All measurements are performed once a day at 6 UTC. The reason for this early morning hour is that around 8 in the morning local time is the coldest point throughout the day, at which point snow melting is not a major factor in snow dynamics. The antenna of the GNSS station is situated on a 3m high concrete pillar, allowing measurements of snow depth up to 2m. SNR data from this station is available since 2004 (seen on figure 7.9).

The methodology of estimating the reflector height using the phase shifts of the SNR, as described in the previous chapter 7.1, is also used for this station. This phase-based dataset is referred to as $GNSS-R\phi$, while the combination of the classical approach with this new technique is referred to as $GNSS-R$. When compared to the SMHI data, the new $GNSS-R\phi$ approach shows correlation of 0.91 and RMSE value of 2.26cm, while the combined $GNSS-R$ has the same correlation, but RMSE figure of 2.48cm. The differences between the datasets are clearly visible on figure 7.10. In this station ERA5 is largely overestimating the snow depth with RMSE value of 4.2cm, compared to the SMHI data and 5.4cm, compared to the GNSS-R data. The correlation between ERA5 and SMHI is the same 0.91, while the correlation between ERA5 and GNSS-R is 0.84 (see figure 7.11). The stated statistics cover the whole snow height dataset, as presented in

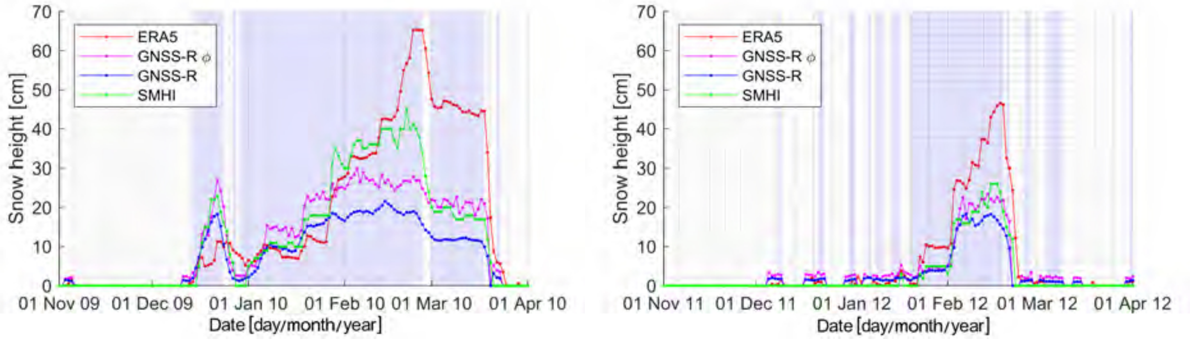

Figure 7.10: Snow height retrievals from IGS station Visby for winters 2009/2010 and 2011/2012. The time periods, marked with blue background indicate temperatures below 0^{o}C.

figure 7.9. In general, ERA5 is systematically overestimating the snow height, but the behaviour of the modelled data is closely related to the measurements and thus can be used as comparison dataset for the following stations.

The maximum recorded snow height in Visby from SMHI for the period between 2004 and 2019 is 45cm on the 21st of February 2010, as measured by SMHI. The maximum snow height from the ERA5 dataset is 65cm for the 26th of February the same year with estimations of 57cm on the 21st. The GNSS datasets give much lower values for this day at 28cm, as seen on figure 7.10 left. A reason for the disparity between the datasets could be the distance between the stations, as well as the presence of a small hut next to the GNSS site, which could alter the snow accumulation. In one third of all winters for this period the maximum recorded snow depth is below 10cm. The minimum amounts of snow cover, as detected by GNSS-R for Visby, are in 2008 and 2015.

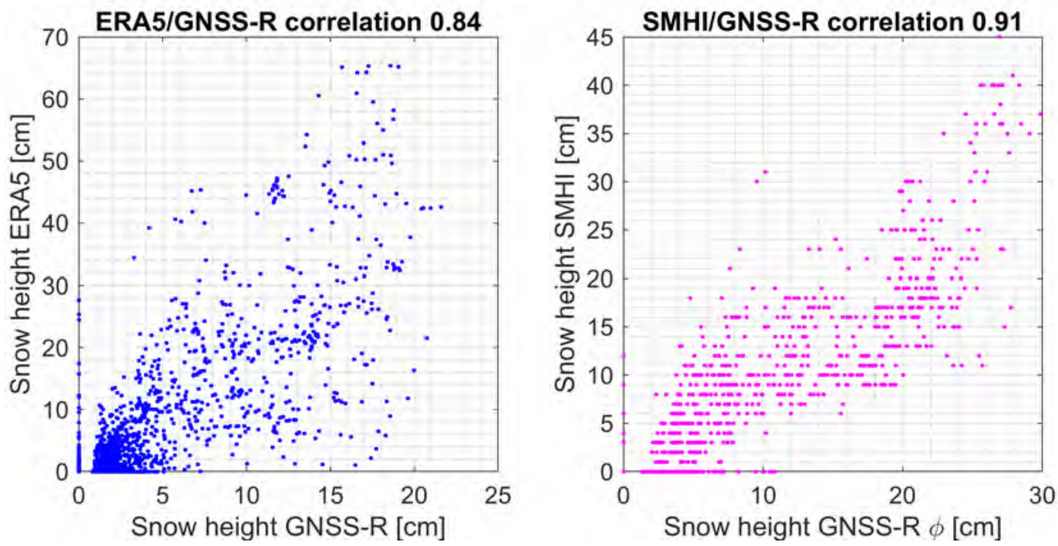

Figure 7.11: Snow height retrieval correlations from IGS station Visby. The correlation between SMHI and ERA5 is presented on the left and between $GNSS - R\phi$ and SMHI on the right.

7.2.2 Metsahovi, Finland

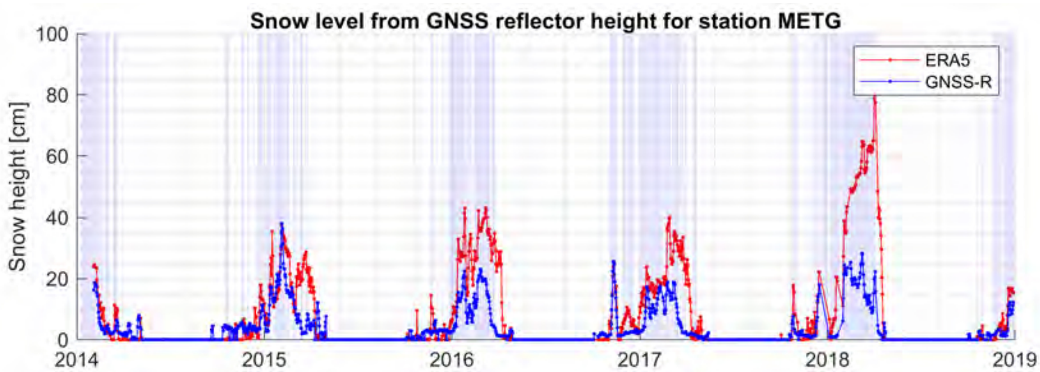

Figure 7.12: Snow height retrievals from IGS station Metsahovi. The time periods, marked with blue background indicate temperatures below 0^{o}C.

The northernmost European station Metsahovi, shows highest snow accumulation during the examined period with the longest time under snow cover. The station antenna is mounted on a 2m high concrete pillar, which guarantees the sufficient accuracy of the GNSS-R estimates at least for snow cover lower than 1m. The station has flat ground in its vicinity, which allows for snow height studies instead. The dataset covers the period between 2014-2019 with correlation between ERA5 and GNSS reflectometry of 0.79 (see figure 7.12). The station is further described in section D.2.1.

7.2.3 Olsztyn, Poland

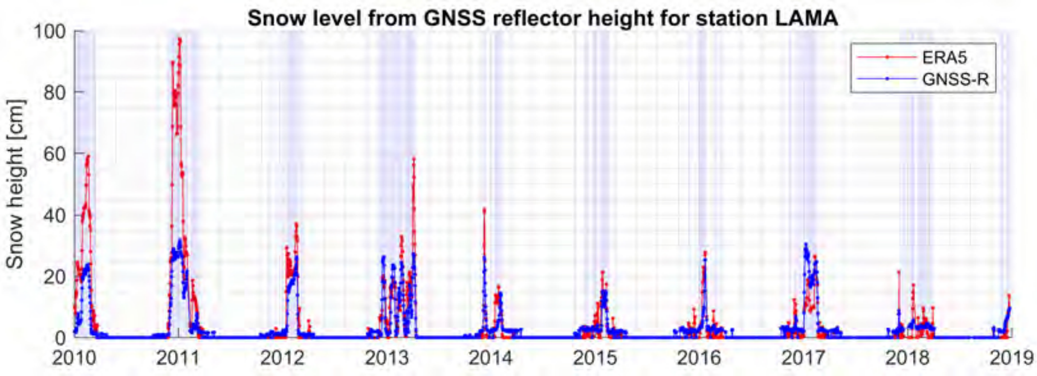

Figure 7.13: Snow height retrievals from IGS station Olsztyn. The time periods, marked with blue background indicate temperatures below 0°C.

The southernmost European station, where snow cover has been measured, is Olsztyn. The antenna is mounted on a 1.5m concrete pillar, allowing snow height measurements of up to 50cm. At this station the snow cover during winter periods is close to the detection sensitivity of the GNSS-R method. In most of the observed winters for this station the snow cover stays above 10cm for not longer than one week (seen on figure 7.13).

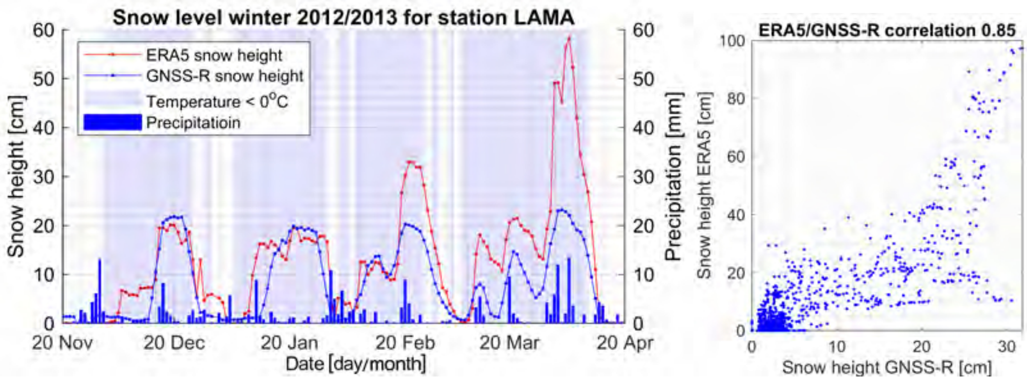

Figure 7.14: Snow height retrievals for station Olsztyn for winter 2012/2013 (left). Snow height scatter plot between ERA5 and GNSS-R (right).

During the winter of 2012/2013 four independent snow cover periods are observed in the station. These four periods are interrupted by warm air masses coming from West, which melted the snow (seen on figure 7.14 left). The correlation between the GNSS-R and ERA5 estimated snow heights is 0.85 (seen on figure 7.14 right) with RMSE of 7.0cm.

7.2.4 Calgary, Canada

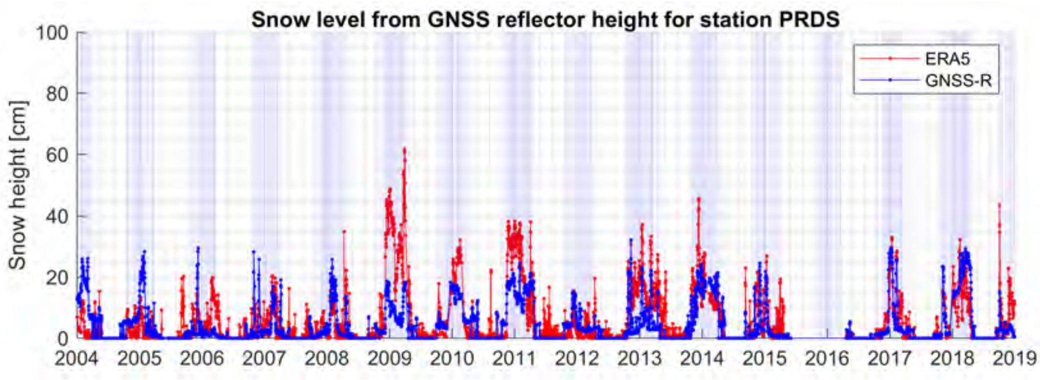

Figure 7.15: Snow height retrievals from IGS station Calgary. The time periods, marked with blue background indicate temperatures below 0^{o}C. Between the second half of 2015 and the first quarter of 2016 GNSS data are missing.

Calgary is the westernmost of the Canadian stations. It is located in the province of Alberta. The GNSS station dataset spans from 2004 until 2019 with a 1 year gap between 2015 and 2016 (figure 7.15). The antenna is mounted on a 2m pillar, allowing snow height measurements of up to 1m. The station is elevated 1247m above sea level. Snowfalls occur in this area between September and May, giving a long season with snow cover. The snow cover in Calgary is higher than 25cm in 6 of the 15 observed winter periods. 2010 is the year with longest observed snow cover in this 15 year period. Snow cover is present in the station until the end of May and the first autumn snowfall is recorded in September (seen on figure 7.16 left).

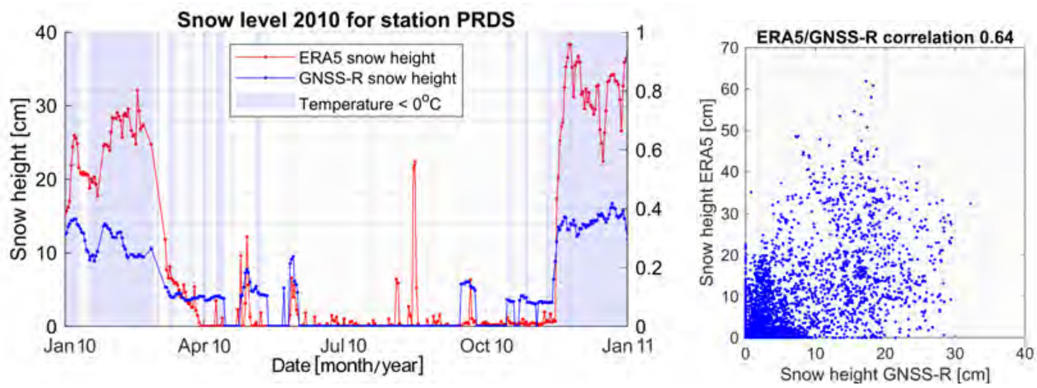

Figure 7.16: Snow height retrievals for station Calgary for 2010 (left). Snow height scatter plot between ERA5 and GNSS-R (right).

The results are further compared with the 1981-2010 Climate Normals and Averages, as recorded by the Canadian meteorological service (*http://climate.weather.gc.ca/*). The data consists of monthly averages of snow depth, temperature and many other meteorological measurements. In the case of Calgary the meteorological reference station is situated in Calgary airport, some 33km away from the GNSS receiver. The station elevation is 1084m asl, which is 163m lower, than the GNSS antenna. Moreover the meteorological station is situated in an airport environment with many planes taking off and the runway has to be cleaned, so that it does not obstruct air traffic, while the GNSS site is situated in the Rothney Astrophysical Observatory with trees blocking the visibility to the GNSS antenna from the North. These are the most probable reasons why the GNSS observations are significantly different from the normals, as measured in the meteorological station (see figure 7.17).

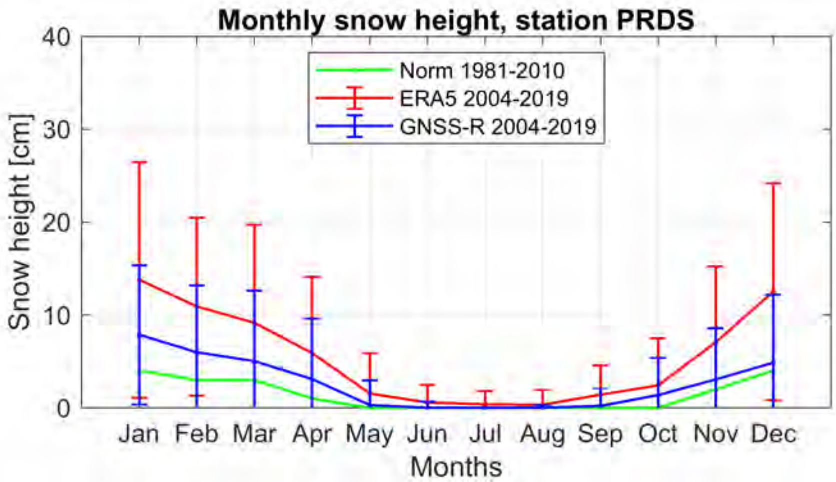

Figure 7.17: Monthly mean snow height in Calgary - a comparison between ERA5, GNSS-R and 1981-2010 climate normals. The error bars indicate standard deviations of ERA5 and GNSS-R.

ERA5 shows significantly higher snow cover throughout the years with snowing in August of 2010, which is not recorded in the GNSS-R observations. The snow depth is systematically overestimated for all months, as compared to the GNSS-R. The correlation between the two datasets is 0.64 with RMSE of 7.6cm.

7.2.5 Pickle Lake, Canada

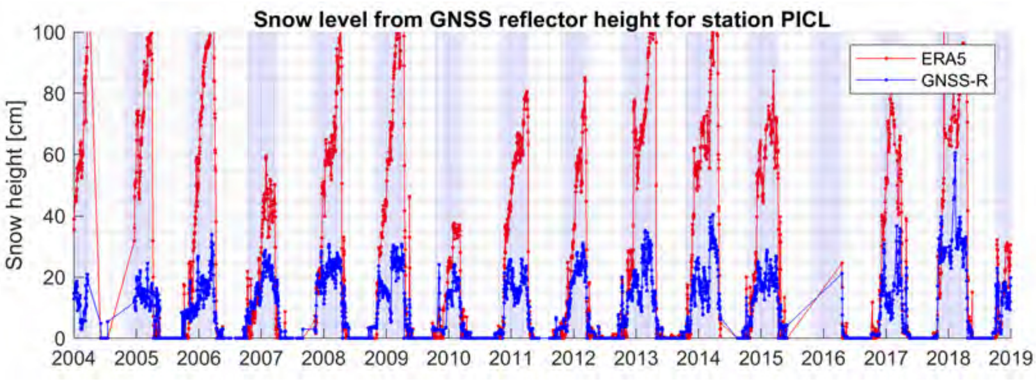

Figure 7.18: Snow height retrievals from IGS station Pickle Lake. The time periods, marked with blue background indicate temperatures below 0^oC.

The GNSS station at Pickle Lake is established in 2001 on a 1.5m high concrete pillar and started to broadcast signal strength data since 2003 (see figure 7.18). The station is elevated at 315m above sea level in the Ontario province of Canada. Unlike Calgary, the station is surrounded by many lakes and water bodies, contributing to a humid continental climate. The annual precipitation in the area is almost double that in Calgary, leading to more soil moisture and precipitation in the summer and deeper snow cover in winter. The deepest snow cover on record is in the winter of 2017/2018 at 57cm, as estimated by GNSS-R. Every winter on record the snow height maximum is above 20cm.

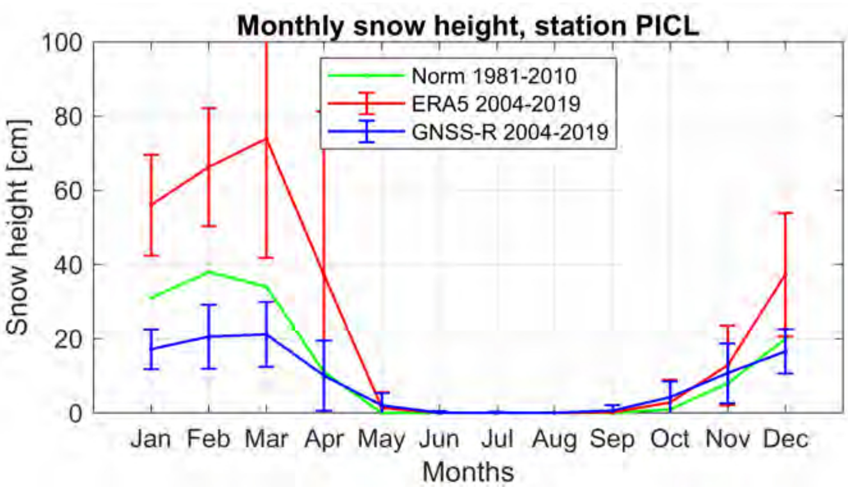

Figure 7.19: Monthly mean snow height in Pickle Lake - a comparison between ERA5, GNSS-R and 1981-2010 climate normals. The error bars indicate standard deviation from ERA5 and GNSS-R.

The 1981-2010 Climate Normals show significantly higher snow depth, than the measurements with the GNSS receiver. The meteorological station is situated once again in an airport, 5km away from the GNSS site. The elevation difference is 71 meters with the GNSS site being lower than the meteorological station (see figure 7.19). As explained with station Neumayer, snow can have very large variations in accumulation within limited area, which is the only explanation for the large difference between GNSS-R and the normals. ERA5 on the other hand significantly overestimates the snow depth. The correlation between ERA5 and GNSS-R is 0.81, which is high. The RMSE between GNSS-R and ERA5 is also very high at 30.7cm.

7.2.6 Fredericton, Canada

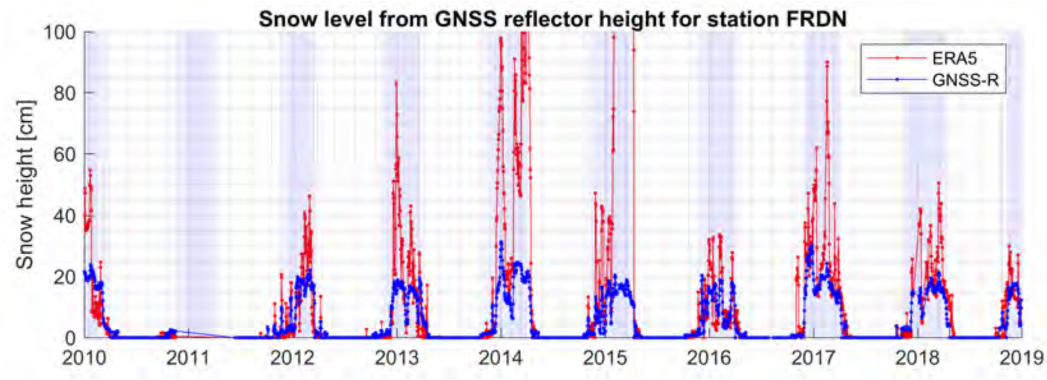

Figure 7.20: Snow height retrievals from IGS station Fredericton. The time periods, marked with blue background indicate temperatures below 0^{o}C.

Station Fredericton is extensively discussed in chapter 5.4. The pillar of the station is 1.5m high and is situated in an open field in the outskirts of Fredericton. The highest measured snow depth in the station for the period between 2010 and 2019 occurred in 2014 at 31cm snow depth (see figure 7.20). The meteorological station, where the 1981-2010 climate normals have been recorded, is only 3.5km away with elevation difference of 56m with the GNSS station being higher.

The comparison to the climate normals shows remarkable agreement, as seen in figure 7.21. ERA5 overestimates the snow height as in all other stations with RMSE between GNSS-R and ERA5 at 26.6cm and correlation of 0.61 for the period of 2010-2019.

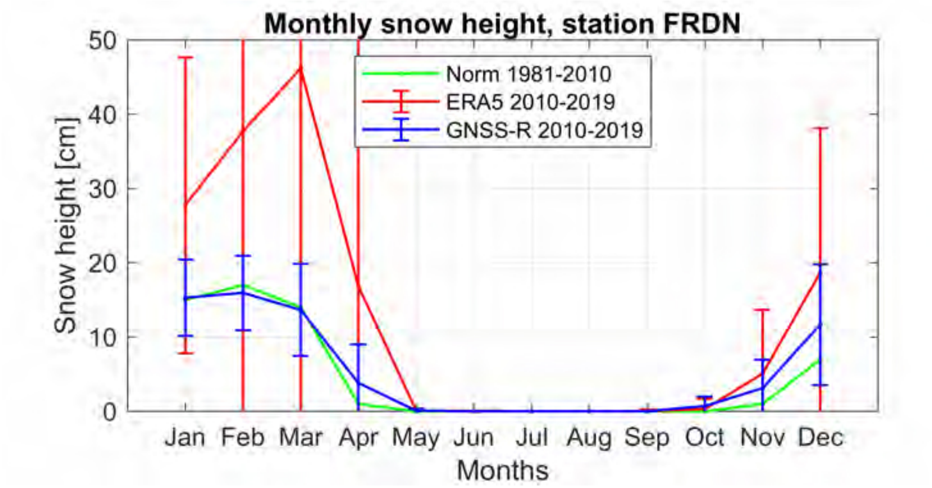

Figure 7.21: Monthly mean snow height in Fredericton - a comparison between ERA5, GNSS-R and 1981-2010 climate normals. The error bars indicate standard deviation from ERA5 and GNSS-R.

7.2.7 Shediac, Canada

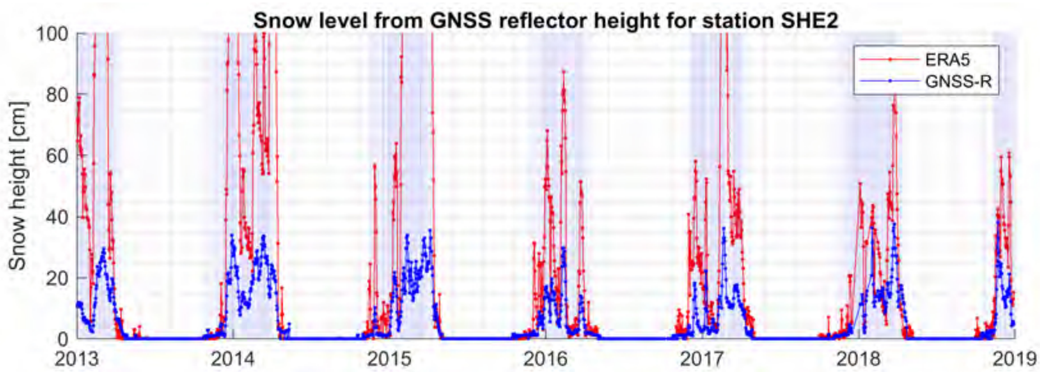

Figure 7.22: Snow height retrievals from IGS station Shediac. The time periods, marked with blue background indicate temperatures below 0^{o}C.

Shediac is the last GNSS station in Canada, where snow height measurements have been performed. The GNSS antenna is mounted on a 2.3m high concrete pillar, just by the coast of Shediac bay on the Northumberland Straights in the province of New Brunswick. Snow height records in close proximity are not available for this station, so the GNSS-R estimates can only be compared with ERA5 data (see figure 7.22). The correlation between the two datasets is relatively high at 0.74, but the RMSE is extremely high, measuring 61cm.

Conclusions and outlook

This study is focused around the applications of ground-based GNSS stations for environmental monitoring. Two distinct methods, namely GNSS Meteorology and GNSS Reflectometry are employed for the derivation and analysis of atmospheric water vapour, soil moisture and snow cover. The study includes development of new software and tools, processing of raw data for the retrieval of water cycle elements and analysis of the obtained data. The datasets cover the territories of Germany, Bulgaria and the world and span between 2000-2019.

In the field of GNSS Meteorology, a database for meteorological and GNSS observations is developed to comprise tropospheric products from leading GNSS Analysis Centers (AC's), meteorological observations and Numerical Weather Prediction (NWP) models simulations. The Sofia University Atmospheric Data Archive (SUADA) is a regional database, currently including data from more than 140 stations, situated mostly in Bulgaria and South-East Europe. The database is designed as a foundation for the GNSS meteorology measurements in this thesis (described in section 4.2) and has become the basis for all GNSS Meteorology research in Bulgaria since. Over 36 000 000 individual GNSS observations and over 500 000 derivatives are stored in the data archive, covering the time period 1997-2019, as well as over 18 000 Radiosoundings, covering the period between 1980-2019. The temporal resolution of GNSS data is from 5 minutes to 6 hours. Data from several NWP models has been included into the database, as well as lidar and gravity observations. The application of SUADA data is shown in case studies during the heat wave in 2007. Despite the difference in the location and sampling rate, the datasets give a negative IWV anomaly in July 2007, with about -4 mm from GNSS-IWV and -5 mm from RS-IWV. The July 2007 has less IWV compared to 2001-2010 with -16 % and -19 % correspondingly for the GNSS-IWV and RS-IWV.

A GNSS processing of a network of 7 stations in Bulgaria is performed with the NAPEOS software and the data is converted and analysed both for seasonal variations, as well as extreme meteorological events. This is one of the first PPP processings with very high temporal resolution executed only for the derivation of tropospheric products. It is also among the first campaigns to be used for validation of high frequency data from NWP. The WRF surface pressure and temperature is evaluated against surface observations from three synoptic stations in Bulgaria. The mean difference for surface pressure between the two datasets is less than $0.5hPa$and the correlation is over 0.99. For the temperature the largest mean difference is $1.1°C$ and the correlation coefficient is over 0.95. The IWV computed with this two datasets has a mean difference is in range of 0.1-1.1 kg/m^2. In order to take advantage of the high temporal resolution of GNSS products for derivation of IWV the surface pressure and temperature from the NWP WRF model is used. The evaluation of WRF on annual basis shows IWV underestimation between 0.5 and 1.5 kg/m^2 at five stations and overestimation at two. In order to link the IWV and precipitation the precipitation efficiency coefficient is computed. The annual precipitation efficiency in 2013 at Lovech and Burgas is about 6 %, which is within the typical values range for low elevation stations in moderate and continental climates. The results from this work have contributed to the COST action ES1206 GNSS4SWEC (*Jones et al.*, 2020).

A climatological study for one GNSS station - Sofia is carried out with comparisons between the tropospheric products from 5 different GNSS processing AC's. The correlations between all used GNSS time series and the Sofia radiosonde measurements are above 0.88. The trend analysis of the datasets shows very different behaviour between the two routine processings and the three reprocessing campaigns. The reprocessings show trends of $0.8\frac{kg/m^2}{decade}$ on average, while the routine processings show -1.3$\frac{kg/m^2}{decade}$ trend on average for the 2000-2009 decade and $0.65\frac{kg/m^2}{decade}$ on average, while the routine processings show $0.8\frac{kg/m^2}{decade}$ trend on average for the 2010-2019 decade.

A bespoke software for estimating soil moisture with GNSS-R in GNSS stations is further developed. The software is validated against available datasets from another data processing center (described in section 5.2). A database for meteorological, GNSS-R and TDR observations is developed to comprise soil moisture measurements, as well as meteorological reanalysis datasets (ERA5). A set of unique soil moisture coefficients is developed to evaluate the quality of the GNSS-R soil moisture retrievals. All results described in section 5.1.

A series of parallel measurements in a couple of experimental GNSS-R site is carried out. Comparisons between state-of-the-art GNSS receivers and low-cost counterparts is carried out. The produced soil moisture datasets are compared to available TDR and meteorological data. Two gravimetric measurements are carried out to further validate the TDR and GNSS-R observations. The GNSS-R derived soil moisture shows highest correlation with TDR during spring, summer and autumn in continental climates. The reflectometry observations show very well the freezing of the soil in the winter period, when sudden drops in the VWC are observed at temperatures below 0°C. GNSS-R can provide soil moisture data with maximum temporal resolution of one day. Retrievals with 3-12 hours are possible using sliding windows approach, but these results can be inaccurate. The signal strength resolution of the GNSS receiver is key for the accuracy of soil moisture retrievals, thus low-cost receivers can be used to derive soil moisture data when SNR resolution below $1\frac{Volt}{Volt}$ is available. With the launch of the new L1C capable

3rd generation of GPS satellites, which will have similar power to the L2C, the low-cost GNSS-R is expected to become an even more potent field of research. The emergence of GNSS receivers with high signal strength resolution will further boost the field. The most important limitation of the position of the GNSS antennae though is not being solved with technological advances, rather with smarter choice of observation sites.

A complete screening of 506 stations, part of the IGS GNSS network for their GNSS-R capabilities is performed for the first time. 30 (6%) of the 506 stations are evaluated as capable of GNSS-R observations for soil moisture determination. The rest of the IGS network is currently incapable of providing useful reflections. Soil moisture estimations from these 30 stations are carried out with comparison to meteorological data and the ERA5 reanalysis. The ERA5 is shown to overestimate the amount of soil moisture in the selected stations. Thus the GNSS stations can be used for validation of results from NWP models and for comparisons with other techniques. Furthermore the precipitation of the ERA5 reanalysis is not well correlated with local measurements. Three of the GNSS-R capable IGS stations (Niue, Tuvalu and Ascention island) are situated on islands in the middle of the world ocean, while most of the inland stations cannot be used for soil moisture retrievals. The longest soil moisture datasets from the IGS network date back to 2004, giving the possibility of further climatological investigations. The analysis of the soil moisture from the IGS stations proved that the method can be applied in all climate conditions.

The effects influencing the precision and accuracy of GNSS-R derived soil moisture are discussed separately, based on available data from two experimental sites in Germany. Data processing experiments are carried out to visualize the robustness of the GNSS-R technique for soil moisture observation. The GNSS-R method provides only relative observations, making it dependent on precise calibration, based on the residual soil moisture for each individual station. Data rate and SNR resolution are shown to be influential on the precision of the measurements. The soil moisture retrieval methodology has proven relatively robust to incorrect reflector height.

A new 1D Empirical Soil Moisture Model (1D-ESMM) using atmospheric parameters is developed. Firstly several Soil Moisture Coefficients SMC's have been proposed to evaluate the accuracy of the GNSS-R soil moisture observations in comparison to precipitation datasets. The development of the SMC's is the basis upon which the empirical soil moisture model is initiated. Several different versions of the bucket model approach are evaluated, with a final version of the model proposed. The newly developed model is then applied to available meteorological datasets and compared with TDR and GNSS-R observations of soil moisture. Furthermore the model is applied in the IGS stations, where atmospheric data is available. In these stations the correlation coefficients and the RMSE is superior to the same metrics when comparing the GNSS-R results to ERA5. The developed model is not diagnostic, but prognostic, so it can be implemented as a compliment to NWP results for soil moisture forecast.

In the field of GNSS-R for snow height, observations are compared to snow buoy measurements in the German Antarctic station Neumayer III. A classical and a new approach for snow height determination from GNSS-R are compared with detailed analysis of the results from the new proposed approach. The results show high correlation of 0.87 between the de-trended snow height measurements, based on the phase changes of the SNR, and the snow buoys. The classical height estimations of the SNR show lower correlation to the snow buoys of 0.60. Snow height observations in 7 IGS stations is performed using the new snow height observation approach. These observations have been validated against climate records and routine observations close to the selected IGS sites, as well as against the ERA5 snow height estimations. The analysis of the data for station Visby, following the new approach, shows very high correlation of 0.91 and low RMSE of 2.26cm, while the classical GNSS-R estimation has RMSE of 2.48cm and ERA5 shows RMSE of 4.2cm when compared to local meteorological observations.

The work on ground-based GNSS-R for soil moisture derivation is continued in GFZ by the establishment of a network of high-end and low-cost GNSS receivers in Argentina. Given, that only two of the South American IGS sites are soil moisture capable, this new network will greatly contribute to the expansion of the technique in a sparsely-covered area. Other areas, lacking IGS GNSS-R-capable sites are Saharan and Sub-Saharan Africa and South-East Asia. The expansion of GNSS networks in these areas can contribute to a world-wide network of soil moisture monitoring sites, using GNSS-R.

With the launch of the new Block IIIA GPS satellites and the completion of the Galileo, the fields of GNSS Meteorology and Reflectometry will gain better potential for high-quality and high-density products. With these new satellites the new L1C GPS signals and the E1 Galileo signals have higher signal strength, compared to the L1C/A GPS signals, currently available. The development of a new generation of low-cost GNSS receivers, capable of multi-frequency tracking and higher SS resolution, in conjunction with the new satellites and signals, will lead to better reflectometry performance of the future low-cost networks.

Apart from soil moisture and snow height, several other environmental parameters can be observed within the IGS network. Several of the IGS stations show potential for sea level observations using GNSS-R. These few coastal stations have not been processed, as far as sea level is not within the scope of this work. Another interesting application of the signal strength data from the IGS network could be examining the GNSS signal attenuation when the receiving antenna is fully covered by snow. Such investigations can be performed in three IGS stations in Antarctica, where the GNSS antennae are situated 10-30cm above ground. Additionally the IGS sites, used for soil moisture observations in this thesis, can also be used for monitoring of the vegetation growth. The full list of stations with description of their surroundings from all directions can be found in the complimentary files and appendices.

The collocation of observations, which is achievable through the methods, described in this work, makes the GNSS networks a very potent candidate for a sensor in the meteorological stations of the future. The development of the concept of such stations has already begun within the WMO Global Basic Observing Network (GBON) initiative.

List of References

Adam, W., H. Dier, and U. Leiterer, 100 years aerology in Lindenberg and first long-time observations in the free atmosphere, *Meteorologische Zeitschrift*, *14*(5), 597–607, doi: 10.1127/0941-2948/2005/0065, 2005.

Ahmed, F., P. Vaclavovic, F. N. Teferle, J. Douša, R. Bingley, and D. Laurichesse, Comparative analysis of real-time Precise Point Positioning Zenith Total Delay estimates, *GPS Solutions*, *20*(2), 187–199, https://doi.org/10.1007/s10291-014-0427-z, 2016.

Ahrens, C. D., *Meteorology today: an introduction to weather, climate, and the environment*, Cengage Learning, iSBN: 978-1337616669, 2012.

Al-Yaari, A., J. Wigneron, Y. Kerr, R. De Jeu, N. Rodriguez-Fernandez, R. Van Der Schalie, A. Al Bitar, A. Mialon, P. Richaume, and A. Dolman, Testing regression equations to derive long-term global soil moisture datasets from passive microwave observations, *Remote Sensing of Environment*, *180*, 453–464, https://doi.org/10.1016/j.rse.2015.11.022, 2016.

Alshawaf, F., K. Balidakis, G. Dick, S. Heise, and J. Wickert, Estimating trends in atmospheric water vapor and temperature time series over Germany, *Atmospheric Measurement Techniques*, *10*(9), 3117, https://doi.org/10.5194/amt-10-3117-2017, 2017.

Anderson, M. G., and J. J. McDonnell, *Encyclopedia of Hydrological Sciences*, vol. 1, Wiley, iSBN: 978-0-471-49103-3, 2005.

Arras, C., J. Wickert, G. Beyerle, S. Heise, T. Schmidt, and C. Jacobi, A global climatology of ionospheric irregularities derived from GPS Radio Occultation, *Geophysical Research Letters*, *35*(14), https://doi.org/10.1029/2008GL034158, 2008.

Asgarimehr, M., V. Zavorotny, J. Wickert, and S. Reich, Can GNSS Reflectometry Detect Precipitation Over Oceans?, *Geophysical Research Letters*, *45*(22), 12–585, https://doi.org/10.1029/2018GL079708, 2018.

Barlage, M., F. Chen, M. Tewari, K. Ikeda, D. Gochis, J. Dudhia, R. Rasmussen, B. Livneh, M. Ek, and K. Mitchell, Noah land surface model modifications to improve snowpack prediction in the Colorado Rocky Mountains, *Journal of Geophysical Research: Atmospheres*, *115*(D22), https://doi.org/10.1029/2009JD013470, 2010.

Behrend, D., R. Haas, D. Pino, L. Gradinarsky, S. Keihm, W. Schwarz, L. Cucurull, and A. Rius, MM5 derived ZWDs compared to observational results from VLBI, GPS and WVR, *Physics and Chemistry of the Earth, Parts A/B/C*, *27*(4), 301–308, https://doi.org/10.1016/S1474-7065(02)00004-9, 2002.

Bender, M., G. Dick, J. Wickert, T. Schmidt, S. Song, G. Gendt, M. Ge, and M. Rothacher, Validation of GPS slant delays using water vapour radiometers and weather models, *Meteorologische Zeitschrift*, *17*(6), 807–812, doi: 10.1127/0941-2948/2008/0341, 2008.

Bender, M., R. Stosius, F. Zus, G. Dick, J. Wickert, and A. Raabe, GNSS water vapour tomography - Expected improvements by combining GPS, GLONASS and Galileo observations, *Advances in Space Research*, *47*(5), 886–897, doi: 10.1016/j.asr.2010.09.011, 2011.

Bergeron, T., On the physics of clouds and precipitation, *Proc. 5th Assembly UGGI, Lisbon, Portugal, 1935*, pp. 156–180, 1935.

Bevis, M., S. Businger, T. Herring, C. Rocken, R. Anthes, and R. Ware, GPS Meteorology: Remote sensing of atmospheric water vapor using the Global Positioning System, *Journal of Geophysical Research*, *97*, 15 787–15 801, doi: 10.1029/92JD01517, 1992.

Blewitt, G., Basics of GPS Technique: Observation Equations. Geodetic Applications of GPS, *Department of Geomatics, University of Newcastle*, pp. 1–46, http://www.nbmg.unr.edu/staff/pdfs/Blewitt%20Basics%20of%20gps.pdf, 1997.

Bock, O., R. Pacione, F. Ahmed, A. Araszkiewicz, Z. Baldysz, K. Balidakis, C. Barroso, S. Bastin, S. Beirle, J. Berckmans, J. Bohm, J. Bogusz, M. Bos, E. Brockmann, M. Cadeddu, B. Chimani, J. Dousa, G. Elgered, M. Elias, R. Fernandes, M. Figurski, E. Fionda, M. Gruszczynska, G. Guerova, J. Guijarro, C. Hackman, R. Heinkelmann, J. Jones, S. Z. Kazanci, A. Klos, D. Landskron, J. P. Martins, V. Mattioli, B. Mircheva, S. Nahmani, R. T. Nilsson, T. Ning, G. Nykiel, A. Parracho, E. Pottiaux, A. Ramos, P. Rebischung, A. Sa, W. Dorigo, H. Schuh, G. Stankunavicius, K. Stepniak, H. Valentim, R. V. Malderen, P. Viterbo, P. Willis, and A. Xaver, *Use of GNSS Tropospheric Products for Climate Monitoring (Working Group 3)*, 267-402 pp., Springer Cham, doi: 10.1007/978-3-030-13901-8_5, 2020.

Boehm, J., A. Niell, P. Tregoning, and H. Schuh, Global Mapping Function (GMF): A new empirical mapping function based on numerical weather model data, *Geophysical Research Letters*, *vol.33, issue 7*, doi: 10.1029/2005GL025546, 2006.

Bolsenga, S., The relationship between total atmospheric water vapor and surface dew point on a mean daily and hourly basis, *Journal of Applied Meteorology*, *4*(3), 430–432, 1965.

Bordi, I., T. Raziei, L. S. Pereira, and A. Sutera, Ground-based GPS measurements of precipitable water vapor and their usefulness for hydrological applications, *Water Resources Management*, *29*(2), 471–486, https://doi.org/10.1007/s11269-014-0672-5, 2015.

Bosy, J., W. Rohm, A. Borkowski, K. Kroszczynski, and M. Figurski, Integration and verification of meteorological observations and NWP model data for the local GNSS tomography, *Atmospheric Research*, *96*(4), 522–530, https://doi.org/10.1016/j.atmosres.2009.12.012, 2010.

Botteron, C., N. Dawes, J. Leclère, J. Skaloud, S. V. Weijs, and P.-A. Farine, Soil moisture & snow properties determination with GNSS in alpine environments: Challenges, status, and perspectives, *Remote Sensing*, *5*(7), 3516–3543, doi:10.3390/rs5073516, 2013.

Brady, N. C., and R. Weil, *Nature and properties of soils: Pearson new international edition*, Pearson Higher Ed, iSBN: 978-1292020792, 2013.

Braham Jr, R. R., The water and energy budgets of the thunderstorm and their relation to thunderstorm development, *Journal of Meteorology*, *9*(4), 227–242, 1952.

Byun, S., and Y. Bar-Sever, A new type of troposphere Zenith Path Delay product of the International GNSS Service, *Journal of Geodesy*, *83*, 367–373, doi 10.1007/s00190-008-0288-8, 2009.

Caissy, M., L. Agrotis, G. Weber, M. Hernandez-Pajares, and U. Hugentobler, The international GNSS real-time service, *GPS World*, *6*(23), 52–58, https://www.gpsworld.com/gnss-systemaugmentation-assistanceinnovation-coming-soon-13044/, 2012.

Cardellach, E., J. Wickert, R. Baggen, J. Benito, A. Camps, N. Catarino, B. Chapron, A. Dielacher, F. Fabra, G. Flato, et al., GNSS Transpolar Earth Reflectometry exploriNg System (G-TERN): Mission Concept, *IEEE Access*, *6*, 13,980–14,018, doi: 10.1109/ACCESS.2018.2814072, 2018.

Chen, M., G. R. Willgoose, and P. M. Saco, Spatial prediction of temporal soil moisture dynamics using HYDRUS-1D, *Hydrological Processes*, *28*(2), 171–185, https://doi.org/10.1002/hyp.9518, 2014.

Chew, C., E. E. Small, and K. M. Larson, An algorithm for soil moisture estimation using GPS-interferometric reflectometry for bare and vegetated soil, *GPS Solutions*, pp. 1–13, https://doi.org/10.1007/s10291-015-0462-4, 2016.

Chew, C. C., E. E. Small, K. M. Larson, and V. U. Zavorotny, Effects of near-surface soil moisture on GPS SNR data: development of a retrieval algorithm for soil moisture, *IEEE Transactions on Geoscience and Remote Sensing*, *52*(1), 537–543, doi: 10.1109/TGRS.2013.2242332, 2014.

Codd, E., A relational model of data for large shared data banks, *Communications of the ACM*, *13, issue 6*, 377–387, doi:10.1145/362384.362685, 1970.

Dach, R., and P. Walser, Bernese GNSS Software Version 5.2, http://www.bernese.unibe.ch/docs/DOCU52.pdf, 2015.

Dach, R., E. Brockmann, S. Schaer, G. Beutler, M. Meindl, L. Prange, H. Bock, A. Jaeggi, and L. Ostini, GNSS processing at CODE: status report, *Journal of Geodesy*, *83(3-4)*, 353–366, https://doi.org/10.1007/s00190-008-0281-2, 2009.

Dee, D. P., S. M. Uppala, A. Simmons, P. Berrisford, P. Poli, S. Kobayashi, U. Andrae, M. Balmaseda, G. Balsamo, d. P. Bauer, et al., The ERA-Interim reanalysis: Configuration and performance of the data assimilation system, *Quarterly Journal of the royal meteorological society*, *137*(656), 553–597, doi:10.1002/qj.828, 2011.

Desbois, M., G. Seze, and G. Szejwach, Automatic classification of clouds on METEOSAT imagery: Application to high-level clouds, *Journal of Applied Meteorology*, *21*(3), 401–412, https://doi.org/10.1175/1520-0450(1982)021<0401:ACOCOM>2.0.CO;2, 1982.

Dessler, A., and S. Sherwood, A matter of humidity, *Science*, *323*, 1020–1021, doi: 10.1126/science.1171264, 2009.

Dick, G., G. Gendt, and C. Reigber, First experience with near real-time water vapor estimation in a German GPS network, *Journal of Atmospheric and Solar-Terrestrial Physics*, *63*(12), 1295–1304, https://doi.org/10.1016/S1364-6826(00)00248-0, 2001.

Dirksen, R., M. Sommer, F. Immler, D. Hurst, R. Kivi, and H. Vömel, Reference quality upper-air measurements: GRUAN data processing for the Vaisala RS92 radiosonde, *Atmospheric Measurement Techniques*, *7*(12), 4463–4490, doi: 10.5194/amtd-7-3727-2014, 2014.

Dousa, J., G. Dick, Y. Altiner, F. Alshawaf, J. Bosy, H. Brenot, E. Brockmann, R. Brozkova, Z. Deng, W. Ding, K. Eben, M. Elias, R. Fernandes, A. Ganas, A. Geiger, G. Guerova, T. Hadas, C. Hill, P. Hordyniec, F. Hurter, J. Jones, M. Kacmarik, K. Kazmierski, J. Kaplon, P. Krc, D. Landskron, X. Li, C. Lu, J. P. Martins, G. Moller, L. Morel, G. Ofeigsson, R. Pacione, C. Pikridas, E. Pottiaux, J. Resler, W. Rohm, A. Sa, J. Sammer, T. Simeonov, W. Sohne, A. Stoycheva, A. Sturze, S. Rozsa, F. N. Teferle,

S. Thorsteinsson, P. Vaclavovic, H. Valentim, B. V. Schaeybroeck, P. Viterbo, K. Wilgan, L. Yang, L. Zhao, N. Zinas, and F. Zus, *Advanced GNSS Processing Techniques (Working Group 1)*, 33-201 pp., Springer Cham, doi: 10.1007/978-3-030-13901-8_3, 2020.

Douša, J., and P. Vaclavovic, Real-time zenith tropospheric delays in support of numerical weather prediction applications, *Advances in Space Research*, *53*(9), 1347–1358, 2014.

Dow, J., R. Neilan, R. Weber, and G. Gendt, Galileo and the IGS: Taking advantage of multiple GNSS constellations, *Advances in Space Research*, *39*, 1545–1551, https://doi.org/10.1016/j.asr.2007.04.064, 2007.

Drusch, M., K. Scipal, P. De Rosnay, G. Balsamo, E. Andersson, P. Bougeault, and P. Viterbo, Towards a Kalman Filter based soil moisture analysis system for the operational ECMWF Integrated Forecast System, *Geophysical Research Letters*, *36*(10), https://doi.org/10.1029/2009GL037716, 2009.

Durand, Y., P. Hallibert, M. Wilson, M. Lekouara, S. Grabarnik, D. Aminou, P. Blythe, B. Napierala, J.-L. Canaud, O. Pigouche, J. Ouaknine, and B. Verez, The flexible combined imager onboard MTG: from design to calibration, in *Sensors, Systems, and Next-Generation Satellites XIX*, vol. 9639, edited by R. Meynart, S. P. Neeck, and H. Shimoda, pp. 1 – 14, International Society for Optics and Photonics, SPIE, doi: 10.1117/12.2196644, 2015.

Egido, A., M. Caparrini, G. Ruffini, S. Paloscia, E. Santi, L. Guerriero, N. Pierdicca, and N. Floury, Global navigation satellite systems reflectometry as a remote sensing tool for agriculture, *Remote Sensing*, *4*(8), 2356–2372, https://doi.org/10.3390/rs4082356, 2012.

Elgered, G., and J. Wickert, *Chapter 38: Monitoring of the Neutral Atmosphere, Springer Handbook of Global Navigation Satellite Systems*, 1109-1138 pp., Springer, ISBN 978-3-319-42926-7, 2017.

Elgered, G., H. Plag, P. van der Marel, S. Barlag, and J. Nash, *COST 716: Exploitation of ground-based GPS for operational numerical weather prediction and climate applications*, European Commission, Brussels, note=http://publications.lib.chalmers.se/records/fulltext/8511/local_8511.pdf, 2005.

Entekhabi, D., E.-G. Njoku, P.-E. O'Neill, K.-H. Kellogg, and W.-T. Crow, The Soil Moisture Active Passive (SMAP) Mission, in *Proceedings of the IEEE*, doi: 10.1109/JPROC.2010.2043918, 2010.

Evett, S., B. Ruthardt, S. Kottkamp, T. Howell, A. Schneider, and J. Tolk, Accuracy and precision of soil water measurements by neutron, capacitance, and TDR methods, in *Proceedings of the 17th Water Conservation Soil Society Symposium, Thailand*, 2002.

Flury, J., and R. Rummel, *Future satellite gravimetry and earth dynamics*, Springer, iSBN 9780387331850, 2005.

Foelsche, U., Tropospheric water vapor imaging by combination of spaceborne and ground-based GNSS sounding data, phD thesis, University Graz, https://inis.iaea.org/search/search.aspx?orig_q=RN:32009424, 1999.

Foti, G., C. Gommenginger, P. Jales, M. Unwin, A. Shaw, C. Robertson, and J. Rosello, Spaceborne GNSS reflectometry for ocean winds: First results from the UK TechDemoSat-1 mission, *Geophysical Research Letters*, *42*(13), 5435–5441, https://doi.org/10.1002/2015GL064204, 2015.

Fuks, I. M., and A. G. Voronovich, Wave diffraction by rough interfaces in an arbitrary plane-layered medium, *Waves in Random Media*, *10*(2), 253–272, https://doi.org/10.1080/13616670009409773, 2000.

Gascoin, S., M. Grizonnet, M. Bouchet, G. Salgues, and O. Hagolle, Theia Snow collection: High-resolution operational snow cover maps from Sentinel-2 and Landsat-8 data, *Earth System Science Data*, *11*(2), 493–514, https://doi.org/10.5194/essd-11-493-2019, 2019.

Gendt, G., G. Dick, A. Rius, and P. Sedo, Comparison of software and techniques for water vapor estimation using German near real-time GPS data, *Physics and Chemistry of the Earth, Part A: Solid Earth and Geodesy*, *26*(6), 417–420, https://doi.org/10.1016/S1464-1895(01)00076-X, 2001.

Gendt, G., G. Dick, C. Reigber, M. Tomassini, Y. Liu, and M. Ramatschi, Near real time GPS water vapor monitoring for numerical weather prediction in Germany, *Journal of the Meteorological Society of Japan. Ser. II*, *82*(1B), 361–370, 2004.

Georgiadou, Y., and A. Kleusberg, On carrier signal multipath effects in relative GPS positioning, *Manuscripta Geodaetica*, *13*(3), 172–179, https://ris.utwente.nl/ws/portalfiles/portal/30136489/Georgiadou1988carrier.pdf, 1988.

Gleason, S., Detecting bistatically reflected GPS signals from low earth orbit over land surfaces, in *Proc. IEEE Int. Geosci. Remote Sens. Symp*, pp. 3086–3089, iSBN: 0-7803-9510-7, 2006.

Gleason, S., and D. Gebre-Egziabher, *GNSS applications and methods*, Artech House, iSBN: 9781596933309, 2009.

Guerova, G., and M. Tomassini, Monitoring IWV from GPS and limited-area forecast model, *University of Bern Institute of Applied Physics Research Rep*, *15*(9), http://publications.iap.unibe.ch/download/729/en/, 2003.

Guerova, G., E. Brockmann, J. Quiby, F. Schubiger, and C. Mätzler, Validation of NWP mesoscale models with Swiss GPS Network AGNES, *Journal of Applied Meteorology*, *42*, 141–150, https://doi.org/10.1175/1520-0450(2003)042<0141:VONMMW>2.0.CO;2, 2003.

Guerova, G., T. Simeonov, and N. Yordanova, The Sofia University Atmospheric Data Archive (SUADA), *Atmospheric Measurement Techniques*, *7*(8), 2683–2694, https://doi.org/10.5194/amt-7-2683-2014, 2014.

Guerova, G., J. Jones, J. Douša, G. Dick, S. de Haan, E. Pottiaux, O. Bock, R. Pacione, G. Elgered, H. Vedel, and M. Bender, Review of the state of the art and future prospects of the ground-based GNSS meteorology in Europe, *Atmospheric Measurement Techniques*, *9*(11), 5385–5406, doi:10.5194/amt-9-5385-2016, 2016a.

Guerova, G., T. Simeonov, and K. Vassileva, Comparison of GNSS tropospheric products obtained by two processing strategies, in Procedings of international symposium of modern technologies, education and profesional practice in geodesy and related fields. ISSN 2367-6051, 2016b.

Guswa, A. J., M. Celia, and I. Rodriguez-Iturbe, Models of soil moisture dynamics in ecohydrology: A comparative study, *Water Resources Research*, *38*(9), 5–1, https://doi.org/10.1029/2001WR000826, 2002.

Haan, S., E. Pottiaux, J. Sanchez-Arriola, M. Bender, J. Berckmans, H. Brenot, C. Bruyninx, L. D. Cruz, G. Dick, N. Dymarska, K. Eben, G. Guerova, J. Jones, P. Krc, M. Lindskog, M. Mile, G. Moller, N. Penov, J. Resler, W. Rohm, M. Slavchev, K. Stoev, A. Stoycheva, E. Trzcina, and F. Zus, *Use of GNSS Tropospheric Products for High-Resolution, Rapid-Update NWP and Severe Weather Forecasting (Working Group 2)*, 203-265 pp., Springer Cham, doi: 10.1007/978-3-030-13901-8_4, 2020.

Haase, J., M. Ge, H. Vedel, and E. Calais, Accuracy and variability of GPS Tropospheric Delay Measurements of Water Vapor in the Western Mediterranean, *Bulletin of the American Meteorological Society*, https://doi.org/10.1175/1520-0450(2003)042<1547:AAVOGT>2.0.CO;2, 2002.

Hallikainen, M. T., F. T. Ulaby, M. C. Dobson, M. A. El-Rayes, and L.-K. Wu, Microwave dielectric behavior of wet soil-part 1: Empirical models and experimental observations, *IEEE Transactions on Geoscience and Remote Sensing*, (1), 25–34, doi: 10.1109/TGRS.1985.289497, 1985.

Hannah, B. M., Modelling and simulation of GPS multipath propagation, Ph.D. thesis, Queensland University of Technology, PhD thesis, 2001.

Haralambous, H., C. Oikonomou, C. Pikridas, G. Guerova, T. Dimitrova, K. Lagouvardos, V. Kotroni, and F. Tymvios, BeRTISS project: Balkan-Mediterranean real-time severe weather service, in *Sixth International Conference on Remote Sensing and Geoinformation of the Environment (RSCy2018)*, vol. 10773, p. 13, International Society for Optics and Photonics, 2018.

Hatch, R. R., Method for precision dynamic differential positioning, US Patent 4,812,991, 1989.

Heise, S., M. Bender, G. Dick, J. Wickert, and F. Zus, GPS atmosphere sounding: Validation of GPS integrated water vapour with microwave radiometer measurements, in *EGU General Assembly Conference Abstracts*, vol. 15, 2013.

Hernández, J. G. R., J. Gracia-Sánchez, T. P. Rodríguez-Martínez, and J. A. Zuñiga-Morales, Correlation between TDR and FDR Soil Moisture Measurements at Different Scales to Establish Water Availability at the South of the Yucatan Peninsula, in *Soil Moisture*, IntechOpen, https://www.intechopen.com/books/soil-moisture/correlation-between-tdr-and-fdr-soil-moisture-measurements-at-different-scales-to-establish-water-av, 2018.

Hobiger, T., and N. Jakowski, *Chapter 6: Atmospheric Signal Propagation, Springer Handbook of Global Navigation Satellite Systems*, 191-220 pp., Springer, ISBN 978-3-319-42926-7, 2017.

Hoffmann-Wellenhof, B., H. Litchtenegger, and Walse.E, *GNSS-Global Navigation Satellite Systems: GPS, GLONASS, Galileo* & *More*, 1 ed., Springer, Wien, New York, iSBN 787-3-211-73012-6, 2008.

Hofmann-Wellenhof, B., H. Lichtenegger, and J. Collins, *Global positioning system: theory and practice*, Springer Science & Business Media, iSBN 9783211828397, 2012.

Hong, S.-Y., Y. Noh, and J. Dudhia, A new vertical diffusion package with an explicit treatment of entrainment processes, *Monthly weather review*, *134* (9), 2318–2341, 2006.

Hong, S.-Y., K.-S. S. Lim, Y.-H. Lee, J.-C. Ha, H.-W. Kim, S.-J. Ham, and J. Dudhia, Evaluation of the WRF double-moment 6-class microphysics scheme for precipitating convection, *Advances in Meteorology*, *2010*, https://doi.org/10.1175/MWR3199.1, 2010.

http://climate.weather.gc.ca/, Environment Canada: Canadian Climate Normals 1981-2010 Climate Normals and Averages.

http://egvap.dmi.dk/, EGVAP project.

https://maps.google.com/, Google Maps.

https://www.google.com/streetview/, Google Street View.

http://www.bulipos.eu/, BULgarian Intelegent POSition determination System, 2013.

http://www.igs.org/, International GNSS Service web portal.

http://www.ogimet.com/, Ogimet Weather Information Service.

Huntington, T. G., Evidence for intensification of the global water cycle: review and synthesis, *Journal of Hydrology*, *319*(1), 83–95, https://doi.org/10.1016/j.jhydrol.2005.07.003, 2006.

Johnston, G., A. Riddell, and G. Hausler, The International GNSS Service, in *Springer handbook of global navigation satellite systems*, pp. 967–982, Springer, 2017.

Jones, J., G. Guerova, J. Dousa, G. Dick, S. de Haan, E. Pottiaux, O. Bock, R. Pacione, and R. van Malderen (Eds.), *COST Action ES1206: Advanced Global Navigation Satellite Systems tropospheric products for monitoring severe weather events and climate*, 563 pp., Springer Cham, iSBN: 978-3-030-13900-1, 2020.

Kargel, J. S., G. J. Leonard, M. P. Bishop, A. Kääb, and B. H. Raup, *Global land ice measurements from space*, Springer, iSBN: 978-3-540-79818-7, 2014.

Katzberg, S. J., O. Torres, M. S. Grant, and D. Masters, Utilizing calibrated GPS reflected signals to estimate soil reflectivity and dielectric constant: Results from SMEX02, *Remote sensing of environment*, *100*(1), 17–28, https://doi.org/10.1016/j.rse.2005.09.015, 2006.

Kerr, Y. H., P. Waldteufel, J.-P. Wigneron, S. Delwart, F. O. Cabot, J. Boutin, M.-J. Escorihuela, J. Font, N. Reul, and C. Gruhier, The SMOS mission: New tool for monitoring key elements of the global water cycle, *Proceedings of the IEEE, Institute of Electrical and Electronics Engineers.*, *98*(5), 666–687, doi: 10.1109/JPROC.2010.2043032, 2010.

Köppen, W., Klassifikation der Klima nach Temperatur, Niederschlag und Jahreslauf, *Pet. Mitt.*, *64*, 243–248, 1918.

Kouba, J., Implementation and testing of the gridded Vienna Mapping Function 1 (VMF1), *Journal of Geodesy*, *82*(4-5), 193–205, https://doi.org/10.1007/s00190-007-0170-0, 2008.

Ladstädter, F., A. Steiner, M. Schwärz, and G. Kirchengast, Climate intercomparison of GPS Radio Occultation, RS90/92 radiosondes and GRUAN from 2002 to 2013, *Atmospheric Measurement Techniques*, *8*(4), 1819, https://doi.org/10.5194/amt-8-1819-2015, 2015.

Larson, K. M., GPS interferometric reflectometry: applications to surface soil moisture, snow depth, and vegetation water content in the western United States, *Wiley Interdisciplinary Reviews: Water*, *3*(6), 775–787, https://doi.org/10.1002/wat2.1167, 2016.

Larson, K. M., and F. G. Nievinski, GPS snow sensing: results from the EarthScope Plate Boundary Observatory, *GPS solutions*, *17*(1), 41–52, https://doi.org/10.1007/s10291-012-0259-7, 2013.

Larson, K. M., E. E. Small, E. Gutmann, A. Bilich, P. Axelrad, and J. Braun, Using GPS multipath to measure soil moisture fluctuations: Initial results, *GPS solutions*, *12*(3), 173–177, https://doi.org/10.1007/s10291-007-0076-6, 2008a.

Larson, K. M., E. E. Small, E. D. Gutmann, A. L. Bilich, J. J. Braun, and V. U. Zavorotny, Use of GPS receivers as a soil moisture network for water cycle studies, *Geophysical Research Letters*, *35*(24), https://doi.org/10.1029/2008GL036013, 2008b.

Larsson, M., J. Nordevall, R. Sirefelt, and E. Staf, Estimering av snödjup genom analys av flervägsreflekterade GPS-signaler, MSc thesis, https://odr.chalmers.se/bitstream/20.500.12380/159021/1/159021.pdf, 2012.

Lawrence, M. G., The relationship between relative humidity and the dewpoint temperature in moist air: A simple conversion and applications, *Bulletin of the American Meteorological Society*, *86*(2), 225–234, https://doi.org/10.1175/BAMS-86-2-225, 2005.

Leib, B. G., J. D. Jabro, and G. R. Matthews, Field evaluation and performance comparison of soil moisture sensors, *Soil Science*, *168*(6), 396–408, doi: 10.1097/01.ss.0000075285.87447.86, 2003.

Li, H., Z. Wang, G. He, and W. Man, Estimating snow depth and snow water equivalence using repeat-pass interferometric SAR in the northern piedmont region of the Tianshan Mountains, *Journal of Sensors*, *2017*, https://doi.org/10.1155/2017/8739598, 2017.

Li, M., W. Li, C. Shi, Q. Zhao, X. Su, L. Qu, and Z. Liu, Assessment of precipitable water vapor derived from ground-based BeiDou observations with Precise Point Positioning approach, *Advances in space research*, *55*(1), 150–162, 2015a.

Li, X., G. Dick, M. Ge, S. Heise, J. Wickert, and M. Bender, Real-time GPS sensing of atmospheric water vapor: Precise point positioning with orbit, clock, and phase delay corrections, *Geophysical research letters*, *41*(10), 3615–3621, https://doi.org/10.1002/2013GL058721, 2014.

Li, X., G. Dick, C. Lu, M. Ge, T. Nilsson, T. Ning, J. Wickert, and H. Schuh, Multi-GNSS meteorology: real-time retrieving of atmospheric water vapor from BeiDou, Galileo, GLONASS, and GPS observations, *IEEE Transactions on Geoscience and Remote Sensing*, *53*(12), 6385–6393, doi: 10.1109/TGRS.2015.2438395, 2015b.

Lievens, H., M. Demuzere, H.-P. Marshall, R. H. Reichle, L. Brucker, I. Brangers, P. de Rosnay, M. Dumont, M. Girotto, W. W. Immerzeel, et al., Snow depth variability in the Northern Hemisphere mountains observed from space, *Nature communications*, *10*(1), 1–12, https://doi.org/10.1038/s41467-019-12566-y, 2019.

Lomb, N. R., Least-squares frequency analysis of unequally spaced data, *Astrophysics and space science*, *39*(2), 447–462, 1976.

Marini, J. W., Correction of satellite tracking data for an arbitrary tropospheric profile, *Radio Science*, *7*(2), 223–231, 1972.

Marvin, C. F., *Psychrometric tables for obtaining the vapor pressure, relative humidity, and temperature of the dew-point*, 235, US Government Printing Office, 1900.

Masters, D., P. Axelrad, and S. Katzberg, Initial results of land-reflected GPS bistatic radar measurements in SMEX02, *Remote sensing of environment*, *92*(4), 507–520, https://doi.org/10.1016/j.rse.2004.05.016, 2004.

Matzarakis, A., C. de Freitas, and D. Scott, *Developments in tourism climatology*, 289 pp., Commission Climate, Tourism and Recreation, International Society of Biometeorology, 2007.

Meindl, M., R. Dach, and Y. Jean, International GNSS Service Technical Report 2011, *Tech. rep.*, IGS Central Bureau.

Michalakes, J., Design of a Next-Generation Regional Weather Research and Forecast Model, *Tech. rep.*, Argonne National Lab., IL (US), 1999.

Michalakes, J., J. Dudhia, D. Gill, T. Henderson, J. Klemp, W. Skamarock, and W. Wang, The Weather Reseach and Forecast Model: Software Architecture and Performance, in *Use of high performance computing in meteorology*, pp. 156–168, World Scientific, https://doi.org/10.1142/9789812701831_ 0012, 2005.

Mircheva, B., M. Tsekov, U. Meyer, and G. Guerova, Anomalies of hydrological cycle components during the 2007 heat wave in Bulgaria, *Journal of atmospheric and solar-terrestrial physics*, *165*, 1–9, https://doi.org/10.1016/j.jastp.2017.10.005, 2017.

Mlawer, E. J., S. J. Taubman, P. D. Brown, M. J. Iacono, and S. A. Clough, Radiative transfer for inhomogeneous atmospheres: RRTM, a validated correlated-k model for the longwave, *Journal of Geophysical Research: Atmospheres*, *102*(D14), 16,663–16,682, https://doi.org/10.1029/97JD00237, 1997.

Morland, J., TROWARA–Tropospheric water vapour radiometer: Radiometer review and new calibration model, *IAP Res. Rep*, *15*, 14–16, 2002.

Morland, J., and C. Mätzler, Spatial interpolation of GPS integrated water vapour measurements made in the Swiss Alps, *Meteorological applications*, *14*, 15–26, 2007.

Morland, J., B. Deuber, D. G. Feist, L. Martin, S. Nyeki, N. Kampfer, C. Mätzler, P. Jeannet, and L. Vuilleumier, The STARTWAVE atmospheric water vapour database, 2006.

Neeck, S. P., T. J. Magner, and G. E. Paules, NASA's small satellite missions for Earth observation, *Acta Astronautica*, *56*(1-2), 187–192, https://www.dlr.de/iaa.symp/Portaldata/49/Resources/dokumente/archiv4/IAA-B4-1001.pdf, 2005.

Nicolaus, M., S. Arndt, S. Hendricks, G. Heygster, M. Hoppmann, M. Huntemann, C. Katlein, D. Langevin, L. Rossmann, and G. König-Langlo, Snow depth and air temperature on sea ice derived from autonomous snow buoy measurements, https://epic.awi.de/id/eprint/40842/1/NicolausSnowBuoysLPS.pdf, 2016.

Niell, A., Global mapping functions for the atmosphere delay at radio wavelengths, *Journal of Geophysical Research: Solid Earth*, *101*(B2), 3227–3246, https://doi.org/10.1029/95JB03048, 1996.

Nievinski, F. G., and K. M. Larson, Inverse modeling of GPS multipath for snow depth estimation—Part I: Formulation and simulations, *IEEE Transactions on Geoscience and Remote Sensing*, *52*(10), 6555–6563, doi: 10.1109/TGRS.2013.2297681, 2014a.

Nievinski, F. G., and K. M. Larson, Inverse modeling of GPS multipath for snow depth estimation—Part II: Application and validation, *IEEE Transactions on Geoscience and Remote Sensing*, *52*(10), 6564–6573, doi: 10.1109/TGRS.2013.2297688, 2014b.

Ning, T., GPS Meteorology: With Focus on Climate Applications, Ph.D. thesis, Chalmers University of Technology, https://core.ac.uk/download/pdf/70594409.pdf, 2012.

Nischan, T., GFZRNX-RINEX GNSS data conversion and manipulation toolbox (Version 1.05), *GFZ Data Services. Potsdam, Germany: German Research Centre for Geosciences (GFZ) https://doi. org/10.5880/GFZ*, *1*(2016.002), doi:10.5880/GFZ.1.1.2016.002, 2016.

Oki, T., and S. Kanae, Global hydrological cycles and world water resources, *science*, *313*(5790), 1068–1072, doi: 10.1126/science.1128845, 2006.

Oltmans, S., and D. Hofmann, Increase in lower-stratospheric water vapour at a mid-latitude Northern Hemisphere site from 1981 to 1994, *Nature*, *374*(6518), 146, https://www.nature.com/articles/374146a0, 1995.

Orsolini, Y., M. Wegmann, E. Dutra, B. Liu, G. Balsamo, K. Yang, P. d. Rosnay, C. Zhu, W. Wang, R. Senan, et al., Evaluation of snow depth and snow cover over the Tibetan Plateau in global reanalyses using in situ and satellite remote sensing observations, *The Cryosphere*, *13*(8), 2221–2239, https://doi.org/10.5194/tc-13-2221-2019, 2019.

O'Gorman, P., and C. Muller, How closely do changes in surface and column water vapor follow Clausius–Clapeyron scaling in climate change simulations?, *Environmental Research Letters*, *5*(2), 025,207, doi:10.1088/1748-9326/5/2/025207, 2010.

Pacione, R., F. Vespe, and B. Pace, Near real-time GPS zenith total delay validation at E-GVAP super sites, *Subcommission for the European Reference Frame (EUREF), Brussels*, pp. 65–77, 2008.

Parkinson, B. W., J. J. Spilker, P. Axelrad, and P. Enge (Eds.), *Global Positioning System: Theory and Applications*, vol. I, American Institute of Aeronautics and Astronautics, iSBN 9781563472497, 2005.

Petrie, E. J., M. A. King, P. Moore, and D. A. Lavallée, A first look at the effects of ionospheric signal bending on a globally processed GPS network, *Journal of Geodesy*, *84*(8), 491–499, doi: 10.1007/s00190-010-0386-2, 2010.

Poli, P., *List of Observations Assimilated in ERA-40 and ERA-interim:(v 1.0)*, ECMWF, https://www.ecmwf.int/file/23554/download?token=GAj9vtCI, 2010.

Poli, P., H. Hersbach, D. P. Dee, P. Berrisford, A. J. Simmons, F. Vitart, P. Laloyaux, D. G. Tan, C. Peubey, J.-N. Thépaut, et al., ERA-20C: An atmospheric reanalysis of the twentieth century, *Journal of Climate*, *29*(11), 4083–4097, 2016.

Press, W. H., and G. B. Rybicki, Fast algorithm for spectral analysis of unevenly sampled data, *The Astrophysical Journal*, *338*, 277–280, 1989.

Rajkai, K., and B. Rydén, Measuring areal soil moisture distribution with the TDR method, *Geoderma*, *52*(1-2), 73–85, https://doi.org/10.1016/0016-7061(92)90076-J, 1992.

Raval, A., and V. Ramanathan, Observational determination of the greenhouse effect, *Nature*, *342*(6251), 758, https://www.nature.com/articles/342758a0, 1989.

Rebischung, P., J.Griffiths, J. Ray, R. Schmid, X. Collilieux, and B.Garayt, IGS08: the IGS realization of ITRF2008, *GPS Solutions*, *16*, 483–494, doi 10.1007/s10291-011-0248-2, 2012.

Reigber, C., G. Gendt, and J. Wickert, GPS-Atmosphären-Sondierungs-Projekt (GASP), *Scientific Technical Report/Geoforschungszentrum Potsdam*, https://gfzpublic.gfz-potsdam.de/rest/items/item_8624_4/component/file_8623/content, 2004.

Reitan, C. H., Surface dew point and water vapor aloft, *Journal of Applied Meteorology*, *2*(6), 776–779, 1963.

Reynolds, S., The gravimetric method of soil moisture determination, *J. Hydrol*, *11*, 258–273, 1970.

Robinson, D., S. B. Jones, J. Wraith, D. Or, and S. Friedman, A review of advances in dielectric and electrical conductivity measurement in soils using time domain reflectometry, *Vadose Zone Journal*, *2*(4), 444–475, https://doi.org/10.2113/2.4.444, 2003.

Rodriguez-Alvarez, N., X. Bosch-Lluis, A. Camps, I. Ramos-Perez, E. Valencia, H. Park, and M. Vall-Llossera, Vegetation water content estimation using GNSS measurements, *IEEE Geoscience and Remote Sensing Letters*, *9*(2), 282–286, doi: 10.1109/LGRS.2011.2166242, 2012.

Roesler, C., and K. M. Larson, Software tools for GNSS interferometric reflectometry (GNSS-IR), *GPS Solutions*, *22*(3), 80, https://doi.org/10.1007/s10291-018-0744-8, 2018.

Rosnay, P., M. Drusch, G. Balsamo, C. Albergel, and L. Isaksen, Extended kalman filter soil-moisture analysis in the ifs, ecmwf newsletter, doi: 10.21957/ik7co53s, 2011.

Rushton, K., V. Eilers, and R. Carter, Improved soil moisture balance methodology for recharge estimation, *Journal of Hydrology*, *318*(1-4), 379–399, https://doi.org/10.1016/j.jhydrol.2005.06.022, 2006.

Saastamoinen, J., Atmospheric correction for the troposphere and stratosphere in radio ranging satellites, *The use of artificial satellites for geodesy*, pp. 247–251, 1972.

Scargle, J. D., Studies in astronomical time series analysis. II-Statistical aspects of spectral analysis of unevenly spaced data, *The Astrophysical Journal*, *263*, 835–853, 1982.

Schlüssel, P., T. H. Hultberg, P. L. Phillips, T. August, and X. Calbet, The operational IASI Level 2 processor, *Advances in space research*, *36*(5), 982–988, doi: 10.1016/j.asr.2005.03.008, 2005.

Schmetz, J., P. Pili, S. Tjemkes, D. Just, J. Kerkmann, S. Rota, and A. Ratier, An introduction to Meteosat second generation (MSG), *Bulletin of the American Meteorological Society*, *83*(7), 977–992, https://doi.org/10.1175/1520-0477(2002)083<0977:AITMSG>2.3.CO;2, 2002.

Schmidt, T., J. Wickert, G. Beyerle, and S. Heise, Global tropopause height trends estimated from GPS radio occultation data, *Geophysical Research Letters*, *35*(11), https://doi.org/10.1029/2008GL034012, 2008.

Schroedter-Homscheidt, M., A. Drews, and S. Heise, Total water vapor column retrieval from MSG-SEVIRI split window measurements exploiting the daily cycle of land surface temperatures, *Remote sensing of environment*, *112*(1), 249–258, https://doi.org/10.1016/j.rse.2007.05.006, 2008.

Schuh, H., and J. Wickert, New developments in space geodetic research: VLBI observations to space probes and GNSS remote sensing, in *Progress on Geodesy and Geodynamics*, pp. 366–384, Hubei Science and Technology Press, 2014.

Schwitalla, T., H.-S. Bauer, V. Wulfmeyer, and G. Zängl, Systematic errors of QPF in low-mountain regions as revealed by MM5 simulations, *Meteorologische Zeitschrift*, *17*(6), 903–919, doi: 10.1127/0941-2948/2008/0338, 2008.

Sellers, P., R. Dickinson, D. Randall, A. Betts, F. Hall, J. Berry, G. Collatz, A. Denning, H. Mooney, C. Nobre, et al., Modeling the exchanges of energy, water, and carbon between continents and the atmosphere, *Science*, *275*(5299), 502–509, doi: 10.1126/science.275.5299.502, 1997.

Shangguan, M., S. Heise, M. Bender, G. Dick, M. Ramatschi, and J. Wickert, Validation of GPS atmospheric water vapor with WVR data in satellite tracking mode, in *Annales of Geophysicae*, vol. 33, pp. 55–61, Copernicus Publications (EGU), https://doi.org/10.5194/angeo-33-55-2015, 2015.

Simeonov, T., and G. Guerova, *Sofia University GNSS analysis center (SUGAC): First processing campaign*, 178-181 pp., Springer Cham, doi: 10.1007/978-3-030-13901-8_3, 2020.

Šimøunek, J., M. Šejna, H. Saito, M. Sakai, and M. T. Van Genuchten, The HYDRUS-1D software package for simulating the movement of water, heat, and multiple solutes in variably saturated media, Version 4.0, *HYDRUS software series*, *3*, 315, https://www.pc-progress.com/Downloads/Pgm_hydrus1D/HYDRUS1D-4.08.pdf, 2008.

Sinha, A., and J. E. Harries, Water vapour and greenhouse trapping: The role of far infrared absorption, *Geophysical Research Letters*, *22*(16), 2147–2150, https://doi.org/10.1029/95GL01891, 1995.

Sissenwine, N., M. Dubin, and H. Wexler, The U.S. Standard Atmosphere, *Journal of Geophysical Research*, *67, issue 9*, 3627–3630, doi: 10.1029/JZ067i009p03627, 1962.

Skamarock, W., J. Klemp, J. Dudhia, D. Gill, D. Barker, M. Duda, X. Huang, W. Wang, and J. Powers, A description of the advanced research WRF Version 3, NCAR technical note, Mesoscale and Microscale Meteorology Division, *National Center for Atmospheric Research, Boulder, Colorado, USA*, https://opensky.ucar.edu/islandora/object/technotes%3A500/datastream/PDF/view, 2008.

Smith, W. L., Note on the relationship between total precipitable water and surface dew point, *Journal of Applied Meteorology*, *5*(5), 726–727, 1966.

Soehne, W., and G. Weber, EUREF Troposphere Combination at BKG-First Results and Improvements, in *Extended Abstracts of the COST-716 Workshop*, 2002.

Speight, J. G., et al., *Lange's handbook of chemistry*, vol. 1, McGraw-Hill New York, iSBN: 9780070161948, 2005.

Stoycheva, A., I. Manafov, K. Vassileva, and G. Guerova, Study of persistent fog in bulgaria with sofia stability index, gnss tropospheric products and wrf simulations, *Journal of Atmospheric and Solar-Terrestrial Physics*, *161*, 160–169, https://doi.org/10.1016/j.jastp.2017.06.011, 2017.

Straub, C., A. Murk, and N. Kämpfer, MIAWARA-C, a new ground based water vapor radiometer for measurement campaigns, *Atmospheric Measurement Techniques*, *3*(5), 1271–1285, doi: 10.5194/amt-3-1271-2010, 2010.

Strode, P. R., and P. D. Groves, GNSS multipath detection using three-frequency signal-to-noise measurements, *GPS solutions*, *20*(3), 399–412, https://doi.org/10.1007/s10291-015-0449-1, 2016.

Tabibi, S., F. G. Nievinski, T. van Dam, and J. F. Monico, Assessment of modernized GPS L5 SNR for ground-based multipath reflectometry applications, *Advances in Space Research*, *55*(4), 1104–1116, https://doi.org/10.1016/j.asr.2014.11.019, 2015.

Teunissen, P., and O. Montenbruck, *Springer Handbook of Global Navigation Satellite Systems*, 1328 pp., Springer, ISBN 978-3-319-42926-7, 2017.

Thayer, G. D., An improved equation for the radio refractive index of air, *Radio Science*, *9*(10), 803–807, https://doi.org/10.1029/RS009i010p00803, 1974.

Thorne, P., H. Vömel, G. Bodeker, M. Sommer, A. Apituley, F. Berger, S. Bojinski, G. Braathen, B. Calpini, B. Demoz, et al., GCOS reference upper air network (GRUAN): Steps towards assuring future climate records, in *AIP Conference Proceedings*, vol. 1552, pp. 1042–1047, AIP, https://doi.org/10.1063/1.4821421, 2013.

Tralli, D. M., and S. M. Lichten, Stochastic estimation of tropospheric path delays in Global Positioning System geodetic measurements, *Bulletin géodésique*, *64, issue 2*, 127–152, doi:10.1007/BF02520642, 1990.

Tregoning, P., R. Boers, D. O'Brien, and M. Hendy, Accuracy of absolute precipitable water vapor estimates from GPS observations, *Journal of Geophysical Research: Atmospheres*, *103*(D22), 28,701–28,710, https://doi.org/10.1029/98JD02516, 1998.

Trizna, D. B., A model for Brewster angle damping and multipath effects on the microwave radar sea echo at low grazing angles, *IEEE Transactions on Geoscience and Remote Sensing*, *35*(5), 1232–1244, 1997.

Tuller, S. E., The world distribution of annual precipitation efficiency, *Journal of Geography*, *70*(4), 219–223, 1971.

Vey, S., A. Güntner, J. Wickert, T. Blume, and M. Ramatschi, Long-term soil moisture dynamics derived from GNSS interferometric reflectometry: A case study for Sutherland, South Africa, *GPS solutions*, *20*(4), 641–654, https://doi.org/10.1007/s10291-015-0474-0, 2016a.

Vey, S., A. Güntner, J. Wickert, T. Blume, H. Thoss, and M. Ramatschi, Monitoring snow depth by GNSS Reflectometry in built-up areas: A case study for Wettzell, Germany, *IEEE Journal of selected topics in applied Earth observations and Remote Sensing*, *9*(10), 4809–4816, doi: 10.1109/JSTARS.2016.2516041, 2016b.

Wagner, W., G. Lemoine, and H. Rott, A method for estimating soil moisture from ERS scatterometer and soil data, *Remote sensing of environment*, *70*(2), 191–207, https://doi.org/10.1016/S0034-4257(99)00036-X, 1999.

Ware, R., C. Alber, C. Rocken, and F. Solheim, Sensing integrated water vapor along GPS ray paths, *Geophysical Research Letters*, *24*(4), 417–420, http://radiometrics.com/data/uploads/2012/11/ware_grl97.pdf, 1997.

Wickert, J., C. Reigber, G. Beyerle, R. König, C. Marquardt, T. Schmidt, L. Grunwaldt, R. Galas, T. K. Meehan, W. G. Melbourne, et al., Atmosphere sounding by GPS Radio Occultation: First results from CHAMP, *Geophysical Research Letters*, *28*(17), 3263–3266, https://doi.org/10.1029/2001GL013117, 2001.

Wickert, J., G. Michalak, T. Schmidt, G. Beyerle, C.-Z. Cheng, S. B. Healy, S. Heise, C.-Y. Huang, N. Jakowski, W. Köhler, et al., GPS Radio Occultation: Results from CHAMP, GRACE and FORMOSAT-3/COSMIC., *Terrestrial, Atmospheric & Oceanic Sciences*, *20*(1), https://doi.org/10.3319/TAO.2007.12.26.01(F3C), 2009.

Wickert, J., E. Cardellach, M. Martín-Neira, J. Bandeiras, L. Bertino, O. B. Andersen, A. Camps, N. Catarino, B. Chapron, F. Fabra, et al., GEROS-ISS: GNSS REflectometry, Radio Occultation, and Scatterometry Onboard the International Space Station, *IEEE Journal of selected topics in applied Earth observations and Remote Sensing*, *9*(10), 4552–4581, doi: 10.1109/JSTARS.2016.2614428, 2016.

Yuan, Y., K. Zhang, W. Rohm, S. Choy, R. Norman, and C.-S. Wang, Real-time retrieval of precipitable water vapor from GPS precise point positioning, *Journal of Geophysical Research: Atmospheres*, *119*(16), 10,044–10,057, 2014.

Zavorotny, V. U., K. M. Larson, J. J. Braun, E. E. Small, E. D. Gutmann, and A. L. Bilich, A physical model for GPS multipath caused by land reflections: Toward bare soil moisture retrievals, *IEEE Journal of Selected Topics in Applied Earth Observations and Remote Sensing*, *3*(1), 100–110, doi: 10.1109/JSTARS.2009.2033608, 2010.

Zazueta, F. S., and J. Xin, Soil moisture sensors, *Soil Sci*, *73*, 391–401, https://pdfs.semanticscholar.org/431b/7c38620a036f11915d8e8219555f67c1f06a.pdf, 1994.

Zhang, S., J.-C. Calvet, J. Darrozes, N. Roussel, F. Frappart, and G. Bouhours, Deriving surface soil moisture from reflected GNSS signal observations from a grassland site in southwestern France, *Hydrology and Earth System Sciences*, *22*(3), 1931–1946, https://doi.org/10.5194/hess-22-1931-2018, 2018.

Zhu, Y., K. Yu, J. Zou, and J. Wickert, Sea ice detection using GNSS-R delay-Doppler maps from UK TechDemoSat-1, in *Geoscience and Remote Sensing Symposium (IGARSS), 2017 IEEE International*, pp. 4110–4113, IEEE, doi: 10.1109/IGARSS.2017.8127904, 2017.

Zinner, T., H. Mannstein, and A. Tafferner, Cb-TRAM: Tracking and monitoring severe convection from onset over rapid development to mature phase using multi-channel Meteosat-8 SEVIRI data, *Meteorology and Atmospheric Physics*, *101*(3-4), 191–210, https://doi.org/10.1007/s00703-008-0290-y, 2008.

Zumberge, J., M. Heflin, D. Jefferson, M. Watkins, and F. H. Webb, Precise Point Positioning for the efficient and robust analysis of GPS data from large networks, *Journal of Geophysical Research: Solid Earth*, *102*(B3), 5005–5017, https://doi.org/10.1029/96JB03860, 1997.

List of Figures

1.1 Water cycle diagram. 1
1.2 Water balance between oceans, land and atmosphere. 2
1.3 Water vapour balance. 5
1.4 Soil water balance. 6

2.1 The RS92 radiosonde from Vaisala. 9
2.2 Map of the GRUAN network. 10
2.3 Microwave radiometer on the roof of A17 building at GFZ. 11
2.4 Microwave radiometer profiles of the atmosphere. 11
2.5 TDR probe. 13
2.6 Drying of soil samples. 14
2.7 Snow buoy. 16
2.8 Water vapour measurement techniques spatio-temporal resolution. 21
2.9 Soil moisture measurement techniques spatio-temporal resolution. 22
2.10 Snow height measurement techniques spatio-temporal resolution. 23

3.1 Timeline of GPS signals availability. 26
3.2 GNSS signals and the layers of the atmosphere. 27
3.3 Visualization of Snell's law and Fermat's principle. 30
3.4 Effect of the neutral atmosphere on the GNSS signals and mapping delays to zenith. 31
3.5 NAPEOS processing scheme for PPP processing, used in this thesis. 34
3.6 EPOS processing scheme. 35
3.7 Evolution of the Bernese GNSS processing software. 36
3.8 IWV processing data flow and data sets. 38
3.9 GNSS signal penetration in wet and dry soils. 39
3.10 GNSS signal polarization during reflection. 40
3.11 Simulated interference patterns in the GNSS signal strength data. 41
3.12 GNSS direct and reflected signals as received by a permanent GNSS station. 42
3.13 Reflection of first Fresnel zone. 44
3.14 Visualization of Fresnel zones. 44

4.1 Monthly anomaly of temperature and precipitation for Sofia, Bulgaria. . . 52
4.2 Monthly mean IWV and anomaly for Sofia, Bulgaria. 53
4.3 IWV for station Sofia from Radiosounding. 54
4.4 IWV for station Sofia from GFZ. 54
4.5 IWV for station Sofia from BKG. 55
4.6 Power spectra of frequencies of the BEK GNSS tropospheric products and Radiosounding. 56
4.7 Map of the ground-based stations of the Bulipos GNSS network. 59
4.8 GNSS IWV and IWV* for station Burgas in 2013. 61
4.9 Correlation and RMSE between WRF and GNSS IWV for all Bulgarian stations for each season. 62
4.10 Comparison of de-trended WRF and GNSS IWV for station Lovech. 62
4.11 Monthly average water vapour from WRF and GNSS and correlations for Bulgarian stations. 63
4.12 Daily cycle with half-hourly resolution of IWV from GNSS and WRF. . . . 65
4.13 IWV during May 17th, 2013 hail storm near Montana. 66
4.14 Precipitation efficiency from WRF and GNSS for Bulgarian stations. . . . 68
4.15 IWV comparison between PPP and network solution processings. 70

5.1 GNSS-R data flow. 73
5.2 Position of station p038 from Unavco web site. 76
5.3 Soil moisture retrievals comparison between GFZ and PBO for station Portales. 76
5.4 Soil moisture scatter comparison between GFZ and PBO for station Portales. 77
5.5 Soil moisture retrievals comparison between GNSS-R and ERA5 for station Portales. 77
5.6 The GNSS station in station Marquardt. 79
5.7 GNSS setups in station Marquardt. The four symbol abbreviations of the stations are used to identify the unique combinations of antennae and receivers. 80
5.8 Fresnel zones of all GNSS stations in Marquardt. 81
5.9 Sector soil moisture retreivals for L2C signals. 82
5.10 Scatter plots of TDR measurements at different depths and GNSS soil moisture. 83
5.11 Seasonal comparrisson of correlation and RMSE. 84
5.12 Winter soil moisture in Marquardt. 85
5.13 Summer soil moisture in Marquardt. 86
5.14 Severe summer rainfall - high resolution GNSS soil moisture experiment. . 87
5.15 Comparison of the signal strength from the installed receivers in Marquardt. 89

5.16 Scatter plot of soil moisture retrievals from GNSS. 90
5.17 Data availability from all GNSS sensors in Marquardt. 90
5.18 Soil moisture from all GNSS receivers from Marquardt. 91
5.19 Collecting gravimetric samples in Marquardt. 92
5.20 Gravimetric measurements, compared to GNSS and TDR for Marquardt. . 93
5.21 Fresnel zones of reflections, observed at GNSS station Fürstensee and seasonal comparison of correlation and RMSE. 94
5.22 Soil moisture comparisons between GNSS and TDR at station Fürstensee. 95
5.23 Soil moisture at station Fürstensee, autumn 2016. 95
5.24 Map of IGS stations, suitable for reflectometry. 97
5.25 List of IGS stations for soil moisture retrieval. 99
5.26 IGS station Visby - Fresnel zones. 100
5.27 Soil moisture retrievals for 2004-2019 from IGS station Visby. 101
5.28 Soil moisture retrievals for 2015 from IGS station Visby. 101
5.29 Cumulative soil moisture and precipitation for 2014-2019 from IGS station Visby. 102
5.30 IGS station Fredericton picture of surroundings. 103
5.31 IGS station Fredericton - Fresnel zones. 103
5.32 Soil moisture change, triggered by precipitation for IGS station Fredericton and soil moisture histogram from GNSS-R and ERA5. 104
5.33 Soil moisture retrievals for 2014-2018 from IGS station Fredericton. 104
5.34 Precipitation measurements in Fredericton, compared to ERA-Interim and ERA5 precipitation estimates. 105
5.35 Soil moisture retrievals for 2015 from IGS station Fredericton. 105
5.36 Soil moisture retrievals for 2016 from IGS station Fredericton. 106
5.37 IGS station Mbarara - Fresnel zones. 107
5.38 Soil moisture retrievals for 2014 from IGS station Mbarara. 107
5.39 GNSS soil moisture for 2004-2019 from IGS station Mbarara. 108
5.40 IGS station Tsukuba - Fresnel zones. 108
5.41 Soil moisture retrievals for 2016 from IGS station Tsukuba. 109
5.43 GNSS soil moisture for 2004-2019 from IGS station Tsukuba. 109
5.42 Soil moisture histogram from GNSS-R and ERA5 for station Tsukuba. . . 109
5.44 IGS station Marlborough - Fresnel zones. 110
5.45 Soil moisture retrievals for 2017 from IGS station Marlborough. 111
5.46 Reflector height modified correlation and RMSE. 112
5.47 Effects of changing sampling rate and signal strength resolution on soil moisture retrievals. 113
5.48 Reflector height modified soil moisture. 114

6.1 Simplified diagram of model soil dynamics. 117
6.2 Soil moisture model variations. 120
6.3 Mathematical model for soil moisture. 121
6.4 First physical model for soil moisture. 121
6.5 Second physical model for soil moisture. 121
6.6 LSA model for soil moisture. 121
6.7 Soil moisture model compared to observations for station Marquardt. . . . 122
6.8 Soil moisture comparison between model and GNSS-R for 2018 for IGS station Sutherland. 123

7.1 Position of the Snow Height mast in the vicinity of Neumayer with imposed Fresnel zones. 126
7.2 The GNSS antenna, mounted on a pillar in Neumayer-III. 127
7.3 Changes of elevation angle to sense the same observation footprint. 127
7.4 Snow height observations from Neumayer-III station in Antarctica. 128
7.5 Snow height retrieval correlations from Neumayer-III station in Antarctica. 129
7.6 De-trended snow retrieval from Neumayer-III station in Antarctica. 130
7.7 De-trended snow retrieval correlations from Neumayer-III station in Antarctica. 130
7.8 Maps of IGS stations capable of detecting snow height in Europe and North America. 131
7.9 Snow height retrievals from IGS station Visby. 133
7.10 Snow height retrievals from IGS station Visby for winters 2009/2010 and 2011/2012. 134
7.11 Snow height retrieval correlations from IGS station Visby. 135
7.12 Snow height retrievals from IGS station Metsahovi. 135
7.13 Snow height retrievals from IGS station Olsztyn. 136
7.14 Snow height retrievals for station Olsztyn. 136
7.15 Snow height retrievals from IGS station Calgary. 137
7.16 Snow height retrievals for station Calgary. 137
7.17 Monthly mean snow height in Calgary. 138
7.18 Snow height retrievals from IGS station Pickle Lake. 139
7.19 Monthly mean snow height in Pickle Lake. 139
7.20 Snow height retrievals from IGS station Fredericton. 140
7.21 Monthly mean snow height in Fredericton. 141
7.22 Snow height retrievals from IGS station Shediac. 141

A.1 Gain pattern of S67 Antcom antenna. 182

B.1 SUADA data structure and data flow. 186

B.2 Balkan IGS stations processed in SUADA. 191
B.3 GRAD database data structure and data flow. 192

C.1 Köppen climate classification world map. 195

D.1 IGS station Metsahovi - Fresnel zones. 202
D.2 Soil moisture retrievals for 2016 from IGS station Metsahovi. 202
D.3 IGS station Olsztyn - Fresnel zones. 203
D.4 Soil moisture retrievals for 2016 from IGS station Olsztyn. 203
D.5 IGS station Redu - Fresnel zones. 204
D.6 Soil moisture retrievals for 2015 from IGS station Redu. 204
D.7 IGS station Nicosia - Fresnel zones. 205
D.8 Soil moisture retrievals for 2016 from IGS station Nicosia. 205
D.9 Soil moisture retrievals for 2018 from IGS station Noto. 206
D.10 IGS station Mitchell - Fresnel zones. 207
D.11 Soil moisture retrievals for 2017 from IGS station Mitchell. 207
D.12 IGS station Boolardy station - Fresnel zones. 208
D.13 Soil moisture retrievals for 2018 from IGS Boolardy station. 208
D.14 Soil moisture histogram from GNSS-R and ERA5 for Boolardy station. . . 208
D.15 IGS station Parkes - Fresnel zones. 209
D.16 Soil moisture retrievals for 2017 from IGS station Parkes. 209
D.17 IGS station Sydney - Fresnel zones. 210
D.18 Soil moisture retrievals for 2017 from IGS station Sydney. 210
D.19 IGS station Ascention Island - Fresnel zones. 211
D.20 Soil moisture retrievals for 2016 from IGS station on Ascension Island. . . 211
D.21 Soil moisture retrievals for 2018 from IGS station Kourou. 212
D.22 Soil moisture retrievals for 2018 from IGS station Alofi. 213
D.23 IGS station Funafiti - Fresnel zones. 214
D.24 Soil moisture retrievals for 2016-2019 from IGS station Funafuti. 214
D.25 IGS station Lombrum - Fresnel zones. 215
D.26 Soil moisture retrievals for 2017 from IGS station Lombrum. 215
D.27 Soil moisture retrievals for 2016 from IGS station Hartebeesthoek. 216
D.28 Soil moisture retrievals for 2016 from IGS station Mafikeng. 217
D.29 IGS station Thohoyandou - Fresnel zones. 218
D.30 Soil moisture retrievals for 2018 from IGS station Thohoyandou. 218
D.31 IGS station Sutherland - Fresnel zones. 219
D.32 Soil moisture retrievals for 2017 from IGS station Sutherland. 219
D.33 Soil moisture retrievals for 2018 from IGS station Calgary. 220
D.34 IGS station Pickle Lake - Fresnel zones. 221
D.35 Soil moisture retrievals for 2018 from IGS station Pickle Lake. 221

D.36 Soil moisture retrievals for 2018 from IGS station Shediac. 222
D.37 Soil moisture retrievals for 2018 from IGS station Torrance. 223
D.38 Soil moisture retrievals for 2018 from IGS station Curitiba. 224

List of Tables

1.1 World water reserves (*Anderson and McDonnell*, 2005, p.14). 3
1.2 Albedo of different surfaces (*Ahrens*, 2012, p.48). Higher albedo indicates higher reflectivity of the surfaces. 7

2.1 General characteristics of numerical models. 17

4.1 GNSS, meteorological and NWP datasets present in the SUADA database as of 1.09.2019. 49
4.2 Used datasets processing strategies and methods. 50
4.3 Comparison of meteorological parameters for year 2007 with the 2001-2010 period for station Sofia, Bulgaria. 51
4.4 Annual and seasonal mean of temperature and precipitation for station Sofia, Bulgaria. 51
4.5 Correlations between IWV sources for Sofia. 55
4.6 IWV trends for station Sofia from various sources. 57
4.7 IWV mean values for station Sofia from all sources. 57
4.8 IWV standard deviation for station Sofia from the de-trended water vapour observations from all sources. 57
4.9 Processed stations in the SUGAC first processing campaign. 59
4.10 Surface pressure and temperature from WRF and SYNOP. 60
4.11 IWV correlations between WRF and GNSS during 8 days with hailstorm precipitation events for the summer of 2013. 66
4.12 IWV comparison between PPP and network solution processings. 69

5.1 Soil moisture coefficients for station Portales. 78
5.2 Correlations between GNSS sensors in Marquardt. 90
5.3 Short description of IGS stations for reflectometry. 99
5.4 Soil moisture coefficients for station Visby. 100
5.5 Soil moisture coefficients for station Fredericton. 106
5.6 Soil moisture coefficients for station Mbarara. 108
5.7 Soil moisture coefficients for station Tsukuba. 110
5.8 Soil moisture coefficients for station Marlborough. 111

6.1 1D-ESMM model parameters. 119
6.2 Model coefficients for all GNSS stations. 122

7.1 IGS stations for snow depth retrieval. 132

B.1 SUADA table structure. 187
B.2 GNSS, meteorological and NWP datasets present in the SUADA database as of 1.09.2019. 189

D.1 List of IGS stations for soil moisture retrieval. 200
D.2 Soil moisture coefficients for all IGS stations. 201

Abbreviations

1D	**1-D**imentional
1D-ESMM	**1-D**imentional **E**mpirical **S**oil **M**oisture **M**odel
4D-Var	**4-D**imentional **Var**iational assimilation
AC	**A**nalysis **C**entre
AIUB	**A**stronomical **I**nstitute of the **U**niversity of **B**ern
ASCAT	**A**dvanced **SCAT**terometer
BEK	**B**ayerische **E**rdmessung **K**omission - Komission für Erdmessung und Glaziologie der Bayerischen Akademie der Wissenschaften
BSW	**B**ernese GNSS **S**oft**w**are
BKG	**B**undesamt für **K**artographie und **G**eodäsie - German Federal Agency for Cartography and Geodesy
CODE	**C**enter for **O**rbit **D**etermination at the Astronomical Institute of the University of Bern
DGNSS	**D**ifferential **GNSS**
DWD	**D**eutscher **W**etter**D**ienst
ECMWF	**E**uropean **C**entre for **M**edium-Range **W**eather **F**orecasts
EPOS	**E**arth **P**arameter and **O**rbit **S**ystem software
EUPOS	**Eu**ropean **Po**sition Determination **S**ystem
EUREF	**Eu**ropean **Re**ference **F**rame
EGVAP	**E**UMETNET EIG **G**NSS water **Va**pour **P**rogramme
ERA	**E**CMWF **R**e-**A**nalysis

ERA5	**E**CMWF **R**e-**A**nalysis 5th implementation
ESA	**E**uropean **S**pace **A**gency
FDR	**F**requency **D**omain **R**eflectometry
GCOS	**G**lobal **C**limate **O**bserving **S**ystem
GEO	**G**eostationary **E**arth **O**rbit
GFS	**G**lobal **F**orecasting **S**ystem model
GFZ	**G**eo**F**orschungs**Z**entrum Potsdam - German Research Centre for Geosciences
GLONASS	**Glo**bal'naya **Na**vigatzionnaya **S**putnikovaya **S**istema (from Russian - Global Navigation Satellite System)
GNSS	**G**lobal **N**avigation **S**atellite **S**ystem
GNSS4SWEC	Advanced **G**lobal **N**avigation **S**atellite **S**ystem tropospheric products for monitoring **S**evere **W**eather **E**vents and **C**limate
GNSS-R	**G**lobal **N**avigation **S**atellite **S**ystem **R**eflectometry
GMF	**G**lobal **M**apping **F**unction
GPS	**G**lobal **P**ositioning **S**ystem
GRAD	**G**FZ **R**eflectometry and **A**tmospheric **D**atabase
GRUAN	**G**COS **R**eference **U**pper **A**tmosphere **N**etwork
IGS	**I**nternational **G**NSS **S**ervice
InSAR	**In**terferometric **S**ynthetic **A**perture **R**adar
ITRF2008	**I**nternational **T**errestrial **R**efference **F**rame, 2008
IWV	**I**ntegrated **W**ater **V**apour
LDAS	**L**and **D**ata **A**ssimilation **S**ystem
LHCP	**L**eft **H**and **C**ircular **P**olarized
LEO	**L**ow **E**arth **O**rbit
LSA	**L**east **S**quare **A**djustment
MEO	**M**edium **E**arth **O**rbit

NAPEOS	**NA**vigation **P**ackage for **E**arth **O**rbiting **S**atellites
NASA	**N**ational **A**eronautics and **S**pace **A**dministration
NCAR	**N**ational **C**enter for **A**tmospheric **R**research
NIMH	**N**ational **I**nstitute of **M**eteorology and **H**ydrology, Bulgaria
NMF	**N**iel **M**apping **F**unction
NWP	**N**umerical **W**eather **P**rediction
PBO	**P**late **B**oundary **O**bservatory
PE	**P**recipitation **E**fficiency
PP	**P**reci**p**itation
PPP	**P**recise **P**oint **P**ositioning
PRN	**P**seudo-**R**andom **N**oise sequence
PW	**P**recipitable **W**ater
PWV	**P**recipitated **W**ater **V**apour
RHCP	**R**ight **H**and **C**ircular **P**olarized
RINEX	**R**eceiver **In**dependent **Ex**change data format
RMSE	**R**oot **M**ean **S**quared **E**rror
RS	**R**adio**s**onde
RTK	**R**eal-**T**ime **K**inematic
SH	**S**now **H**eight
SMAP	**S**oil **M**oisture **A**ctive **P**assive
SMC	**S**oil **M**oisture **C**oefficient
SMOS	**S**oil **M**oisture and **O**cean **S**alinity
SMHI	**S**wedish **M**eteorological and **H**ydrological **I**nstitute
SNR	**S**ignal-to-**N**oise **R**atio
SQL	**S**tructured **Q**uery **L**anguage

SS	**S**ignal **S**trength
SUADA	**S**ofia **U**niversity **A**tmospheric **D**ata **A**rchive
SUGAC	**S**ofia **U**niversity **G**NSS **A**nalysis **C**enter
SVN	**S**pace **V**ehicle **N**umber
SWE	**S**now **W**et **E**quivalence
SYNOP	**Synop**tical obsevations
TDR	**T**ime **D**omain **R**eflectometry
VMF	**V**ienna **M**apping **F**unction
VWC	**V**olumetric **W**ater **C**ontent
WMO	**W**orld **M**eteorological **O**rganization
WRF	**W**eather **R**esearch and **F**orecasting model
ZHD	**Z**enith **H**ydrostatic **D**elay
ZTD	**Z**enith **T**otal **D**elay
ZWD	**Z**enith **W**et **D**elay

Acknowledgements

The person who trusted me in completing this work is my PhD supervisor, Prof. Jens Wickert. During my stay in GFZ Prof. Wickert introduced me to many leading scientists in the field, taught me how to structure my scientific work and advised me on how to tune every small detail. He is also the reason for the existence of the custom graphical visualisations in this study. Thank you very much, Jens, for your support and advices! I will be honoured to find my place among the successful scientists, who have worked under your guidance.

These GNSS studies were started from my bachelor studies with Dr. Guergana Guerova back in 2011. We did together my BSc thesis, then my MSc thesis, established the SUADA database in Sofia University. I have profited from her dedicated efforts to teach her students greatly. Thank you, Geri! I am sure, that our scientific journey does not end here.

I heard of GNSS Reflectometry for the first time from Prof. Kristine Larson. Together with Dr. Sibylle Vey, they guided me in reading, understanding and analysing reflected signals. Thank you both for your support and for answering my numerous, often elementary questions with patience and care. At all time I remain at your service.

One of the driving forces behind my research progress was the COST ES1206 project, lead by Dr. Jonathan Jones, Dr. Galina Dick and Dr. Jan Douša among others. The project lasted from 2013 until 2017 and enabled me to get to know the brightest names of the European GNSS community. It also enabled me to work briefly with Prof. Norman Teferle, who hosted me on a Short-term scientific mission, during which I learned a lot about GNSS processing. Thank you, dear colleagues, for enabling me this opportunity.

I would like to thank specifically our section leader Prof. Harald Schuh for attracting such a enormous group of successfull scientists to work in GFZ, our GNSS-R working group leader Dr. Maximilian Semmling for his insightful questions and comments, Dr. Kyriakos Balidakis for providing the ERA5 data, Christian Hochmann for so carefully maintaining the experimental GNSS sites and my ex-office mates Milad Asgarimehr, Dr. Yongchao Zhu and Nikolaos Antonoglou for their support and the provision of a nice atmosphere, so important to a meteorologist.

Since I came to GFZ I got to know some remarkable scientists, who shaped my view of the world of science. I would like to cheer all the Telegrafenberg colleagues who made my experience unforgettable in Potsdam.

Apart from the scientific help, there is also the human support. This creature comfort and human touch was undeniably, unconditionally and generously provided to me by my closest ones - my mother, my brother, my girlfriend and my whole family. Without them all of these pages of work would not matter.

Appendix A

Used instruments

A.1 Javad TRE_G3TH GNSS receiver

The Javad TRE_G3TH receiver is the preferred receiver by the GFZ IGS processing center. It is installed on all GFZ GNSS sites, including Marquardt and Fürstensee. The receiver is a multy-system multi-frequency receiver with standard sampling rate of up to 100Hz. The receiver is able to track GPS L1C/A, L1C, L2, L2C, L5, Galileo E1, E5A and GLONASS L1 and L2 frequencies. The receiver has 216 receiving channels with 10cm code and 1mm phase precision. The receiver can be installed in diverse environments within the temperature interval between -40°C - +80°C. These receivers provide carrier phase, pseudorange, doppler and signal strength observations with maximum resolution of the signal strength of $0.25dB - Hz$. The receiver is capable of outputting data in RINEX 3 format. It is very flexible and it can adopt many modifications. This is the reason that it is mainly preferred in research applications.

These receivers are used as standard receivers for all stations, maintained by GFZ.

A.2 Javad GrAnt GNSS antenna

This antenna can track all constellations in all possible frequencies and it is appropriate for high-accuracy applications. Using some filters, it protects from interferences and the overall performance of the GNSS receivers is improved. Operating Temperature -45°C +85°C, Humidity Waterproof, 100Mechanical Antenna type Microstrip Connector TNC Weight 450 g 515 g Dimensions 140 mm x 140 mm x 62 mm Enclosure Radome: ABS Base: Aluminum Color Green Mounting 5/8-11 or 1-14 inches mount, or 4 holes M5 G3T-JS is a versatile high performance antenna. It can be mounted on flat surfaces with four screws or mounted on standard poles (5/8-11 or 1-14 inches thread). The antenna cable can be connected via the standard TNC (N-type optional) connector on its side or routed through the center of the antenna for ultimate protection in harsh environments.

G3T-JS can track GPS, GLONASS, GALILEO, WAAS, EGNOS, MSAS, GAGAN and QZSS signals.

A.3 Antcom S67 GNSS antenna

The Antcom S67 series are dual-band L1/L2 active GPS antenna providing coverage at 1227.6 MHz and 1575.42 MHz. Their spherical radius molded radomes provide enhanced protection against rain, ice and lightning strikes and qualifies them for high speed military aircraft and dual frequency surveying applications. The amplifier is integrated under the radome. Additional filtering provides significant out-of-band rejection and reduced possibility of saturation by non-GPS signals. DC bias is provided through the coax connector.

These antennae are used in GFZ mainly for measurements on flying platforms, such as UAV's, the German research High Altitude Long Range Research Aircraft (HALO) and on Zeppelins.

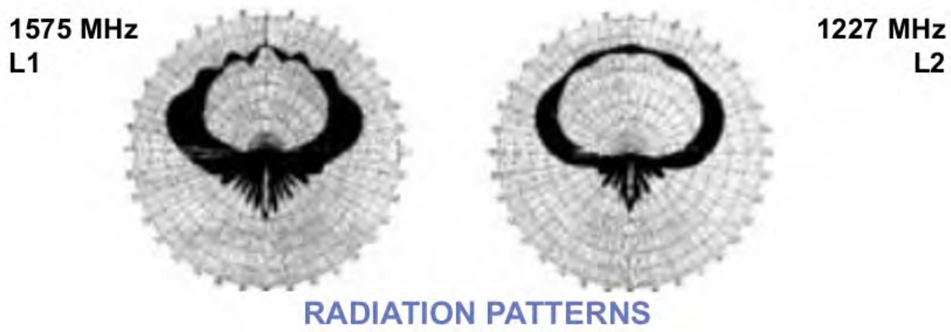

Figure A.1: Gain pattern of S67 Antcom antenna (figure from Antcom S67 leaflet).

A.4 U-blox GNSS antenna and receiver

U-blox is a Swiss company, specialized in producing low-cost high quality GNSS antennae and receivers for positioning applications. The u-blox system, used in this research (see section 5.3.3) is single-frequency coupled GPS antenna and receiver with maximum sampling rate of 10Hz and SNR resolution of $1dB - Hz$. The u-blox EVK-M8T chip is used for timing applications and supports simultaneous reception of all GNSS. The reasons for this choice are the quality of the chip and the fact that it provides raw measurements. The same manufacturer sells various modules of the same quality that do not provide raw measurements. The chip is integrated on a board with USB and serial ports and a 3-axis magnetometer. The receiver can be connected to a patch antenna (like MAR3 station), as well as to external antenna (such as in MAR4).

A.5 Vaisala WXT520 combined meteorological sensor

Weather Transmitter WXT520 is a small and lightweight transmitter that offers six weather parameters in one compact package. WXT520 measures wind speed and direction, precipitation, atmospheric pressure, temperature and relative humidity. The transmitter housing is IP65/IP66 rated. The following options are available: heating function for the precipitation and wind sensors, bird spike kit, bushing and grounding kit. To improve the accuracy of measurements an optional heating for the wind and precipitation sensors is available.

A.6 Vaisala radiosondes

In station Sofia, Bulgaria, routine daily sounding are preformed at 12 UTC. The station is operated by the Central Aerological Observatory at the National Institute of Meteorology and Hydrology (NIMH). Since 2005 Vaisala RS92KL probe has been used. The relative humidity sensor is a thin-film capacitor heated twin sensor with measurement range between 0 and 100%, resolution 1% and total uncertainty in sounding 5%. Apart from the humidity, the sonde also carries a thin wire platinum capacitive thermometer and a silicon pressure sensor.

Vaisala radiosonde RS41 offers excellent data availability and accuracy of humidity, temperature, pressure, and wind measurement. The radiosonde is fast and stable with individual, SI-standard traceable calibration. Vaisala radiosonde RS41 temperature sensor utilizes linear resistive platinum technology. The small size of the sensor results in low solar radiation error and guarantees fast response. Wind data, height and pressure are derived from Vaisala radiosonde RS41 GPS data combined with differential corrected GPS data from the ground station. Robust design, Physical Zero Humidity Check and In-built Functional Temperature Check ensure reliable performance in every situation. The radiosonde is also easy to use. For example, there is no need for the user to connect the batteries to the radiosonde to activate it. The radiosonde is automatically activated when placed on the ground check device. To make it easier to check the status of the radiosonde, the radiosonde has LED light indicators visible on the cover.

A.7 TDR sensor

The TDR sensor set-ups used in this work consist of Campbell Scientific CS645 probes, connected through a SDM8X50 multiplexer to a TDR100 Time Domain Reflectometor.

The CS645 is used in TDR100- and TDR200-based systems. This probe consists of a Santoprene head, three pointed rods, and a low-loss LMR200DB cable. The length of each rod is 7.5 centimeters, allowing the probe to be used in very high electrical conductivity soils or in laboratory column applications (maximum soil bulk electrical conductivity of 5 deciSiemens/meter). The low-loss cable is suitable for lengths up to 25 meters as measured from the tips of the probe's rods to the reflectometer. A similar probe, the CS640, is available for applications using shorter cable lengths (up to 15 meters). The CS640 and CS645 differ only in their cables.

The SDM8X50 is a 50 ohm, coaxial, 8:1 multiplexer used in a Campbell Scientific time-domain reflectometer system. It consists of a surge-protected multiplexer circuit board enclosed in a metal housing and a separate strain-relief bracket for the coaxial cables. Both the multiplexer housing and strain relief bracket have holes drilled at a 1 in. spacing. This enables you to mount the SDM8X50 to a wall or attach it to the backplate of a user-supplied enclosure or Campbell Scientific enclosure.

The TDR100 Time-Domain Reflectometer is the core of the Campbell Scientific time-domain reflectometry system. This system is used to accurately determine soil volumetric water content, soil bulk electrical conductivity, rock mass deformation, or user-specific time-domain measurement. Up to 16 TDR100s can be controlled using a single Campbell Scientific data logger. PC-TDR software is used with our TDR100-based systems during system setup and troubleshooting. It can be downloaded from the Downloads section of the web page.

Appendix B

Used software

B.1 Sofia University Atmospheric Data Archive (SUADA)

The SUADA database contains data from several European GNSS processing centers for stations in Bulgaria and Europe:

- Ground-based Global Navigation Satellite Systems (GNSS) observations from:
  - EUREF,
  - IGS repro 1,
  - IGS CODE repro 2,
  - SUGAC data for 7 stations in Bulgaria between January and December 2013,
  - ZenitGEO,
  - GFZ.
- Radiosonde IWV data for station Sofia (1997-2019).

The SUADA is a regional database aiming at: 1) achieving atmospheric water vapour observations from different techniques and 2) using the data for meteorological and climatic studies in Bulgaria/South-East Europe. Similar to STARTWAVE database (*Morland et al.*, 2006), SUADA is designed to enhance and facilitate the atmospheric research in the Sofia University, but also to provide online data access, via e web portal, for interested researchers in Bulgaria and the neighbouring countries.

SUADA is developed using the Structured Query Language (SQL) for relational database management system (*Codd*, 1970). The SUADA tables are structured as peers with additional relations between them as shown in figure B.1. The first group of tables are "Information tables": INSTRUMENT, STATION, COORDINATE, SENSOR and SOURCE (rows 1 and 2 on figure B.1). The second group of tables are the "Primary tables": NWP_IN, SYNOP, GNSS_IN and RADIOSONDE_IN (row 3 on figure B.1). The

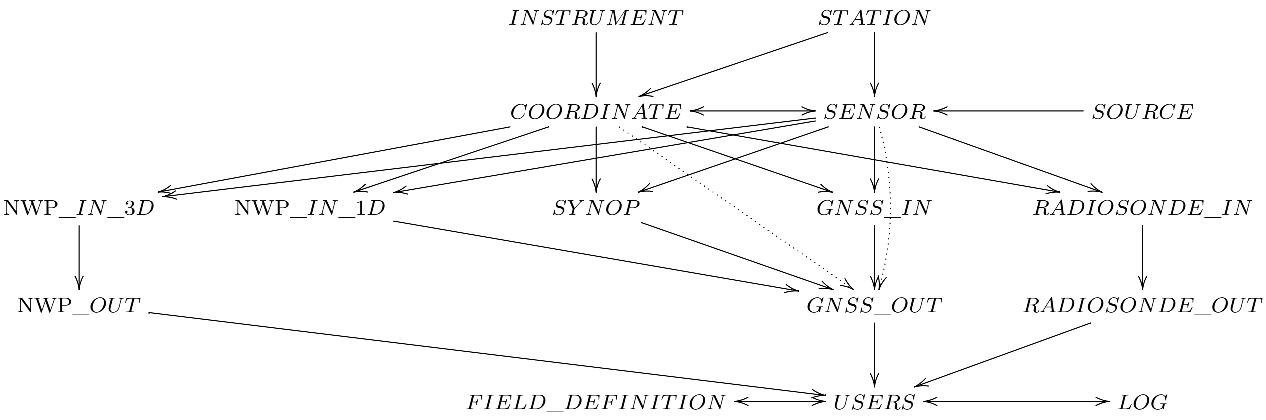

Figure B.1: SUADA data structure and data flow.

third group of tables are the "Secondary tables": NWP_OUT, GNSS_OUT and RADIOSONDE_OUT (row 4 on figure B.1). The last group of tables are the "Information tables for the web portal": FIELD_DEFINITION, USERS and LOG (row 5 on figure B.1). The tables are also accessible from the SUADA web portal.

B.1.1 SUADA structure

Table name	Summary
INSTRUMENT	Indicates measuring system - whether it is a meteorological or GNSS station or NWP model and its identification number
STATION	Station name and number
SOURCE	Contact information of SUADA data providers (name, institution, telephones, etc.)
COORDINATE	Coordinates of the GNSS, SYNOP and radiosonde stations
SENSOR	Combines information from STATION and SOURCE tables
SYNOP	Surface observations from the network of the national meteorological services
GNSS_IN	Tropspheric products from ground-based GNSS networks or individual station
NWP_IN_1D	Model data for the 2m surface levels, equivalent to standard meteorological measurements

NWP_IN_3D	Model data for the state of the atmosphere above the surface model point, equivalent to radiosonde measurements
GCM	Model data from Global Climate Models for long time series comparison
RADIOSONDE_IN	Data from the radiosonde network or individual stations
RADIOSONDE_IN_IWV	Data from the radiosonde network or individual stations, processed by the met service with the IWV data available
LIDAR	Data from ceilometer measurements
GRACE	Data from the GRACE satellite
GNSS_OUT	Processed GNSS data (IWV, ZHD and other)
NWP_OUT	Model data for IWV and other integrated values, calculated using data from NWP_IN_3D table
RADIOSONDE_OUT	Processed radiosonde data (IWV)
FIELD_DEFINITION	List of abbreviations used in the SUADA tables
USERS	Contact information about SUADA data users (external and internal)
LOG	User log in history

Table B.1: SUADA table structure.

The INSTRUMENT table stores information about the measuring instrument. At the time of writing there are 5 different measurement and data acquiring techniques, which are mentioned in this table. They are: GNSS, SYNOP, radiosonde, NWP, lidar, GCM and GRACE. Five of these instruments are measurement techniques (GNSS, SYNOP, radiosonde, lidar and GRACE), while NWP and GCM are numerical simulations.

The STATION table defines the name of the nearest town or city with the ID number of the nearby set of stations. It is to be noted that for several similar instruments, located nearby, different ID's are registered. Table SOURCE table holds data and contact information of data partners/providers. The ID's are divided in groups: 1-20 - GNSS data providers of ZTD's (21-40 - GNSS RINEX data providers, 41-60 - meteorological measurements, 61-70 - climate models, 71-99 NWP data sources). The COORDINATE table is a key-table for storing the coordinates of a station like latitude, longitude and altitudes. If the station coordinates are not available the station can not be processed.

The SENSOR table is a key-table of SUADA. Its purpose of this table is to account for different data sources for a single station. For example station Sofia_Plana with StationID number 31 uses multiple sources - 3-EUREF_BKG and 21-SUGAC (this station uses much more sources, but for this example for simplicity only who are mentioned). In order to take into account that station 31 can be used with data sources 3 and 21, two lines in the SENSOR table are made: line 1 for station 31 with data source 3 and line two for station 31 with data source 21. With the adding of station Sofia_City with StationID number 33 another set for lines were added. It is very important to remember, that the SYNOP observations from the meteorological station Sofia are used for both Sofia_Plana and Sofia_City stations. In order to implement this in the database, the two different combinations of StationID and SourceID have the same ID number in the SENSOR table. Thus the data for each meteorological station is recorded only once, but can be used for both GNSS stations.

The SYNOP table contains input meteorological data from the National Institute of Meteorology and Hydrology and other national Meteorological Offices, who provide data for the World Meteorological Organization. The information from this table is used in the GNSS data flow in SUADA.

The GNSS_IN table stores observed GNSS data from different sources. Since SUADA version 1 the table has been called GPS_IN. The information from this table is used in the GNSS data flow in SUADA. The GNSS_OUT table stores processed GNSS data. In earlier versions of the SUADA this table is named GPS_OUT. Data stored in GNSS_IN, STATION, SOURCE, SYNOP and NWP_IN_1D tables is required for the SUGAC processing (described in section 4.3). The GNSS meteorology method presented in is used for deriving IWV from the observed Zenith Total Delay. The IWV_500 field stores IWV with altitude correction described in *Morland and Mätzler* (2007).

The NWP_IN_1D table stores Numerical Weather Prediction model data. The data for the stations is taken from the nearest grid point without interpolation. The information from this table is used in the GNSS data flow in SUADA. The NWP_IN_3D table stores Numerical Weather Prediction model data. This table stores vertical profiles from the nearest grid point to the stations without interpolation. The information from this table is used in the MODEL data flow in SUADA. The NWP_OUT table is intended to store Numerical Weather Prediction model data, processed in the MODEL data flow in SUADA.

The RADIOSONDE_IN table stores observed radiosonde profiles. Each observation is stored in the table in several lines from different heights (vertical profiles). The RADIOSONDE_IN_IWV table stores pre-calculated by the radiosonde software IWV. The RADIOSONDE_OUT table stores processed radiosonde data using data from STATION and RADIOSONDE_IN tables. In contrast to RADIOSONDE_IN table, in RADIOSONDE_OUT table one line equals to one measurement.

The GCM table stores data from Global Climate Models.So far this table is independent of other data sources and the information in it is used for comparison of long time series. The LIDAR table stores data from ceilometers and lidars. As of February 2016 the only lidar included in the database is situated in Sofia. The GRACE table stores data from the GRACE satellite. The GRACE measures anomalies in the gravity field of the Earth in order to calculate the water storage in the soil layers under the surface of the Earth.

B.1.2 SUADA datasets

dataset name	tropos. product	available yyyy - yyyy	number of stations	observation frequency	number of observations
IGS repro 1	ZTD	1995 - 2019	9	5 min	8 262 322
IGS repro 1	IWV	2000 - 2019	1	3 hours	42 554
CODE repro 2	ZTD	1996 - 2019	7	5 min	613 527
CODE repro 2	IWV	2003 - 2019	1	3 hours	27 022
EUREF	ZTD	1997 - 2019	8	5 min	507 002
EUREF	IWV	1999 - 2019	1	3 hours	47 481
ZenitGEO	ZTD	2011 - 2013	30	5 min	26 043 846
ZenitGEO	IWV	2012	30	3 hours	299 598
SUGAC	ZTD	2013	7	5 min	581 003
SUGAC	IWV	2013	7	30 min	104 812
Balkan	ZTD	2007 - 2014	23	5 min	21 607
Balkan	IWV	2011 - 2014	10	3 hours	6 480
GFZ	ZTD	2010 - 2019	1	5 min	217 748
GFZ	IWV	2010 - 2019	1	3 hours	16 665
Radiosonde	Profiles	1980 - 2019	1	1 day	18 989
SYNOP	surface P, T	1999 - 2019	26	3 hours	437 865
WRF	Profiles	2010 - 2019	139	30 min	6 086 961
WRF	IWV	2011 - 2019	139	30 min	640 245

Table B.2: A summary of the GNSS, meteorological and NWP datasets present in the SUADA database as of 1.09.2019. More information on the datasets can be found in appendix B.1.2.

The first SUADA GNSS dataset is IGS-repro1. In 2008, the International GNSS Service (IGS) initiated global GNSS data reprocessing campaign (IGS-repro1 (*Rebischung et al.*, 2012; *Byun and Bar-Sever*, 2009)). Nine IGS Analysis Centers contributed to the reanalysis of the GPS data collected by the IGS global permanent network since 1994 using the latest models and methodology. The IGS-repro1 campaign started after adoption of a new set of antenna phase center calibrations for 65 out of 232 sites of the global IGS network. Archived in SUADA are IGS-repro1 tropospheric products for station SOFI for the period 2001-2007. The ZTD and gradients are processed with the Jet Propulsion Laboratory (JPL) developed GIPSY/OASIS software and are available every 5 min for the period 1997-2007. The estimation approach is as follows: 1) fixed orbits and clocks: IGS Final Re-Analysed Combined (1995-2007), and IGS Final Combined 2008-Current, 2) earth orientation: IGS Final Re-Analysed Combined (1995-2007), and IGS Final Combined (2008-Current), 3) transmit antenna phase center map: IGS Standards, 4) receiver antenna phase center map: IGS Standards, 5) elevation angle cutoff: 7 degrees, 6) mapping function (hydrostatic and wet): GMF, 7) data arc: 24 hours, 8) data rate: 5 minutes, 10) estimated parameters: station clock (white noise), station position, wet zenith and 11) delay ($3cm/hour$ random walk), delay gradients (0.3 cm/hour random walk), phase biases (white noise).

The second SUADA GNSS dataset is CODE-repro2. This is the Center for Orbit Determination in Europe (CODE), at the Astronomical Institute of the University of Bern (*Dach et al.*, 2009), contribution for the second IGS reprocessing campaign (*Meindl et al.*) initiated in 2013. In SUADA are archived CODE-repro2 tropospheric products with 2 hour resolution for SOFI for the period 2001-2010. GNSS data (GPS and Glonass) is processed with Bernese GNSS Software v.5.3 using 1) ITRF2008 reference frame, 2) elevation cut-off angle 3 degrees, 3) ECMWF-based hydrostatic delay mapped with hydrostatic VMF1 (*Dach et al.*, 2009). In addition to SOFI station archived are also six European IGS stations: Zimmerwald (ZIMM), Switzerland; Onsala (ONSA), Sweden; Ondrejov (GOPE), Czech Republic; Medicina (MEDI), Italy; Matera (MATE), Italy; Potsdam (POTS), Germany.

The third SUADA GNSS dataset is produced by European Reference Frame (EUREF). EUREF is an European network operating since 1995 with objective to provide a standard precise GNSS-based reference system for Europe. Since June 2001, tropospheric parameters are estimated, by EUREF Local Analysis Centers, on a weekly basis (post-processing mode EUREF-BKG) with 2 hourly sampling rate for more than 200 GNSS tracking stations of the permanent EUREF network (*Soehne and Weber*, 2002). On the Balkan Peninsula there are 15 EUREF stations: 5 stations in Greece and Romania each and 1 station in Turkey, Croatia, Macedonia, Slovenia and Bulgaria, totalling 15 stations. The Bulgarian station SOFI is part of the EUREF permanent network since 1997. In SUADA are uploaded SOFI tropospheric products from 2001 to 2004 processed by the BKG Analysis Center in Germany. BKG produces daily tropospheric solutions using fixed coordinates from weekly solution with Bernese software, 10 degree elevation cut-off angle and elevation dependent weighting. No a priori tropospheric model is used but the zenith total delay is estimated at 1 hour intervals for each station and the mapping function is Dry NMF (*Niell*, 1996).

The forth SUADA GNSS dataset is provided by the private company ZenitGEO (`http://www.zenitgeo.com/home_en.html`). Since 2009, the company operates a GNSS network with 30 GNSS stations, evenly distributed over Bulgaria. ZenitGEO processes the GNSS data and provides tropospheric products with very high temporal resolution of 5 min (300 s). Currently, IWV is derived for 11 stations namely: Vidin, Oryahovo, Lovech, Veliko Tarnovo, Ruse, Razgrad, Silistra, Shabla, Kyustendil, Pazardzhik and Sliven. It is to be noted that 8 of them are in North Bulgaria. The high temporal resolution of the GNSS product is degraded due to low temporal resolution of the meteorological dataset (GNSS ZTD resolution at 30 minutes, while SYNOP observations every 3 hours) therefore in the near future use of NWP model data will be considered. This will also allow to increase the spatial resolution for Bulgaria.

The fifth SUADA GNSS dataset is a targeted processing for the period 19-26 2007. GPS data from 19 GNSS permanent stations (AUT1, NOA1, BUCU, COST, DUBR, GLSV, GRAZ, MATE, ORID, PENC, POLV, ROZH, SOFI, SULP, MIKL, WTZR, ZIMM, VARN, CRAI) from Central and Eastern Europe are processed with the Bernese software, version 5.0. Sixteen of them are IGS and EUREF stations. Seven sessions of 24 hours have been created. For each session hourly station coordinates and ZTD are estimated. The troposphere model used is *Saastamoinen* (1972) dry model with *Niell* (1996) dry mapping and tilting gradient model. Corrections to the introduced zenith values are estimated and the ZTD and gradients are obtained. Tropospheric products for the stations in South-East Europe: Sofia (SOFI), Dubrovnik (DUBR), Athens (NOA1), Thessaloniki (AUT1), Craiova (CRAI), Constanta (COST), Bucharest (BUCU) and Varna (VARN) (marked with red dots in figure B.2) are uploaded in the SUADA.

Figure B.2: Balkan IGS stations processed in SUADA.

Surface observations of: 1) pressure, 2) 2 m temperature, 3) 10 m wind speed and direction, 4) precipitation, 5) cloud cover and 6) current weather are archived in SUADA.

The measurements are from the surface observation network (SYNOP) of the National Institute of Meteorology and Hydrology (NIMH) in Bulgaria. The surface data is collected manually every 3 hours at 00, 03, 06, 09, 12, 15, 18 and 21 UTC. The data is available from OGIMET weather information server (*http://www.ogimet.com/*). In addtion, surface observations from 3 stations in Romania (Constanta, Craiova and Bucharest) with hourly update and measurements by automatic weather stations are saved. The surface data is used for derivation of IWV from the GNSS tropospheric products. The frequency of the surface observations is a limiting factor in obtaining high temporal resolution of water vapour. Often the surface data is not collocated with the GNSS station and altitude corrections are applied, which reduce the quality of the product.

B.2 GFZ Reflectometry and Atmospheric Database (GRAD)

Unlike SUADA, the GRAD database is created in PostgreSQL (or PSQL). The major reason for using PSQL over MySQL is server maintenance on the part of GFZ, rather than the search for superior performance. PSQL is optimised for fast data retrieval from large data volumes through indexing. The indexing methodology allows for data to be grouped in sequences to one another, thus enabling faster fetching of the data, compared to MySQL. Since the GRAD database is envisaged as an internal tool, rather than an operational database, the indexing option is omitted for simplicity.

Similar to the SUADA database (technical description in appendix B.1), the GRAD has two types of tables - information tables and data storage tables (seen in figure B.3. The information tables contain station names, locations, etc. and are used for more efficient data organization. The storage tables are self-explanatory.

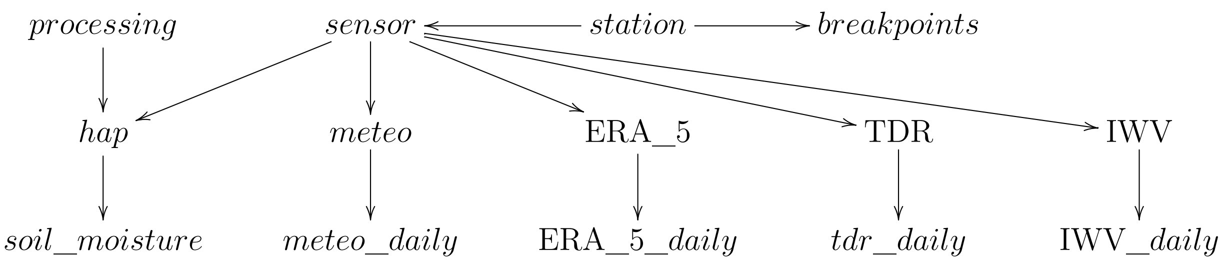

Figure B.3: GRAD database data structure and data flow.

The *station* table holds information not only about the station name, but also the 4-character IGS name of the GNSS site.

The *sensor* table, as in SUADA is central for the database structure. All sites have different equipment, installed. Thus in the *sensor* table the differentiation between meteorological and geodetic observations is being done, as well as the separation of L1, L2 and L5 signals. Each of these observations has its own unique *id*, including TDR, IWV and ERA5 observations. The list of observables can be expanded with new tables and *id*'s for each site.

The *processing* table, unlike the previous two, is unique to GRAD. It holds processing numbers with descriptions. The description includes information about the type of data, frequency of sampling, SNR resolution, scaling factors, smoothing, dates of processing and processing strategies.

The *breakpoints* table holds information about events, occurring in the stations, which would make the quality of the retrieved SNR-based products lower. Such is the case with the ploughed field in Marquardt, where SNR observations are available, but the ploughing made the reflective surface very rough, not allowing for useful reflections to be observed.

The *hap* table is the first data table. It contains height, amplitude and phase observations from each individual observed reflection in the stations. This is the raw processed data, after the Lomb-Scargle has been applied and the data has been fitted to the SNR observation equation 3.24. The reflections from every selected satellite and every direction are recorded with their timestamps, allowing for deriving soil moisture from certain directions around the station. The observations are marked with the used GPS frequency.

The *soil_moisture* table contains GNSS-R derived soil moisture observations, processed from the data in table *hap* with the GNSS-R processing software. Every observation is stored with its timestamp, processing id from the *processing* table, marker for used frequency and station marker.

The *meteo* and *meteo_daily* tables store meteorological data from closely located to the GNSS stations meteorological observations. The difference between the two is that the *meteo* table holds data from observations with various time resolutions, while in table *meteo_daily* these observations are recalculated in to average values for surface pressure and temperature and to accumulated precipitation. Similarly, the *tdr* and *tdr_daily* and the *iwv* and *iwv_daily* tables store observations with maximum resolution and with daily averages in the *_daily* tables. The *ERA_5* and *ERA_5_daily* tables store corresponding modelled observations to the meteorological and soil observations.

B.3 RINEX data format

GNSS data are recorded in a specially created Receiver Independent Exchange format (RINEX). This universal data format for all receivers was initially created in 1989, when version 1 of the format was launched. The data file consists of a header (describing which observations are recorded) and a main body, where all observations are stored epoch by epoch. GNSS observables include three fundamental quantities that need to be defined: Time, Phase and Range. Standard GNSS receivers record data every second, while specialized receivers can achieve recording frequency up several hundred times per second. The RINEX format incorporates the following observations:

- Epoch - the epoch of the measurement is the receiver time of the received signals, identical for the phase and range measurements and is identical for all satellites observed at that epoch;
- **C** - code (pseudorange) is the distance from the receiver antenna to the satellite antenna including receiver and satellite clock offsets (and other biases, such as atmospheric delays);
- **L** - the phase is the carrier-phase measured in whole cycles;
- **D** - Doppler observations, representing the Doppler shift, induced by the movement of the satellites, positive numbers representing approaching satellites,
- **S** - signal strength, giving the raw strength of the carrier to noise ratio in $dB - Hz$,
- **I** - ionosphere phase delay pseudo-observable, added after applying an ionospheric model to the data,
- **X** - receiver channel numbers pseudo-observable, added by the receiver to specific satellites.

Signal strength measurements were included into RINEX since version 2.10, released in 2002. In this version only one GNSS observation per frequency is stored, selected from the firmware options of the receivers. Some receivers recorded L2C under S2, some L2P. Since RINEX version 3, released in 2006, every modulation of every frequency is stored in the RINEX, thus a contemporary file can up to 9 different observations in L1 (L1C/A, L1P, L1C (three code variations), L1Y, L1M, L1 with Z-tracking and L1 codeless), each of them either for code observations, or any of the other (phase, Doppler, strength), 10 in L2 (similar to L1) and 3 in L5.

Appendix C

Köppen climate classification

The Köppen climate classification is a widely used system of thresholds, designed to identify regions of the world with similar climate conditions, based on monthly averages of temperatures and precipitation. This system was developed by the German climatologist Waldimir Köppen and first published in 1918. Since then the system is refined and modified, based on the much larger network of meteorological and climatological stations, expanded in the XX century. The climates on the Earth can be divided into five major meridional climatic types and one special (*Köppen*, 1918).

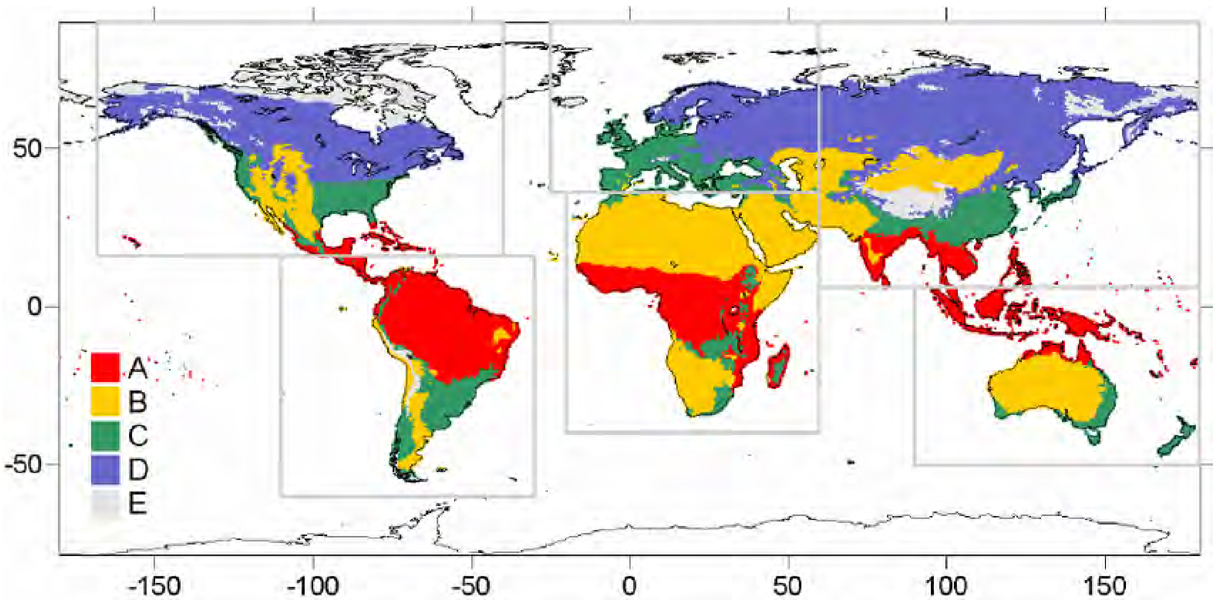

Figure C.1: Köppen climate classification world map. Source: https://www.researchgate.net/figure/Spatial-distribution-of-the-five-main-Koeppen-climate-types-determined-for-the-period-1951_fig1_255532038

A - Tropical moist climates

The primary characteristic of tropical moist climates is that all months have average temperatures above 18^{o}C. This climate zone is usually divided into 3 sub-climate regions.

Af Tropical wet

All seasons are wet with minimum of 60mm of precipitation per month. Tropical rain forests in Africa, the Amazon, parts of South-East Asia and tropical Oceania are associated with this climate zone. The seasonal and daily temperature variations in this climate are very low (3-5^{o}C).

Aw Tropical wet and dry

In this climate regions the seasonal variability is defined not through temperature (spring, summer, autumn and winter), but through precipitation seasonality - wet and dry seasons. Savannah's are located in these climate zones.

Am Tropical monsoon

This climate region is very similar to the **Aw**, but with more precipitation during the dry season. Commonly observed in Southern India and the coastal regions of the Amazon.

B - Dry climates

Dry climates are characterized with precipitation deficit and higher evaporation then precipitation. Two dominant climate subclasses are defined within dry climates - deserts (BW) and steppes (BS). Each of these subclasses can be further divided into hot (BWh, BSh) and cold (BWk, BSk).

BS Dry semi-arid

The steppes inland of the continents are usually described as dry semi-arid climate zones.

BW Dry arid

Warm and cold deserts are classified under the Dry arid climate subclass. This climate type is observed in the Sahara, Arabic peninsula, the Australian deserts and also includes cold deserts, such as the Gobi in Mongolia. These regions are characterized by very large daily amplitudes in temperature and lack of precipitation.

C - Moist mid-latitude climates with mild winter

Moist mid-latitude climates with mild winter are areas where the average temperature of the warmest month is above 18^{o}C and the coldest month - above -3^{o}C. The climate is characterized with distinct summer and winter seasons and are usually situated in the mid-latitudes. This zone is divided into subclasses with dry winters (Cw), dry summers (Cs) and lack of precipitation seasonality (Cf). Each of the subclasses is further divided into areas with long and hot summers (Cwa, Csa, Cfa), areas with long and cool summers (Cwb, Csb, Cfb) and areas with short and cool summers (Cwc, Csc, Cfc).

Cw Dry winter sub-tropical

A humid subtropical climate is a zone of climate characterized by hot and humid summers, and cold winters. These climate conditions can be found in China, Eastern India and in Southern Europe.

Cs Dry summer sub-tropical

The dry summer sub-tropical climate is also known as hot summer sub-tropical or Mediterranean climate. It is dominant in the Mediterranean region, on the coasts of southern Australia and west-coast US.

Cf Humid sub-tropical

Humid sub-tropical is a zone of climate characterized by hot and humid summers, and mild winters. These climate conditions are typical for the regions of the South-Eastern states of the US, south Brazil, Uruguay and west Argentina and can also be observed in Australia.

D - Moist mid-latitude climates with severe winter

Regions, where the average temperature of the warmest month is above 10^{o}C and the coldest month - below -3^{o}C belong to the moist mid-latitude climates with severe winter. These climates are more commonly known as continental. This climate type is subdivided similarly to the **C** type climates to regions with dry winters (Dw), regions with wet winters (Ds) and regions with lack of precipitation seasonality (Dw). Each of the subclasses is further divided into areas with long and hot summers (Dwa, Dsa, Dfa), areas with long and cool summers (Dwb, Dsb, Dfb), areas with short and cool summers (Dwc, Dsc, Dfc) and areas with short and cool summers and severe winters (Dwd, Dsd, Dfd).

Dw Continental climate with dry winter

The Continental climate with dry winter is characterized with average rainfall of the wettest summer month at least 10 times larger, than the precipitation in the driest month. This climate type is relatively seldom observed.

Ds Continental climate with dry summer

The continental climate with dry summer is characterized with average rainfall of the wettest winter month at least 3 times larger, than the precipitation in the driest month.

Df Continental climate

The more general continental climates are the predominant subtype of climate and are widely observed in North America and the plains of Central, Eastern Europe and Siberia.

E - Polar climate

Polar climates are the regions where the average temperature of the warmest month is below 10^oC. This climate zone consists of two subclasses - Tundra and Ice cap climates.

ET Tundra climate

These are regions, where the average temperature of the warmest month is above 0^oC, but below 10^oC. This climate is observable in the far northern regions of North America and Eurasia.

EF Ice cap climate

This type of climate is observed in regions where the average temperature of the warmest month is below 0^oC. These regions include Greenland, Antarctica and archipelagos close to the North Pole.

H - Highlands climate

The highlands or mountains climate is a special climate type, associated with high mountains at altitudes above 3000m. This includes the regions of the Himalayas, Karakorum, Alps, Andes and all mountain ranges above 3000m. The mountain climates are specific, because with the increase in altitude characteristics of all other types of climate can be observed in terms of temperature ranges. The precipitation in this climate type is mountain specific and is dependent on the position of the nearest large water reservoir.

Appendix D

List of IGS stations and description

Each individual station is represented with a Fresnel zones graph, short description of the climate and dataset and one or two plots from soil moisture observations. In the Fresnel zones figures the different colours indicate different PRN numbers of the GPS satellites and the images are created using *Roesler and Larson* (2018) software, based on Google Earth imaging. The stations, where snow height observations were performed are described in this appendix once again for their soil moisture properties.

The climate descriptions for each station are taken from various sources and are not cited in this work. In most cases the data comes from climate reports of the stations by the local meteorological service, or by larger online climate portals. The values of precipitation and temperature are rounded in order to avoid inaccuracies in tenths of degrees, or tens of mm of precipitation. This climatological data is used to describe the station in general in order to better put into context the soil moisture observations.

D.1 List of stations

Stations	City & Country	Coordinates	Köppen climate zone	Year since
PRDS	Calgary, Canada	50.8^{o}N 114.2^{o}W	Dwb	2001
KOUR	Kourou, French Guiana	5.2^{o}N 52.8^{o}W	Am	2001
SUTH	Sutherland, RSA	32.4^{o}S 20.8^{o}E	Cfb	2001
PICL	Pickle Lake, Canada	51.5^{o}N 90.1^{o}W	Dfb	2003
HARB	Hartebeesthoek, RSA	25.9^{o}S 27.7^{o}E	Cwa	2004
VIS0	Visby, Sweden	57.6^{o}N 18.4^{o}E	Cfb	2004
TASH*	Tashkent, Uzbekistan	41.3^{o}N 69.2^{o}E	Dsa	2004
TSK2	Tsukuba, Japan	36.1^{o}N 140.1^{o}E	Cfa	2005
FRDN	Fredericton, Canada	45.9^{o}N 66.6^{o}W	Dfb	2005
NIUM	Alofi, Niue	19.0^{o}S 169.9^{o}W	Af	2006
SHE2	Shediac, Canada	46.2^{o}N 64.5^{o}W	Dfc	2007
LAMA	Olsztin, Poland	53.8^{o}N 20.7^{o}E	Dfb	2009
SUTM*	Sutherland, RSA	32.4^{o}S 20.8^{o}E	Cfb	2009
WTZR	Wettzel, Germany	49.1^{o}N 12.8^{o}E	Cfb	2012
NICO	Nicosia, Cyprus	35.1^{o}N 33.3^{o}E	BSh	2012
MFKG	Mafikeng, RSA	25.8^{o}S 25.5^{o}E	Cwa	2012
TDOU	Thohoyandou, RSA	23.1^{o}S 30.4^{o}E	Cwa	2012
TORP	Torrance, USA	33.8^{o}N 118.3^{o}W	Csb	2014
TUVA	Funafuti, Tuvalu	8.5^{o}S 179.1^{o}E	Af	2014
REDU	Redu, Belgium	50.0^{o}N 5.1^{o}E	Cfb	2015
METG	Metsahovi, Finland	60.2^{o}N 24.3^{o}E	Dwb	2015
MCHL	Mitchell, Australia	26.3^{o}S 148.1^{o}E	Cfa	2015
MBAR	Mbarara, Uganda	0.6^{o}N 30.7^{o}E	Aw	2015
MRO1	Boolardy Station, Australia	26.7^{o}S 116.6^{o}E	BS	2015
PNGM	Lombrum, Papua New Guinea	2.0^{o}S 147.3^{o}E	Af	2015
ASCG	Ascession Island	7.9^{o}S 14.3^{o}W	BWh	2016
PARK	Parkes, Australia	33.0^{o}S 148.2^{o}E	Cfa	2016
SYDN	Sydney, Australia	33.8^{o}S 151.1^{o}E	Cfa	2016
MRL1	Marlborough, New Zealand	41.6^{o}S 173.7^{o}E	Cfb	2016
UFPR	Curitiba, Brazil	25.4^{o}S 49.2^{o}W	Cfb	2017
NOT1	Noto, Italy	36.8^{o}N 15.0^{o}E	Csa	2017

Table D.1: List of IGS stations for soil moisture retrieval, analysed in this work, ordered by longest datasets. The stations with (*) were processed in other studies and presented in the following papers: (*Larson et al.*, 2008b; *Vey et al.*, 2016a)

	SMC_1	SMC_2	SMC_3	SMC_4	SMC_5
LAMA	0.72	0.87	0.66	0.61	0.06
LAMA ERA5	0.97	0.96	0.54	0.14	0.08
VIS0	0.37	1.13	0.59	0.82	0.04
VIS0 ERA5	0.98	1.05	0.55	0.16	0.13
REDU	0.50	0.99	0.60	0.70	0.05
REDU ERA5	0.97	1.19	0.54	0.15	0.09
NOT1 ERA5	0.94	2.08	0.57	0.26	0.20
NICO	0.01	0.97	0.51	1.00	0.02
NICO ERA5	0.80	1.05	0.65	0.52	0.22
FRDN	0.39	0.97	0.59	0.79	0.02
FRDN ERA5	0.99	1.04	0.57	0.22	0.04
KOUR	1.00	0.85	0.40	0.01	-0.01
KOUR ERA5	1.00	∞	0.48	0.01	0.04
PICL ERA5	0.97	0.58	0.58	0.24	0.06
PRDS	0.52	1.01	0.65	0.78	0.08
PRDS ERA5	0.95	0.98	0.57	0.21	0.06
SHE2 ERA5	0.98	2.23	0.58	0.21	0.12
TORP ERA5	0.90	1.77	0.64	0.47	0.32
UFPR ERA5	0.99	1.00	0.52	0.10	0.15
TSK2	0.76	1.23	0.72	0.71	0.18
TSK2 ERA5	0.99	1.37	0.56	0.18	0.16
SUTH	0.27	1.40	0.63	0.95	0.09
SUTH ERA5	0.87	1.45	0.68	0.53	0.27
HARB	0.10	1.56	0.58	0.98	0.08
HARB ERA5	0.70	1.47	0.59	0.51	0.16
MBAR ERA5	0.99	0.76	0.52	0.10	0.11
MFKG	0.34	1.74	0.62	0.90	0.06
MFKG ERA5	0.70	1.62	0.60	0.53	0.07
TDOU ERA5	0.88	1.41	0.60	0.34	0.13
MCHL	0.19	1.76	0.61	0.98	0.13
MCHL ERA5	0.81	1.55	0.69	0.62	0.25
ASCG ERA5	1.00	1.00	0.50	0.06	0.01
MRL1 ERA5	0.99	1.35	0.55	0.18	0.22
MRO1 ERA5	0.60	1.13	0.62	0.65	0.10
NIUM ERA5	1.00	∞	0.50	0.03	0.09
PARK ERA5	0.91	1.61	0.65	0.47	0.24
PNGM ERA5	0.99	∞	0.48	0.04	0.01
SYDN	0.33	1.04	0.55	0.74	-0.06
SYDN ERA5	0.95	1.05	0.51	0.18	0.18
TUVA	0.03	0.70	0.50	1.00	0.00
TUVA ERA5	0.99	0.96	0.50	0.01	0.08

Table D.2: Soil moisture coefficients for all IGS stations, according to definitions in chapter 5.2. Only $SMC_2 \in [0;\infty]$, while all others $SMC_{1,3-5} \in [0;1]$ with larger value being better.

D.2 Description of individual stations

D.2.1 Metsahovi, Finland

Metsahovi is a town in Southern Finland, where the Metsahovi Radio Observatory is situated. The climate in Metsahovi is humid continental and is highly influenced by air masses, coming from the Baltic sea. The average daily temperatures during the boreal summer are around 18°C and during the winter down to -4°C. The yearly accumulated precipitation accounts for around 650mm/year with a minimum in spring and maximum in autumn.

Figure D.1: IGS station Metsahovi - Fresnel zones.

The GNSS station METG is established in 2012, but the earliest GNSS station on site, METS is established in 1992. A third GNSS site is also present, MET3, but together with METS they are not providing useful reflections for the GNSS-R method. SNR data from METG is available since 2014 with the reflections providing information about the soil moisture (see figure D.2), as well as about the snow height (see section 7.2.2).

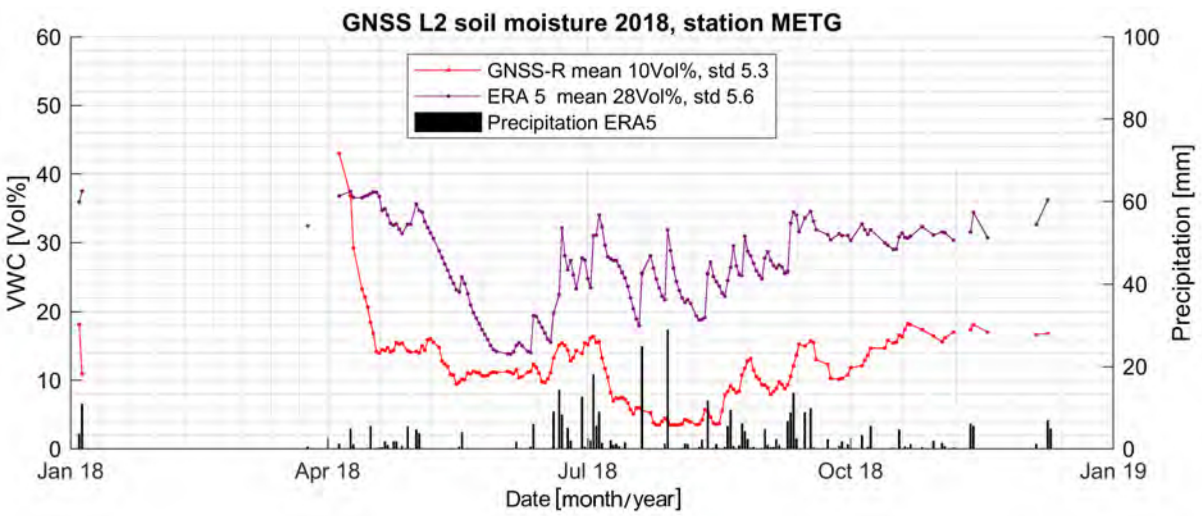

Figure D.2: Soil moisture retrievals for 2016 from IGS station Metsahovi.

D.2.2 Olsztyn, Poland

Olsztyn is a town, located in Northern Poland, 90km south of the Baltic sea. This area of the country is described, according to Köppen classification as Marine West Coast Climate (see appendix C). The temperatures in the station during the summer period reach maximum monthly average of 17°C in July and minimum monthly temperatures of -6°C in February. The region is highly influenced in summer by the northern path of the Atlantic cyclones, which are more common during positive NAO index and the western extents of the Siberian maximum in winter, which brings cold and dry air masses over the region, decreasing the temperatures for longer periods below -10°C. The precipitation in this region is also highly dependent on the atmospheric circulation with the most rainy month being July, again influenced by the Atlantic cyclones and the driest being November. The annual precipitation in Olsztyn is 630mm/year.

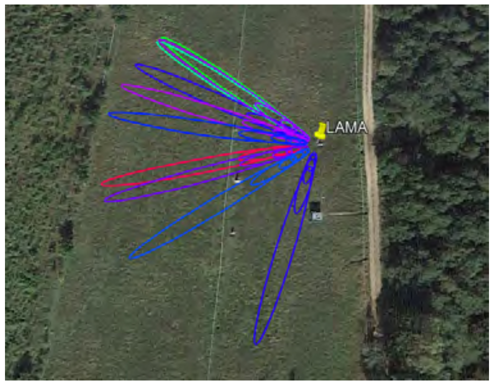

Figure D.3: IGS station Olsztyn - Fresnel zones.

GNSS station LAMA is located outside the city in a forested environment. The view to the station from the East is blocked by the forested area and all utilized reflections come from the westerly direction (as seen in figure D.3). The station is established in 1992 and provides signal strength data from GNSS since 2009 for both L2 and L5 frequencies of GPS.

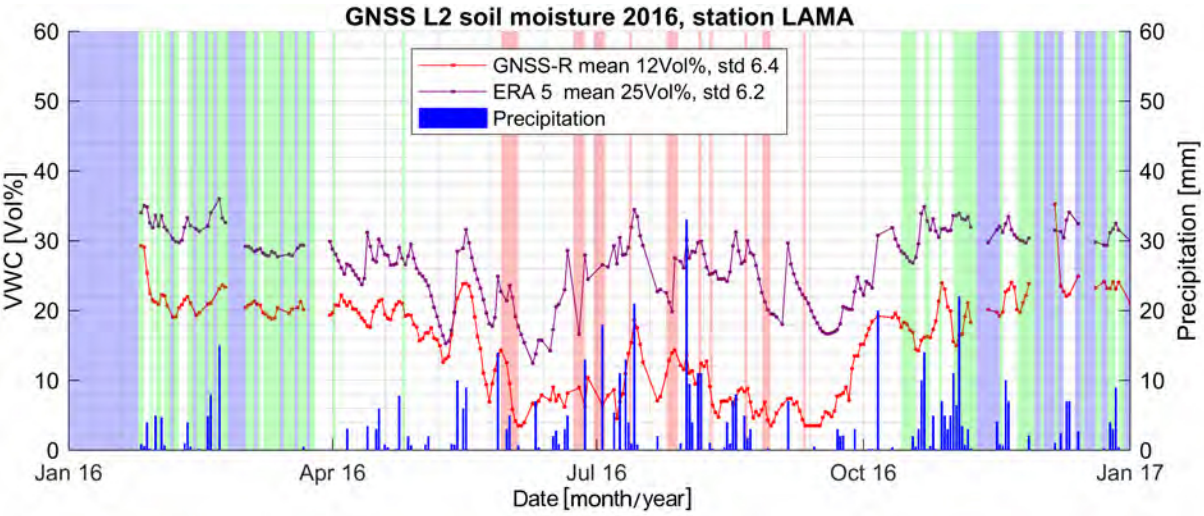

Figure D.4: Soil moisture retrievals for 2016 from IGS station Olsztyn. Precipitation in blue comes from SYNOP observations in nearby meteorological station, while precipitation in red is interpolated from ERA-Interim. The soil moisture line in purple is from ERA5.

D.2.3 Redu, Belgium

Station Redu is located near the Redu village in southern Belgium, close to the border with Luxembourg. The GNSS station is established in 2003 in the premises of the ESTRACK Redu station of the ESA. This station is responsible for tracking and communication with ESA spacecraft. SNR from this station is available in several periods between 2003 and 2010, but the current continuous dataset starts from 2015. Redu is located in an area with temperate oceanic climate, according to the Köppen classification (see appendix C), which means an annual precipitation of more that 1000mm/year. The average temperatures during the summer reach 20°C, while in winter the average temperatures drop to -2°C with no permanent snow cover.

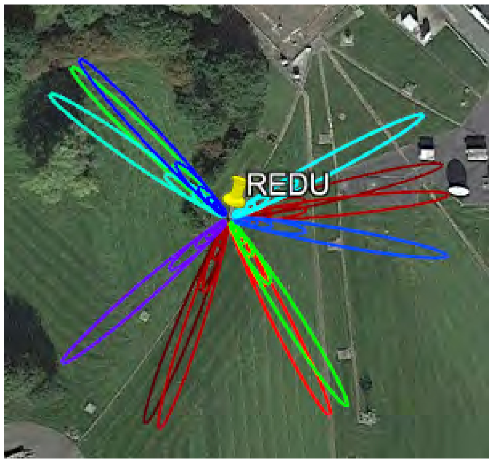

Figure D.5: IGS station Redu - Fresnel zones.

The station is one of the most unlikely to produce soil moisture observations from the ones, that can, since the height of the antenna is just 1 metre above ground. This brings higher uncertainty in the soil moisture record, but the observations still reply to precipitation events, as seen on figure D.6.

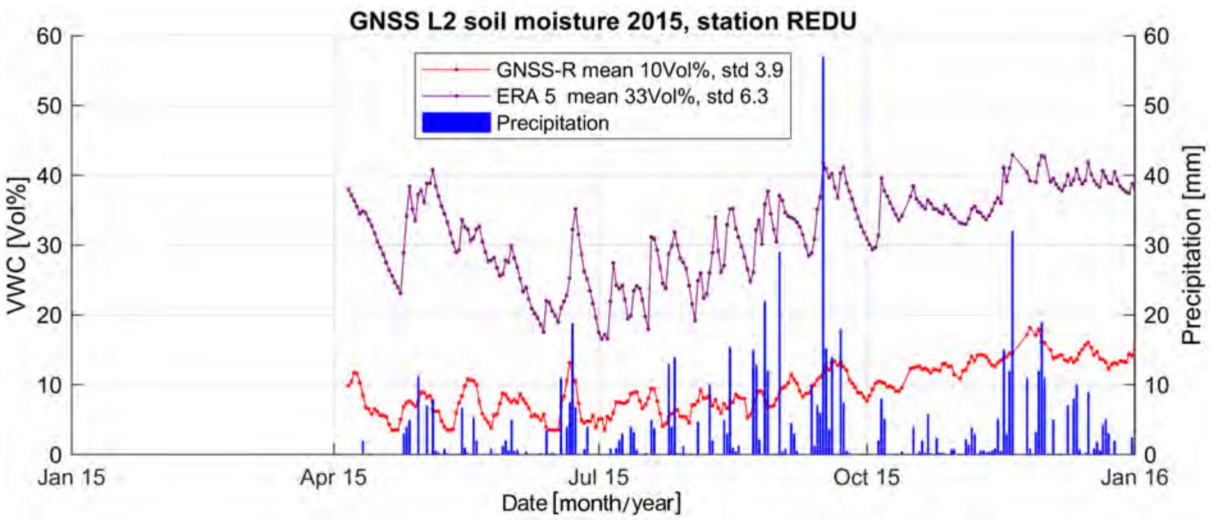

Figure D.6: Soil moisture retrievals for 2016 from IGS station Redu. Precipitation in blue comes from SYNOP observations in nearby meteorological station.

D.2.4 Nicosia, Cyprus

GNSS station Nicosia is situated in the surroundings of the capital city of Cyprus. The GNSS station is established in 2012. The island of Cyprus is situated in the Eastern part of the Mediterranean sea and belongs to the Semi-arid climate zone. The area is subject to around 350mm precipitation per year, with summer average temperatures reaching 37^{o}C and winter averages not going below 5^{o}C. Snowfalls are not typical for this region of Europe. Most of the precipitation occurs during the winter period, while the summer is very hot, with prolonged sunshine hours and little to no precipitation.

Figure D.7: IGS station Nicosia - Fresnel zones.

The behaviour of the soil moisture follows the climate trends with very low VWC during the summer months and peaks during winter, triggered by the sporadic rainfall events (seen on figure D.8). This GNSS station is one of only 2 in Southern Europe, suitable for soil moisture observations, along with Noto in Italy. Although meteorological observations for Nicosia are available, no precipitation data is included into them, which is the reason why the soil moisture is compared to ERA5 precipitation.

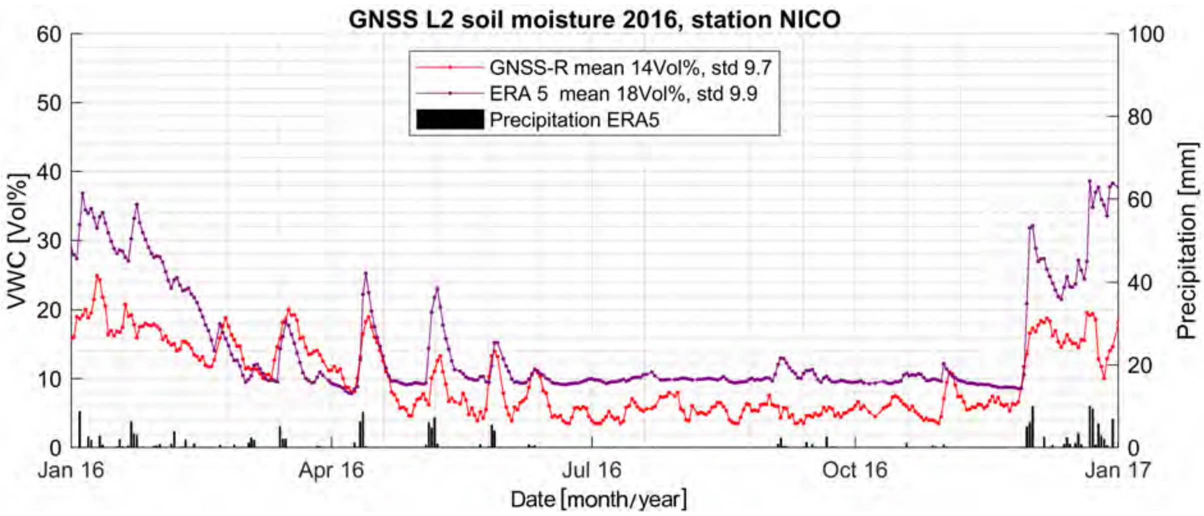

Figure D.8: Soil moisture retrievals for 2016 from IGS station Nicosia. Precipitation in black is from ERA5.

D.2.5 Noto, Italy

The Italian town of Noto is located on the island of Sicily, some 20km to the north of the city of Syracuse. The island of Sicily is situated in a Hot Mediterranean climate zone, according to the Köppen classification (see appendix C). The average high temperatures during summer reach 31^{o}C, while the average winter temperatures do not go below 7^{o}C. The annual precipitation is in the range of below 550mm/year with maximum during the winter and minimum in the summer months.

The GNSS site is established in 2000, but provides GNSS reflectometry data only since the fall of 2017, giving only 1 full year of observations, as of the beginning of 2019. With only ERA5 precipitation available for the station, the analysis possibilities for soil moisture are limited. The correlation between the ERA5 and GNSS-R soil moisture is the very low 0.29.

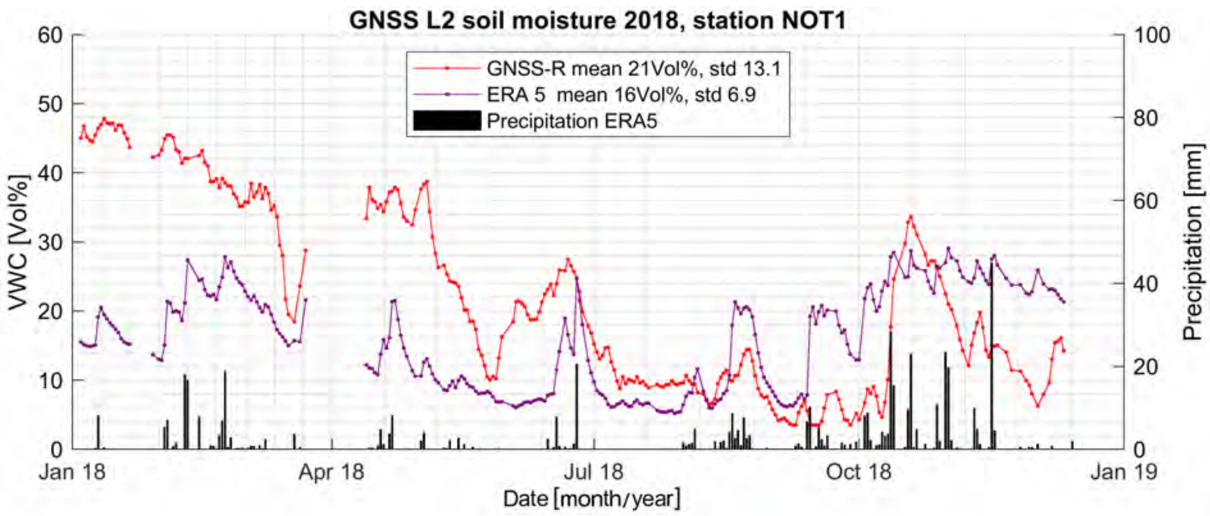

Figure D.9: Soil moisture retrievals for 2018 from IGS station Noto. Precipitation in black is from ERA5.

D.2.6 Mitchell, Australia

Station Mitchell is a GNSS site, established in 2015 near the city of Mitchell in Queensland Australia, in the North-East part of the continent. According to the Köppen climate classification Mitchell is situated in a humid subtropical zone (see appendix C). The daily mean temperatures are relatively high, reaching above 19^{o}C in the austral winter and above 32^{o}C in the summer. The maximum of precipitation occurs during the austral summer with annual precipitation totalling less than 600mm/year. Such dry climates are especially good for calibrating the soil moisture retrievals from GNSS, as far as the difference in soil conditions between the precipitation events and the evaporation, triggered by the high temperature show distinguishable soil moisture dynamics.

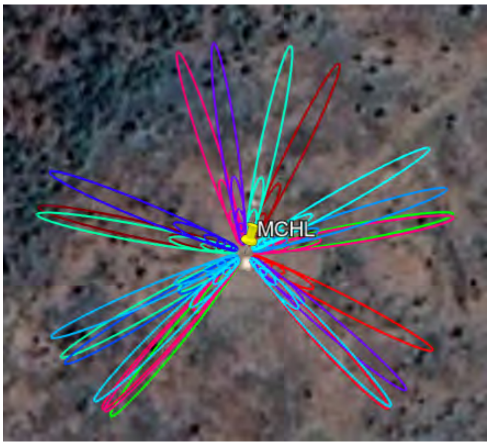

Figure D.10: IGS station Mitchell - Fresnel zones.

The high evaporation in Mitchell is providing very good conditions for the residual soil moisture to reach its absolute minimum. This can be observed on a number of occasions every year, but the ERA5 dataset does not indicate such a behaviour. This fact gives us the opportunity to state once again, that the ERA5 soil moisture is overestimated, particularly in climates with high contrast between dry and wet periods.

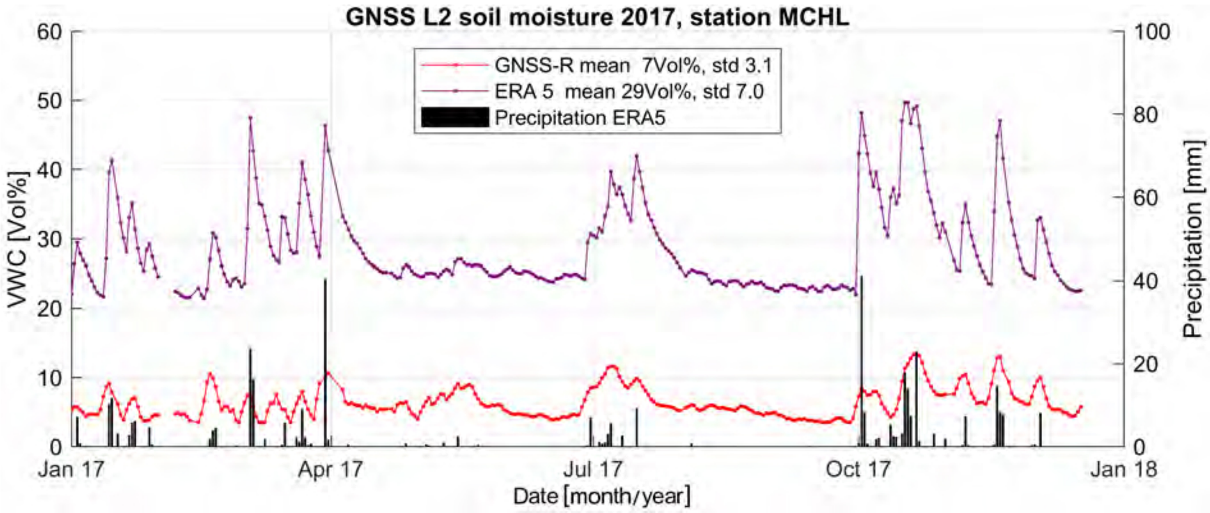

Figure D.11: Soil moisture retrievals for 2017 from IGS station Mitchell. Precipitation in black is from ERA5.

D.2.7 Boolardy station, Australia

The IGS site in Boolardy station is situated in near the Square Kilometre Array, a new large radio telescope site in Western Australia, some 250km inland from the Indian Ocean. The climate in the region is very hot and dry and is situated in a Semi-arid region by the Köppen classification (see appendix C). The average annual rainfall is below 400mm/year and the average high temperatures are higher than 35^{o}C in the austral summer and the lowest reach 7^{o}C in the winter.

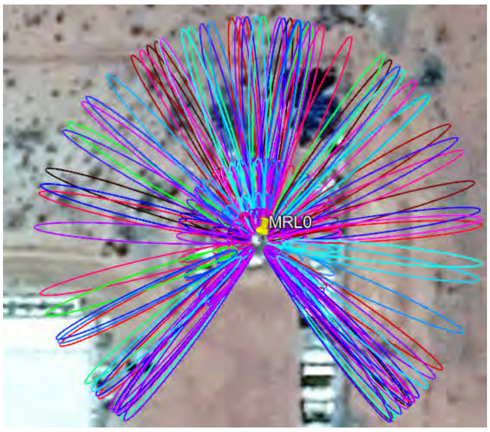

Figure D.12: IGS station Boolardy station - Fresnel zones.

Interestingly, Boolardy is one of the very few sites, where the soil moisture in the ERA5 datasets reach as low values, as the GNSS calibrated observations. As it can be seen from the soil moisture histograms (figure D.14), ERA5 shows even lower results than GNSS-R for the soil moisture.

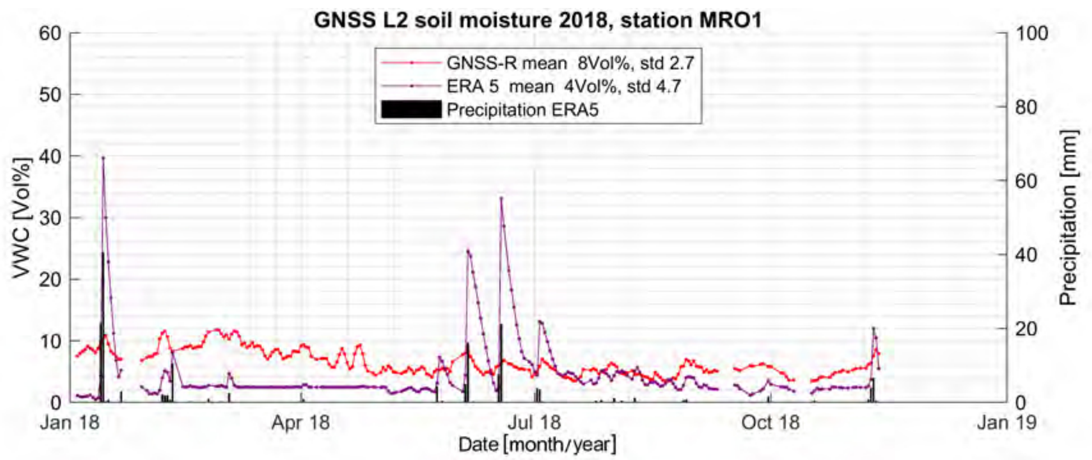

Figure D.13: Soil moisture retrievals for 2018 from IGS Boolardy station. Precipitation in black is from ERA5.

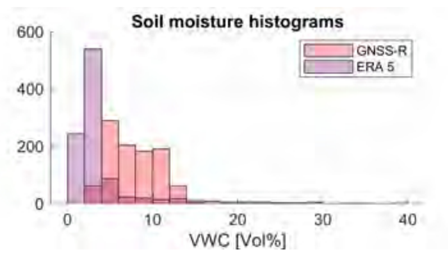

Figure D.14: Soil moisture histogram from GNSS-R and ERA5 for Boolardy station.

D.2.8 Parkes, Australia

Situated in New South Wales, close to the eastern coast of Australia, Parkes is located in temperate oceanic climate zone, according to the Köppen classification (see appendix C). The average high temperatures during the austral winter reach up to 32^{o}C, while the average low temperatures during winter go down to 4^{o}C. The annual precipitation of around 600mm/year is spread relatively evenly throughout the year with no distinct seasonality.

Figure D.15: IGS station Parkes - Fresnel zones.[2]

GNSS station Parkes is established in 2005 with the first SNR observations being broadcast in 2016. The station shows typical soil moisture behaviour with minimum soil moisture reached during the local summer and having significant residual soil moisture during the winter period. The winter values of ERA5 comply very well with the GNSS-R derived values, but during the summer period the residual VWC from ERA5 is too high for the station.

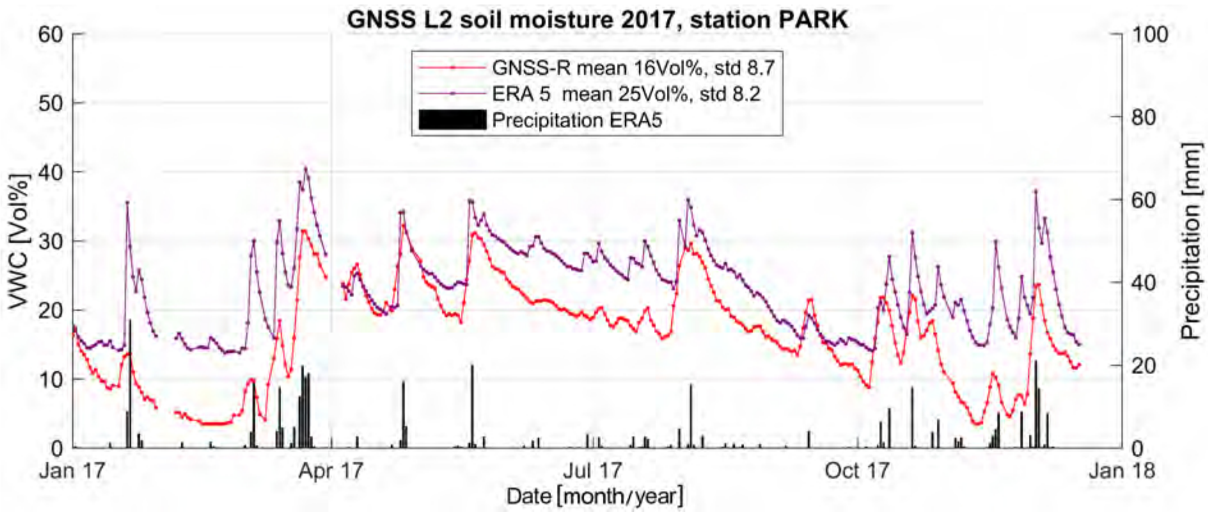

Figure D.16: Soil moisture retrievals for 2017 from IGS station Parkes. Precipitation in black is from ERA5.

D.2.9 Sydney, Australia

GNSS station Sydney is situated in the Northern part of the city with the antenna being mounted 1.5 metres above ground. Sydney itself is located in a humid subtropical climate area, according to the Köppen classification (see appendix C). The pronounced seasonality between the wet and dry seasons is typical for this kind of climates. The annual precipitation in particular is 1200mm/year with a maximum during the austral autumn and minimum during the austral spring. The daily mean temperature during the austral summer is 23°C with the lowest average during the austral winter being 13°C. The temperatures in Sydney have never reached readings below 0°C, so no snow height measurements have been recorded.

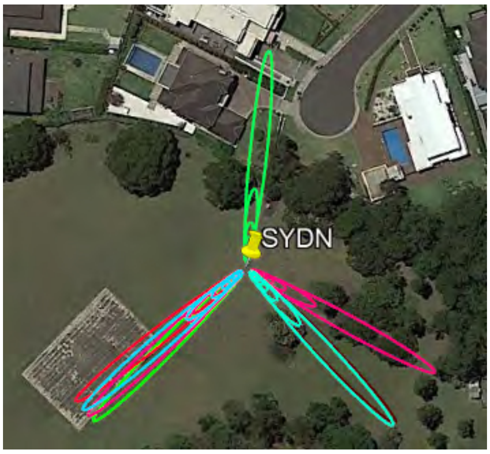

Figure D.17: IGS station Sydney - Fresnel zones.

The GNSS station is active since 2004 and is broadcasting SNR data since 2016. The soil moisture record shows very clear response to precipitation events throughout. The dataset is dense between 2016 and 2017, but for 2018 data is lacking with sporadic SNR availability.

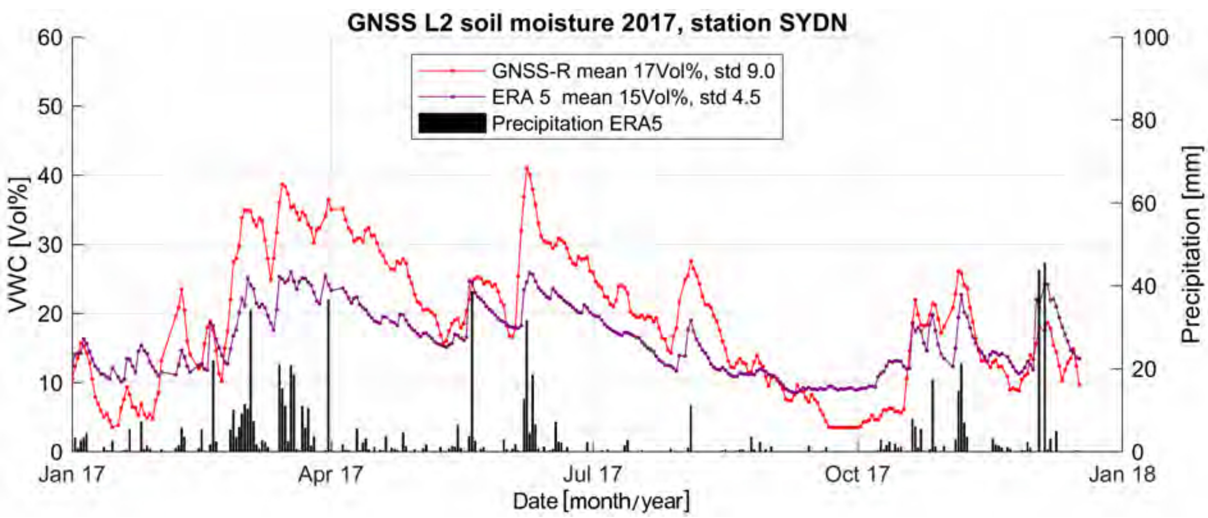

Figure D.18: Soil moisture retrievals for 2017 from IGS station Sydney. Precipitation in black is from ERA5.

D.2.10 Ascention Island

The IGS site on Ascension Island is a core IGS station, located in the North-East part of the island, part of the British overseas territories. The island hosts one of the 4 ground tracking stations of the GPS ground segment. Ascension Island is situated in the middle of the Atlantic Ocean, south of the Equator and is established in 2016. The climate of the island is classified, according to Köppen as a hot desert (see appendix C). It experiences very low precipitation throughout the year with peak in March and no significant seasonality in the temperatures record.

Figure D.19: IGS station Boolardy station - Fresnel zones.[4]

The surrounding surface of the GNSS site is rocky, but still moisture signal can be detected. The low precipitation throughout the year, combined with the high temperatures, lead to small moisture content. GNSS reflections respond to the ERA5 modelled rainfall. Since the island is small, ERA5 does not recognize it as land surface and does not produce soil moisture values. SYNOP data could not be found from the island in *http://www.ogimet.com/*.

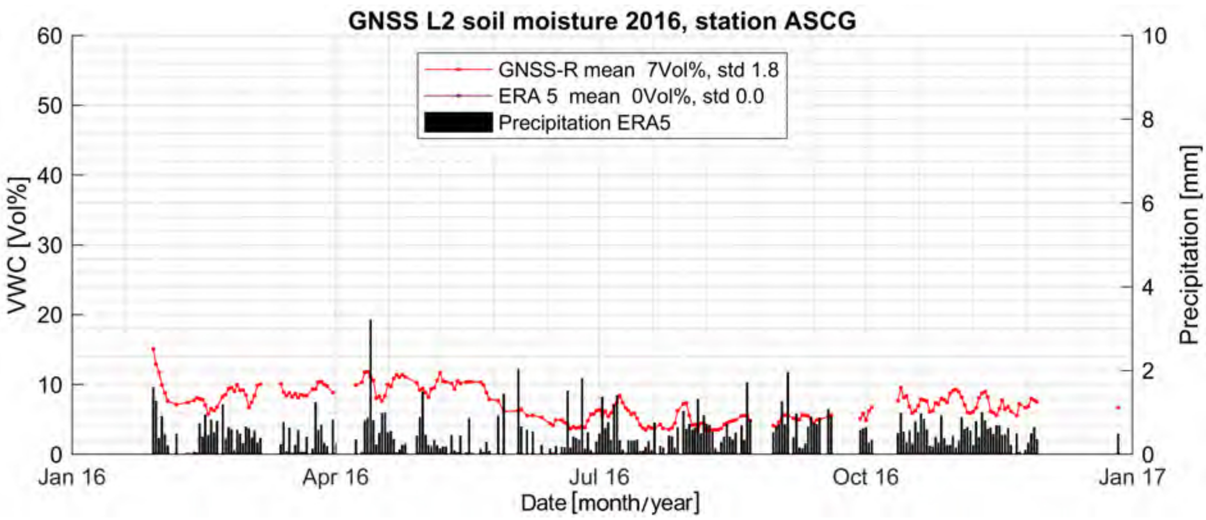

Figure D.20: Soil moisture retrievals for 2016 from IGS station on Ascension Island. Precipitation in black is from ERA5.

D.2.11 Kourou, French Guiana

The IGS station in Kourou, French Guiana is located in the Guiana Space Center, which is the European Space Agency's main space port. The GNSS site is established in 2001 and has been operational since. Kourou is a French commune in South America, part of the European Overseas Territories. The climate of the area is classified as Tropical monsoon climate, according to Köppen (see appendix C). The annual precipitation exceeds 2500mm and has a distinct seasonality with peak in April and minimum in August. The temperatures are high throughout the year with no significant seasonality.

This very wet climate is the reason for extremely wet soil and a minimum in soil moisture in the boreal autumn, as can be seen in figure D.21. The VWC, observed by the GNSS-R has questionable accuracy, due to the very wet environment throughout all seasons. It is highly likely, that the residual soil moisture never reaches its minimum possible value. The reason for this is described in chapter 5.5. Although meteorological observations for Kourou are available, the precipitation record shows highly improbable behaviour (up to 23000mm/day), which is the reason why the soil moisture is compared to ERA5 precipitation.

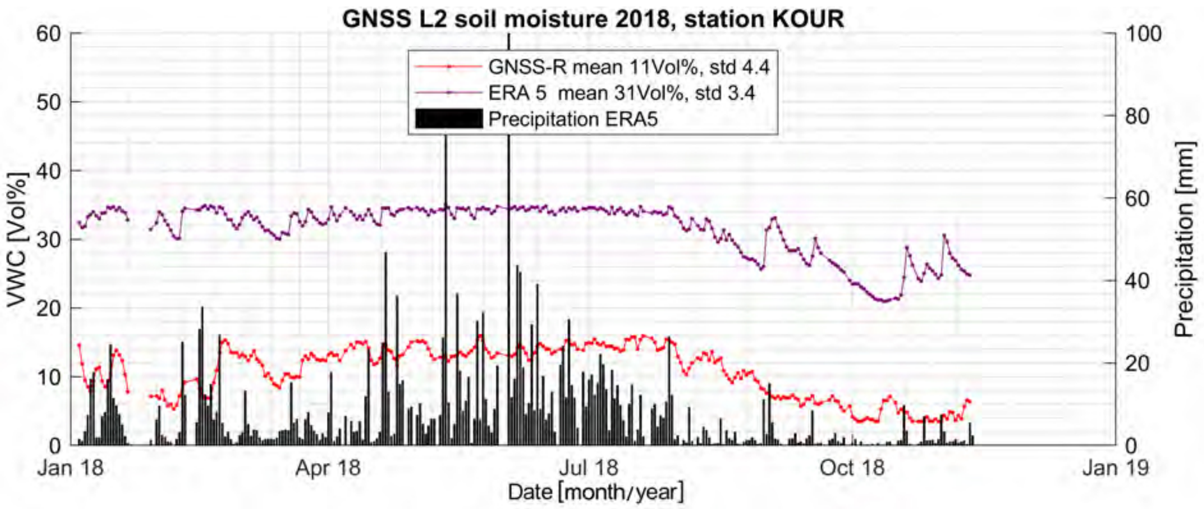

Figure D.21: Soil moisture retrievals for 2018 from IGS station Kourou. Precipitation in black is from ERA5.

D.2.12 Alofi, Niue

Alofi is the capital of the tropical island of Niue. Niue is a tropical island in the Pacific Ocean, situated 2400 km to the North-East from New Zealand. The island is located in Tropical climate zone, according to Köppen, with annual precipitation of around 2000mm/year (see appendix C). The precipitation seasonality is characterized with minimum in June (during the austral winter) and maximum in March. The temperature on the island shows no significant seasonality with average daily temperatures of between 22-27^{o}C throughout the year.

The GNSS station in Alofi is established in late 2005 and started broadcasting SNR data since 2006. The station is located in the airfield of the island, giving good reflections from direction west. Just as any other station in tropical climate, the accuracy of the derived soil moisture is questionable since the residual soil moisture is most probably above the minimum possible. Nevertheless, the soil moisture signature shows clear maximums after precipitation events, observed in ERA5.

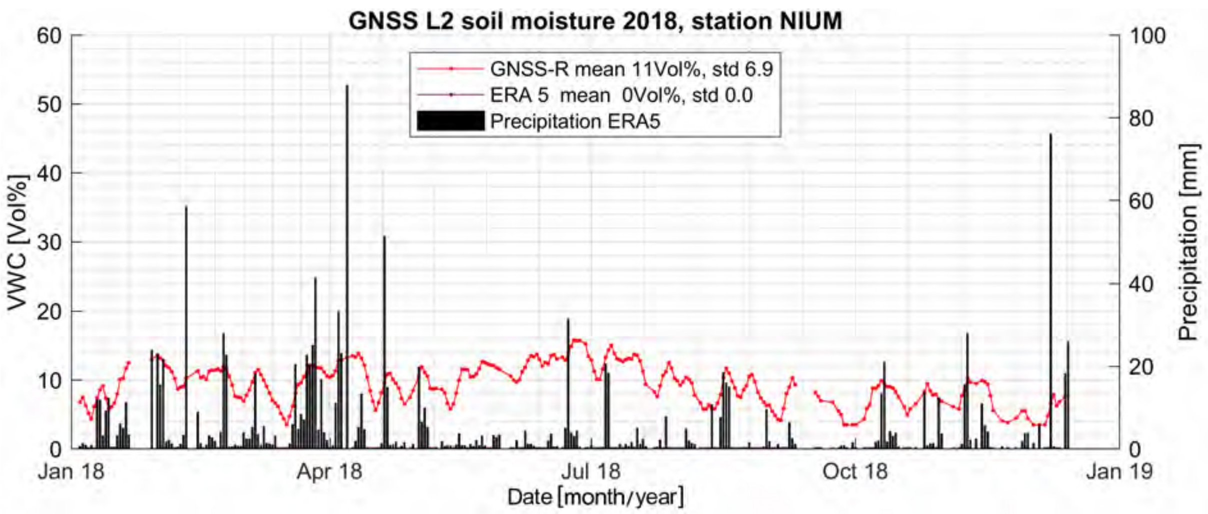

Figure D.22: Soil moisture retrievals for 2018 from IGS station Alofi. Precipitation in black is from ERA5.

D.2.13 Funafuti, Tuvalu

Funafuti is the capital of the tropical nation of Tuvalu, situated in the middle of the Pacific Ocean. It is situated on the largest atoll in the country with total land area of 275 square kilometres. The width of the land strip of the atoll varies between 20 and 400 metres. The GNSS station in Funafuti is established in 2001 and started providing SNR data since 2014. It is located in the island airport, which is also the thickest part of the atoll. The climate of Tuvalu is tropical rainforest, according to Köppen, although the land area is too small to sustain such an ecosystem (see appendix C). The accumulated annual precipitation is more than 3500mm with minimum during the austral winter. The daily mean temperatures throughout the year are around 28°C without any seasonality.

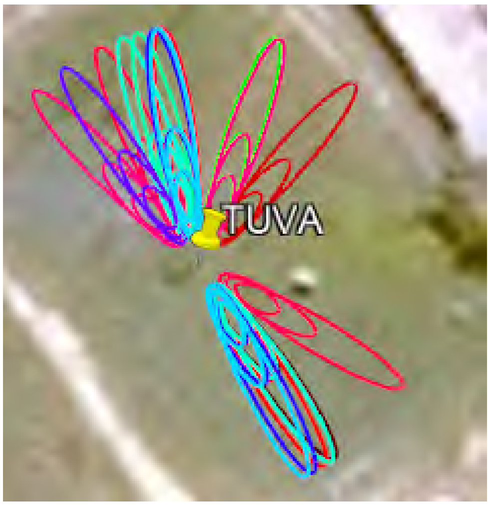

Figure D.23: IGS station Funafuti - Fresnel zones.[6]

This station has low significance, since the country of Tuvalu develops no agriculture and is subject to regular intense precipitation without any drought possibilities. Still producing soil moisture observations in this environment is unprecedented amount soil moisture measurement techniques. Just like with station Niue (page 213) and others, the residual soil moisture in the station surroundings is probably higher, than the minimal possible, so the accuracy of the soil moisture observations from GNSS-R are questionable. On the other hand, the reflections show clear response pattern to significant precipitation events. ERA5 soil moisture data is not available, as well as precipitation measurements from SYNOP.

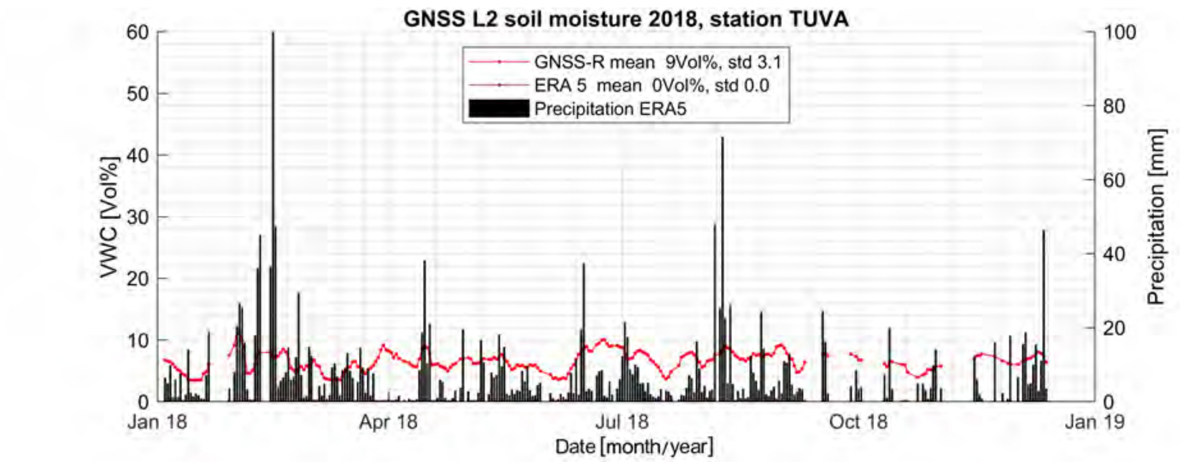

Figure D.24: Soil moisture retrievals for 2016-2019 from IGS station Funafuti. Precipitation in black is from ERA5.

D.2.14 Lombrum, Papua New Guinea

The GNSS station in Lombrum is established in 2002 with first available SNR measurements since 2015. The PNGM antenna is mounted on a 1.5m high pole with many reflections coming from direction South. The island of Manus in northern Papua New Guinea, where Lombrum is situated, is in a tropical rainforest climate, according to Köppen classification (see appendix C). Since the station is located 2° South from the Equator, there is no seasonality in the temperature record with average values of 28°C. The annual accumulated precipitation for this part of Papua New Guinea exceeds 3500mm/year with monthly rainfall minimum of 260mm/month. This leaves the soil extremely wet during the year with no particular wet or dry season, meaning that the soil in this region can never dry out completely. Thus the residual soil moisture is far above the minimum values, making the GNSS-R soil moisture not accurate.

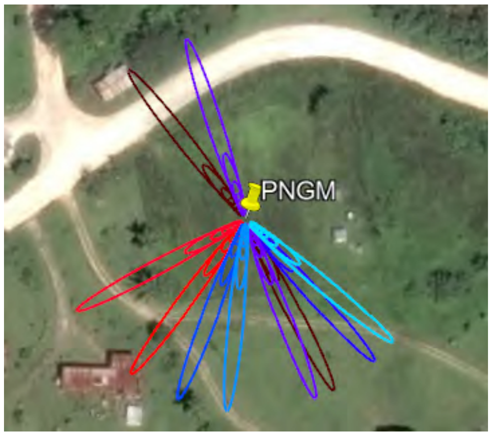

Figure D.25: IGS station Lombrum - Fresnel zones.

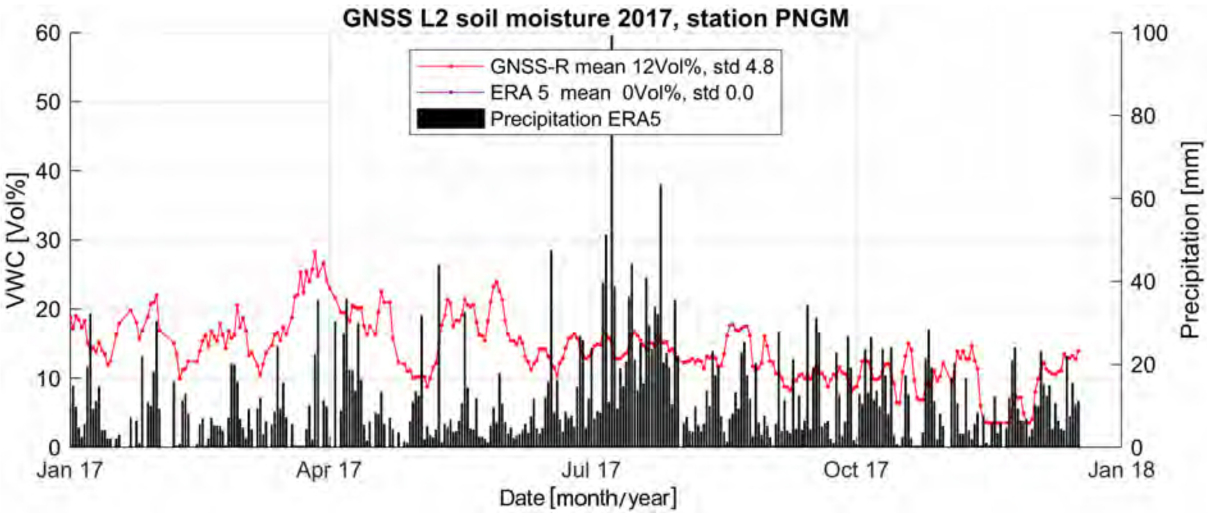

Figure D.26: Soil moisture retrievals for 2017 from IGS station Lombrum. Precipitation in black is from ERA5.

D.2.15 Hartebeesthoek, South Africa

Station HARB in Hartebeesthoek Radio Astronomy Observatory (HartRAO) is established in 2000 next to a VLBI site. The antenna is 3 meters high and the first SNR data were transmitted by the receiver in 2004 with uninterrupted broadcast since 2012. HartRAO is located in a Humid subtropical climate zone, according to the Köppen classification (see appendix C). With annual precipitation between 650-700mm/year and average high temperatures during the austral summer of 33^{O}C, the region is subject to strong evaporation and not so strong precipitation, leaving it relatively dry. The seasonal maximum of precipitation falls on the summer period with almost no precipitation during the winter, when the average low temperatures reach less than 5^{o}C.

Just as in any other station with strong evaporation and medium precipitation amounts, the soil moisture pattern in the station is very distinguishable. The lowest amounts of soil moisture are measured during the local winter, because of the limited precipitation during that season.

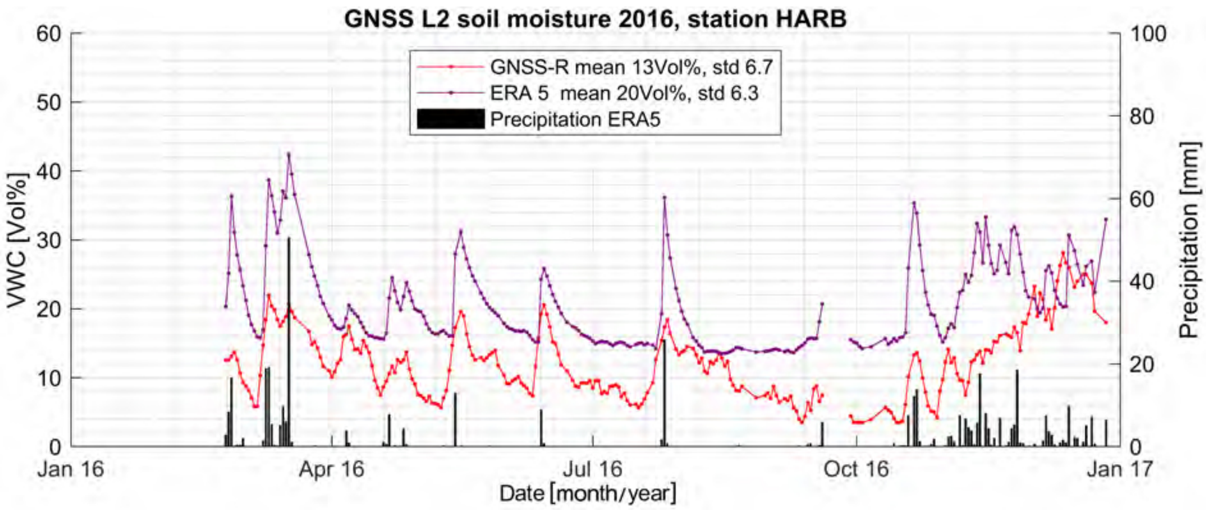

Figure D.27: Soil moisture retrievals for 2016 from IGS station Hartebeesthoek. Precipitation in black is from ERA5.

D.2.16 Mafikeng, South Africa

GNSS station Mafikeng is established in 2001 on a 2.4 metre high fundament in the airport of Mafikeng, North-West province of South Africa. Located at elevation of 1500m asl, the climate of the region is described as Semi-arid, according to the Köppen classification of climates (see appendix C). The annual precipitation totals around 550mm per year with minimum in the austral winter and maximum during January. The mean high temperatures over summer reach 31^{o}C, while the average low in winter go down to 4^{o}C.

The GNSS derived soil moisture starts since 2012 when the station started broadcasting SNR data. The large contrast in precipitation during the year provides very distinguishable soil moisture patterns (seen in figure D.28). Interestingly, the local winter provides the driest records for the station due to the lack of precipitation.

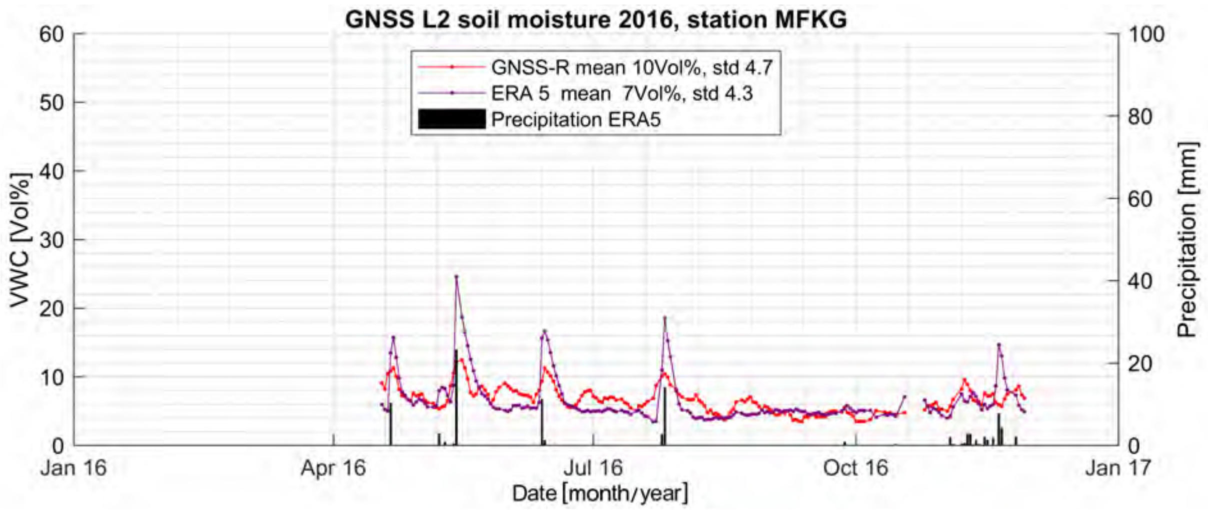

Figure D.28: Soil moisture retrievals for 2016 from IGS station Mafikeng. Precipitation in black is from ERA5.

D.2.17 Thohoyandou, South Africa

Thohoyandou is a city in northern South Africa and is situated in a semi-arid climate area, according to the Köppen classification (see appendix C). The daily mean temperature during the austral summer reaches 22°C with the minimum mean daily temperatures during June/July reaching 12°C. The annual accumulated precipitation is less than 500mm/year with maximum during the local summer. During the austral winter the monthly precipitation is close to 0.

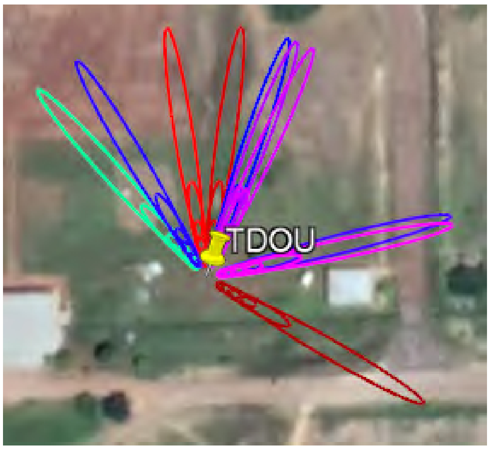

Figure D.29: IGS station Thohoyandou - Fresnel zones.

The GNSS station in Thohoyandou is established in 2001 with SNR first broadcast in 2012. The soil moisture record shows high amplitudes between rain events and dry season. In general the record agrees with the ERA5 data, but the residual soil moisture, as in most other stations is too high in the ERA5 dataset.

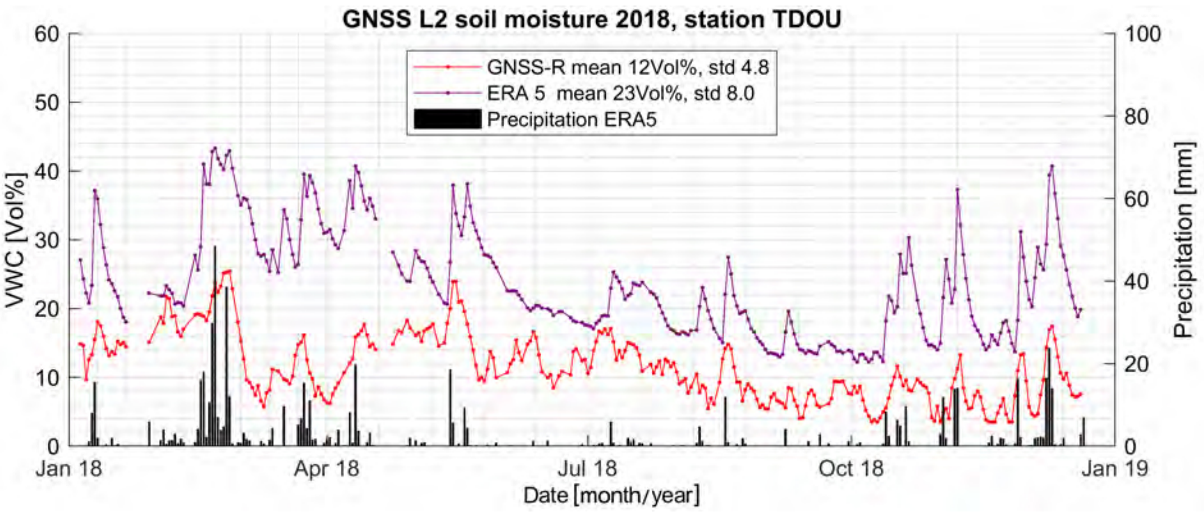

Figure D.30: Soil moisture retrievals for 2018 from IGS station Thohoyandou. Precipitation in black is from ERA5.

D.2.18 Sutherland, South Africa

GNSS station Sutherland (SUTH) is established in 1997 in the Sutherland observatory, South Africa. It is collocated with a VLBI station, as well as several GNSS sites, one of them being SUTM (*Vey et al.*, 2016a). Several buildings surround the station, but still many reflections come from bare soil and can be used for soil moisture evaluation the first SNR data were broadcast in 2001. The GNSS antenna is mounted on a 2 metre high pillar, 1800m asl The station surroundings are relatively dry and cold for the region with annual precipitation of less than 250mm/year. The peak of precipitation occurs during the austral winter. The average high temperatures during the local summer reach 27^{o}C, while the average lows during the local winter go down to -2^{o}C.

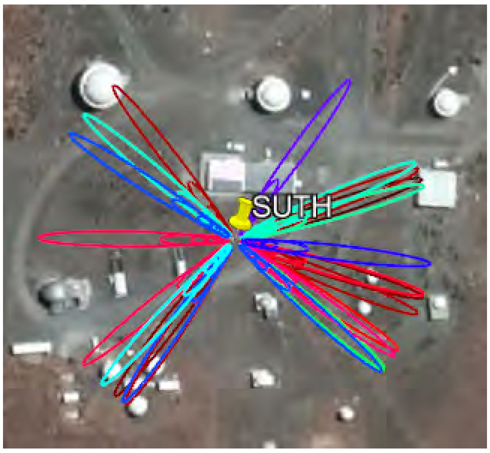

Figure D.31: IGS station Sutherland - Fresnel zones.

The soil moisture record responds precisely to the rare precipitation events. The ERA5 soil moisture estimates show low residual soil moisture, which complies with the GNSS observations. The station provides long enough reflections dataset for climate studies. Although meteorological observations for Sutherland are available, the recorded precipitation amounts are below reasonable (maximum daily precipitation of 2mm), which is the reason why the soil moisture is compared to ERA5 precipitation.

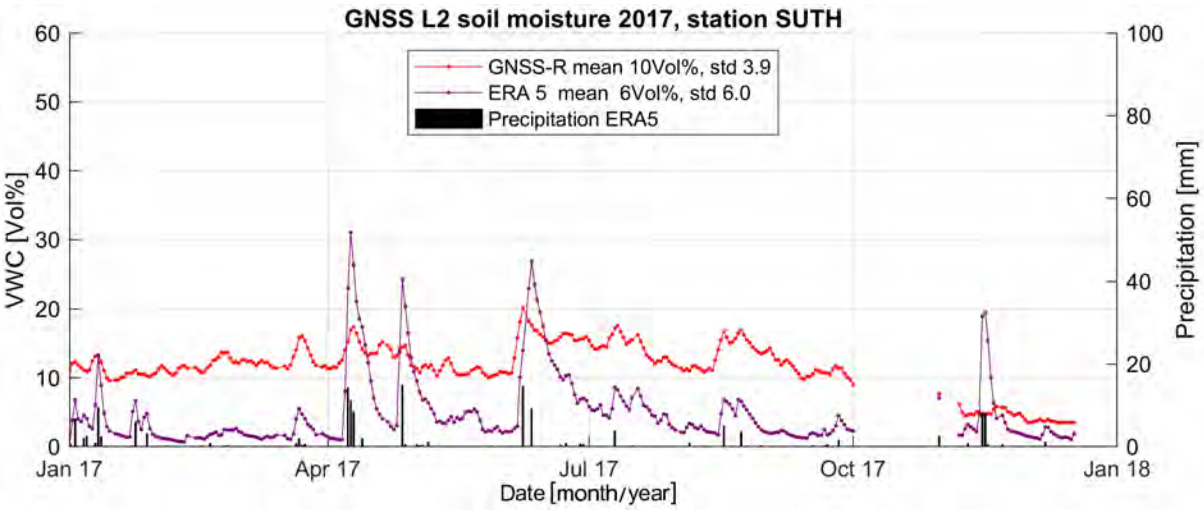

Figure D.32: Soil moisture retrievals for 2017 from IGS station Sutherland. Precipitation in black is from ERA5.

D.2.19 Calgary, Canada

As described in section 7.2.4, station Calgary is established in 1992 with first SNR data available since 2004. Calgary is situated in the state of Alberta on a mountain plateau 1247m asl The climate in this station, according to Köppen can be described as Humid continental (see appendix C). The annual rainfall for the region is around 320mm/year with with distinct maximum in the summer period. Rainfalls in winter are substituted with snowfalls, adding another 100mm/year of liquid water. The average high temperatures for the surrounding area are 31^{o}C in summer and the average low temperatures in winter reach -13^{o}C.

The soil record for the station is influenced greatly by the presence of snow cover during most of the snow season. The average temperatures in Calgary drop below 0^{o}C in October and then go above freezing in March. This shorter soil moisture observation season can be observed in the presented data for 2018 in figure D.33.

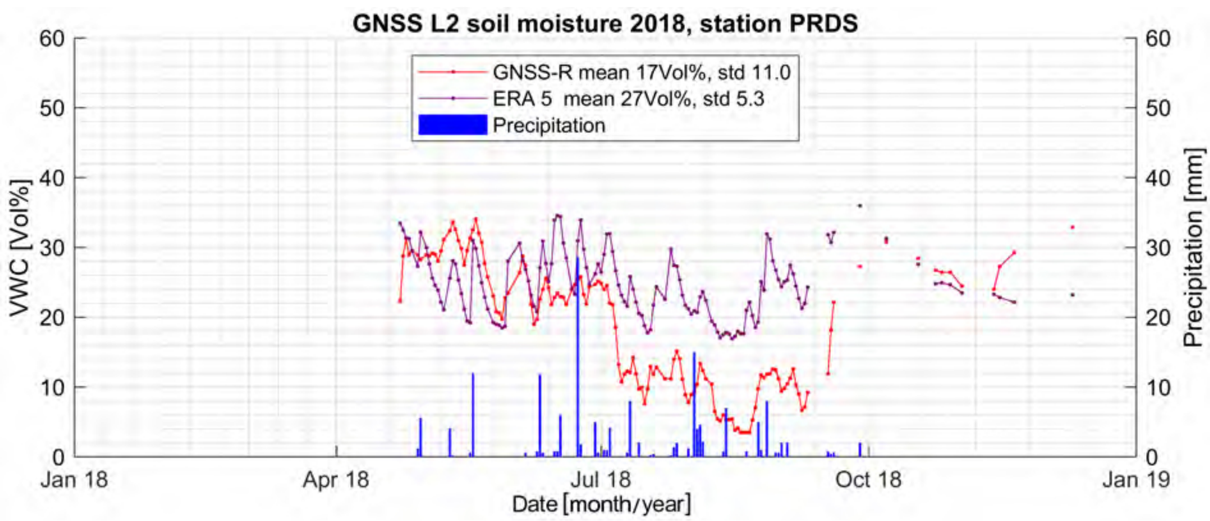

Figure D.33: Soil moisture retrievals for 2018 from IGS station Calgary. Precipitation in blue is from SYNOP observations.

D.2.20 Pickle Lake, Canada

Station Pickle Lake is located in a small village in province Ontario and is surrounded by many lakes. It is the only Subarctic station in this study, where soil moisture observations have been retrieved. The annual precipitation totals 520mm/year with additional 200mm/year of liquid snow equivalent. The precipitation maximum occurs during the short summer season, when the average temperatures reach 18 ^{o}C. The average temperature during the coldest month of January reaches -19^{o}C. The period when the average temperatures are above freezing is between April and October, leaving a short interval for soil moisture observations.

Figure D.34: IGS station Pickle Lake - Fresnel zones.

The soil moisture dataset, retrieved from Pickle Lake shows good responses to precipitation events. It should be noted, that the precipitation events from ERA5 not always coincide in time and magnitude with the real precipitation events. This is most probably the reason why the strongest precipitation, marked on figure D.35 coincides with a minimum in the soil moisture from GNSS-R and is shortly followed by the local maximum. The dataset has long gaps due to snowfall events.

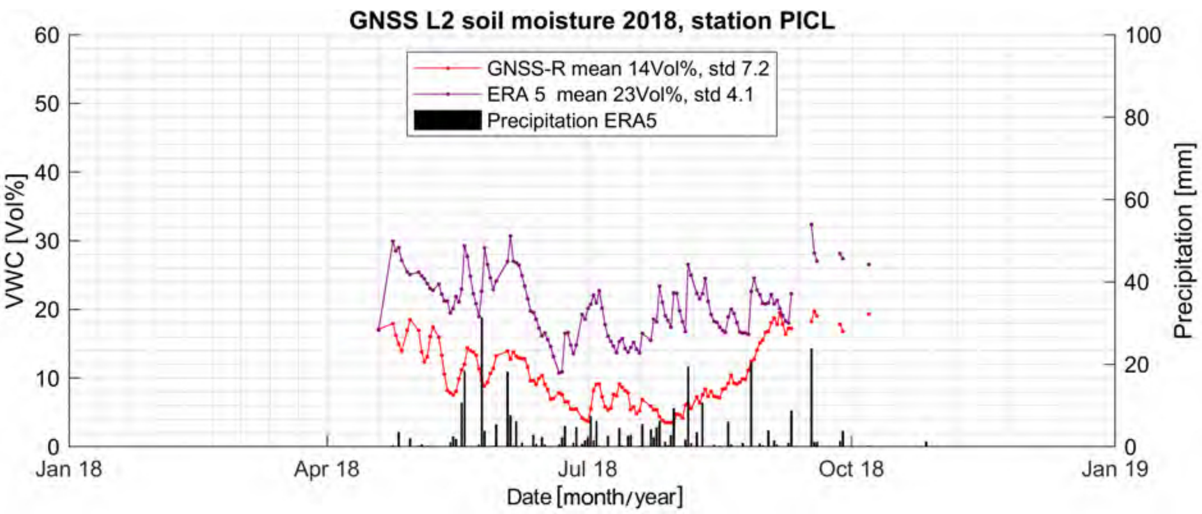

Figure D.35: Soil moisture retrievals for 2018 from IGS station Pickle Lake. Precipitation in black is from ERA5.

D.2.21 Shediac, Canada

GNSS station Shediac, just as described in section 7.2.7, is mounted on a 2.3m high concrete pillar, just by the coast of Shediac bay on the Northumberland Straights in the province of New Brunswick. The GNSS station is installed in 2004 and provides SNR data since 2007. The soil moisture retrievals cover the period since 2013, since problems in the SNR data is detected before that. The station is situated in a humid continental climate, according to the Köppen classification (see appendix C). The climate is strongly influenced by the cold water Labrador currents in the Northumberland straights. The average temperatures during the summer reach 20°C, while in winter the average temperatures go as low as -10°C.

The observed soil moisture response to precipitation events is strong (as seen on figure D.36). The minimum of soil moisture in the station is reached in late summer, which is typical for continental climates.

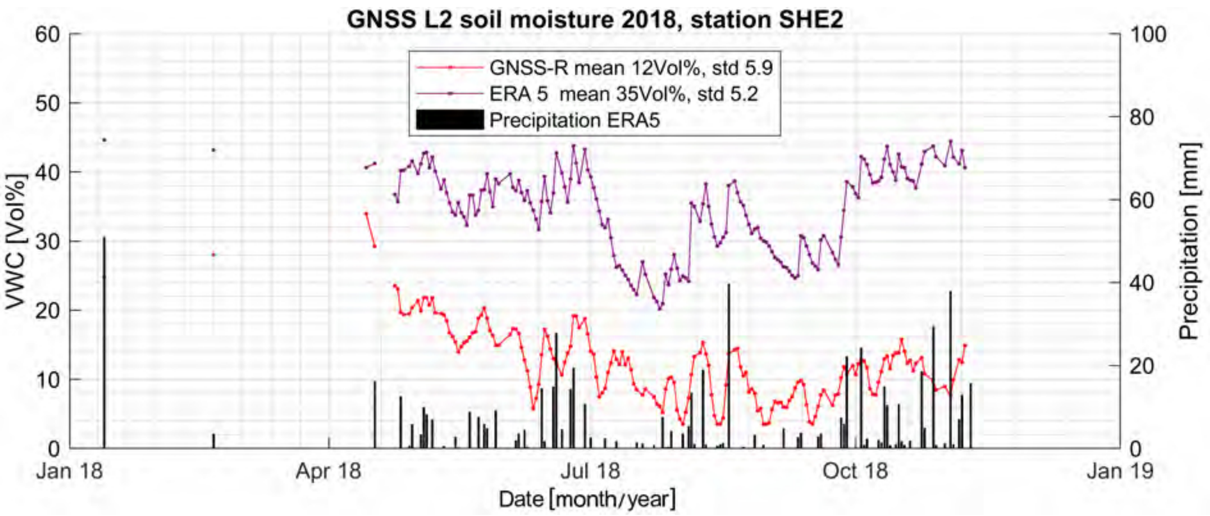

Figure D.36: Soil moisture retrievals for 2018 from IGS station Shediac. Precipitation in black is from ERA5.

D.2.22 Torrance, USA

Torrance is a city in the state of California, located on the Pacific coast south from Los Angeles. The city has Mediterranean climate, according to Köppen, and is influenced by the subtropical highland climate from the inland (see appendix C). The temperatures throughout the year vary from 19°C in winter to 26°C in summer on average. The precipitation has very distinct seasonality with maximum in precipitation during winter and almost no precipitation between May and September. The annual accumulated precipitation totals around 370mm/year, making the climate very dry.

The soil moisture record shows very precisely the low VWC amounts during the no rain summer periods with distinct precipitation events only during the boreal winter (see figure D.37). The residual soil moisture is with great certainty the minimum possible VWC in the record. ERA5 also shows very low soil moisture, thus verifying the GNSS-R results.

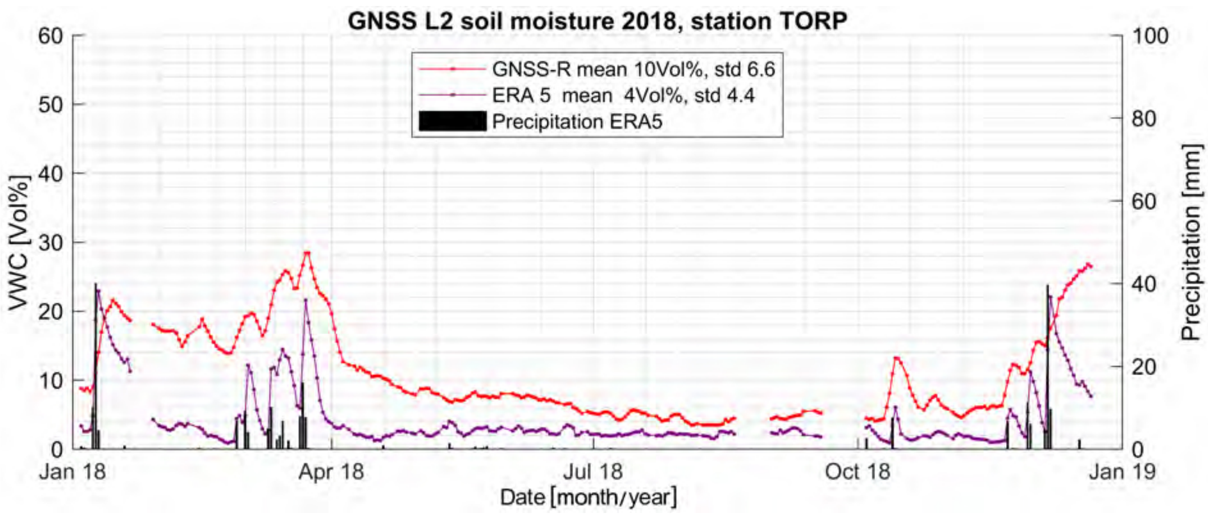

Figure D.37: Soil moisture retrievals for 2018 from IGS station torrance. Precipitation in black is from ERA5.

D.2.23 Curitiba, Brazil

GNSS station Curitiba is the only GNSS station from the IGS network, allowing soil moisture observations in the southern part of South America. The station is established in 2007 and started transmitting SNR data fairly recently, compared to the others - since late 2017. Curitiba is situated at the shores of the Atlantic Ocean in the southern part of Brazil and thus has Subtropical climate with oceanic influence, according to Köppen (see appendix C). The oceanic influence keeps the annual temperature amplitude low, thus the average temperature during the austral summer is around 21°C, while during winter around 13°C. Precipitation also has seasonality with January being the wettest month and August the driest. The annual precipitation is around 1500mm/year. The relative humidity in the region is also fairly high throughout the year.

Since the precipitation in Curitiba is significant and although there is precipitation seasonality, the soil moisture observation record for 2018 does not show significant seasonality. It is highly probable that the residual soil moisture, used for calibration of the dataset, does not reach its minimum values throughout the year and thus makes the GNSS-R observations inaccurate.

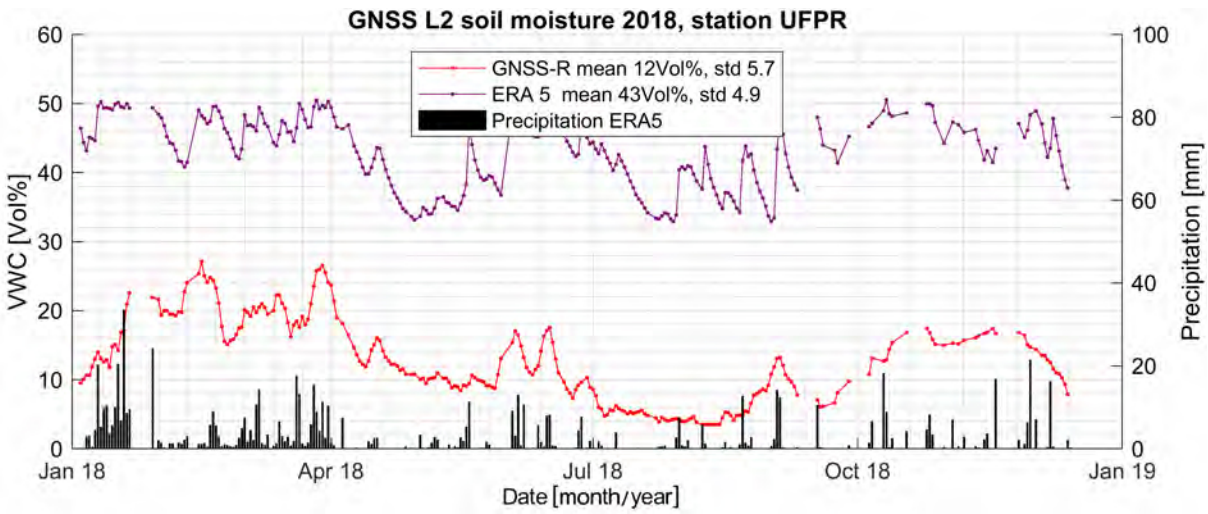

Figure D.38: Soil moisture retrievals for 2018 from IGS station Curitiba. Precipitation in black is from ERA5.

,